國立交通大學

電信工程研究所

博 士 論 文

無線定位追蹤訊號處理技術

Signal Processing for Mobile Location Estimation and Tracking in Wireless Networks

研 究 生：曾柏軒

指 導 教 授：方凱田 博士

中 華 民 國 一百 年 五 月

無線定位追蹤訊號處理技術

Signal Processing for Mobile Location Estimation and Tracking in Wireless Networks

研 究 生：曾柏軒　　Student：Po-Hsuan Tseng

指導教授：方凱田　　Advisor：Kai-Ten Feng

國 立 交 通 大 學

電 信 工 程 研 究 所

博 士 論 文

A Dissertation

Submitted to Institute of Communications Engineering

College of Electrical and Computer Engineering

National Chiao Tung University

in Partial Fulfillment of the Requirements

for the Degree of

Doctor of Philosophy

in

Communications Engineering

May 2011

Hsinchu, Taiwan, Republic of China

中華民國一百年五月

無線定位追蹤訊號處理技術

學生：曾柏軒　　指導教授：方凱田

國立交通大學電信工程研究所博士班

摘　　要

隨著位基服務商用價值俱增，即時定位演算法如何根據不同網路環境提升精準度是位基服務應用關鍵技術。本論文旨由統計訊號處理觀點提出適用於即時建置的無線定位追蹤演算法，並考慮以下無線環境：1)室外衛星定位系統；2)室內無線感測網路；3)手機蜂巢式系統。衛星定位系統在未被阻隔的室外環境中擁有較佳的效能。在衛星訊號微弱的環境中，無線感測網路適用於室內小範圍傳輸；手機蜂巢式系統可涵蓋前兩者訊號被遮掩或傳輸半徑不足的問題，並提供手機系統在資源管理中所需的基本精準度要求。本論文先以 4G 網路候選 IEEE 802.16m 系統討論定位精準度與其限制，作為如何在不同網路中啓動定位機制的範例。

為提供即時服務所需的定位資訊，本論文探討具封閉解特性、低演算複雜度的二階段最小方差法及卡曼濾波器。針對線性最小方差法推導其線性 Cramer-Rao lower bound (CRLB)，歸結出三項影響精準度的因素：1)***幾何效應***；2)***訊號模型及雜訊變異性***；3)***定位訊號源數目***。透過線性 CRLB 的分析，發現線性最小方差演算法手持裝置在訊號源所圍成幾何區域外的精準度因線性化產生偏差。本論文提出一幾何輔助線性定位演算(Geometry-assisted linearized localization, GALL) 彌補源於定位裝置與訊號的***幾何效應***所造成定位精準度差異。

以衛星及蜂巢式系統為例，考量兩系統不同的***訊號模型及雜訊變異***所提出的混合式定位架構來增進定位精準度。融合式 (Fusion-based hybrid, FH) 混合定位可有效整合兩系統定位結果，統一式（Unified-hybrid, UH) 混合定位架構包含混合訊號選擇及混合線性最小方差定位估測器，可採納異質網路訊號於單一估測器中。兩系統訊號結合可針對以下狀況增進精準度：1)市區：手機訊號密集但衛星訊號被阻隔；2)郊區：手機基地台訊號不足但衛星訊號品質佳。

當***定位訊號源數目***不足時，傳統定位追蹤演算法會因訊號源小於待估測參數的維度而導致無法定位的問題。針對行動裝置移動模型及透過速度與加速度的追蹤，以預測資訊作為幾何限制設計幾何輔助式預測性定位追蹤演算法 (Geometry-assisted predictive location tracking, GPLT)，在訊號源不足狀況下增進精準度。

根據合作式偵測，探討在混合直徑與非直徑環境中定位追蹤的問題。本論文提出一考量結合位置和通道狀況估測的自我導航演算法 (Cooperative self-navigation, CSN)，可有效結合其他行動裝置的量測訊號解決***訊號源不足***的問題，亦可在通道狀況追蹤有效整合不同***訊號模型及雜訊變異***。

Signal Processing for Mobile Location Estimation and Tracking in Wireless Networks

Student：Po-Hsuan Tseng　　Advisor：Dr. Kai-Ten Feng

Institute of Communications Engineering
National Chiao Tung University

ABSTRACT

With rising interests in location-based services (LBS) over the past decade, real-time localization algorithms with enhanced precision become critical for various applications under potentially challenging circumstances. Based on statistical signal processing theory, this dissertation solves the location estimation and tracking problems by incorporating the methods suitable for real-time implementation in different wireless network scenarios: 1) Global positioning system (GPS); 2) Wireless sensor network (WSN) system; and 3) Cellular-based positioning system. GPS is popular in commercial system and accurate in unobstructed outdoor environments. In environment where GPS coverage is either weak or absent, WSN can operate in a short-range indoor environment with high accuracy. On the other hand,cellular-based positioning based on the densely deployed base stations (BSs) in the city can cover the areas with weak GPS signal to maintain the LBS for resource management purpose. Note that the system level simulation of the fourth generation telecommunication system, e.g., IEEE 802.16m WiMAX system is first evaluated to discuss how to enable LBS and the performance limitation using the cellular system as an example.

In order to employ the location estimation and tracking for real-time services, closed-form signal processing techniques such as two-step least squares estimator and Kalman filter are adopted due to their lower computation complexities. Through the study of Cramer-Rao lower bound (CRLB), the limiting factors affecting the estimation accuracy include: 1) ***Geometric effect***; 2) ***Signal model or noise variance***; and 3) ***Number of signal sources***. This dissertation first characterizes the linearization effect by the proposed linearized location estimation problem based CRLB (L-CRLB). As further suggested by the L-CRLB, higher estimation accuracy can be achieved if the mobile station (MS) is located inside the geometry confined by the BSs compared to the case that the MS is situated outside of the geometric layout. This result motivates the design of geometry-assisted linearized localization (GALL) algorithm in order to compensate the linearization lost from the ***geometric effect***.

Hybrid location estimation schemes, which combine both the satellite- and cellular-based signal, are proposed to deal with the location estimation and tracking problem under various ***signal models or noise variances***. The proposed fusion-based hybrid (FH) architecture integrates the estimation results acquired from both the satellite- and cellular-based systems. On the other hand, the unified hybrid (UH) architecture employs the proposed hybrid signal selection scheme and the hybrid least squares estimator, which is capable of conducting location estimation within a selected set of signal sources from the heterogeneous networks. The proposed hybrid location architectures can provide accurate location estimation by adapting themselves under different environments, e.g., urban or rural area.

The location estimator associated with the Kalman filter, known as the two-stage location tracking architecture, is exploited in this dissertation to acquire location estimation and tracking for the MS.

However, most of the existing schemes become inapplicable for location tracking due to insufficient ***number of signal sources***. The proposed predictive location tracking (PLT) scheme utilizes the predictive information obtained from the Kalman filter to provide additional signal inputs for location estimator. Furthermore, the geometry-assisted PLT (GPLT) scheme incorporates the geometric dilution of precision (GDOP) information into algorithm design to achieve persistent accuracy for location tracking.

The problem of cooperative localization for MSs in the mixed line-of-sight/non-line-of-sight (LOS/NLOS) environment is investigated based on cooperative sensing. The proposed cooperative self-navigation (CSN) with joint position and channel tracking takes advantage over the noncooperative methods with the extra cooperative measurements to overcome the insufficient ***number of signal sources*** problem and over the methods without LOS/NLOS channel tracking to consider the effect of different ***signal models or noise variances***.

To summarize, the main contribution of this dissertation is to investigate the mobile location estimation and tracking problem. The methods suitable for real-time implementation is applied and analyzed based on statistical signal processing theory. In this dissertation, we have improved the estimation accuracy for real-time methods under three limiting factors as follows: 1) ***Geometric effect***; 2) ***Signal model or noise variance***; and 3) ***Number of signal sources***.

誌　　謝

首先感謝指導教授方凱田老師，提供多元且快樂的研究環境，鼓勵我們往不同方向發展，並給與學術上充裕的建議與支持。老師對與學生討論付出的心力，常從下午一路討論到半夜，還有對文章或計畫的要求，專注和仔細求證的態度都是我很好的學習典範。感謝 Prof. Zhi Ding 常深入淺出的提出建議，讓我更習慣從理論面思考問題。感謝電信所老師們的指導，十年來不同課程中的學習，讓我打下學術上的基礎。也感謝計畫合作過的老師及思考模式很實用的工程師們，提問間常帶給我許多不同的壓力，讓我更擅於整理和表達自己的想法。感謝口委們蒞臨指導，最後口試的洗禮讓我能用不同角度重新審視自己所完成的研究。

感謝家人的支持，讓我在沒有經濟壓力的狀況，自私地追逐我渴求的知識。感謝親愛的媽媽和妹妹，在我成長過程中一路的陪伴與鼓勵，分享我的苦與樂。也很感謝贊助過我的單位，像是嚴慶齡中心提供豐厚的出國補助，中技社、交大聯發科研究中心的獎助學金，及國科會千里馬計畫提供國內博士生增進研究視野，期許有昭一日也能幫助別人。

感謝所有 Mint Lab 至今的所有成員，讓我的研究生活充滿愜意愉快的氣氛。特別謝謝昭霖學長開拓的領域且不時產生充滿創意的想法，建華學長在多年共同討論中不時提供嚴謹的理論建議，仲賢學長的經驗傳授及對於計畫中標準研讀的指導。也感謝和我合作過的同學及學弟，和育群同學的合作不可思議地順利到我以為我可以申請教職，林志學弟對數學的熱愛完成了一個題目，完全不需操心的承澤學弟對於問題的不同詮釋方式和專注解救了一個想法，信龍學弟擅於陳述自己的題目讓大家有合作的機會。好鄰居裕彬同學專研不同理論的態度與研究精神值得我效仿。Mint Lab 扛霸子佳仕學弟敏銳的思路所帶給我的啓發，並承接了我的爛攤子，及多年同學文俊在研究過程中的苦水分享，同時追尋學位的過程讓我有很好的對照可以推著自己前進。

感謝大學同學們，看著你們出社會的順遂發展，不時地分享工作與及對研究狀態的鼓勵，也讓我能在安逸的學校環境中找尋努力的目標與方向。感謝所有朋友們每次見面必問的什麼時候畢業，讓我能砥礪自己加快腳步，此外也感謝身邊很晚出現的那個人的陪伴。

最後將這篇論文獻給我親愛的老爸，解決統計估測理論的問題算是跟最佳化理論沾上邊了。

柏軒 于從小生長的新竹及交大

民國一百年七月十九日

Contents

List of Figures

Chapter 1

Dissertation Overview

1.1 Introduction

Wireless positioning technologies for estimating the position of a *mobile station* (MS) have attracted a lot of attention over the past decade. The quality-of-service of positioning accuracy has been announced due to the issue of *enhanced 911* subscriber safety service requirements [1] in telecommunication system. With the assistance of information derived from the positioning system, the required performance and objectives for the targeted MS can be achieved with augmented robustness. In particular, there are increasing demands for commercial applications to adopt the location information within their system design, such as the self-navigation systems, the target tracking, the location-based billing, electronic healthcare, the wireless sensor networks (WSNs) [2, 3, 4], and the intelligent robotic [5] or transportation control management [6, 7]. With rising interest in location-based services (LBS) [8], localization algorithms with enhanced precision become critical for various applications under potentially challenging circumstance.

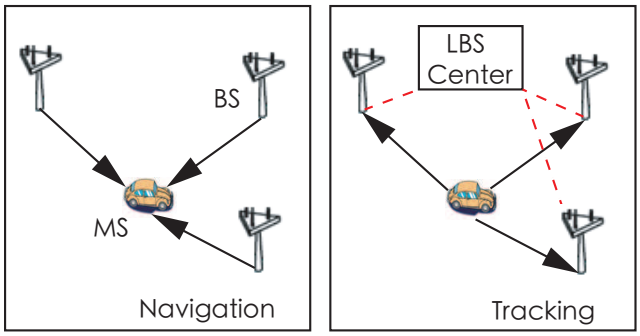

Figure 1.1: Schematic diagrams of the self-navigation and target tracking.

Self-navigation and target tracking are the two main applications as shown in Fig. 1.1. For self-navigation, a mobile unit needs to determine its own position based on its signal receptions from multiple radio stations of known positions. These radio stations are known as base stations

(BSs). The direction of the distance measurements is downlink and the location estimation can be performed at the MS. On the other hand, the target tracking or source localization problem refers to a network desire to monitor the MS's position. The MS broadcasts the uplink signal to multiple BSs. A LBS center then estimates the MS's position from the collection of BSs signal measurements. In fact, the self-navigation problem is a dual problem to the tracking problem in the mathematic perspective. In practice, the BS usually has better measurement quality. From a complexity point of view, uplink measurement results in higher system complexity since negotiation between the BSs is required. Localization determination time of the uplink scheme is also longer since the BSs should wait until all the measurements collected through the backbone network from the neighboring BSs have been communicated. On the other hand, the MS has all the measurements and does not require extra measurement exchange for downlink approaches. The other issue is that the power consumption of transmitting signals is regarded to be larger than receiving signals. Therefore, uplink transmission will consume more power which can be an important issue at the MS side. The architecture of the downlink (i.e., mobile-based) and the uplink (i.e., mobile-assisted) in telecommunication system is discussed in Chapter 6.

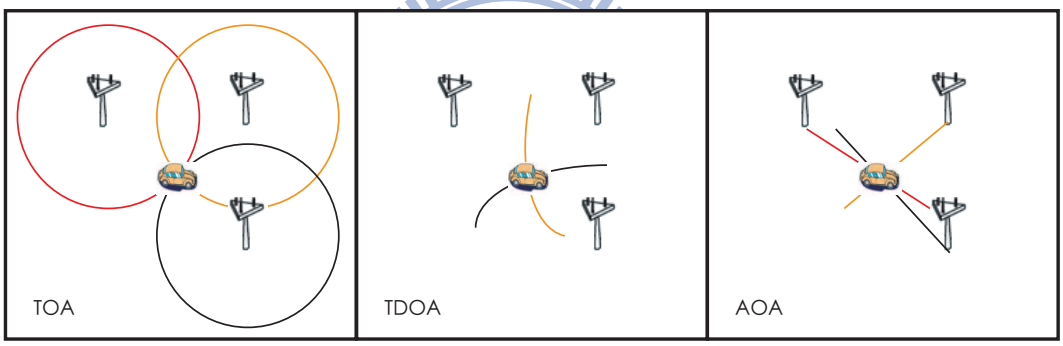

Figure 1.2: Geometric diagrams of the TOA, TDOA, and AOA measurement.

In general, the location determination process is composed of two parts as shown in Fig. 1.4: the distance or angle measurement and location estimation. A number of wireless positioning methods have been widely studied with various types of signal measurements, including time-of-arrival (TOA) [9], time difference-of-arrival (TDOA) [10], the received signal strength (RSS) [11] and the angle-of-arrival (AOA) [12] in Fig. 1.2. The signal models are different according to the environments, e.g., the satellite systems, the telecommunication systems, and the wireless sensor networks. With the signal measurements and the known position references, the location estimation schemes locate the position of an MS based on the measured radio signals from its neighborhood BSs. In a wireless environment with rich scatters, RSS measurement can be difficult to model and noisy. Therefore, alternative measurement models are more practical. In the TOA model, each receive unit only needs to identify a special signal feature such as a known preamble signal and record its time of arrival. TDOA is a common procedure to efficiently eliminate the clock bias

between the MS and the BSs by using measurements at two BSs, which is a main option in the telecommunication system. With the antenna arrays in the modern communication system, the AOA can also be obtained by measuring the difference in received phase at each element in the antenna array. Note that the location estimation process is the main focus of the dissertation.

Note that the global positioning system (GPS) is regarded as a mature commercialize system. Providing that the mobile device carries a GPS receiver, either GPS-based or a hybrid GPS with other types of measurements (e.g., signals from cellular system covered in Chapter 6) can be utilized to obtain a location estimate. However, the additional GPS receiver within an MS will increase the cost of the handset device. Further, the poor indoor coverage of GPS will result in decreased location estimation accuracy. In environment where GPS coverage is either weak or absent, wireless navigation and localization for mobile users have various practical applications. Different distance and angle measurement models are adopted to examine the location estimation and tracking problem in different wireless network environments.

1.2 Problem Statement

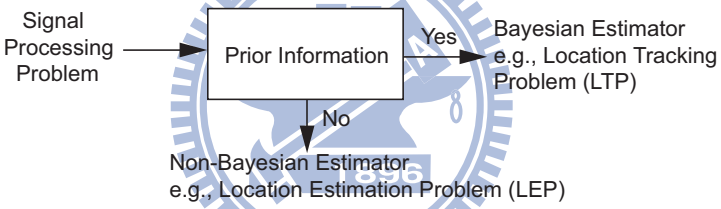

Figure 1.3: A schematic diagram of problem formulation.

The location estimation problem, which does not have any prior information about the MS's location, can be solved by a non-Bayesian class estimator, such as least squares (LS) estimator.

Problem 1.1 (Location Estimation Problem (LEP))**.** By collecting the measurements $\boldsymbol{r}$, the goal of the LEP is to generate a m-dimensional estimate $\hat{\boldsymbol{x}}$ of the MS's location. ◇

Considering that the MS moves dynamically following a state model, the distance measurements can be collected at every sample step. The historical distance measurements and location estimates can be regarded as the prior information for the location estimate. The location tracking problem, which has prior information about the MS's location, utilizes a Bayesian class estimator such as Kalman filter.

Problem 1.2 (Location Tracking Problem (LTP))**.** By collecting the measurements $\boldsymbol{r}^{(1:t)}$ from time instant 1 to t, the goal of the LTP is to generate a m-dimensional estimate $\hat{\boldsymbol{x}}^{(t)}$ of the MS's location at time instant t. ◇

The objectives of the dissertation are to enable signal processing techniques for the location estimation and tracking problems under different network scenarios.

1.3 Dissertation Organization

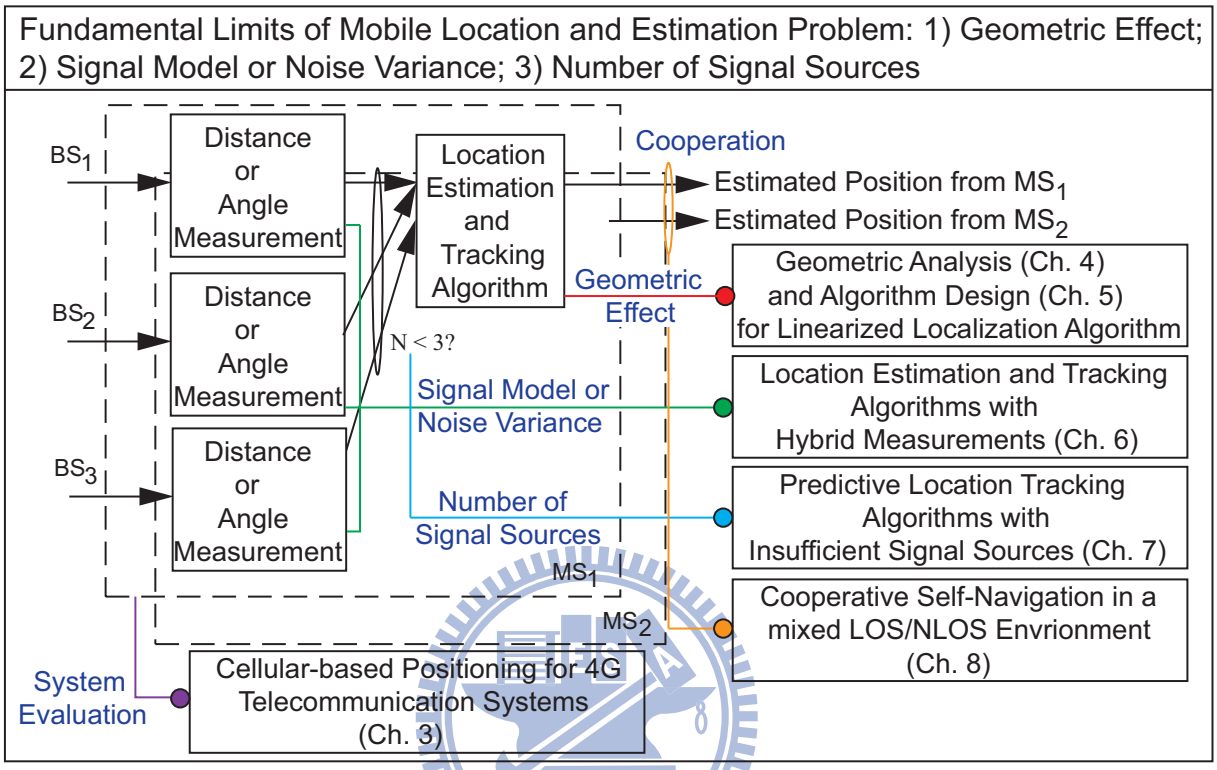

Figure 1.4: A schematic diagram of dissertation organization.

Chapter 2 illustrates the measurement models (i.e., TOA, TDOA and AOA) and the noise models (i.e., timing, and angle measurement noise models) which are utilized in this dissertation. Meanwhile, the linear least squares (LLS) and the two-step least squares (TSLS) estimators, which are the baseline non-Bayesian estimation algorithms in the dissertation, are introduced. The Kalman filter, which is the baseline Bayesian estimation algorithm, is also described in this chapter. Based on the preliminaries, the remaining chapters is organized as follows. The schematic diagram of dissertation organization is illustrated in Fig. 1.4.

This dissertation solves the location estimation and tracking problems by incorporating the methods suitable for real-time implementation from statistical signal processing theory in different wireless network scenarios: 1) GPS; 2) WSN; 3) cellular-based positioning system. Note that different distance and angle signals are measured and modeled in different wireless network environments. GPS is popular in commercial system and accurate in unobstructed outdoor environment. In environment where GPS coverage is either weak or absent, WSN can operate in a short-range indoor environment with high accuracy; cellular-based positioning based on the dense BSs deployments in the city can cover the corner for the weak GPS signal to maintain the LBS for resource management purpose. Note that the system level simulation of the fourth generation telecommu-

nication system (e.g., IEEE 802.16m WiMAX system) is first evaluated to discuss the performance limitation of positioning techniques using the cellular system as an example. In order to fulfill the positioning accuracy requirement of E-911 subscriber safety services, mobile telecommunication systems, e.g., Global System for Mobile Communications (GSM), High-Speed Downlink Packet Access (HSDPA), or potentially next generation telecommunication systems, adopt LBS as one of the key functions. Currently, two campaigns by 3rd Generation Partnership Project (3GPP) and the Institute of Electrical and Electronics Engineers (IEEE) are specifying standard drafts to meet the requirements of International Mobile Telecommunications (IMT)-Advanced for fourth-generation (4G) systems. LBS will be covered in both standards for the E-911 requirement and resource management purposes. It is well accepted that the multiple access technique for 4G networks will be orthogonal frequency division multiple access (OFDMA). Chapter 3 aims at both providing a framework for enabling LBS using next-generation systems and investigating the positioning accuracy for an OFDMA system. The feature of purely cellular-based positioning in the next generation system is illustrated, including the procedures for both the downlink (DL) and uplink (UL) timing measurements. Moreover, case studies of DL and UL system-level simulations for the IEEE 802.16m standard are performed and compared by considering the effects from multi-path, shadowing, and intercell interference.

It is recognized that the distance measurements [13] associated with the wireless location estimation schemes are inherently nonlinear. Linear estimators have been extensively utilized for wireless location estimation for their simplicity and closed-form property. In order to employ the location estimation and tracking for real-time service, the closed-form signal processing techniques such as two-step least squares estimator and Kalman filter are adopted due to lower computation complexity. In Chapter 4, the class of linear estimator by introducing an additional variable is discussed, e.g., the well-adopted LLS estimator. There exists information lost from the linearization of location estimator to the nonlinear location estimation, which prevents the linear estimator from approaching the Cramer-Rao lower bound (CRLB). Although linear estimator has been utilized for a long period, the linearized location estimation problem based CRLB (L-CRLB) is first derived to provide a portrayal that can fully characterize the behavior for this type of linearized location estimator. The relationships between the proposed L-CRLB and the conventional CRLB are obtained and theoretically proven. Furthermore, the geometric layout between the MS and the BSs that can achieve the minimum L-CRLB is also acquired. The geometric analysis will be beneficial to the deployment of BSs or the signal selection schemes targeting for this class of location estimation. Simulation results utilizing the LLS estimator as one of the implementation of the linearized location estimators further validate the theoretical proofs and the effectiveness of the L-CRLB.

Through the study of CRLB as shown in Remark 1, the limiting factors affect the estimation accuracy as: 1) **geometric effect**; 2) **signal model or noise variance**; 3) **number of signal sources**. As further suggested by the L-CRLB, higher estimation accuracy can be achieved if the MS is located inside the geometry confined by the BSs compared to the case that the MS is situated

outside of the geometric layout. This result motivates the proposal of geometry-assisted linearized localization (GALL) algorithm in Chapter 5 in order to consider the **geometric effect** associated with the linearization lost. Based on the initial estimation, the GALL algorithm fictitiously moves the BSs based on the L-CRLB criteria. Two different implementations, including the GALL with TSLS estimator (GALL-TSLS) and the GALL with Kalman filter (GALL-KF), are proposed to consider the situations with and without the adoption of MS's historical estimation. Simulation results show that the GALL-KF scheme can compensate the linearization lost and improve the performance of conventional location estimators.

Location algorithms for the MSs can generally be categorized into network- and satellite-based systems. Both types of systems have their advantages and limitations under different environments (i.e., urban or rural area). In Chapter 6, hybrid location estimation schemes, which combine both the satellite- and the network-based signals, are proposed to provide adaptation to various measurement models (i.e., TOA, TDOA, and AOA) to consider different **signal models or noise variances** for location estimation problem. By exploiting the fusion algorithm, the proposed fusion-based hybrid (FH) architecture integrates the estimation results that are acquired from both the satellite- and the network-based systems. Two different types of signal selection schemes are adopted within the FH architecture: 1) the fixed set of signal inputs approach and 2) the selective set of signal inputs approach. On the other hand, the unified hybrid architecture employs the proposed hybrid signal-selection scheme and the hybrid least square estimator, which can conduct location estimation within a selected set of signal sources from the heterogeneous networks. The Kalman filtering technique is exploited in the proposed algorithms to both eliminate the measurement noises and to track the trajectories of the MSs. Numerical results demonstrate that the proposed hybrid location schemes can provide accurate location estimation by adapting themselves to different environments.

The location estimators associated with the Kalman filtering techniques, as known as two-stage location tracking architecture, are exploited to both acquire location estimation and trajectory tracking for the mobile devices. However, most of the existing schemes become inapplicable for location tracking due to the deficiency of signal sources. In Chapter 7, two predictive location tracking algorithms are proposed to alleviate the insufficient **number of signal sources**. The Predictive Location Tracking (PLT) scheme utilizes the predictive information obtained from the Kalman filter in order to provide the additional signal inputs for the location estimator. Furthermore, the Geometry-assisted Predictive Location Tracking (GPLT) scheme incorporates the Geometric Dilution of Precision (GDOP) as **geometric effect** information into the algorithm design. Persistent accuracy for location tracking can be achieved by adopting the proposed GPLT scheme, especially with inadequate signal sources. Numerical results demonstrate that the GPLT algorithm can achieve better precision in comparison with other network-based location tracking schemes.

In Chapter 8, the cooperative measurements are adopted to generate a location estimate along

with the conventional non-cooperative measurement. We investigate the problem of cooperative self-navigation (CSN) for multiple mobile sensors in the mixed LOS and NLOS environment based on measuring TOA from the cooperative sensing. We derive an optimized recursive Bayesian solution to adopt a multiple model sampling based importance resampling particle filter to develop CSN that can accommodate non-linear and non-Gaussian position movement under different levels of channel knowledge. The CSN with joint position and channel tracking exhibits advantage over the noncooperative methods by utilizing additional cooperative measurements to increase the **number of signal sources**. It also shows improvement over the methods without channel tracking to consider different **signal models or noise variances**. Simulation results validate the advantage of cooperative sensing and channel condition tracking in mixed LOS/NLOS environment.

Chapter 2

Preliminaries

2.1 Mathematical Modeling of Signal Sources

In the dissertation, various signal sources are considered in different wireless network scenarios. In this section, generic models of signal sources are described with single MS estimation case. The notations would be slightly different according to different problem in each chapter. Note that the cooperative localization in Chapter 8 which considers multiple MSs estimation would have different notations.

2.1.1 Time of Arrival (TOA) Model

The signal model for the TOA measurements is utilized for m-dimensional (e.g., $m = 2$ or 3) location estimation and tracking problem. The set $\boldsymbol{r}^{(t)}$ contains all the available measured relative distance at time instant t, i.e., $\boldsymbol{r}^{(t)} = [r_1^{(t)}, \ldots, r_i^{(t)}, \ldots, r_{N^{(t)}}^{(t)}]$ where $N^{(t)}$ denotes the number of available BSs at time instant t. For notational simplicity, the TOA measurement from the anchor to the MS is multiplied by the speed of light c. Thus, the effective TOA measured relative distance between the MS and the i-th BS can be represented as

$$r_i^{(t)} = \zeta_i^{(t)} + n_i^{(t)} + e_i^{(t)} + b, \qquad \text{for} \quad i = 1, 2, ..., N^{(t)}, \tag{2.1}$$

The TOA measurement is contaminated with two types of noises: 1) the line-of-sight (LOS) noise $n_i^{(t)}$: a zero-mean random variable and 2) the none-line-of-sight (NLOS) noise $e_i^{(t)}$: a random variable with mean larger than zero. In the dissertation, the LOS noise would refer to the case $e_i^{(t)} = 0$. On the other hand, the NLOS noise would refer to both the $n_i^{(t)}$ and $e_i^{(t)}$ exist. The parameter b refers to the clock bias between the MS and the network, where the BS is assumed to synchronize with each other. In the synchronous network case considered in Chapter 4, 5, 7, and 8, the clock bias is assumed to be efficiently eliminated by the synchronous method as $b = 0$. Note that the time instant t would be removed for the notational simplicity in the case that the

parameter is irrelevant with the time. For example, the measurement considered in a non-Bayesian class location estimation is made at only one time instant, e.g., $r_i = \zeta_i + n_i + e_i + b$. On the other hand, the clock bias b between the MS and the network is the same at each time instant unless the clock adjustment has been made. The noiseless relative distance $\zeta_i^{(t)}$ in (2.1) between the MS's true position and the i-th BS can be acquired as

$$\zeta_i^{(t)} = \|\boldsymbol{x}^{(t)} - \boldsymbol{b}_i\|, \qquad \text{for} \quad i = 1, 2, ..., N^{(t)}, \tag{2.2}$$

where $\boldsymbol{x}^{(t)}$ represents m-dimensional MS's true position at time instant t and $\boldsymbol{b}_i$ is m-dimensional coordinate of the i-th BS (e.g., 3-dimensional coordinate of the i-th BS $\boldsymbol{b}_i = [x_i,\ y_i,\ z_i]^T$). The notations $\|.\|$ denotes the Euclidean norm of a vector and $[.]^T$ represents the transpose operator.

2.1.2 Time Difference of Arrival (TDOA) Model

Jointly estimating $\boldsymbol{x}^{(t)}$ and $b^{(t)}$ can be a challenging problem. In order to efficiently eliminate the clock bias in (2.1), the TDOA measurement can be obtained by calculating the time difference between the MS with respect to the i-th and the j-th BSs as

$$u_{i,j}^{(t)} = r_i^{(t)} - r_j^{(t)} = (\zeta_i^{(t)} - \zeta_j^{(t)}) + (n_i^{(t)} - n_j^{(t)}) + (e_i^{(t)} - e_j^{(t)}). \tag{2.3}$$

Note that TDOA measurement is a common procedure to estimate the position in the cellular system. The reference BS (i.e., $\boldsymbol{b}_j$ in (3.6)) is usually chosen as the serving BS (i.e., $\boldsymbol{b}_1$). The procedure transfers a circular equation of TOA measurement into a hyperbolic equation of TDOA measurement. Note that the two timing measurements (i.e., $r_i^{(t)}$ and $r_j^{(t)}$) coming from the i- and j-th BSs have independent noises. Though the clock bias is eliminated in the TDOA measurement, the noise is enhanced by 3 dB.

2.1.3 Angle of Arrival (AOA) Model

The horizontal and the vertical AOA measurements, which are available from the i-th BS with 3-dimensional coordinate $\boldsymbol{b}_i = [x_i,\ y_i,\ z_i]^T$, can be obtained as

$$\theta_i^{(t)} = \tan^{-1}\left(\frac{y^{(t)} - y_i}{x^{(t)} - x_i}\right) + n_{\theta_i}^{(t)}, \tag{2.4}$$

$$\phi_i^{(t)} = \tan^{-1}\left(\frac{z^{(t)} - z_i}{\sqrt{(x^{(t)} - x_i)^2 + (y^{(t)} - y_i)^2}}\right) + n_{\phi_i}^{(t)}, \tag{2.5}$$

where $\theta_i^{(t)}$ and $\phi_i^{(t)}$ represent the horizontal (azimuth) and the vertical (elevation) angles between the MS and i-th BS at time instant t. The AOA measurements in the cellular system is usually measured by the antenna array of the serving BS (i.e., $\boldsymbol{b}_1$). Note that 3-dimensional MS's coordinate at time instant t is denoted as $\boldsymbol{x}^{(t)} = [x^{(t)}, y^{(t)}, z^{(t)}]^T$. The parameters $n_{\theta_i}^{(t)}$ and $n_{\phi_i}^{(t)}$ are the combined noises associated with the angles $\theta_i^{(t)}$ and $\phi_i^{(t)}$.

2.2 Noise Model

2.2.1 Timing Measurement Noise Model

2.2.1.1 LOS Noise Model

The TOA LOS noises between the i-th BS and the MS (i.e., $n_i^{(t)}$ in (2.1)) are considered Gaussian-distributed as $n_i^{(t)} \sim \mathcal{N}(0, \sigma_n^2)$ with different noise standard deviation σ_n. The NLOS noise $e_i^{(t)}$ is assumed to be zero in the case.

2.2.1.2 Timing Measurement Noise Model in Cellular Network

In the cellular-based network, the fading including multi-path and shadowing fading affect the timing measurement result. The traveling distance in the cellular network would be positive bias, which refers to the NLOS problem. In fact, the NLOS problem in timing measurement comes from both power and delay effects. The path gain of the NLOS signal suffers higher shadowing variance, higher attenuation (i.e., power decays within the exponent of the distance), and penetration loss by traveling through walls. The limited received power degrades the performance of the timing measurement. On the other hand, the delay of NLOS propagation is biased by the multi-path model. The first arriving path will not necessarily be the strongest signal because of multi-path unresolvable. An exponential distribution is assumed for the NLOS model in [14], which considers the power attenuation, shadowing, and the multi-path fading in the model, with the distribution of $p_{e_i^{(t)}}(\upsilon)$ as

$$p_{e_i^{(t)}}(\upsilon) = \begin{cases} \frac{1}{\upsilon_i} e^{\frac{-\upsilon}{\upsilon_i}} & \upsilon > 0 \\ 0 & \upsilon \leq 0 \end{cases} \tag{2.6}$$

where $\upsilon_i = c \cdot \tau_i = c \cdot \tau_m \zeta_i^{\varepsilon} \omega$. The parameter τ_i is the root mean square delay spread between the i-th BS to the MS; τ_m is the median value of τ_i according to the environments, whose value is selected as 0.4 μs and 0.1 μs for the urban and rural environment, respectively. ε is the path loss exponent which is assumed to be 0.5. The shadow fading factor ω is a log-normal random variable with zero mean and standard deviation σ_ω chosen as 4 dB in the simulations. The TOA LOS noises between the i-th BS and the MS (i.e., $n_i^{(t)}$ in (2.1)) are considered Gaussian-distributed

as $n_i^{(t)} \sim \mathcal{N}(0, \sigma_n^2)$.

2.2.1.3 Timing Measurement Noise Model in Satellite Network

The probability distribution of the LOS noise $p_{n_i^{(t)}}(\gamma)$ for the set of satellites is selected as

$$p_{n_i^{(t)}}(\gamma) = \mathcal{N}(0, \sigma_n^2(\gamma)) \tag{2.7}$$

where the variance is defined as $\sigma_n(\gamma) = [a + d^2 \cdot 10^{\frac{-\gamma}{10}}]^{\frac{1}{2}}$. The parameters $a = 10$ m^2 and $d = 150$ m^2 are determined by user equipment. The SNR value γ, which is adopted from [15] as an input to a variance model for GPS pseudo-range measurement, is an uniform distributed random variable. Note that the timing measurement of satellite network is usually considered as LOS measurement, which leaves $e_i^{(t)} = 0$.

2.2.2 Angle Measurement Noise Model in Cellular Network

The noise models for the AOA measurements (i.e., n_θ and n_ϕ in (2.4) and (2.5)) are both assumed as Gaussian-distributed with $\mathcal{N}(0, \sigma_\theta^2)$ and $\mathcal{N}(0, \sigma_\phi^2)$, where σ_θ and σ_ϕ are chosen as 10^o and 5^o respectively for the urban and rural environment.

2.3 Linear Least Squares (LLS) Estimator

The linear least squares (LLS) estimator [16] is one of the representative methods to transfer the original nonlinear location estimation problem (LEP) into a linear problem by introducing an extra variable. In this section, 2-dimensional LLS estimator is illustrated as an example based on the TOA measurements. The time instant t is removed since the LLS estimator is a non-Bayesian estimator. By deriving (2.2) with the relationship $R = x^2 + y^2$, the following matrix can be acquired as

$$\mathbf{M}_1 \boldsymbol{\theta} = \mathbf{J}_1, \tag{2.8}$$

where

$$\mathbf{M}_1 = \begin{bmatrix} -2x_1 & -2y_1 & 1 \\ -2x_2 & -2y_2 & 1 \\ . & . & . \\ -2x_N & -2y_N & 1 \end{bmatrix}, \quad \theta = \begin{bmatrix} x \\ y \\ R \end{bmatrix}, \quad \mathbf{J}_1 = \begin{bmatrix} r_1^2 - \kappa_1 \\ r_2^2 - \kappa_2 \\ . \\ r_N^2 - \kappa_N \end{bmatrix}. \tag{2.9}$$

where $\kappa_i = x_i^2 + y_i^2$. Without any prior information on the statistics of the TOA measurements, the LEP defined in Problem 1.1 can be directly solved by finding the optimum $\hat{\boldsymbol{\theta}}$ by minimizing

the LS objective function

$$\hat{\boldsymbol{\theta}}_{LS} = \arg\min_{\boldsymbol{\theta}} ||\mathbf{M}_1\boldsymbol{\theta} - \mathbf{J}_1||^2. \tag{2.10}$$

No assumption about the measurement noise distribution has been made by utilizing LS objective function. Note that when the measurement noise is Gaussian distributed, (2.10) becomes a ML estimation.

The LS cost function is a quadratic function in $\boldsymbol{\theta}$ indicating that there is a unique minimum in (2.10). By considering the weighted LS (WLS) estimator, the estimation error is obtained as $\psi_1 = \mathbf{M}_1\hat{\boldsymbol{\theta}} - \mathbf{J}_1 = 2\mathbf{B}_1\mathbf{n}_1 + \mathbf{n}_1^2$ where $\mathbf{n}_1 = [n_1, \ldots, n_i, \ldots, n_N]$ represents the measurement noise vector in (2.1). The weight matrix $\boldsymbol{\Psi}_1$ can be acquired by neglecting the square term $\mathbf{n}_1^2$ as

$$\boldsymbol{\Psi}_1 = E[\psi_1\psi_1^T] = 4\mathbf{B}_1\, E[\mathbf{n}_1\mathbf{n}_1^T]\, \mathbf{B}_1 = 4\mathbf{B}_1\mathbf{I}_{\boldsymbol{\zeta}}\mathbf{B}_1, \tag{2.11}$$

where $\mathbf{B}_1 = \text{diag}\{[r_1, \ldots, r_i, \ldots, r_N]\}$ and $\mathbf{I}_{\boldsymbol{\zeta}} = \text{diag}\{[\sigma_1^2, \ldots, \sigma_i^2, \ldots, \sigma_N^2]\}$. The LLS position estimate is simply extracted from the first and second entries of $\hat{\boldsymbol{\theta}}$ (i.e., $\hat{\boldsymbol{\theta}}_{LS} = [\hat{x}_{LS}, \hat{y}_{LS}, \hat{R}_{LS}]^T$) by adopting the LLS method (i.e., $\hat{\boldsymbol{x}}_{LS} = [\hat{x}_{LS}, \hat{y}_{LS}]^T$)

$$\hat{\boldsymbol{x}}_{LS} = \mathbf{P}\,(\mathbf{M}_1^T\boldsymbol{\Psi}_1^{-1}\mathbf{M}_1)^{-1}\mathbf{M}_1^T\boldsymbol{\Psi}_1^{-1}\mathbf{J}_1, \tag{2.12}$$

where $\mathbf{P} = [1\,0\,0;\ 0\,1\,0]$.

2.4 Two-Step Least Squares (TSLS) Estimator

In this section, the 2-dimensional two-step LS (TSLS) estimator [17] is illustrated as an example based on the TOA measurements. The concept of TSLS method is to acquire an intermediate location estimate in the first step by assuming that $\boldsymbol{x}$ and R are not correlated. Note that this first step is exactly the LLS method in Section 2.3 which solves the linearized LEP instead of the conventional LEP. Without any prior information on the statistics of the TOA measurements, the LEP can be directly solved by finding the optimum $\hat{\boldsymbol{x}} = [\hat{x},\ \hat{y}]^T$ by minimizing the LS objective function with the constraint $R = x^2 + y^2$

$$\hat{\boldsymbol{x}} = \arg \min_{\substack{\boldsymbol{\theta}=[x,\ y,\ R]^T \\ R=x^2+y^2}} ||\mathbf{M}_1\boldsymbol{\theta} - \mathbf{J}_1||^2. \tag{2.13}$$

Based on the result from the LLS estimator $\hat{\boldsymbol{x}}_{LS}$, the TSLS method approximates the (2.13) by forming another linear equation to solve the (2.13) by releasing the assumption that $\boldsymbol{x}$ and R are uncorrelated by adjusting the intermediate result to obtain an improved location estimate. Therefore, the correlation relationship can be applied and the elements within the second step of

the TSLS estimator formulation, i.e., $\mathbf{M}_2[\hat{\boldsymbol{x}}]^{(2)} = \mathbf{J}_2$, are obtained as

$$\mathbf{M}_2 = \begin{bmatrix} 1 & 0 & 0 \\ 0 & 1 & 0 \\ 1 & 1 & 0 \end{bmatrix}, \qquad \mathbf{J}_2 = \begin{bmatrix} (x_{LS})^2 \\ (y_{LS})^2 \\ R_{LS} \end{bmatrix}, \tag{2.14}$$

with $[\hat{\boldsymbol{x}}]^{(2)} = [([\hat{x}]^{(2)})^2, ([\hat{y}]^{(2)})^2\ ]^T$. It can also be solved by the weighted LS formulation with the weighting matrix $\boldsymbol{\Psi}_2$ of the second step as

$$\boldsymbol{\Psi}_2 = 4\mathbf{B}_2 \mathrm{cov}(\hat{\boldsymbol{\theta}})\mathbf{B}_2 = 4\mathbf{B}_2(\mathbf{M}_1{}^T\boldsymbol{\Psi}_1{}^{-1}\mathbf{M}_1)^{-1}\mathbf{B}_2, \tag{2.15}$$

where $\mathbf{B}_2 = \mathrm{diag}\{[x_{LS},\ y_{LS},\ 1/2]\}$. With the relationship of $R = x^2 + y^2$, it can be observed that the variable R is removed from $\boldsymbol{\theta}$ such as to form the reduced dimension vector of $[\hat{\boldsymbol{x}}]^{(2)}$. The MS's position estimate by using the TSLS estimator can be obtained by taking element-wise square root as $\hat{\boldsymbol{x}}_T = ([\hat{\boldsymbol{x}}]^{(2)})^{1/2} = [[\hat{x}]^{(2)},\ [\hat{y}]^{(2)}]^T$.

2.5 Kalman Filter

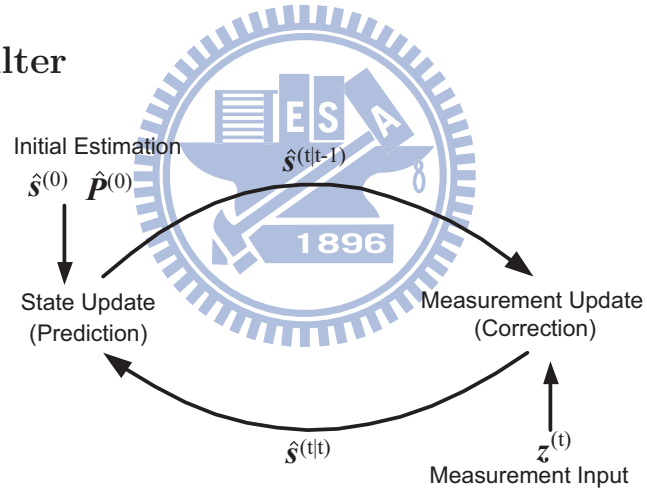

Figure 2.1: A schematic diagram of the Kalman filter.

The Kalman filter [18, 19], which is a linear model based on the Markov chain perturbed by Gaussian noise, is one of the efficient Bayesian class estimator to solve the location tracking problem (LTP) in Problem 1.2. Fig. 2.1 illustrates the concept of Kalman filter. With the prior information coming from the state update and the likelihood information coming from the measurement update, the Kalman filter obtains a posterior estimate in a minimum mean square error estimation sense. The measurement and state equations for the Kalman filter can be represented as

$$\boldsymbol{z}^{(t)} = \mathbf{E}\hat{\boldsymbol{s}}^{(t)} + \boldsymbol{m}^{(t)}, \tag{2.16}$$

$$\hat{\boldsymbol{s}}^{(t)} = \mathbf{F}\hat{\boldsymbol{s}}^{(t-1)} + \boldsymbol{p}^{(t)}, \tag{2.17}$$

where $\hat{\boldsymbol{s}}^{(t)}$ represents the estimated state/output and $\boldsymbol{z}^{(t)}$ denotes the measurement input of the Kalman filter. The states that we are interested in the LTP include the MS's position, velocity and acceleration. The matrix $\mathbf{E}$ and $\mathbf{F}$ refers to the linear relations for the measurement and state model. The variables $\boldsymbol{m}^{(t)}$ and $\boldsymbol{p}^{(t)}$ denote the measurement and the process noises associated with the covariance matrices $\mathbf{R}$ and $\mathbf{Q}$ within the Kalman filter formulation.

With the measurement and state equations as in (2.16) and (2.17), the Kalman filter estimates the state as the prediction phase in Fig. 2.1,

- Predicted (a prior) state estimate: $\hat{\mathbf{s}}^{(t|t-1)} = \mathbf{F}\hat{\mathbf{s}}^{(t-1|t-1)}$
- Predicted (a prior) estimate covariance: $\mathbf{P}^{(t|t-1)} = \mathbf{F}\mathbf{P}^{(t-1|t-1)}\mathbf{F}^{\mathrm{T}} + \mathbf{Q}^{(t)}$

and the correction phase in Fig. 2.1

- Innovation or measurement residual: $\tilde{\mathbf{y}}^{(t)} = \mathbf{z}^{(t)} - \mathbf{E}\hat{\mathbf{s}}^{(t|t-1)}$
- Innovation (or residual) covariance: $\mathbf{S}^{(t)} = \mathbf{E}\mathbf{P}^{(t|t-1)}\mathbf{E}^{\mathrm{T}} + \mathbf{R}^{(t)}$
- Optimal Kalman gain: $\mathbf{K}^{(t)} = \mathbf{P}^{(t|t-1)}\mathbf{E}^{\mathrm{T}}[\mathbf{S}^{(t)}]^{-1}$
- Updated (a posterior) state estimate: $\hat{\mathbf{s}}^{(t|t)} = \hat{\mathbf{s}}^{(t|t-1)} + \mathbf{K}^{(t)}\tilde{\mathbf{y}}^{(t)}$
- Updated (a posterior) estimate covariance: $\mathbf{P}^{(t|t)} = (I - \mathbf{K}^{(t)}\mathbf{E})\mathbf{P}^{(t|t-1)}$

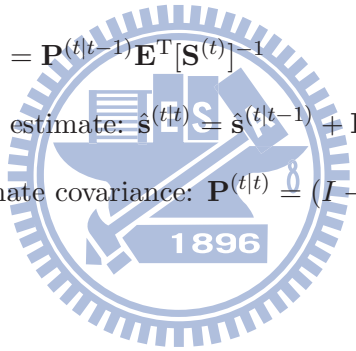

Chapter 3

Cellular-based Positioning for Next Generation Telecommunication Systems

- Since various wireless networks are considered in the dissertation, the chapter serves as an guideline on how to enable location estimation and tracking and evaluate the system level simulation using a 4G network. We discuss the limitations of the positioning in the downlink and uplink directions. [1]

3.1 Introduction

In order to meet positioning accuracy requirements, existing mobile telecommunication systems, e.g., Global System for Mobile Communications (GSM), High-Speed Downlink Packet Access (HSDPA), adopt LBS as one of the key functions due to public safety considerations. It should be noted that the positioning accuracy should meet the system requirements that are defined for emergency 911 (E-911) [1], i.e., less than 100 meters of estimation error 67% of the time and less than 300 meters 95% of the time. Currently, two campaigns by 3GPP and IEEE are specifying standard drafts to meet the requirements of international mobile telecommunications (IMT)-advanced for fourth-generation (4G) systems. LBS will be covered in both standards in order to meet the E911 requirement and for the resource management purposes. It is well-accepted that the multiple access technique for 4G networks will be orthogonal frequency-division multiple access (OFDMA). This chapter aims at both providing a framework for enabling LBS using next generation systems and investigating the limiting factors of positioning accuracy for an OFDMA system. Since the

[1] The chapter is based on [B-1] Po-Hsuan Tseng, and Kai-Ten Feng, "Chapter 31. Cellular-based Positioning for Next Generation Telecommunication Systems," accept and to appear as a book chapter of *Handbook of Position Location: Theory, Practice and Advances*, Wiley-IEEE Press, ISBN: 978-0-470-94342-7.

standardization schedule of the IEEE campaign is earlier than 3GPP for a potential IMT-advanced standard up to now, this chapter is thus based on the IEEE 802.16m [20] standard.

It is also noted that the possibility of using global positioning system (GPS) measurements is also specified in the IEEE 802.16m standard. Providing that the MS carries a GPS receiver, either GPS-based or a hybrid GPS and cellular-based estimate [21] can be utilized to obtain a location estimate. However, the additional GPS receiver within an MS will increase the cost of the handset device. Further, the poor indoor coverage of GPS will result in decreased location estimation accuracy. On the other hand, pure cellular-based measurements do not require an additional receiver for the acquisition of satellite signals and the indoor coverage problem can be resolved by proper cellular planning. Therefore, in this chapter, we aim at evaluating location estimation performance based on purely cellular network signals.

In general, the location determination process is composed of two parts: the distance or angle measurement and location estimation. The positioning technique locates the position of a MS based on the measured radio signals from its nearby base stations (BSs). The distance measurement requires the negotiation between the MS, the serving BSs and the neighboring BSs. Therefore, the mechanism for distance measurement is specified in the standard, while the distance and the location estimation algorithms are open to the manufacturer. There are several distance-related measurements that can be obtained within the IEEE 802.16m standard, which are classified as follows: (a) Signal strength measurement: received signal strength indicator (RSSI), carrier to interference-plus-noise ratio (CINR); (b) Angle measurement: direction-of-arrival (DOA); and (c) Timing measurement: time difference of arrival (TDOA), time of arrival (TOA). Since signal strength measurements are considered to be sensitive to the network environment, it is necessary to obtain channel statistics in advance. Furthermore, angle measurement error when the MS is far from the BS can result in a large ambiguity region which equates to large MS location error. On the other hand, the higher bandwidth of the IEEE 802.16m system compared to existing telecommunication systems makes timing estimation more reliable. In this chapter, we will focus on the different options to perform timing measurements in the IEEE 802.16m standard. By adopting the well-known maximum correlation method for timing estimation and the Taylor series approach for location estimation [22], the positioning accuracy will be evaluated. The detailed mechanisms for wireless positioning will be discussed by using the downlink/uplink (DL/UL) timing measurements defined in the IEEE 802.16m standard.

In the IEEE 802.16m specification, the BSs are defined to be synchronized with GPS, where all the time frames broadcast by the BSs are considered to be aligned. However, clock synchronization between the MS and the BSs is difficult to maintain. Thus, TDOA is a common procedure to efficiently eliminate the clock bias between the MS and the BSs by using measurements at two BSs. In order to maintain the orthogonality property, both timing and frequency synchronization are required for the DL and UL in an OFDMA system. The basic LBS support is to utilize the specified waveform in the IEEE 802.16m standard, such as preamble sequences for the DL and

ranging codes for the UL, to measure the distance information. In the DL direction, the preamble sequence is utilized for initial access, channel estimation, and synchronization. By obtaining the preamble sequences from different BSs, the MS can estimate the time difference by computing the correlation of preambles from these BSs. On the other hand, the ranging channel is designed for the BS to measure the assigned code sequence which is transmitted by the MS. The ranging scheme measures the round-trip delay, when the BS assigns a code sequence to the MS and the MS sends the sequence back at a rendezvous time. The time of arrival information between the MS and the BSs can consequently be obtained. Using a TOA information exchange through the backbone network, the UL TDOAs can be calculated based on the ranging results.

In order to further illustrate the LBS performance of the IEEE 802.16m system, both link level and system level simulation are performed in this chapter to demonstrate the limiting factors that affect the performance for DL/UL estimation. The timing estimation is corrupted by several channel effects such as multipath fading, shadow fading, and inter-cell interference. As for DL LBS, inter-cell interference can be considered as the main performance-limiting factor. Two different approaches are utilized to deal with inter-cell interference for enhanced LBS support, including signal processing at the physical layer and scheduling algorithms at the medium access control (MAC) layer. From the physical layer perspective, interference cancellation techniques [23] can be conducted at the receiver. The strongest preamble from the serving BS will be identified by the estimation method first and consequently be removed. The second and third preamble signals can therefore be detected with less interference from the serving BS. The second scheme refers to the enhanced LBS support [24] [25] in the IEEE 802.16m standard, which allows a specific enhanced LBS waveform to be transmitted. From the MAC layer perspective, designated BSs are grouped together as preamble location groups (PLGs) in order to form a DL LBS zone (D-LBS zone). Each PLG transmits a preamble signal in a different time slot, which reduces the number of concurrent preamble transmissions to efficiently reduce the inter-cell interference. A cell-grouping example which adopts the coordination of three BSs to mitigate the inter-cell interference is desrcibed in this chapter. Clearly, there will be less inter-cell interference as compared to the case where the BSs are simultaneously broadcasting preamble signals. The limitation of the UL performance is the hearability problem, i.e., the received signal quality at the neighboring BS is worse. Note that this is a fundamental conflict between the cellular concept and positioning requirements. In other words, cellular is based on signals only being heard by a single base station (or perhaps two or more for diversity) to maximize spatial reuse. Position location, on the other hand, is improved by having many base stations receive the signal which would result in reduced spatial reuse. The hearability problem comes from: (a) The maximum transmission power of the MS is less than a half of the transmission power of the BS; (b) Power control to the serving BS is performed. The comparisons between the basic, enhanced DL and the basic UL positioning techniques are illustrated in this chapter with a detailed performance evaluation.

To summarize, the contents that will be covered in this chapter are as follows:

- The basic features of cellular-based positioning in next generation 4G systems (as exemplified by the 802.16m standard) will be illustrated.
- The detailed procedures for both UL and DL timing measurements (e.g., TDOA) for positioning will be described.
- The impact of TDOA on positioning in the DL and UL will be assessed.
- System-level simulations for an IEEE 802.16m compliant system will be performed including the effects from multipath, shadowing, and inter-cell interference.
- The limiting factors for positioning accuracy will be discussed.
- Two approaches for dealing with inter-cell interferences on the DL transmission (specifically, signal processing and scheduling methods) will be compared and discussed.

3.2 An Overview of LBS in 4G Telecommunication Systems

The support for LBS in the IEEE 802.16m standard is classified into two categories: (a) basic LBS (b) enhanced LBS support. The basic LBS support refers to the scheme that it can be performed with the predefined sequences such as the preamble sequences or the ranging codes. The enhanced LBS support such as D-LBS zone includes special location beacons which should be coordinated by multiple BSs. In this section, we focus on the options of applying TDOA measurements for both basic and enhanced LBS, which are considered suitable for the cellular-based positioning.

3.2.1 Basic LBS Support: DL Preamble Measurements

The IEEE 802.16m standard adopts an OFDMA based technique, which implies that the MS and the serving BS should synchronize in both time and frequency domains in order to receive the data correctly. Therefore, it is necessary to place a preamble sequence in each OFDMA frame. The preamble sequence has good autocorrelation properties which is helpful for time and frequency synchronizations. Meanwhile, the system information, including system bandwidth, carrier configuration, cell identity (cell ID), and sector ID, is also carried in the preamble sequence. Therefore, with proper cell planning, the MS can detect the preamble sequence of the serving BS. Note that preamble sequences can also be utilized for channel estimation.

Figure 3.1 illustrates the frame structure of the IEEE 802.16m standard [20]. It is noted that the superframe contains four frames and each frame occupies 5 milliseconds. The DL subframes and UL subframes are further partitioned in each frame. There are three different designs to carry the information of BSs as follows: (a) Primary advanced preamble (PA-preamble) contains the information about system bandwidth and carrier configuration; (b) Secondary advanced preamble

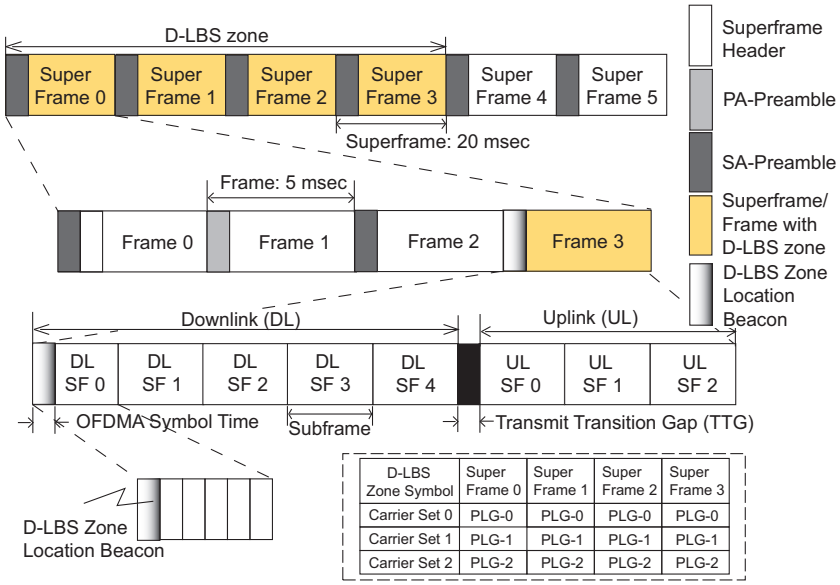

Figure 3.1: Frame structure with the hierarchical preamble design and the location of the D-LBS zone beacon in the IEEE 802.16m standard [20].

(SA-preamble) contains one of the 768 different cell-IDs for the MS to distinguish the sender; and (c) The superframe header provides system parameters and the configuration of the BSs. Advanced preamble (A-preamble) design in the IEEE 802.16m standard is hierarchical, containing one PA-preamble and three SA-preambles in each superframe. The design of the A-preamble position allows the MS to first decode the PA-preamble (e.g., in frame 1 of superframe 1) and then decode the SA-preamble three times (e.g., in frames 2 and 3 of superframe 1 and frame 0 of superframe 2) to assure correctness before decoding the superframe header (e.g., frame 0 of superframe 2).

In the following, we address how the A-preamble works and why a preamble sequence is important to an OFDMA system by an initial access example. The MS scans for the A-preamble to synchronize with the frame time. Once the PA-preamble is decoded, the system bandwidth and carrier information of the BS are obtained. Matching the SA-preambles further provides the DL physical layer synchronization with an identified target cell. Afterwards, the MS decodes the superframe for acquiring the system essential information to complete the MAC layer DL synchronization with the target BS. Furthermore, the MS also needs to synchronize to the UL subframe in order to provide authentication and to transmit without interfering with the other user. The UL ranging process will be introduced in the next section.

After synchronization with the target BS, the MS will receive information about the neighboring BS from the target BS. The SA-preamble and the coordinate of the neighboring BS can be obtained. For purpose of location estimation, preambles can be utilized for timing measurements. The original purpose of the A-preamble design was to allow the MS to detect the strongest A-preamble and to synchronize to a target cell in a short period of time. However, in the two-dimensional (2-D)

localization problem, at least three BSs are required to be involved for the timing measurement process. In order to distinguish different A-preambles coming from various cells, SA-preambles that carry different cell-IDs are utilized for the timing estimation. It is noted that the original purpose of synchronization to the target cell and the location estimation problem are somewhat contradictory with each other. The design of the synchronization process only requires one of the strongest BS to be received; while location estimation needs signals from at least three BSs to be concurrently received which violate the design principle of the preamble. In the next section, we will discuss the effect of inter-cell interference to the performance of location estimation by directly measuring the timing information with several SA-preambles from different cells.

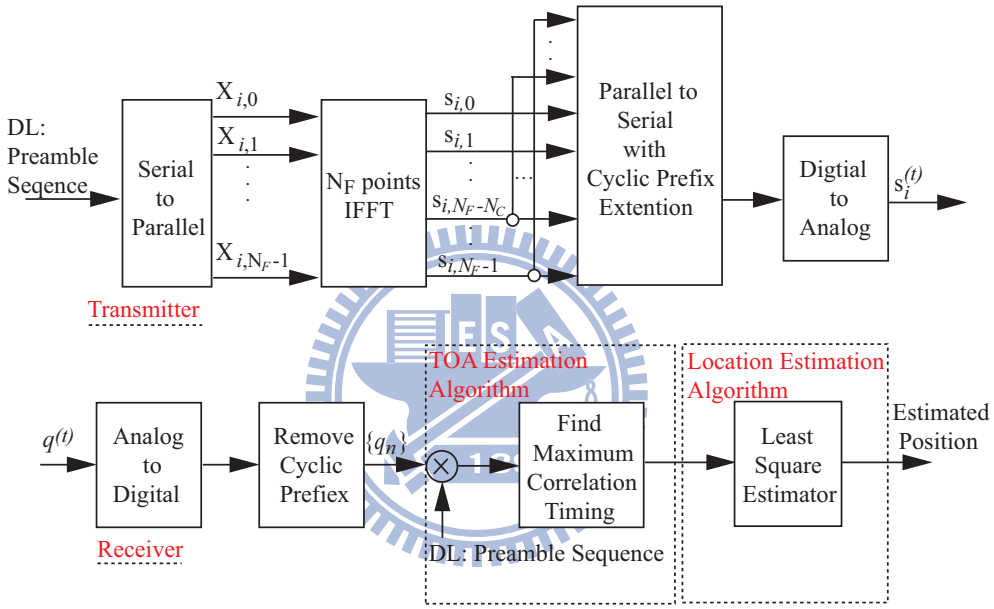

Figure 3.2: Function blocks of DL preamble transmission and reception for an OFDMA system.

In Figure 3.2, function blocks of the location determination process utilizing a DL preamble measurement are illustrated. It is noted that different positioning techniques adopt different sequences as the input of the TOA estimation algorithm. In DL basic LBS support, the MS measures the broadcasted SA-preambles for TOA estimation. The SA-preamble is formed by quadrature phase-shift keying (QPSK) symbols and grouped into sub-blocks. At the transmitter (i.e., the BS) side, the SA-preamble is allocated to an orthogonal subcarrier in the frequency domain. Each sub-block contains three different SA-preamble carrier sets mapping to three sectors consecutively with right circular shift. For example, in an OFDMA symbol, the number of subcarriers allocated to each sector is 288 (i.e., three sectors occupy 864 subcarriers) for a 1024 point fast Fourier transform (FFT) transmission mode in the IEEE 802.16m standard. The time domain signal of the SA-preamble which is obtained after taking an inverse fast Fourier transform (IFFT) of length N_F is denoted as

$s_{i,n}$ of the ith BS, i.e.,

$$s_{i,n} = s_i^{(t)}|_{t=nT_d} = \frac{1}{\sqrt{N_F}} \sum_{k=0}^{N_F-1} X_{i,k} e^{j2\pi \frac{k}{N_F} n} \quad n = 0, ..., N_F - 1 \tag{3.1}$$

$X_{i,k}$ indicates the kth subcarrier of an OFDMA symbol which is allocated by the SA-preamble of the ith BS. T_d represents the sampling period which is defined according to the bandwidth usage in the IEEE 802.16m standard. $s_i^{(t)}$ denotes the transmitted OFDMA signal of the ith BS which is processed using the IFFT of SA-preamble and the digital to analog conversion at time t. The Cyclic prefix (CP) is inserted in the front by copying the last N_C samples of the symbol. The inter-carrier interference due to the delayed subcarriers can be eliminated efficiently through CP insertion. Further, the CP requires simple frequency domain processing due to the circular shift property of FFT. The length of the CP is described by a defined ratio g, i.e., $N_C = g \cdot N_F$, and the ratio differs based on the transmission mode (e.g., $g = 1/8$) to overcome multipath effects.

Considering channel fading effects, the signal received by the MS can be represented as $q^{(t)}$ as

$$q^{(t)} = \sum_{i=0}^{N_{BS}-1} \sum_{\ell=1}^{L} \alpha_i(\ell) \cdot s_i^{(t-\tau_i(\ell))} + v^{(t)} \tag{3.2}$$

where N_{BS} is the number of BSs that transmit their SA-preambles simultaneously. In the LBS evaluation model in [26], N_{BS} is set as 19 by considering the transmitting effect of two-tiers of cells. L is the total number of the multipath taps. $\alpha_i(\ell)$ denotes the channel gain of the ℓth path. $\tau_i(\ell)$ represents the travel time from the ith BS to the MS of the ℓth path which contains the line-of-sight propagation time and the channel delay caused by the mutlipath fading. $v^{(t)}$ denotes additive white Gaussian noise (AWGN). By removing the CP, the time domain received signal r_n can thus be obtained by analog to digital conversion. In (3.2), non-line of sight (NLOS) propagation causes both power and delay effects. The path gain $\alpha_i(\ell)$ of the NLOS signal suffers higher shadowing variance, higher attenuation, and penetration loss by traveling through walls. The delay of $\tau_i(\ell)$ is biased by the power-delay multipath model. The first arriving path will not necessarily be the strongest signal because of multipath unresolvable. Moreover, all the BSs broadcast the SA-preamble simultaneously (i.e., consider the summation in (3.2)), which can cause severe inter-cell interferences.

It is noted that the time frames broadcast by the BSs are considered to be aligned in the IEEE 802.16m standard. After the MS achieves physical layer synchronization, the SA-preamble of the serving BS and the SA-preambles of the neighboring BSs can be obtained. Since the serving BS and the neighboring BSs broadcast their SA-preambles concurrently, the TDOA is estimated from the difference in the arrival time between the serving BS and the neighboring BSs. To implement this, the cross-correlation $\rho_{i,n}$ between the received signal and the SA-preamble of the ith BS can

be calculated as

$$\rho_{i,n} = \sum_{k=0}^{N_d-1} s^*_{i,n+k} \cdot q_n \quad n = 0, ..., N_d - 1 \tag{3.3}$$

where the $*$ symbol denotes the conjugate operation. N_d represents the detection window and the size of N_d can be determined by the inter-cell distance between the BSs to reduce the detection complexity. The parameter $\rho_{i,n}$ will be compared to a predefined threshold to avoid false alarm. The timing estimate $\tilde{t}_i$ from the ith BS to the MS can be calculated by

$$\tilde{t}_i = \arg\max \rho_{i,n} \quad n = 0, ..., N_d - 1 \tag{3.4}$$

Based on the system requirement of the IEEE 802.16m standard, the location determination process should be completed in 1 second. Therefore, the timing estimation $\hat{t}_i$ can be performed several times and take an average as

$$\hat{t}_i = \sum_{j=0}^{N_n-1} \tilde{t}_i^{(j)} \tag{3.5}$$

where N_n denotes the number of frames for non-coherent combining which increases the accuracy by averaging the fast fading effect. The TDOA measurement $\hat{t}_{i0}$ can be obtained by computing the time difference of arrival between the ith BS and the serving BS (i.e., the BS with the index 0) as

$$\hat{t}_{i0} = \hat{t}_i - \hat{t}_0 \quad i = 1, ..., N_{BS} - 1 \tag{3.6}$$

By collecting at least two TDOA measurements, 2-D location estimation can be performed. The Gauss-Newton method of the nonlinear least squares method is chosen to evaluate the LBS performance.

3.2.1.1 Basic LBS Support with Interference Cancellation

In order to limit the interference from concurrent transmissions, interference cancellation was proposed in [23] which subtracts the signal coming from the serving BS in order to increase the accuracy of TDOA estimation. The main idea of the scheme is to utilize the channel information of the serving BS (i.e., BS_0), which can be obtained such that the MS can decode data. Therefore, the time-domain SA-preamble signal from the serving BS (i.e., $s_0^{(t)}$) can be reconstructed using the IFFT. By subtracting the SA-preamble of the serving BS assuming perfect channel estimation, the

received signal can be written as

$$q^{(t)} = \sum_{i=1}^{N_{BS}-1} \sum_{\ell=1}^{L} \alpha_i(\ell) \cdot s_i^{(t-\tau_i(\ell))} + v^{(t)} \tag{3.7}$$

As the example shown in Figure 3.3, the interference from sector 1 of BS_0 to sector 1 of BS_1 and that from sector 2 of BS_0 to sector 2 of BS_2 can consequently be mitigated. By employing interference cancellation, the interference can be effectively limited at the cost of a more complex receiver design.

3.2.2 Enhanced LBS Support: D-LBS Zones

In the IEEE 802.16m standard, enhanced LBS support is specified for the BS to transmit a special waveform for the purpose of LBS in order to enhance measurement accuracy. Figure 3.1 illustrates an example of D-LBS zone [24] [25] for enhanced LBS support. One D-LBS zone contains four superframes. The original superframe contains SA-, PA-, SA- and SA-preambles for signal synchronization. The D-LBS beacon is placed at the beginning of the last frame to replace the position of the SA-preamble, i.e., the sequence is SA-, PA-, SA-preambles followed by the D-LBS beacon. In basic LBS support, each sector transmits a different SA-preamble, which is recognized as a cell-ID. A cell-ID contains the index of the sector n (e.g., n = 0, 1 and 2) and the index of the BS m, e.g., cell-ID = $256 * n + m$. In enhanced LBS support, the concept of LBS zone is to partition all cell-IDs into Q PLGs to efficiently handle inter-cell interference, e.g., PLG-# = mod(mod(cell-ID,256),Q), where mod represents the modulo operation. All the sectors should transmit the same SA-Preamble sequence in D-LBS zone. Note that there are a total of four superframes and each can be allocated to three different carrier sets for a D-LBS zone as shown in Figure 3.1. The D-LBS transmission can be scheduled with a predefined pattern. The partitions of PLGs are designable to enhance the LBS performance. In order to evaluate the effectiveness of the LBS zone method, a cell-grouping example that efficiently mitigates the inter-cell interference for the purpose of LBS is explained as follows. It is noted that 2-D location estimation using range estimate (i.e., lateration) requires at least three BSs. Therefore, cell grouping by utilizing frequency reuse within three cells is illustrated in Figure 3.3. Since the minimum number of BSs involved in a location estimate is 3, there are a total of 3 PLGs in this example. In the symbol of the LBS zone shown in Figure 3.1, the BSs belonging to PLG-0, PLG-1, and PLG-2 should transmit the signal accordingly. The MS can measure the corresponding PLGs of neighboring BSs as the indication from the serving BS.

By mapping this frame structure to the layout in Figure 3.3, the MS of the quadrangular with the solid-line can measure the preamble and pick the strongest PLG-0 of BS_0, PLG-1 of BS_1, and PLG-2 of BS_2 to perform location estimation. The MS of the quadrangular with the dotted-line can measure another preamble set and pick the strongest PLG-0 of BS_0, PLG-1 of BS_1 and PLG-2 of BS_8

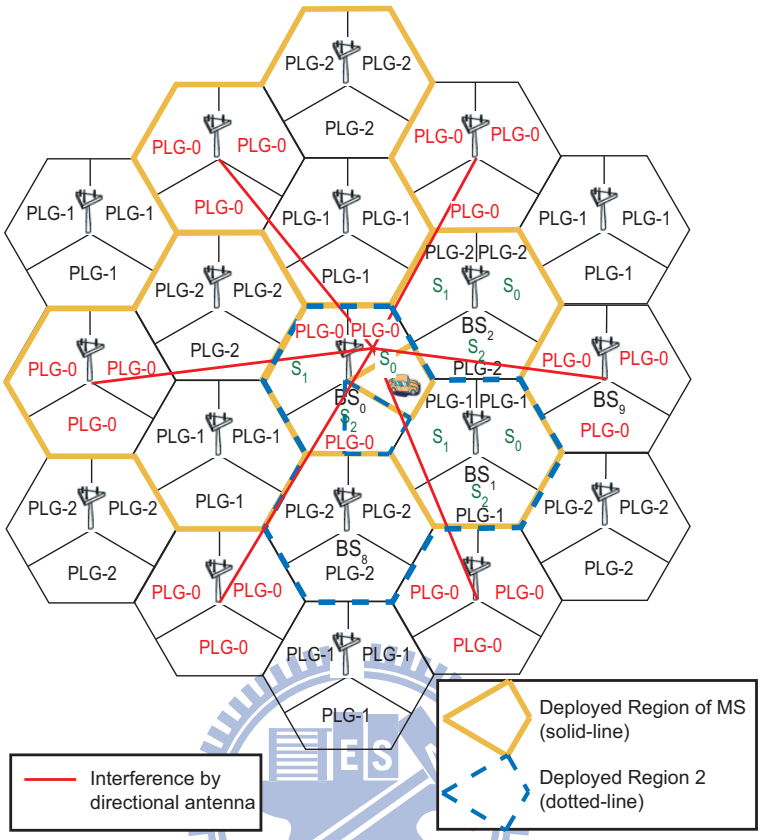

Figure 3.3: An example of PLGs of a D-LBS zone with the deployment of the MS and the BSs for the LBS performance evaluation.

to perform location estimation. Therefore, PLG assignment can be considered similar to the concept of frequency reuse. The benefit of the assignment is to schedule all the six concurrent transmissions in the same frequency band at least two cells away, e.g., PLG-0 of BS_0 and PLG-0 of BS_9. Therefore, the PLGs help to mitigate the inter-cell interference by scheduling the transmissions in different time slots. The scheduling which sacrifices the transmission bandwidth (i.e., LBS zone replaces the original synchronization slot and delays the average synchronization time) can effectively increase the location estimation accuracy. There are different methods to determine the PLGs and the transmission pattern. More PLGs can result in less inter-cell interference; however, the LBS will require more time slots to complete the timing measurement process.

3.2.3 Basic LBS Support: UL Ranging Measurements

The ranging scheme is conducted by the MS sending its assigned ranging codes to the serving BS in order to measure the UL distance related parameter, e.g., the timing advance value. In order to illustrate the design concept of the ranging channel, the synchronization process to the UL is illustrated. Providing that an MS intends to join an IEEE 802.16 network, it conducts ranging with

the serving BS to obtain the synchronization parameter for UL communication. At first, the MS should listen to the BS's broadcast message to capture the ranging opportunity in the advanced map (A-MAP), which indicates the transmission opportunity in other words the time slots during which the MS can receive and transmit data. The MS conducts contention-based initial ranging to obtain related parameters and then the MS is permitted to join the network. After the MS establishes a link with its serving BS, the MS performs periodic ranging in order to maintain synchronization while the MS moves or the channel conditions vary.

It is noted that the timing advance value (i.e., t_{adv} in Figure 3.4) is the round-trip time between the MS and the serving BS. The timing advance information is utilized to reserve the proper timing for the UL transmission. By performing the ranging scheme, the serving BS measures the timing adjustment according to the previously recorded timing advance information to update the distance between the MS and the serving BS. In order to support for the MS's mobility, a scanning scheme is specified for the MS to perform ranging with its neighboring BSs. With the negotiation between the serving BS and neighboring BSs, the scanning scheme can directly obtain ranging opportunities without contention.

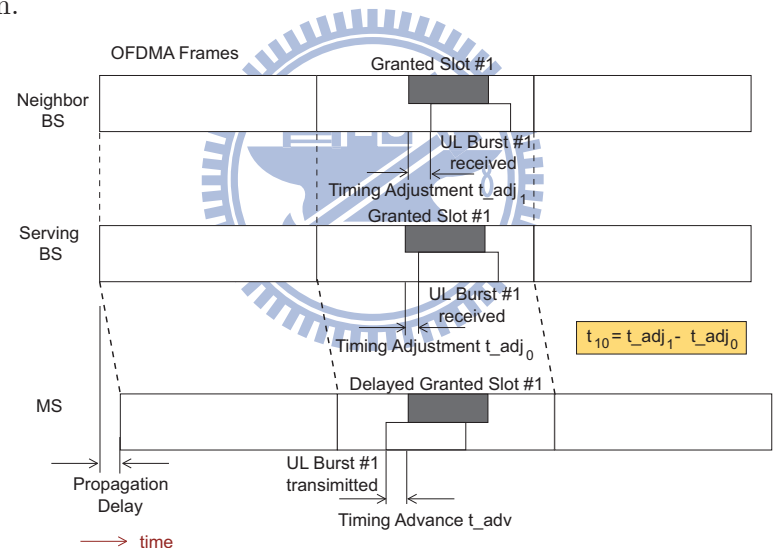

Figure 3.4: The timing diagram of the special U-TDOA measurement proposed in the IEEE 802.16m standard [20].

The frame structure of the ranging channel for non-synchronous MS format 0 is illustrated in Figure 3.5. It is noted that the MS will not synchronize to both its serving BS and the neighboring BSs simultaneously. The neighboring BSs provide the dedicated ranging channel opportunity for non-synchronous MS by assigning the ranging code through the serving BSs. As shown in Figure 3.5, the six symbols duration (i.e., $6T_b + 6T_g$) is not entirely occupied by the ranging preamble (RP) and ranging cyclic prefix (RCP). The remaining time duration is reserved to prevent interference between the adjacent subframes. The ranging code is generated with Zadoff-Chu sequences and the length of the RP code is defined as $N_{RP} = 139$ for format 0. Compared to the DL pream-

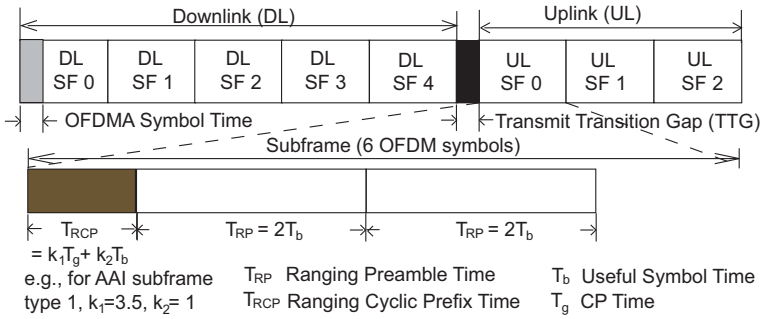

Figure 3.5: Frame structure of ranging channel for non-synchronous MS in the IEEE 802.16m standard [20].

ble measurement, the UL ranging measurement requires negotiation between the serving and the neighboring BSs. In order to describe how UL TDOA (U-TDOA) works, the timing diagram and the measurement procedure are explained as follows. It is noted that the special TDOA method specified in the IEEE 802.16m standard can be considered as the case that the frequency reuse factor is equal to one. Therefore, the serving BS and the neighboring BSs can negotiate a ranging channel in the same OFDMA subframe to process the TDOA measurement.

Figure 3.4 illustrates the timing diagram of the special U-TDOA measurement. The serving BS and the neighboring BSs first negotiate a ranging channel and send ranging information to the MS. For example, the frame time of the serving BS and the neighboring BSs are aligned while the frame time of the MS is added with the propagation delay compared to that from the serving BS. The granted slot is the original assigned ranging channel indicated by A-MAP. The UL transmitted burst indicates the actual time at which the frame is transmitted and the UL received burst indicates the actual time at which the frame is received.

Due to the delay of the time frame at the MS, the ranging code is sent to the MS at a timing advance prior to the granted time. The serving BS and the neighboring BS measure the timing adjustment t_adj_0 and t_adj_1 respectively, and the neighboring BS reports t_adj_1 to the serving BS. The timing advance value t_adv remains the same since the MS does not make any timing adjustments while conducting ranging with both the serving and the neighboring BSs. Therefore, the serving BS calculates the time difference $t_{10} = (t\_adj_1 - t\_adj_0)$.

Figure 3.6 illustrates the message exchange sequences for the special U-TDOA measurement. The serving BS negotiates with neighboring BSs to assign a dedicated ranging opportunity for the MS. Through the ranging response (RNG-RSP) message, the serving BS will assign a rendezvous time, a ranging code, and a transmission (Tx) opportunity offset for the MS. When the rendezvous time has expired, the MS will transmit the allocated ranging code within the regular ranging region. The involved BSs reserve a granted slot and measure the arrival time by utilizing the timing estimation method described in the previous section. The neighboring BSs will send the timing adjustment value to the serving BS. Therefore, the serving BS can calculate the position of

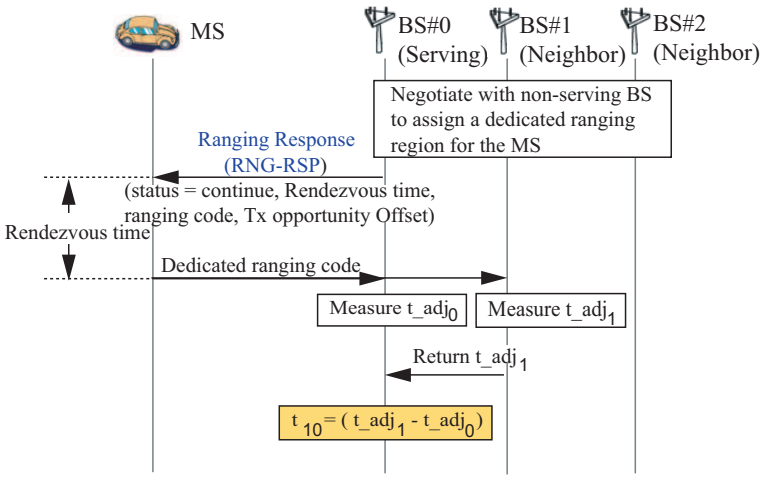

Figure 3.6: The message exchange sequences of the special U-TDOA measurement method proposed in the IEEE 802.16m standard [20].

MS to complete the U-TDOA measurement.

As for the timing estimation of the UL case, the serving BS and the neighboring BSs perform timing estimation similar to the DL case in the previous section. The difference of the received signal $q_i^{(t)}$ by the ith BS can be denoted as

$$q_i^{(t)} = \sum_{\ell=1}^{L} \alpha_i(\ell) s^{(t-\tau_i^{(\ell)})} + I_i^{(t)} + v_i^{(t)} \tag{3.8}$$

In the special U-TDOA case, the BSs participating to measure the TDOA will receive the same signal (i.e., the ranging code) with different channel gains and AWGN noises. However, if the other BSs that are not involved in the measurement schedule a transmission in the same channel, interference $I_i^{(t)}$ will occur to the ith BS. The inter-cell interference from the UL transmission can be mitigated by adopting power control. However, the number of BSs involved for the LBS will also be limited since power control decreases the transmission range.

3.3 A Case Study: LBS Performance of the IEEE 802.16m

In the section, the main focus is to evaluate the LBS performance of the IEEE 802.16m standard. Link level simulations are performed to evaluate the robustness of the preamble and ranging sequence design against the multipath channel at different signal-to-noise ratio (SNR) values. As for the system level simulation, the evaluation methodologies of DL and UL LBS performance are described respectively. In general, DL system level performance is easier to set up and analyze since concurrent transmission only happens at the BSs. It is noted that different positioning techniques, i.e., the basic and the enhanced LBS support, for the DL LBS will be compared. As for

Table 3.1: LBS evaluation parameter for the IEEE 802.16m Standard[26]

Scenario \ Parameters	Baseline
Cell to Cell Distance	1.5 km
Network topology	Hexagonal deployment, 19 cells, 3 sectors
Carrier	2.5 GHz
Operating Bandwidth	10 MHz
Sampling Frequency	11.2 MHz
FFT size (N_F)	1024
Frame Length	5 msec
BS Maximum Transmission Power	46 dBm
MS Maximum Transmission Power	23 dBm
Pass Loss Model	Loss(dB)=130.19+37.6log_{10}R
Lognormal Shadowing	Standard Deviation 8 dB
Small Scale Channel Model	ITU-PedB 3 km/hr
Propagation Delay	The real propagation delay from MS to BS
BS&MS Antenna Gain	17 dBi & 0 dBi
BS Antenna 3dB Beamwidth	70°
BS Antenna front-to-back ratio	20 dB
Penetration Loss	10 dB
Noise Figure of MS	7 dB
Detection Window Size (N_d)	192
Non-coherent Combing Frames (N_n)	10

the UL system level simulation, concurrent transmission will depend on the number of MSs in a cell, the traffic load and the scheduling method. The UL simulation is performed by introducing an interference over thermal (IoT) ratio to simulate the inter-cell interference at the BS side.

3.3.1 Link Level Simulation: TOA Estimation of the IEEE 802.16m Standard

In a location estimation problem, there are multiple links with different channel conditions between the MS and the BSs. Before a system level simulation, the purpose of performing a link level simulation for the timing estimation is to examine the performance of the SA-preamble and ranging sequence. In general, it takes longer time to conduct a system level simulation. The result of the link level simulation provides the information about the channel conditions and helps us to further decide which parameters should be adopted before the system level simulation is conducted.

The evaluation model of LBS [26] is listed in Table 3.1. The 10 MHz bandwidth mode is utilized for performance evaluation. For 1024-FFT, the number of subcarriers allocated to each SA-preamble carrier is 288. The non-synchronous ranging channel format 0 is adopted as shown in Figure 3.5 and the number of subcarriers in each symbol is 139. The channel effect includes the SNR to simulate different channel gains against AWGN and multipath effects. The multipath power delay profile adopted in the LBS evaluation methodology [26] is a modified ITU pedestrian B (eITU PedB) channel [27]. It is noted that there are a total of 24 paths in the eITU PedB model and the root mean square (RMS) delay spread of eITU PedB is around 640 nanosecond (nsec), i.e., 192 meters. TOA RMS error is defined as the root mean square error between the estimated TOA

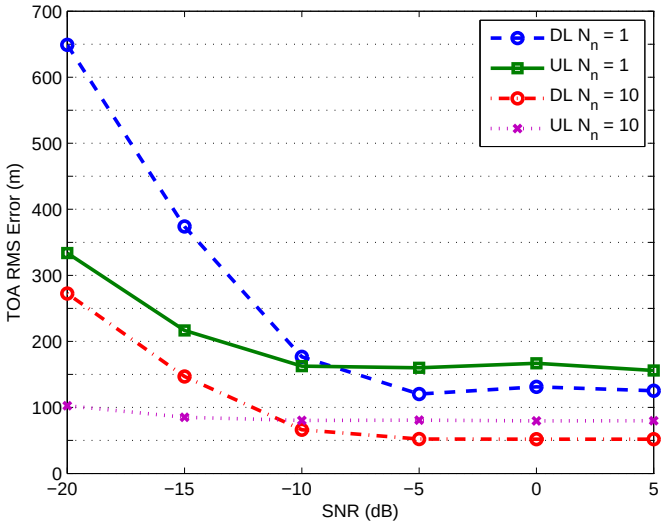

Figure 3.7: Link level simulation: TOA RMS error (in meter) versus SNR.

$\hat{\boldsymbol{t}}(j)$ and the true TOA τ, i.e., TOA RMS error $= \left[\sum_{j=1}^{N_r} \|\tau - \hat{\boldsymbol{t}}(j)\|^2 / N_r\right]^{1/2}$, where $N_r = 2,000$ indicates the number of simulation runs. TOA RMS error versus SNR is utilized to examine the effectiveness of the ranging sequences in Figure 3.7. TOA RMS error with a preamble sequence (i.e., DL) is approximately 125 meters and that with ranging sequence (i.e., UL) is approximately 155 meters in the $N_n = 1$ case. Both DL and UL schemes can achieve better timing estimation than the RMS delay of the eITU PedB multipath channel profile (i.e., 192 meters) when SNR is larger than -5 dB. When the SNR is lower, e.g., when the transmission distance is longer or the shadowing effect is more severe, the timing estimation would be worse. The DL preamble sequence has more subcarriers (i.e., in frequency domain) as compared to the ranging sequence, i.e., 288 vs 139. Therefore, TOA estimation performance on the DL is better than that on the UL under higher SNR conditions. The UL channel utilizes two consecutive symbols in time domain for timing estimation as shown in Figure 3.5. It is noted that the channel conditions of each trial is generated independently. However, the channel conditions remain the same for consecutive symbols on the UL. Therefore, UL transmission takes advantage of longer ranging channel time to estimate under lower SNR condition. The performance of non-coherent combing is examined for the case of $N_n = 10$. It is also noted that estimation error 67% of the time (i.e., the statistical meaning of the RMS value) should be less than 100 meters. TOA RMS errors using the DL preamble and the UL ranging sequence are around 50 meters and 85 meters respectively. With practical considerations for the number of non-coherent combinations, $N_n = 10$ is adopted in the system simulation in the following sections.

3.3.2 System Level Simulation: DL LBS Performance of IEEE 802.16m Standard

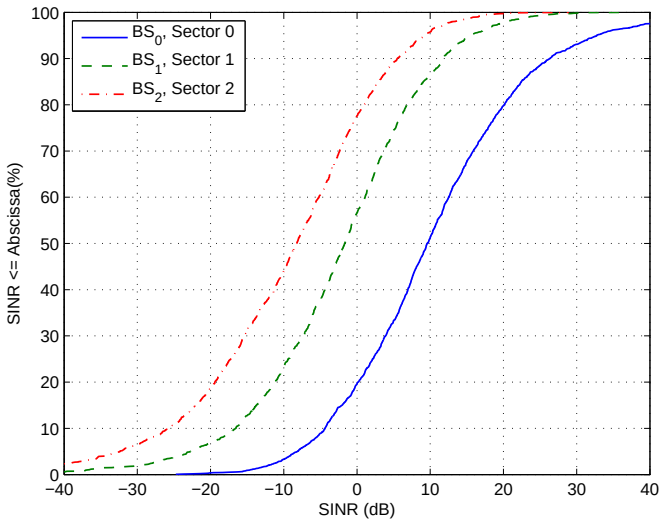

Figure 3.8: The SINR distribution of the deployed MS in Figure 3.3.

In this section, the performance of DL system level simulations are presented. It is noted that the DL preamble measurement described in section 3.2.1 is one of the most applicable schemes for basic LBS support in the IEEE 802.16m standard. The evaluation model of LBS [26] is listed in Table 3.1. Three-sector antennas with directional gains are applied for each sector. For SA-preamble transmission, the BSs radiate the maximum allowable power at 46 dBm. Path loss, penetration loss, shadowing fading, and multipath fading are considered for the channel model. The simulation is performed after initial synchronization, i.e., a random uniformly distributed ± 10 sample intervals is assumed for initial synchronization accuracy. After CP removal with simulated initial synchronization error, the timing estimation of the received signal (3.2) is performed by finding the maximum correlation within the detection window.

The cell deployment is shown in Figure 3.3 where the cell to cell distance is 1.5 km. Two-tiers of (i.e., $N_{BS} = 19$) BSs are simulated for the concurrent transmissions between different BSs. Moreover, random OFDMA data is appended after the SA-preamble in order to simulate the data transmission of each BS. In Figure 3.3, it is noted that the MS to be estimated is uniformly distributed in the quadrangle with the solid-line. The region covered by the quadrangle with the solid-line is the closest area to the serving BS (i.e., BS_0) and the two neighboring BSs (i.e., BS_1 and BS_2). The positioning accuracy of the MS obtained from this region can be assumed to represent the performance of the MS at any place near the three closest BSs. The distribution of the signal to interference plus noise ratio (SINR) of the MS is illustrated in Figure 3.8. The expected strongest received signals from different BSs for the MS located in the region are sector 0 (S0) of BS_0, sector

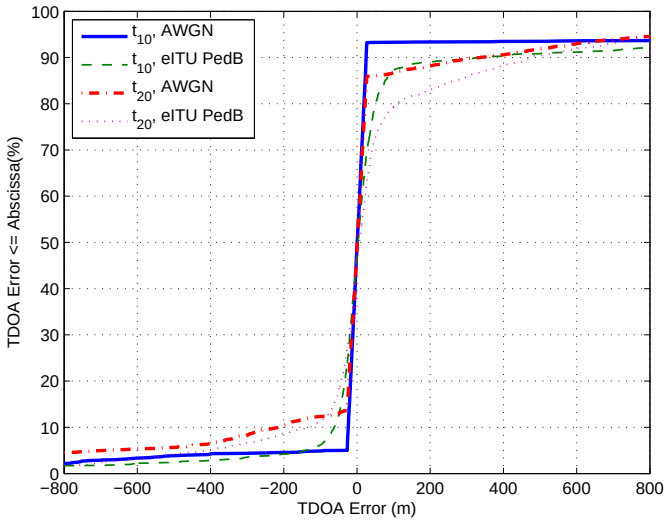

Figure 3.9: The TDOA estimation error (in meter) of the deployed MS in Figure 3.3.

1 (S1) of BS_1 and sector 2 (S2) of BS_2. It is noted that the SINR of the signal from BS_1 is larger than that from BS_2 because of the gain of the sector antenna. More specifically, the gain is larger at the center of the sector than at the side of the sector. It should also be noted that the serving BS of the quadrangle with the solid-line is BS_0, which also serves as the reference of the TDOA measurement in the simulation.

Figure 3.9 illustrates the TDOA performance between the BS_1, BS_2 and BS_0. It is noted that the performance of the TDOA measurement will be affected by interference as shown in (3.2). Therefore, with the same reference BS (i.e., BS_0), the TDOA performance (i.e., t_{10} and t_{20}) is proportional to the received SINR of the neighboring BSs (i.e., BS_1 and BS_2). With the higher received SINR of the neighboring BS, the TDOA error is more concentrated around the zero point. In Figure 3.9, the eITU PedB line represents the performance in the presence of both multipath and AWGN effects, while the AWGN line represents the case where there is no multipath in order to investigate multipath effect on the estimation. It can be observed that multipath degrades the TDOA estimation performance.

The location estimation performance of DL preamble measurement method using different numbers of non-coherent combinations (N_n) is depicted in Figure 3.10. The Taylor series approach for location estimation [22] method is adopted in the simulation. The initial point for the MS in the Taylor series expansion is set to be the central point of the received BSs. The estimation is calculated iteratively at most 10 times. The AWGN line here serves as an upper bound for the severe interference environment. Even though multipath effect is not present in the AWGN cases, the performance of basic LBS support still cannot reach the required accuracy defined by E-911. The simulation is also performed with different values of N_n. Path loss and shadow fading are con-

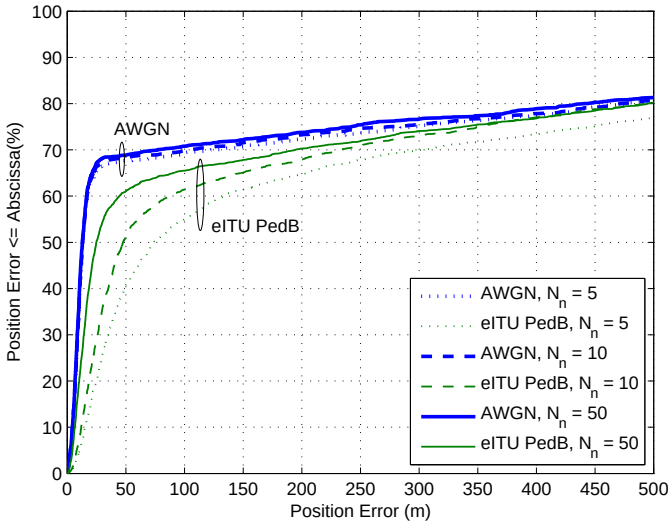

Figure 3.10: Position error of basic LBS support with different number of non-coherent combing.

sidered the same for all the links during multiple transmissions combined during the non-coherent combining. Therefore, a larger N_n can mitigate only the multipath effect, but not shadowing effect. On the other hand, there is no significant improvement for the AWGN channel with the increment of N_n. The proper choice of N_n can help to reduce multipath fading and increase the system performance. However, with increased value of N_n, it will take a longer time to complete the location determination process. Similar to the conclusion of the link level simulations, $N_n = 10$ is chosen to consider the performance and computation tradeoffs.

The original design of the preamble is to assist the MS to quickly identify the cell ID and achieve synchronization with a single BS, i.e., the serving BS. However, in the location estimation problem, at least three measurements with sufficient signal quality should be obtained from the BSs. There is a tradeoff between the preamble detection and timing estimation from the three BSs. For example, providing that the MS is located nearby its serving BS, a strong preamble signal coming from the serving BS will cause severe interference to the preamble signals from the other neighboring BSs which can deteriorate the positioning accuracy of the MS. This is the major reason why simply using the DL preamble measurements in the basic LBS support will not bring satisfactory performance for location estimation.

Figure 3.11 shows a comparison of the positioning accuracy for DL preamble measurements with the layout in Figure 3.3. It is noted that basic LBS support by utilizing the SA-preamble for DL measurement will not waste additional channel bandwidth. Without adopting advanced positioning techniques, it is observed that the positioning accuracy cannot reach the system requirements that are defined in the IEEE 802.16m standard, i.e., less than 100 meters of estimation error 67% of the time and less than 300 meters 95% of the time. Inter-cell interference is considered the dominant

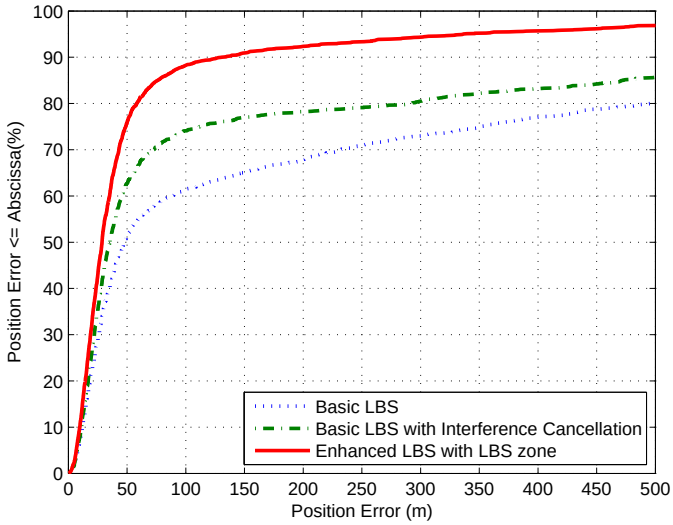

Figure 3.11: Performance comparison between the DL basic and enhanced LBS support.

limiting factor compared to the others, e.g., multipath effect. The BSs that simultaneously broadcast their preamble sequence result in inter-cell interference to limit the performance of basic LBS support.

As for interference cancellation within the basic LBS support, channel estimation is assumed to be perfect in the simulation. In other words, the green curve can serve as an upper bound for interference cancellation scheme. In this situation, timing estimation is performed after the neighboring BSs perfectly cancel the SA-preamble of the serving BS. Without the interference from the serving BS, the SINR of the preamble signals from the neighboring BSs increases. Interference cancellation improves the performance of the basic LBS support. Moreover, compared to the basic LBS support, enhanced LBS support mitigates inter-cell interference by transmitting the SA-preamble in different time slots. In the simulation, 3 PLGs are applied and the partitions of the sectors are shown in Figure 3.3. The location determination process of enhanced LBS support requires three symbols in average to obtain DL measurement. The inter-cell interference by adopting the grouping of BSs comes from the BSs at a distance equal to twice the distance away. In Figure 3.11, the red curve shows that the performance of enhanced LBS support can reach the requirements for E-911 location estimation.

3.3.3 System Level Simulation: UL LBS Performance of IEEE 802.16m standard.

In this section, UL TDOA simulations are performed with the same setup as the DL case in Table 3.1. It is noted that the transmission power of the MS (i.e., 23 dBm) is smaller than that of the BS. Therefore, the received signal quality of the neighboring BS is worse due to the smaller

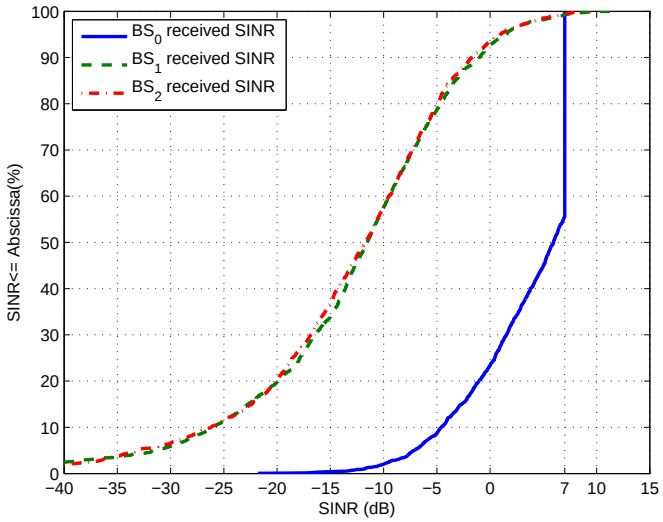

Figure 3.12: The SINR distribution at the BS side transmitted by the deployed MS in Figure 3.3.

received signal strength. Meanwhile, the power control of the MS is required to avoid causing interference to the users in the other cells. In the simulation, the received SNR at the BS is fixed at 10 dB. It is noted that the MS broadcasts the ranging signal to the serving and neighboring BSs in special TDOA scheme. Due to power control, the maximum transmission power from the MS is set to force the received SNR at the serving BS equal to 10 dB. Therefore, the quality of the transmission to the neighboring BSs is limited.

As for inter-cell interference, it is noted that ranging channel assignment requires negotiation between BSs. However, even if the subcarrier is assigned between the involved BSs, the other BS which have transmission in the subcarrier would still cause inter-cell interference. In general, the inter-cell interference can be modeled as IoT,

$$IoT(dB) = 10\log\frac{I}{N} \tag{3.9}$$

where I represents the interference power and N represents the noise power. With the IoT definition, the SINR can be calculated from the SNR and IoT as

$$SINR(dB) = 10\log\frac{S}{I+N} = 10\log\frac{S}{N} + 10\log\frac{1}{I/N+1} \tag{3.10}$$

In the simulation, the distribution of IoT is Gaussian with mean [0, 3.5, 7] dB and variance 3 dB. Based on the SNR and IoT setting, the power control is to force the maximum received SINR at the serving BS to [7, 4.9, 2.2] dB respectively. For example, an IoT of 0 dB refers to the case where the interference power is the same as the AWGN noise power. Therefore, the SINR value can be

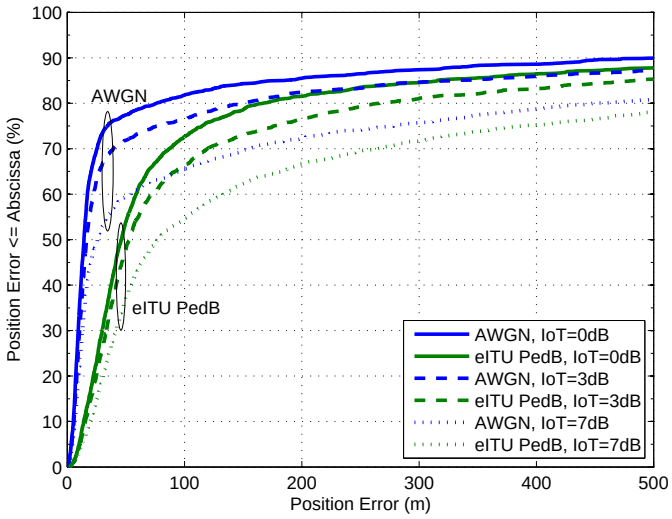

Figure 3.13: Position error of basic UL LBS support with different IoT.

calculated as $SINR = 10 + 10\log[1/(1+1)] = 10 - 3 = 7$ dB. ◇

The transmitted MS is located uniformly in the quadrangle with the solid-line in Figure 3.3. The received SINR of the serving BS (i.e., BS_0) and the two neighboring BSs (i.e., BS_1 and BS_2) is illustrated in the Figure 3.12. Due to the power limitation of the MS and the power control scheme, the hearability problem occurs in a certain region, e.g., when the MS is close to the serving BS, the ranging signal cannot be detected at the neighboring BSs. It can be observed that nearly 20% of the received SINR values of BS_1 and BS_2 are worse than -20 dB in Figure 3.7. Figure 3.13 illustrates the accuracy of special UL TDOA method. It is noted that larger IoT which is regarded as larger inter-cell interference to UL transmission causes worse location estimation performance. However, even the light inter-cell interference (i.e., IoT = 0 dB) in the multipath-free case (i.e., as the AWGN case) can still suffer from the hearability problem in the UL case.

3.3.4 Comparison of DL and UL LBS

In the section, the pros and cons of DL and UL measurements are assessed. From the performance point of view, basic LBS support cannot satisfy the LBS performance requirement since the 95% of the time the error should be less than 300 meters, which it isn't as shown in Figures 3.11 and 3.13. It is noted that 20% of the positions for DL basic LBS support and 15% of the positions for the UL basic LBS support cannot be estimated with satisfactory performance. Although the DL signal is transmitted with higher transmission power by the BS, inter-cell interference limits the possibility of having multiple reliable TOA measurements concurrently. On the other hand, inter-cell interference $I^{(t)}$ can be mitigated by the negotiation and scheduling scheme on the UL. By comparing (3.2) and (3.8), there is less interference for UL TDOA. However, the received signal

quality is limited due to the smaller transmission power of the MS especially when combined with power control, which will cause hearability problem to occur in certain regions. In general, basic UL TDOA is considered to provide better location estimation accuracy than that from basic DL TDOA. However, the limitation due to inter-cell interference from concurrent transmissions on DL can be easier to deal with as compared to the hearability problem for the UL. The D-LBS zone method efficiently eases inter-cell interference and satisfies the performance requirement.

From a complexity point of view, UL measurement results in higher system complexity since negotiation between the BSs is required. Localization determination time of the UL scheme is also longer since the BSs should wait until all the measurements collected through the backbone network from the neighboring BSs have been communicated. On the other hand, the MS has all the measurements and does not require extra measurement exchange for DL approaches. The other issue is that the power consumption of transmitting signals is regarded to be larger than receiving signals. Therefore, UL TDOA will consume more power which can be an important issue at the MS side. Consequently, from an implementation point of view, DL TDOA is considered to be more suitable in practical systems.

3.4 Concluding Remarks

This chapter describes cellular-based location estimation using timing estimates for next generation telecommunication networks. Different ranging techniques are introduced and simulated with the standard location-based service (LBS) evolution methodology. By studying the performance of the downlink (DL) preamble measurement, inter-cell interference is found to be the limiting factor. On the other hand, uplink (UL) ranging measurement suffers hearability problem. Neither DL nor UL basic LBS support can achieve the performance requirement of emergency 911 (E-911). In DL measurements, the mobile station (MS) measures the secondary advanced preamble from the BSs which results in less network information exchange between base stations (BSs) and less power consumption. The properties provide the feasibility for DL LBS to be implemented in practice. Furthermore, the performance of the basic LBS support can be enhanced by adopting inter-cell cancellation methods at the physical layer or interference avoidance at the media access control (MAC) layer. The former approach utilizes signal processing techniques to cancel the interference with channel estimation. The performance for location estimation can be enhanced at the cost of increasing complexity at the receiver. On the other hand, the latter approach groups the preamble location groups (PLGs) to schedule concurrent transmission of BSs located within two cell-to-cell distances. The simulation results confirm that enhanced LBS support satisfies the requirement for E-911 positioning accuracy.

Chapter 4

Geometric Analysis of Linear Least Squares Estimator for Wireless Location Systems

- Linear estimators, including the well-adopted linear least squares (LLS) estimator, have been extensively utilized for wireless location estimation for their simplicity and closed-form property. However, the analysis of this class of estimators has not been addressed in the literatures. In this chapter, the linearized location estimation problem based CRLB (L-CRLB) is derived to provide a geometric portrayal in order to fully characterize the behavior of the linearized location estimator.

4.1 Introduction

It is recognized that the equations associated with the TOA estimation schemes are inherently nonlinear. The uncertainties induced by the measurement noises make it more difficult to acquire the MS's estimated position with tolerable precision. There are several representative techniques which are widely utilized in practical localization systems to deal with the nonlinear location estimation problem (LEP) (i.e., Problem 1.1), such as the Taylor series expansion (TSE) [22] based method, the fingerprinting method, and the linear least squares (LLS) [16] method. The TSE method approximates the localization problem by taking the first two orders of Taylor expansion on the measurement inputs. Initial MS's position estimate and the iterative processes are required to obtain a location estimate from the linearized system based on the TSE scheme. The major drawback of the TSE method is that it may suffer from the convergence problem due to an incorrect initial guess of the MS's position. The pattern-matching localization based on the fingerprinting approach [28, 29, 30, 31] is another popular method for the LEP, e.g., RADAR in [28]. However, a large amount of measurements are required to be collected from a database before the estimation.

On the other hand, the original nonlinear estimation problem can be transformed into a linear relationship for the computation of MS's position by introducing an additional variable. This type of linearized methods deal with the linearized location estimation problem (L-LEP) and will be the major discussion in the chapter. In general, the LLS is one of the popular techniques to solve the L-LEP in practical localization systems, e.g., the Cricket system [32], and has been continuously investigated from research perspectives [33, 34, 17, 35, 21]. Moreover, the closed-form characteristic of LLS estimator is suitable for real-time implementation due to its computational efficiency.

The location estimator discussed in this chapter belongs to non-Bayesian approach, i.e., without a priori knowledge of the parameter. The Cramer-Rao lower bound (CRLB) [36, 37] serves as a benchmark of the non-Bayesian estimator. An estimator that can achieve the CRLB under regularity conditions is the maximum likelihood (ML) estimator. The CRLB for the conventional LEP is derived in [37]. Since the wireless location estimation schemes are inherently nonlinear, the original LEP is often transformed into a L-LEP by introducing an additional variable to transfer the nonlinear equation into a linear equation for the computation of MS's position in practice. This transformation leads to a different parameterization and the analysis of the L-LEP has not been fully addressed in the previous research work.

Based on the concept of the CRLB, the theoretic lower bound of the L-LEP is derived as the L-LEP based CRLB (L-CRLB) in the chapter. The major target of this chapter is to derive the L-CRLB as a new performance metric for the LLS estimator and also observes the geometric properties associated with the proposed L-CRLB. The closed-forms formulation of the Fisher information matrix (FIM) for the derived L-CRLB provides a comparison between the L-LEP and the conventional LEP. Since it is required for the L-LEP to estimate an additional variable other than the MS's position, it can be proved that the value of L-CRLB is greater than or equal to the conventional CRLB. The geometric layout between the MS and the BSs for the L-CRLB to be equivalent to the CRLB is also derived.

Note that the LLS method is one of the methods to solve the L-LEP. In the chapter, the unbiased property of the LLS estimator is proven under the situation that the noiseless distance is much greater than the combined noise for each measurement. Besides, the LLS method becomes a ML estimator in a linear problem when the noise is assumed to be Gaussian distributed. It is validated in the simulations that the L-CRLB can be served as a tight lower bound for the mean square error of the LLS estimator. Therefore, the L-CRLB can be adopted as the benchmark of LLS estimator and all the properties of L-CRLB derived in the chapter will be feasible to characterize the behaviors of LLS estimator. From the geometric point of view, it can be inferred from the proposed L-CRLB that the LLS estimator will provide better performance if the MS is located inside the geometry constrained by the BSs; while inferior performance is acquired if the MS is outside of the geometric layout. This result can also be validates by the observations as was simulated in [16]. By adopting the proposed L-CRLB under different geometric layouts, the LLS estimator can be regarded as an efficient estimator while the MS is located within the geometry formed by the

BSs. This observation will be beneficial for the signal selection schemes of measurement inputs which should try to avoid positioning the signal sources that makes the MS to locate outside of the geometric layout.

The remainder of this chapter is organized as follows. Section 4.2 describes the modeling and geometric properties of both the CRLB and the L-CRLB. The realization of the LLS estimator for the L-LEP and the situation that the LLS estimator is unbiased are presented in Section 2.3. Section 4.4 illustrates the performance validation and evaluation for the both the proposed L-CRLB and the LLS estimator. Section 4.5 draws the conclusion.

4.2 Analysis of CRLB and L-CRLB

4.2.1 Mathematical Modeling of Signal Sources

The signal model for the TOA measurements in a synchronous network is utilized for two-dimension (2-D) location estimation, which can be referred to Section 2.1.1. The LOS noise model in Section 2.2.1.1 is discussed in the chapter. Since the non-Bayesian class estimator is discussed, the time instant t would be removed for the notational simplicity in the Chapter.

Definition 4.1 (BS's Orientation). Considering the MS as a vertex in geometry, the orientation of i-th BS (α_i) is defined as the angle between the MS to the i-th BS and the positive x axis. Without loss of generality, the index i of BSs are sorted such that the i-th BS is located at the angle $\alpha_1 \leq \alpha_2 \leq \ldots \alpha_i \ldots \leq \alpha_N$ for $i = 1$ to N. ◇

Based on the definition of α_i, the following geometric relationship can also be obtained as $\cos\alpha_i = (x_i - x)/\zeta_i$ and $\sin\alpha_i = (y_i - y)/\zeta_i$.

4.2.2 Properties of CRLB

The CRLB represents the theoretical lowest error variance of an unknown parameter for any unbiased estimator. Note that the CRLB in the rest of this chapter refers to the CRLB for the conventional LEP in Problem 1.1. Therefore, based on the TOA-based LEP as in (2.1) and (2.2), the variance of the MS's estimated position $\hat{\boldsymbol{x}}$ will be greater or equal to the CRLB ($\mathcal{C}$) as

$$E\{\|\hat{\boldsymbol{x}} - \boldsymbol{x}\|^2\} \geq \mathcal{C} = [\mathbf{I}_{\boldsymbol{x}}^{-1}]_{11} + [\mathbf{I}_{\boldsymbol{x}}^{-1}]_{22}, \tag{4.1}$$

where the CRLB $\mathcal{C} = [\mathbf{I}_{\boldsymbol{x}}^{-1}]_{11} + [\mathbf{I}_{\boldsymbol{x}}^{-1}]_{22}$ inherently represents the theoretical minimum mean square error (MMSE) of position. It is noted that $[\mathbf{I}_{\boldsymbol{x}}^{-1}]_{11}$ and $[\mathbf{I}_{\boldsymbol{x}}^{-1}]_{22}$ correspond to the first and second diagonal terms of the inverse of 2×2 FIM $\mathbf{I}_{\boldsymbol{x}}$, which can be obtained as

$$\mathbf{I}_{\boldsymbol{x}} = \mathbf{G} \cdot \mathbf{I}_{\boldsymbol{\zeta}} \cdot \mathbf{G}^T, \tag{4.2}$$

where

$$\mathbf{G} = \frac{\partial \boldsymbol{\zeta}}{\partial \boldsymbol{x}} = \begin{bmatrix} \frac{x_1 - x}{\zeta_1} & \cdots & \frac{x_i - x}{\zeta_i} & \cdots & \frac{x_N - x}{\zeta_N} \\ \frac{y_1 - y}{\zeta_1} & \cdots & \frac{y_i - y}{\zeta_i} & \cdots & \frac{y - y_N}{\zeta_N} \end{bmatrix} = \begin{bmatrix} \cos\alpha_1 & \cdots & \cos\alpha_i & \cdots & \cos\alpha_N \\ \sin\alpha_1 & \cdots & \sin\alpha_i & \cdots & \sin\alpha_N \end{bmatrix}, \tag{4.3}$$

$$\mathbf{I}_{\boldsymbol{\zeta}} = E\left[\frac{\partial}{\partial \boldsymbol{\zeta}} \ln f(\boldsymbol{r}|\boldsymbol{\zeta}) \cdot \left(\frac{\partial}{\partial \boldsymbol{\zeta}} \ln f(\boldsymbol{r}|\boldsymbol{\zeta})\right)^T\right]. \tag{4.4}$$

The $f(\boldsymbol{r}|\boldsymbol{\zeta})$ function in (4.4) denotes the probability density function for $\boldsymbol{r}$ conditioning on $\boldsymbol{\zeta}$, where $\boldsymbol{\zeta} = [\zeta_1, \ldots, \zeta_i, \ldots, \zeta_N]$. The matrices $\mathbf{G}$ and $\mathbf{I}_{\boldsymbol{\zeta}}$ are introduced as the change of variables since $\mathbf{I}_{\boldsymbol{x}}$ is unobtainable owing to the unknown MS's true position $\boldsymbol{x}$.

Lemma 4.1. *Considering the TOA-based LEP, the noise model for each measurement r_i is an i.i.d. Gaussian distribution with zero mean and a fixed set of variances $\sigma_{r_i}^2$ as $n_i \sim \mathcal{N}(0, \sigma_{r_i}^2)$. The minimum CRLB $\mathcal{C}_m$ with respect to the angle α_i can be achieved in [37] as*

$$\mathcal{C}_m = \frac{4}{\sum_{i=1}^{N} \frac{1}{\sigma_{r_i}^2}}, \tag{4.5}$$

if the following two conditions hold:

$$\begin{cases} \sum_{i=1}^{N} \frac{1}{\sigma_{r_i}^2} \sin 2\alpha_i = 0 \\ \sum_{i=1}^{N} \frac{1}{\sigma_{r_i}^2} \cos 2\alpha_i = 0 \end{cases}. \tag{4.6}$$

Proof. Based on (2.1), $f(\boldsymbol{r}|\boldsymbol{\zeta})$ can be obtained as

$$f(\boldsymbol{r}|\boldsymbol{\zeta}) \propto \prod_{i=1}^{N} \exp\left[-\frac{1}{2\sigma_{r_i}^2}(r_i - \zeta_i)^2\right]. \tag{4.7}$$

Therefore, the matrix $\mathbf{I}_{\boldsymbol{\zeta}}$ can be derived from (4.4) as $\mathbf{I}_{\boldsymbol{\zeta}} = \mathrm{diag}\{[\sigma_{r_1}^{-2}, \sigma_{r_2}^{-2}, \ldots, \sigma_{r_i}^{-2}, \ldots, \sigma_{r_N}^{-2}]\}$. The 2×2 matrix $\mathbf{I}_{\boldsymbol{x}}$ can be obtained from (4.2) and (4.4) as

$$\mathbf{I}_{\boldsymbol{x}} = \begin{bmatrix} [\mathbf{I}_{\boldsymbol{x}}]_{11} & [\mathbf{I}_{\boldsymbol{x}}]_{12} \\ [\mathbf{I}_{\boldsymbol{x}}]_{21} & [\mathbf{I}_{\boldsymbol{x}}]_{22} \end{bmatrix} = \begin{bmatrix} \sum_{i=1}^{N} \frac{1}{\sigma_{r_i}^2} \cos^2\alpha_i & \sum_{i=1}^{N} \frac{1}{\sigma_{r_i}^2} \cos\alpha_i \cdot \sin\alpha_i \\ \sum_{i=1}^{N} \frac{1}{\sigma_{r_i}^2} \cos\alpha_i \cdot \sin\alpha_i & \sum_{i=1}^{N} \frac{1}{\sigma_{r_i}^2} \sin^2\alpha_i \end{bmatrix}. \tag{4.8}$$

In order to obtain the minimum CRLB, (4.1) can further be derived as

$$E\{(\hat{\boldsymbol{x}} - \boldsymbol{x})^2\} \geq [\mathbf{I}_{\boldsymbol{x}}^{-1}]_{11} + [\mathbf{I}_{\boldsymbol{x}}^{-1}]_{22} = \frac{[\mathbf{I}_{\boldsymbol{x}}]_{11} + [\mathbf{I}_{\boldsymbol{x}}]_{22}}{[\mathbf{I}_{\boldsymbol{x}}]_{11} \cdot [\mathbf{I}_{\boldsymbol{x}}]_{22} - [\mathbf{I}_{\boldsymbol{x}}]_{12}^2} \geq \frac{[\mathbf{I}_{\boldsymbol{x}}]_{11} + [\mathbf{I}_{\boldsymbol{x}}]_{22}}{[\mathbf{I}_{\boldsymbol{x}}]_{11} \cdot [\mathbf{I}_{\boldsymbol{x}}]_{22}}. \tag{4.9}$$

Noted that the second inequality in (4.9) is valid since the quadratic term $[\mathbf{I}_{\boldsymbol{x}}]_{12}^2 \geq 0$ for all α_i. There-

fore, one of the necessary conditions to achieve minimum CRLB will be $[\mathbf{I}_{\boldsymbol{x}}]_{12} = \sum_{i=1}^{N} \frac{1}{\sigma_{r_i}^2} \cos\alpha_i \cdot \sin\alpha_i = 0$, which validates the first equation of (4.6). Moreover, since $\cos^2\alpha_i + \sin^2\alpha_i = 1$ for all α_i, the numerator in (4.9) becomes $[\mathbf{I}_{\boldsymbol{x}}]_{11} + [\mathbf{I}_{\boldsymbol{x}}]_{22} = \sum_{i=1}^{N} 1/\sigma_{r_i}^2$. Consequently, to acquire the minimum value of CRLB corresponds to maximizing the denominator $[\mathbf{I}_{\boldsymbol{x}}]_{11} \cdot [\mathbf{I}_{\boldsymbol{x}}]_{22}$ in (4.9). According to the *inequality of arithmetic and geometric means*, the following relationship can be obtained:

$$\sqrt{[\mathbf{I}_{\boldsymbol{x}}]_{11} \cdot [\mathbf{I}_{\boldsymbol{x}}]_{22}} \leq \frac{[\mathbf{I}_{\boldsymbol{x}}]_{11} + [\mathbf{I}_{\boldsymbol{x}}]_{22}}{2} = \frac{1}{2}\sum_{i=1}^{N} \frac{1}{\sigma_{r_i}^2}, \tag{4.10}$$

where the equality holds if and only if $[\mathbf{I}_{\boldsymbol{x}}]_{11} = [\mathbf{I}_{\boldsymbol{x}}]_{22}$, which corresponds to the second equation in (4.6). By substituting (4.10) into (4.9), the minimum CRLB can be obtained as $\mathcal{C}_m = 4/(\sum_{i=1}^{N} \frac{1}{\sigma_{r_i}^2})$. This completes the proof. □

Example 4.1 (Network Layout with Minimum CRLB)**.** Following the requirement as in Lemma 4.1 with $N = 3$ and all the variances are equivalent $\sigma_{r_i}^2 = \sigma_r^2$ for $i = 1$ to 3, the best geometric layout that can achieve the minimum CRLB $\mathcal{C}_m = 4\sigma_r^2/3$ is acquired at either the angle sets $\{\alpha_1, \alpha_2, \alpha_3\} = \{\gamma, \gamma + 120°, \gamma + 240°\}$ or $\{\alpha_1, \alpha_2, \alpha_3\} = \{\gamma, \gamma + 60°, \gamma + 120°\}$ $\forall\ \gamma = [0°, 360°)$. ◇

Note that this dissertation is devoted to discuss these three positioning limiting factors under various mobile location estimation and tracking environment, which can be observed from the CRLB and stated in Remark 1.

Remark 1 (Limiting Factors for LEP)**.** Through the study of CRLB, the limiting factors affect the estimation accuracy as: 1) **Geometric effect** between the MS and BSs as matrix $\mathbf{G}$ in (4.3); 2) **Signal model or noise variance** as matrix $\mathbf{I}_{\boldsymbol{\zeta}}$ in (4.4); 3) **Number of signal sources** as N in (4.5).

Fig. 4.1 illustrates a schematic about how to solve the LEP within the statistical signal processing theory. The ML estimator for the TOA-based LEP following the signal model in (2.2) can be obtained as

$$\hat{\boldsymbol{x}}_{\mathrm{ML}} = \arg\max_{\boldsymbol{x}} p_{\boldsymbol{r}|\boldsymbol{x}}(\boldsymbol{r}|\boldsymbol{x}). \tag{4.11}$$

Note that the likelihood function has to be known for the ML estimation. It requires higher computation complexity. Since the LEP is nonlinear, [38] has shown that the ML can only approach CRLB under the condition that SNR is sufficiently high. Otherwise, no efficient estimator exists due to the nonlinearity. In the case that likelihood function is unobtainable, the least squares cost function is adopted as the objective of the optimization problem.

$$\hat{\boldsymbol{x}}_{\mathrm{NLS}} = \arg\min_{\boldsymbol{x}} \sum_{i=1}^{N} (\boldsymbol{r}_i - ||\boldsymbol{x} - \boldsymbol{b}_i||)^2. \tag{4.12}$$

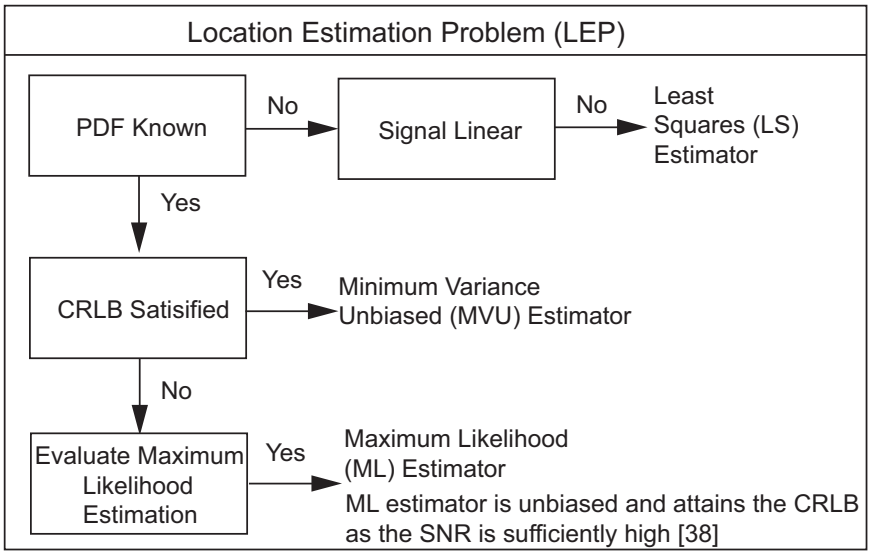

Figure 4.1: A schematic diagram of the LEP.

Note that the least squares objective function does not make any assumption on the distribution. The method refers to the nonlinear least squares (NLS) in [22]. The initial guess is required and the calculations are performed iteratively. Since the ML requires high computation overhead and the NLS requires iterative calculations, the LEP is often transformed into the L-LEP, which will be described in the following section.

4.2.3 Properties of Proposed L-CRLB

Problem 4.1 (Linearized Location Estimation Problem (L-LEP))**.** In order to estimate the MS's position $\boldsymbol{x}$, the nonlinear terms x^2 and y^2 in (2.2) are replaced by a new parameter $R = x^2+y^2$. The goal of the L-LEP is to generate an estimate $\hat{\boldsymbol{\theta}} = [\hat{x}_L, \hat{y}_L, \hat{R}]^T$ based on the collecting measurements $\boldsymbol{r}$. ◇

Note that the MS's estimated position $\hat{\boldsymbol{x}}_L = [\hat{x}_L, \hat{y}_L]^T$ of the L-LEP is in general not optimal compared to the original LEP since an additional nonlinear parameter R is also estimated, which reduces the estimation precision for $\hat{\boldsymbol{x}}_L$ under fixed set of measurement inputs. This intuitive observation explains that the conventional CRLB cannot be achieved by the linearized location estimator for LEP. In order to appropriately describe the behavior of linearized location estimator, the L-CRLB is defined based on the relationships in (2.1) and (2.2) as follows.

Definition 4.2 (L-CRLB)**.** The L-CRLB ($\mathcal{C}_L$) is defined for linearized location estimation in terms of the estimated parameters $\hat{\boldsymbol{x}}_L$ as

$$E\{\|\hat{\boldsymbol{x}}_L - \boldsymbol{x}\|^2\} \geq \mathcal{C}_L = [\mathbf{I}_{\boldsymbol{\theta}}^{-1}]_{11} + [\mathbf{I}_{\boldsymbol{\theta}}^{-1}]_{22}, \tag{4.13}$$

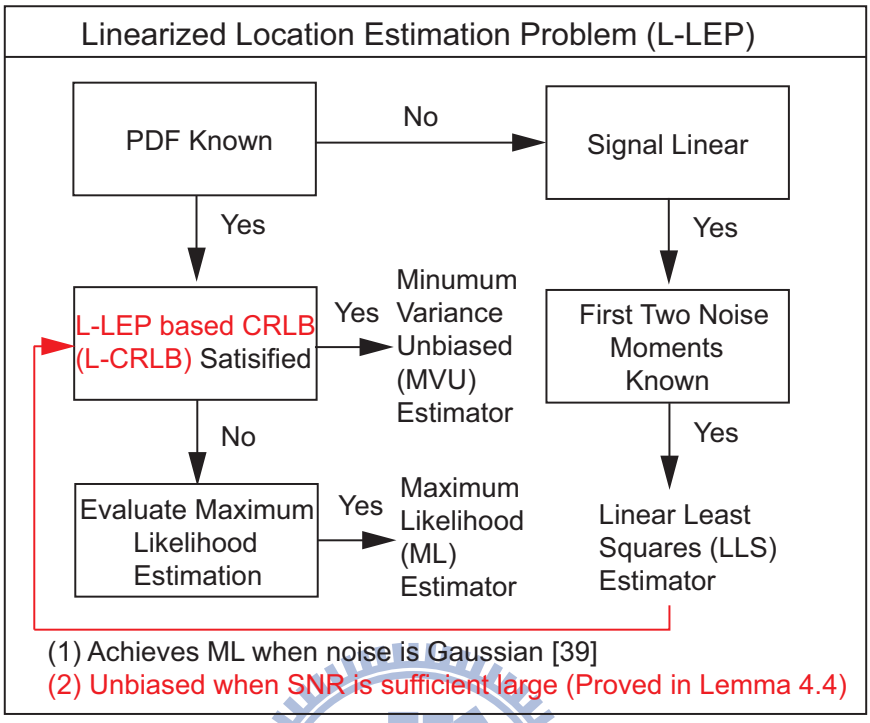

Figure 4.2: A schematic diagram of the LEP.

where $[\mathbf{I}_{\boldsymbol{\theta}}^{-1}]_{11}$ and $[\mathbf{I}_{\boldsymbol{\theta}}^{-1}]_{22}$ respectively denotes the first and second diagonal terms of the inverse of 3×3 FIM matrix $\mathbf{I}_{\boldsymbol{\theta}}$ as

$$\mathbf{I}_{\boldsymbol{\theta}} = \mathbf{H} \cdot \mathbf{I}_{\boldsymbol{\zeta}} \cdot \mathbf{H}^T, \tag{4.14}$$

with

$$\mathbf{H} = \frac{\partial \boldsymbol{\zeta}}{\partial \boldsymbol{\theta}} = \begin{bmatrix} \cos\alpha_1 & \dots & \cos\alpha_i & \dots & \cos\alpha_N \\ \sin\alpha_1 & \dots & \sin\alpha_i & \dots & \sin\alpha_N \\ \frac{1}{2\zeta_1} & \dots & \frac{1}{2\zeta_i} & \dots & \frac{1}{2\zeta_N} \end{bmatrix}, \tag{4.15}$$

and $\mathbf{I}_{\boldsymbol{\zeta}}$ obtained from (4.4). ◇

Note that the derivation of the inequality (4.13) is neglected in this chapter, which can be similarly referred from the derivation of CRLB in [39]. Based on the theory of CRLB, the closed-forms of FIM in (4.14) can be formulated and the relevant matrix in (4.15) is derived. In other words, the proposed L-CRLB is utilized to denote the minimum variance for any estimator that estimates the parameter vector $\boldsymbol{\theta}$ from the TOA measurements.

Fig. 4.2 illustrates a schematic diagram about how to solve the L-LEP within the statistical signal processing theory. The L-CRLB serves as a theoretic lower bound in this problem. Since the estimated parameters and measurement are in linear, the LLS can achieve the CRLB under two

conditions: 1) Gaussian noise: the LLS achieves ML under Gaussian noise which has been proven in [39]; 2) Unbiased property: we will proved in Lemma 4.4 when the SNR is sufficient large. Based on these conditions, we can conclude that the L-LEP can be solved by the LLS estimator efficiently. In this chapter, we would like to utilize the L-CRLB as an index to observe the lost from the original LEP to the L-LEP. In the following lemma, the fact that the L-CRLB is greater than or equal to the CRLB will be proved.

Lemma 4.2. *Considering that there exists sufficient measurement inputs for location estimation with zero mean Gaussian noises, the L-CRLB is greater than or equal to the CRLB, i.e.,* $\mathcal{C}_L \geq \mathcal{C}$.

Proof. The 3×3 matrix $\mathbf{I}_{\boldsymbol{\theta}}$ can be obtained from (4.4) and (4.14) as

$$\mathbf{I}_{\boldsymbol{\theta}} = \begin{bmatrix} \mathbf{I}_{\boldsymbol{x}} & \mathbf{B} \\ \mathbf{B}^T & \mathbf{C} \end{bmatrix} = \begin{bmatrix} \sum_{i=1}^{N} \frac{1}{\sigma_{r_i}^2} \cos^2 \alpha_i & \sum_{i=1}^{N} \frac{1}{\sigma_{r_i}^2} \cos \alpha_i \cdot \sin \alpha_i & \sum_{i=1}^{N} \frac{1}{\sigma_{r_i}^2} \frac{\cos \alpha_i}{2\zeta_i} \\ \sum_{i=1}^{N} \frac{1}{\sigma_{r_i}^2} \cos \alpha_i \cdot \sin \alpha_i & \sum_{i=1}^{N} \frac{1}{\sigma_{r_i}^2} \sin^2 \alpha_i & \sum_{i=1}^{N} \frac{1}{\sigma_{r_i}^2} \frac{\sin \alpha_i}{2\zeta_i} \\ \sum_{i=1}^{N} \frac{1}{\sigma_{r_i}^2} \frac{\cos \alpha_i}{2\zeta_i} & \sum_{i=1}^{N} \frac{1}{\sigma_{r_i}^2} \frac{\sin \alpha_i}{2\zeta_i} & \sum_{i=1}^{N} \frac{1}{4\sigma_{r_i}^2 \zeta_i^2} \end{bmatrix}, \quad (4.16)$$

where the matrices $\mathbf{B} = \begin{bmatrix} \sum_{i=1}^{N} \frac{1}{\sigma_{r_i}^2} \frac{\cos \alpha_i}{2\zeta_i} & \sum_{i=1}^{N} \frac{1}{\sigma_{r_i}^2} \frac{\sin \alpha_i}{2\zeta_i} \end{bmatrix}^T$ and $\mathbf{C} = \begin{bmatrix} \sum_{i=1}^{N} \frac{1}{4\sigma_{r_i}^2 \zeta_i^2} \end{bmatrix}$. Note that the 2×2 matrix $\mathbf{I}_{\boldsymbol{x}}$ is the same as that obtained from (4.2). Moreover, the inverse of the covariance matrix $\mathbf{I}_{\boldsymbol{\theta}}$ can be represented as

$$\mathbf{I}_{\boldsymbol{\theta}}^{-1} = \begin{bmatrix} [\mathbf{I}_{\boldsymbol{\theta}}]_{2\times 2}^{-1} & \mathbf{B}' \\ \mathbf{B}'^T & \mathbf{C}' \end{bmatrix}, \quad (4.17)$$

where the 2×2 submatrix $[\mathbf{I}_{\boldsymbol{\theta}}]_{2\times 2}^{-1}$ of $\mathbf{I}_{\boldsymbol{\theta}}^{-1}$ can be obtained as $[\mathbf{I}_{\boldsymbol{\theta}}]_{2\times 2}^{-1} = (\mathbf{I}_{\boldsymbol{x}} - \mathbf{B} \cdot \mathbf{C}^{-1} \cdot \mathbf{B}^T)^{-1}$ based on the matrix inversion lemma. Considering that there are sufficient measurement inputs for the linearized location estimation, i.e., $N \geq 3$, both the covariance matrices $\mathbf{I}_{\boldsymbol{\theta}}$ and $\mathbf{I}_{\boldsymbol{x}}$ are non-singular which corresponds to positive definite matrices. Consequently, the submatrix $[\mathbf{I}_{\boldsymbol{\theta}}]_{2\times 2}$ and their corresponding inverse matrices $\mathbf{I}_{\boldsymbol{\theta}}^{-1}$, $\mathbf{I}_{\boldsymbol{x}}^{-1}$, and $[\mathbf{I}_{\boldsymbol{\theta}}]_{2\times 2}^{-1}$ are positive definite. Furthermore, both $\mathbf{C}$ and $\mathbf{C}^{-1}$ are positive definite since $\mathbf{C} = \begin{bmatrix} \sum_{i=1}^{N} \frac{1}{4\sigma_{r_i}^2 \zeta_i^2} \end{bmatrix} > 0$. Therefore, it can be shown that $[\mathbf{I}_{\boldsymbol{\theta}}]_{2\times 2} = (\mathbf{I}_{\boldsymbol{x}} - \mathbf{B} \cdot \mathbf{C}^{-1} \cdot \mathbf{B}^T) \leq \mathbf{I}_{\boldsymbol{x}}$ since $\mathbf{C}^{-1}$ is positive definite and the equality only occurs with zero matrix $\mathbf{B}$. Given two positive definite matrices $[\mathbf{I}_{\boldsymbol{\theta}}]_{2\times 2}$ and $\mathbf{I}_{\boldsymbol{x}}$, $\mathbf{I}_{\boldsymbol{x}} \geq [\mathbf{I}_{\boldsymbol{\theta}}]_{2\times 2}$ if and only if $[\mathbf{I}_{\boldsymbol{\theta}}]_{2\times 2}^{-1} \geq \mathbf{I}_{\boldsymbol{x}}^{-1} > 0$. Furthermore, since $[\mathbf{I}_{\boldsymbol{\theta}}]_{2\times 2}^{-1} \geq \mathbf{I}_{\boldsymbol{x}}^{-1}$, their corresponding traces will follow as $\text{trace}([\mathbf{I}_{\boldsymbol{\theta}}]_{2\times 2}^{-1}) \geq \text{trace}(\mathbf{I}_{\boldsymbol{x}}^{-1})$ which consequently results in $[\mathbf{I}_{\boldsymbol{\theta}}]_{11}^{-1} + [\mathbf{I}_{\boldsymbol{\theta}}]_{22}^{-1} \geq [\mathbf{I}_{\boldsymbol{x}}]_{11}^{-1} + [\mathbf{I}_{\boldsymbol{x}}]_{22}^{-1}$. This completes the proof. □

Corollary 4.1. *The L-CRLB is equivalent to the CRLB if the following two conditions hold*

$$\begin{cases} \sum_{i=1}^{N} \frac{1}{\sigma_{r_i}^2} \frac{\sin \alpha_i}{\zeta_i} = 0 \\ \sum_{i=1}^{N} \frac{1}{\sigma_{r_i}^2} \frac{\cos \alpha_i}{\zeta_i} = 0 \end{cases}. \quad (4.18)$$

Proof. As stated in Lemma 4.2, the necessary and sufficient condition for both L-CRLB and CRLB to be equivalent is that $\mathbf{B}$ is a zero matrix. Therefore, the two matrix elements in $\mathbf{B}$, i.e., $\sum_{i=1}^{N} \cos\alpha_i/(\sigma_{r_i}^2\zeta_i)$ and $\sum_{i=1}^{N} \sin\alpha_i/(\sigma_{r_i}^2\zeta_i)$, will be equal to zero. □

It can be generalized from Corollary 4.1 that the two error terms $\varepsilon_1 = \sum_{i=1}^{N} \cos\alpha_i/(\sigma_{r_i}^2\zeta_i)$ and $\varepsilon_2 = \sum_{i=1}^{N} \sin\alpha_i/(\sigma_{r_i}^2\zeta_i)$ will influence the value of L-CRLB, which consequently affect the precision of linearized location estimators. Under the geometric layout with smaller values of ε_1 and ε_2, smaller difference between the CRLB and L-CRLB value can be obtained, which indicates that the linearization lost by adopting linearized location estimators is smaller. ε_1 and ε_2 can be mapping to the x- and y-direction vectors from the MS to the BS. The noise variance terms can be regarded as the weighting of the direction vector. The minimum linearization lost for the linearized location estimator is achieved when the sum of the weighted direction vector from the MS to the BS is equal to zero. Besides, consider the case that the MS is situated outside of the polygon formed by the BSs, all the angles α_i will be in the range of $[0, 180°]$ which results in larger value of the error terms ε_1 and ε_2. As a result, the estimation errors acquired from the linearized location estimator will be comparably large in this type of geometric relationship. The following example is given to demonstrate the scenario where the L-CRLB is equal to CRLB.

Example 4.2 (Network Layout for Equivalent L-CRLB and CRLB)**.** Assuming that the variances σ_{r_i} from all the measurement noises are equivalent, the L-CRLB can achieve the CRLB if (a) the noiseless distances ζ_i from the MS to all the corresponding BSs are equal, and (b) the orientation angles α_i from the MS to all the BSs are uniformly distributed in $[0°, 360°)$ as $\alpha_i = 360° \cdot (i-1)/N + \gamma$, $\forall\ \gamma = [0°, 360°)$ and $i = 1$ to N. ◇

Proof. By substituting the conditions $\zeta_1 = \zeta_2 = ... = \zeta_N$ and $\sigma_{r_1} = \sigma_{r_2} = ... = \sigma_{r_N}$ into (4.18), the necessary condition for the L-CRLB and the CRLB to be equivalent becomes $\sum_{i=1}^{N} \cos\alpha_i = 0$ and $\sum_{i=1}^{N} \sin\alpha_i = 0$. Based on the assumptions as stated above, an unit vector can be utilized to represent the distance from the MS to the ith BS as $\nu_i = [\cos\alpha_i, \sin\alpha_i]$ for $i = 1$ to N. In order to satisfy the conditions for both $\sum_{i=1}^{N} \cos\alpha_i = 0$ and $\sum_{i=1}^{N} \sin\alpha_i = 0$, the summation for projecting all unit vectors ν_i for $i = 1$ to N on the x-axis and y-axis respectively should be equal to zero. In order to achieve this condition, it can be verified that the angles α_i will be uniformly distributed in $[0°, 360°)$ with its value equal to $\alpha_i = 360° \cdot (i-1)/N + \gamma$, $\forall\ \gamma = [0°, 360°)$. This completes the proof. □

Corollary 4.2. *The minimum L-CRLB ($\mathcal{C}_{L,m}$) is achieved if the conditions stated in (4.6) and (4.18) are satisfied.*

Proof. It has been indicated that the minimum CRLB ($\mathcal{C}_m$) can be obtained if the conditions in (4.6) hold. Moreover, Corollary 4.1 proves that (4.18) should be satisfied for both L-CRLB and CRLB to be equivalent. Therefore, the minimum L-CRLB ($\mathcal{C}_{L,m}$) can be achieved if (4.6) and (4.18) are satisfied. □

It can be observed from Corollary 4.2 that additional condition (4.18) should be satisfied for achieving minimum L-CRLB comparing with the minimum CRLB. The major difference is that the CRLB is affected by the angles α_i and signal variances $\sigma_{r_i}^2$; while the L-CRLB additionally depends on the distance information ζ_i. Therefore, the performance of the L-LEP is affected by the additional relative distance information between the MS and BSs. In order to provide intuitive explanation, the exemplified network layout for achieving minimum L-CRLB is shown as follows.

Example 4.3 (Network Layout with Minimum L-CRLB)**.** Following the requirement as in Lemmas 4.1 and 4.2 with $N = 3$ and all the variances are equivalent, i.e., $\sigma_{r_i}^2 = \sigma_r^2$ for $i = 1$ to 3, and further assuming that the noiseless distances ζ_i from the MS to all the three BSs are equivalent, the minimum L-CRLB can be achieved only at the angle sets $\{\alpha_1, \alpha_2, \alpha_3\} = \{\gamma, \gamma + 120°, \gamma + 240°\}$ $\forall\, \gamma = [0°, 360°)$.

Proof. Considering $N = 3$ and $\sigma_{r_1} = \sigma_{r_2} = \sigma_{r_3} = \sigma_r$ in (4.6), the following relationship is obtained:

$$\begin{cases} \sin 2\alpha_1 + \sin 2\alpha_2 + \sin 2\alpha_3 = 0 \\ \cos 2\alpha_1 + \cos 2\alpha_2 + \cos 2\alpha_3 = 0 \end{cases}. \tag{4.19}$$

It can be verified that both conditions in (4.19) are only satisfied at either one of the following angle sets: $\{\alpha_1, \alpha_2, \alpha_3\} = \{\gamma, \gamma+120°, \gamma+240°\}$ and $\{\alpha_1, \alpha_2, \alpha_3\} = \{\gamma, \gamma+60°, \gamma+120°\}$ $\forall\, \gamma = [0°, 360°)$. The corresponding minimum CRLB can be calculated from (4.5) as $\mathcal{C}_m = 4\sigma_r^2/3$.

On the other hand, according to Lemma 4.2, the conditions (4.6) and (4.18) must be satisfied in order to achieve minimum L-CRLB. Considering the $N = 3$ case with $\zeta_1 = \zeta_2 = \zeta_3$, condition (4.18) is rewritten as

$$\begin{cases} \sin \alpha_1 + \sin \alpha_2 + \sin \alpha_3 = 0 \\ \cos \alpha_1 + \cos \alpha_2 + \cos \alpha_3 = 0 \end{cases}. \tag{4.20}$$

It can be verified that only the angle sets $\{\alpha_1, \alpha_2, \alpha_3\} = \{\gamma, \gamma+120°, \gamma+240°\}$ $\forall\, \gamma = [0°, 360°)$ can satisfy all the three conditions as defined in (4.19) and (4.20) for achieving the minimum value of L-CRLB. This completes the proof. □

In other words, when the MS is positioned at the center of a regular polygon formed by the BSs, the proposed L-CRLB will be equivalent to the CRLB based on the conditions stated in (4.18). Example 4.3 describes the fact that minimum CRLB can be achieved under two different set of orientation angles; while the minimum L-CRLB is reached by one of its subset of angles. This indicates the situation that the L-CRLB provides a more stringent criterion compared to the CRLB for achieving its minimum value. Even though certain network layouts are suggested to achieve minimum CRLB, it does not guarantee that the corresponding L-CRLB can reach the same value. Therefore, the CRLB does not provide sufficient information to be utilized as the criterion for the

linearized location estimator of the L-LEP; while the L-CRLB can be more feasible to reveal the geometric properties and requirements.

In order to provide better explanation on the properties of CRLB and L-CRLB, the definitions of several geometric relationships between the MS and the BSs are described as follows.

Definition 4.3 (BS's Adjacent Included Angle)**.** Based on the BS's orientation α_i, the adjacent included angle between two neighboring i-th and $(i+1)$-th BSs is defined as $\beta_i = \alpha_{i+1} - \alpha_i$ for $i = 1$ to $N-1$, and $\beta_N = 360^\circ + \alpha_1 - \alpha_N$. ◇

Definition 4.4 (BS Polygon)**.** Considering the locations of BSs as the vertices in geometry, the BS polygon is defined by connecting the adjacent BSs as the edges of the polygon from BS_1 to BS_N. ◇

Definition 4.5 (Inside-Polygon Layout (IPL))**.** Given the BS's adjacent included angle set $\boldsymbol{\beta} = \{\beta_1, \ldots, \beta_i, \ldots, \beta_N\}$, an inside-polygon layout (IPL) is defined if the MS is located inside the BS polygon where $0^\circ < \beta_i < 180^\circ \ \forall\ i$ from 1 to N. ◇

Definition 4.6 (Outside-Polygon Layout (OPL))**.** Given the BS's adjacent included angle set $\boldsymbol{\beta} = \{\beta_1, \ldots, \beta_i, \ldots, \beta_N\}$, a outside-polygon layout (OPL) is defined if the MS is located outside the BS polygon where there exists an adjacent included angle $180^\circ \le \beta_i < 360^\circ \ \forall\ i$ from 1 to N. ◇

Lemma 4.3. *Consider two types of layouts, IPL and OPL, between the MS and three BSs under the requirements with equivalent variances $\sigma_{r_i}^2$ and noiseless distances ζ_i for $i = 1$ to 3. There can exist both IPL and OPL that possess the same CRLB value; while the corresponding L-CRLB value of the IPL is smaller than that of the OPL.*

Proof. Given an IPL, the set of BS's adjacent included angle is defined as $\boldsymbol{\beta}_{in} = \{\beta_1, \beta_2, \beta_3 = 360^\circ - \beta_1 - \beta_2\}$ where $0^\circ < \beta_i < 180^\circ \ \forall\ i = 1$ to 3. The set of BS's orientation between the MS and three BSs can be represented as $\boldsymbol{\alpha}_{in} = \{\alpha_1 = 0, \alpha_2 = \beta_1, \alpha_3 = \beta_1 + \beta_2\}$. Without lose of generality, α_1 is set with zero degree according to the rotation property as proven in [37] for CRLB. In order to establish an OPL, the third BS is repositioned to the reflected side with respect to the MS, which results in its BS's orientation as $\boldsymbol{\alpha}_{out} = \{\alpha_1 = 0, \alpha_2 = \beta_1, \alpha_3' = \beta_1 + \beta_2 - 180^\circ\}$. By substituting both IPL and OPL cases with $\boldsymbol{\alpha}_{in} = \{0, \alpha_2, \alpha_3\}$ and $\boldsymbol{\alpha}_{out} = \{0, \alpha_2, \alpha_3 - 180^\circ\}$ respectively into (4.1), it can be observed that same value of CRLB is achieved by both OPL and OPL.

Moreover, in order to compare the L-CRLB for the IPL and OPL, i.e., $\mathcal{C}_{L,in}$ and $\mathcal{C}_{L,out}$, the difference of L-CRLB for both layouts is derived from (4.13) to (4.15) with the substitution of $\boldsymbol{\alpha}_{in}$ and $\boldsymbol{\alpha}_{out}$ as

$$\begin{aligned}\delta &= \mathcal{C}_{L,in} - \mathcal{C}_{L,out} = [\mathbf{I}_{\theta,in}]_{11}^{-1} + [\mathbf{I}_{\theta,in}]_{22}^{-1} - [\mathbf{I}_{\theta,out}]_{11}^{-1} - [\mathbf{I}_{\theta,out}]_{22}^{-1} \\ &= \frac{1}{D_{\mathbf{I}_{\theta,in}} D_{\mathbf{I}_{\theta,out}}} \left\{ -8 \cos\frac{\alpha_2}{2} \cos\frac{2\alpha_3 - \alpha_2}{2} (1 - \cos\alpha_2)[2\cos\alpha_2 + 2\cos\alpha_3 \cos(\alpha_2 - \alpha_3) - 4] \right\},\end{aligned} \tag{4.21}$$

where $D_{\mathbf{I}_{\theta,in}}$ and $D_{\mathbf{I}_{\theta,out}}$ denote the determinants of the FIM matrix $\mathbf{I}_{\theta,in}$ and $\mathbf{I}_{\theta,out}$ for the L-CRLB of IPL and OPL respectively. Since both $\mathbf{I}_{\theta,in}$ and $\mathbf{I}_{\theta,out}$ are positive definite, their corresponding determinants $D_{\mathbf{I}_{\theta,in}}$ and $D_{\mathbf{I}_{\theta,out}}$ will be positive values. Furthermore, the following conditions hold since the BS's orientation set $\boldsymbol{\alpha}_{in}$ corresponds to an IPL: $0^\circ < \alpha_2 < 180^\circ$, $0^\circ < \alpha_3 - \alpha_2 < 180^\circ$, and $180^\circ < \alpha_3 < 360^\circ$. Therefore, the following conditions hold for the numerator terms in (4.21): $\cos(\alpha_2/2) > 0$ since $0^\circ < \alpha_2/2 < 90^\circ$, $\cos[(2\alpha_3 - \alpha_2)/2] < 0$ since $90^\circ < (2\alpha_3 - \alpha_2)/2 < 270^\circ$, $(1-\cos\alpha_2) > 0$ since $-1 < \cos\alpha_2 < 1$, and $2\cos\alpha_2 + 2\cos\alpha_3\cos(\alpha_2-\alpha_3) < 4$ since $-1 < \cos\alpha_2 < 1$ and $-1 < \cos\alpha_3\cos(\alpha_2 - \alpha_3) < 1$. As a consequence, the difference $\delta = \mathcal{C}_{L,in} - \mathcal{C}_{L,out} < 0$ which corresponds to the result that the L-CRLB of the IPL is smaller than that of the OPL. This completes the proof. □

A key contribution of this chapter is obtained from Lemma 4.3 that the proposed L-CRLB can describe the geometric relationship between the MS and its corresponding BSs, i.e., either the IPL or OPL; while the conventional CRLB criterion observes the same value for both cases. It is found in Lemma 4.3 that the L-CRLB for MS to locate inside the BS polygon will be smaller than that for MS situated outside the BS polygon. This result implicitly indicates that the estimation accuracy from a linearized location estimator will be higher for the IPL compared to the OPL case. The conjecture to possess higher estimation precision for the IPL compared to that for the OPL will be validated via simulations in Section 4.4.

4.3 Unbiased Condition of LLS

As observed from the difference between the L-CRLB and the conventional CRLB in Section 4.2, the additional nonlinear parameter R prevents the LLS to approach the CRLB. However, the LLS method can approach the L-CRLB well under the Gaussian Noise assumption. Note that both the CRLB and the L-CRLB represent lower bounds for unbiased estimators. Therefore, the target of this following lemma is to identify the conditions for the unbiased properties to be satisfied associated with the LLS location estimator based on TOA signals. Note that the formulation of LLS can be referred to Section 2.3.

Lemma 4.4. *The LLS estimator is an unbiased estimator for the location estimation providing that all the TOA measurements are line-of-sight (LOS) signals and the corresponding noiseless distance is much greater than the combined noise for each measurement.*

Proof. The primary concern of this proof is to acquire the expected value of estimation error $\Delta\hat{\boldsymbol{x}}_{LS} = [\Delta\hat{x}_{LS}, \Delta\hat{y}_{LS}]^T$, which can be obtained by rewriting (2.12) as

$$\Delta\hat{\boldsymbol{x}}_{LS} = \mathbf{P}\cdot(\mathbf{M}^T\mathbf{M})^{-1}\mathbf{M}^T\Delta\mathbf{J}. \tag{4.22}$$

It is noted that (4.22) indicates that the estimation error vector $\Delta\hat{\boldsymbol{x}}_{LS}$ is incurred by the variation within the vector $\mathbf{J}$. The value of $\Delta\mathbf{J}$ is obtained by considering the variations from the measurement inputs, i.e., $r_i = \zeta_i + n_i$ in (2.1), with $N = 3$ case as

$$\Delta\mathbf{J} = \begin{bmatrix} 2\,\zeta_1\,n_1 + (n_1)^2 \\ 2\,\zeta_2\,n_2 + (n_2)^2 \\ 2\,\zeta_3\,n_3 + (n_3)^2 \end{bmatrix} \simeq \begin{bmatrix} 2\,\zeta_1\,n_1 \\ 2\,\zeta_2\,n_2 \\ 2\,\zeta_3\,n_3 \end{bmatrix}. \tag{4.23}$$

It is noted that the approximation from the second equality within (4.23) is valid by considering that the noiseless distance ζ_i is in general much greater than the combined noise effect n_i in practice, i.e., $\zeta_i >> n_i$. Without lose of generality, coordinate transformation can be adopted within (4.22) such that $(x_1,\, y_1) = (0,\, 0)$. The expected value of estimation error can therefore be acquired by expanding (4.22) as

$$\begin{aligned} E[\Delta\hat{x}_{LS}] &= E\left[\frac{\zeta_3 n_3 y_2 - \zeta_2 n_2 y_3 - \zeta_1 n_1 (y_3 - y_2)}{x_2 y_3 - x_3 y_2}\right] \\ &= \frac{\zeta_3 y_2 \cdot E[n_3] - \zeta_2 y_3 \cdot E[n_2] - \zeta_1 (y_3 - y_2) \cdot E[n_1]}{x_2 y_3 - x_3 y_2}, \end{aligned} \tag{4.24}$$

$$\begin{aligned} E[\Delta\hat{y}_{LS}] &= E\left[\frac{\zeta_3 n_3 x_2 - \zeta_2 n_2 x_3 - \zeta_1 n_1 (x_3 - x_2)}{x_2 y_3 - x_3 y_2}\right] \\ &= \frac{\zeta_3 x_2 \cdot E[n_3] - \zeta_2 x_3 \cdot E[n_2] - \zeta_1 (x_3 - x_2) \cdot E[n_1]}{x_2 y_3 - x_3 y_2}. \end{aligned} \tag{4.25}$$

From (4.24) and (4.25), it can be clearly observed that the expected value of estimation error is zero under the assumption that its associated measurement are considered LOS signals as zero mean random variables, i.e., $E[n_i] = 0\ \forall i$. This completes the proof. □

Lemma 4.4 reveals the fact that the LLS estimator can be regarded as an unbiased estimator under the condition $\zeta_i >> n_i$. Note that this result consists with the proposition in [38] that the MLE of the MS position is an unbiased estimate as SNR is sufficiently large. Since the L-CRLB represents the theoretical lower bound for any unbiased estimator in the L-LEP, it can therefore be utilized as the lower bound for the LLS estimator. Moreover, the mean square error of LLS estimator can also be derived from (4.24) and (4.25) under the situation that the measurement noises are independent with each other, i.e., $E[n_i \cdot n_j] = 0\ \forall i \neq j$, which is obtained as

$$E[\Delta\hat{x}_{LS}^2] = \frac{\zeta_2^2 y_3^2 \sigma_{n_2}^2 + \zeta_3^2 y_2^2 \sigma_{n_3}^2 + \zeta_1^2 (y_3 - y_2)^2 \sigma_{n_1}^2}{(x_3 y_2 - x_2 y_3)^2}, \tag{4.26}$$

$$E[\Delta\hat{y}_{LS}^2] = \frac{\zeta_2^2 x_3^2 \sigma_{n_2}^2 + \zeta_3^2 x_2^2 \sigma_{n_3}^2 + \zeta_1^2 (x_3 - x_2)^2 \sigma_{n_1}^2}{(x_3 y_2 - x_2 y_3)^2}. \tag{4.27}$$

Noted that (4.26) and (4.27) are also derived based on the condition that $\zeta_i >> n_i$. Meanwhile, it is interesting to notice that the variance of LLS estimator calculated from (4.26) and (4.27) will be numerically identical to the L-CRLB computed via (4.13), which will be validated and shown in the following section. Therefore, the LLS estimator will approach its defined lower bound L-CRLB under the situation with smaller measurement noises. Furthermore, the L-CRLB will become the conventional CRLB under specific geometric layout as described in Corollary 4.1. As a result, under specific conditions as stated above, the LLS estimator can be claimed as the best estimator since it can finally reach the theoretical lower bound, i.e., CRLB, for unbiased estimators.

4.4 Performance Evaluation

In order to verify the effectiveness of L-CRLB derived in Subsection 4.2.3, different scenarios are provided in the section to validate the correctness of the formulation. The model for the measurement noise of TOA signal n_i as in (2.1) is selected as the Gaussian distribution with zero mean and standard deviation σ_{r_i}, i.e., $n_i \sim \mathcal{N}(0, \sigma_{r_i}^2)$ (i.e., LOS noise model in Section 2.2.1.1). Subsection 4.4.1 presents the contour plots in order to numerically describe the difference between the CRLB and L-CRLB, which also validate the correctness of Lemmas 4.1 to 4.2 and Corollaries 4.1 to 4.2. Subsection 4.4.2 simulates the performance of LLS method by comparing the L-CRLB and LLS estimator in the regular BS polygon layout. Subsection 4.4.3 illustrates the performance comparison of LLS estimator under both the IPL and OPL cases. Performance comparison under realistic WSN scenario is described in Subsection 4.4.4.

4.4.1 Numerical Validation of CRLB and L-CRLB with a Regular Triangular Layout

Example 4.4 (CRLB and L-CRLB contour)**.** In order to observe the difference between the CRLB and L-CRLB, their corresponding contour plots under the number of BSs $N = 3$ are shown in Figs. 4.3(a) and 4.3(b), respectively. Note that the three BSs are located at the vertexes of a regular triangular which are denoted with red circles in Figs. 4.3(a) and 4.3(b). The positions of BSs are $\boldsymbol{b}_1 = [300, 200]^T$ with $\alpha_1 = 0°$, $\boldsymbol{b}_2 = [150, 286.6]^T$ with $\alpha_2 = 120°$, and $\boldsymbol{b}_3 = [150, 113.4]^T$ with $\alpha_3 = 240°$. Based on the three BS's positions, each individual contour point represents the corresponding CRLB or L-CRLB value when the MS is situated at that geographical location. The standard deviation of measurement noises σ_{r_i} is chosen as 1 m for simplicity. It can be observed from Fig. 4.3(a) that there are four minimum points for the CRLB value equal to $\mathcal{C}_m = 1.33$ with MS's positions as $\boldsymbol{x} = [200, 200]^T$, $[100, 200]^T$, $[260, 120]^T$, and $[260, 280]^T$. The conditions for minimum CRLB can be verified by substituting the corresponding parameters into the condition

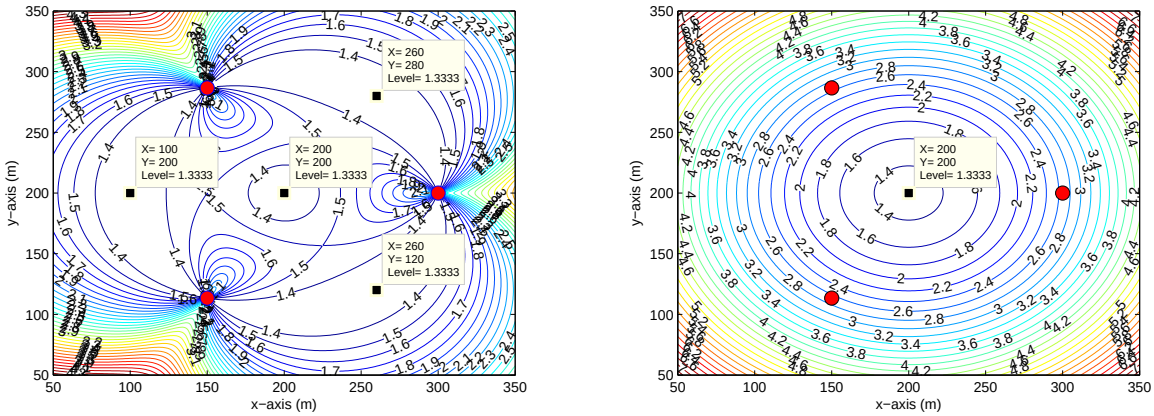

(a) (b)

Figure 4.3: (a) CRLB contour under $N = 3$; (b) L-CRLB contour under $N = 3$. Red circles denote the positions of BSs.

(4.6). The minimum CRLB value can also be validated to satisfy (4.5), which demonstrates the correctness of Lemma 4.1.

On the other hand, by comparing Figs. 4.3(a) and 4.3(b), it is observed that the distribution of L-CRLB is different from that of CRLB. The only minimum L-CRLB value identical to that of the CRLB, i.e., $\mathcal{C}_{L,m} = \mathcal{C}_m = 1.33$, is located at the center of regular triangle formed by the three BSs, i.e., $\boldsymbol{x} = [200, 200]^T$. Starting at the MS's position with minimum L-CRLB, the L-CRLB value will increase in all directions. Except for the minimum L-CRLB at the center of the triangle, the relationship that $\mathcal{C}_L > \mathcal{C}$ can be observed from both Figs. 4.3(a) and 4.3(b). Moreover, the difference between the L-CRLB and CRLB inside the triangle is smaller than that outside of the triangle. The reason can be contributed to the estimation of parameter R by adopting the L-CRLB criterion, which introduces the two terms ε_1 and ε_2. Owing to the nonlinear behavior of location estimation, the additional consideration of R within the L-CRLB can better characterize the performance of linearized location estimator for the L-LEP. The correctness of minimum L-CRLB value obtained from Fig. 4.3(b) can also be verified by substituting corresponding parameters into the conditions stated in Lemma 4.2, i.e., the conditions (4.6) and (4.18) can all be satisfied. By comparing the results from Figs. 4.3(a) and 4.3(b), Corollaries 4.1 to 4.2 and Examples 4.2 to 4.3 can all be validated by substituting the corresponding numerical values. ◇

4.4.2 Performance Validation of LLS Estimator with a Regular BS Polygon Layout

In this subsection, the performance of LLS estimator is simulated to further validate the relationship between the estimator and the lower bound.

Table 4.1: Simulation Parameters

Number of BSs	i-th BS's Coordinate $\boldsymbol{b}_i$ in meter		
3 BSs	0°: $[300, 200]^T$	120°: $[150, 286.6]^T$	240°: $[150, 113.4]^T$
4 BSs	0°: $[300, 200]^T$ 270°: $[200, 100]^T$	90°: $[200, 300]^T$	180°: $[100, 200]^T$
5 BSs	0°: $[300, 200]^T$ 216°: $[119.1, 141.2]^T$	72°: $[230.9, 295.1]^T$ 288°: $[230.9, 104.9]^T$	144°: $[119.1, 258.8]^T$
6 BSs	0°: $[300, 200]^T$ 180°: $[100, 200]^T$	60°: $[250, 286.6]^T$ 240°: $[150, 113.4]^T$	120°: $[150, 286.6]^T$ 300°: $[250, 113.4]^T$
7 BSs	0°: $[300, 200]^T$ 154.3°: $[109.9, 243.4]^T$ 308.6°: $[262.3, 121.8]^T$	51.4°: $[262.3, 278.2]^T$ 205.7°: $[109.9, 156.6]^T$	102.8°: $[177.7, 297.5]^T$ 257.1°: $[177.7, 102.5]^T$
8 BSs	0°: $[300, 200]^T$ 135°: $[129.3, 270.7]^T$ 270°: $[200, 100]^T$	45°: $[270.7, 270.7]^T$ 180°: $[100, 200]^T$ 315°: $[270.7, 129.3]^T$	90°: $[200, 300]^T$ 225°: $[129.3, 129.3]^T$

Example 4.5 (A Regular BS Polygon Layout at $N = 3$)**.** Fig. 4.4 illustrates the performance comparison under different noise standard deviations in the regular triangular layout, i.e., $N = 3$. The coordinates of the 3 BSs are listed in the 3 BS case of Table 4.1, and the MS is located at the coordinate $\boldsymbol{x} = [200, 200]^T$. Moreover, Fig. 4.5 shows the performance comparison between different numbers BSs of regular BS polygon layout where the MS lies at $\boldsymbol{x} = [200, 200]^T$ and the standard deviation of measurement noise is equal to 10 m. The BS's coordinates correspond to different numbers of BSs' layout are listed in Table 4.1. Regarding the comparison metrics, instead of showing the variances, the root mean square error (RMSE) is obtained in order to clearly illustrate the difference between different curves, i.e., RMSE $= \left[\sum_{i=1}^{N_r} \|\boldsymbol{x} - \hat{\boldsymbol{x}}(i)\|^2 / N_r\right]^{1/2}$, where $N_r = 10,000$ indicates the number of simulation runs. As for the curves within Figs. 4.4 and 4.5, the LLS estimator denotes the RMSE of $\hat{\boldsymbol{x}}_{LS}$ acquired from (2.12) by simulating the Gaussian noises with corresponding noise standard deviations. Since the CRLB and the L-CRLB represent the variance of an unbiased estimator, both the CRLB and L-CRLB curves are obtained by taking the square root in order to compared with the RMSE values of LLS estimator. Furthermore, the curve of LLS standard deviation in Fig. 4.4 is obtained as the square root of LLS variance derived from (4.26) and (4.27).

It can be observed from Fig. 4.4 that the CRLB, L-CRLB, and LLS standard deviation can achieve the same values in the regular triangular layout. The reason for the CRLB and L-CRLB to possess the same value is identical to the conditions as stated in Lemmas 4.1 and 4.2. As described in Section 2.3, the LLS standard deviation is numerically validated in this figure to be identical to the square roots of CRLB and L-CRLB under the condition $\zeta_i >> n_i$. The performance of LLS estimator obtained from simulations can also approach both lower bounds, i.e., the CRLB and L-CRLB, under the cases with smaller measurement noises. This result demonstrates that the LLS estimator can be considered as an efficient estimator for the LEP and L-LEP under smaller

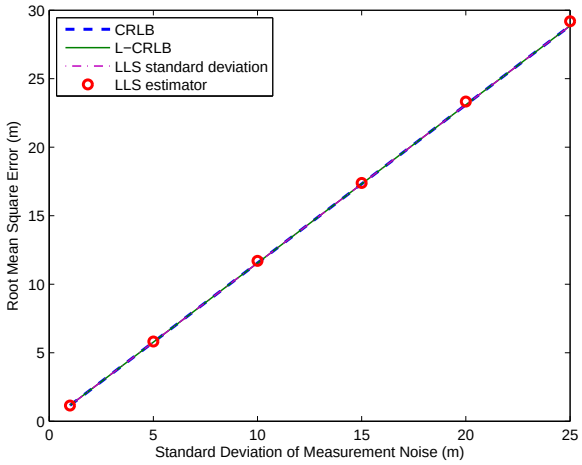

Figure 4.4: Performance comparison for location estimation with MS at the center of a regular triangle formed by 3 BSs as listed in Table 4.1: RMSE vs. standard deviation of measurement noise. The CRLB, L-CRLB, and LLS standard deviation achieve the same values.

measurement noises. On the other hand, as the noise becomes larger which disobeys the relationship $\zeta_i >> n_i$, it is observed that the RMSE of LLS estimator will be slightly higher than that obtained from the L-CRLB. ◇

Example 4.6 (A Regular BS Polygon Layout at different number of BSs)**.** Fig. 4.5 validates the performance of LLS estimator in the regular BS polygon layouts under different numbers of BSs. In order to observe the difference between the LLS estimator and the L-CRLB, the error confidential level (δ) is defined as the difference between the RMSE of LLS estimator ($\mathcal{R}_{LS}$) and the square root of L-CRLB ($\mathcal{R}_L$), i.e., $\delta = |\mathcal{R}_{LS} - \mathcal{R}_L|/\mathcal{R}_L$. In Fig. 4.5, the error confidential levels can be obtained as $\delta = [0.67, 0.53, 0.20, 0.27, 0.41, 0.17]\%$ under the number of BSs equal to $[3, 4, 5, 6, 7, 8]$. It is observed that the LLS estimator can closely approach both of the lower bounds CRLB and L-CRLB under different numbers of available BSs. ◇

4.4.3 Performance Comparison of LLS Estimation with IPL and OPL

In the subsection, the IPL and OPL which achieve the same CRLB value are adopted to validate the correctness of Lemma 4.3.

Example 4.7 (IPL and OPL Comparision)**.** The MS is placed at the position $\boldsymbol{x} = [200, 200]^T$ m, and the distances from all the BSs to the MS are designed to be equal to 100 m. The angle set for the IPL is assigned as $\{0°, 70°, 240°\}$, and that for the OPL is $\{0°, 60°, 70°\}$. That is, the three BSs of IPL is placed at $[300, 200]^T$, $[234.2, 294]^T$, and $[150, 113.4]^T$, and that for the OPL is located at $[300, 200]^T$, $[250, 286.6]^T$, and $[234.2, 294]^T$. It is noted that the square roots of CRLB for both the IPL and the OPL are obtained to have the same value as 1.34.

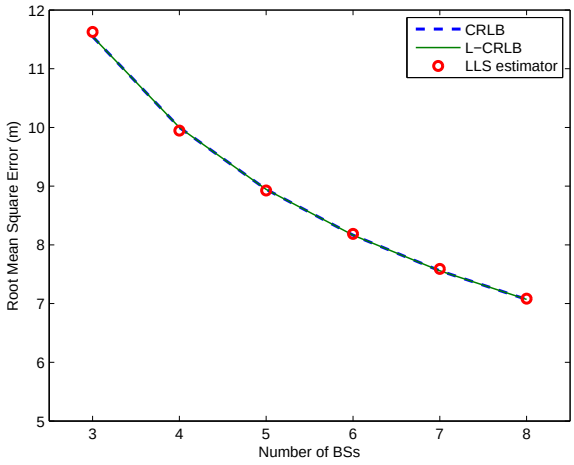

Figure 4.5: Performance comparison for location estimation with MS at the center of a regular BS polygon formed by the BSs as listed in Table 4.1: RMSE vs. the number of BSs. The standard deviation of measurement noise is 10 m. The CRLB and L-CRLB achieve the same values.

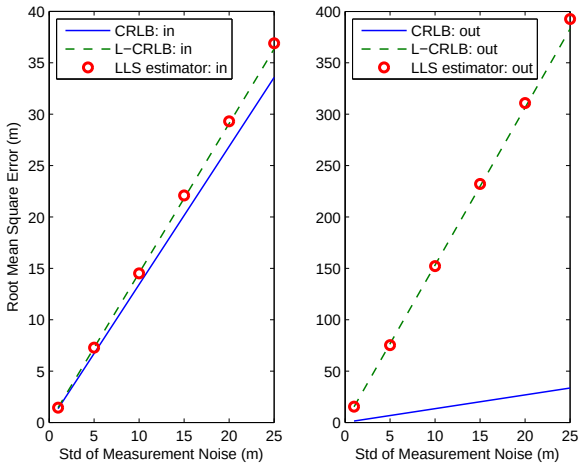

Figure 4.6: Performance comparison for location estimation under 3 BSs triangular layout: RMSE vs. standard deviation of measurement noise. Left plot: the MS is located inside the triangle formed by BSs; Right plot: the MS is outside of the triangle formed by BSs. The CRLB values are the same in both plots.

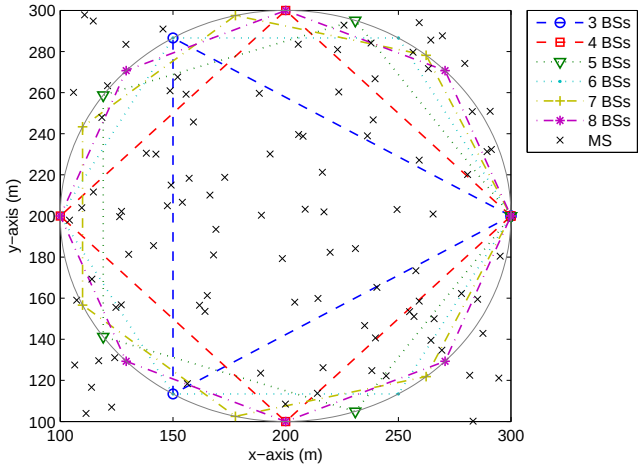

Figure 4.7: Layout of the WSN scenario formed by different numbers of BSs. The MS lies in a rectangular room with both x-coordinates and y-coordinates uniformly distributed between $[100, 300]$. The BS's coordinates are listed in Table 4.1.

The left subplot of Fig. 4.6 shows the performance of LLS estimator comparing with both CRLB and L-CRLB under the IPL; while the right subplot of Fig. 4.6 corresponds to that for the OPL. In order to clearly show the difference between these curves, different scales are utilized in both plots. It can be observed that the performance of LLS estimator still matches that of the L-CRLB under the cases with smaller measurement noises for both plots, which again shows that the L-CRLB can closely characterize the behaviors of LLS estimator. However, the difference between the L-CRLB and the CRLB in the OPL is comparably larger than the IPL case, which validates the correctness of Lemma 4.3. Therefore, it is concluded that the LLS estimator can provide better performance in the IPL compared to the OPL even though both layouts result in same value of CRLB. ◇

4.4.4 Performance Comparison of LLS Estimation in a WSN Scenario

In order to consider more realistic environments, Fig. 4.7 illustrates the simulation scenarios of a WSN with the coordinates of both the MSs and BSs under different BS polygon layouts. The MS's positions are placed at 100 different locations uniformly distributed in a two-dimensional rectangular plane with both the x-coordinate and y-coordinate in the region of $[100, 300]$ m. The coordinates of BSs for different deployments of BS polygon are listed in Table 4.1. According to the random deployment, some of the MSs will be located in the IPL and the others are in the OPL.

Example 4.8 (A WSN Scenario)**.** Based on the WSN setup, Fig. 4.8 shows the performance evaluation of LLS estimator in comparison with both CRLB and L-CRLB under different numbers of BSs. Noted that each RMSE value of LLS estimator in Fig. 4.8 is obtained by averaging the

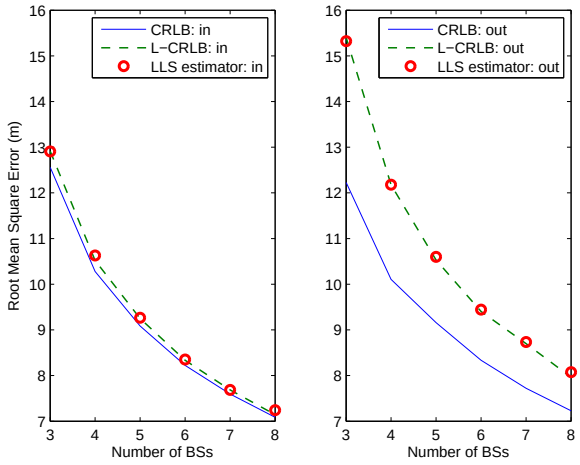

Figure 4.8: Performance comparison for location estimation with uniformly distributed MS and the BS's coordinates listed in Table 4.1: RMSE vs. number of BSs. The standard deviation of measurement noise is 10 m. Left plot: the MS is located inside the BS polygon; Right plot: the MS is situated outside of the BS polygon.

RMSE value from 100 different MS's positions, where the RMSE of each MS's position is simulated with 100 times, i.e., $N_r = 100$. Both the CRLB and L-CRLB are also obtained by averaging the corresponding values from 100 different MS's positions. The simulation scenario is regarded as a more generic case since the distances from the MS to BSs will not be the same in every simulation point. Comparing with the CRLB, it can be observed that the proposed L-CRLB can better characterize the simulation results for LLS estimator under both the IPL and OPL cases. Moreover, the LLS estimator can still provide better performance within the IPL in comparison with that in the OPL. This conclusion is both validated via theoretical proof in Lemma 4.3 and simulation results in Fig. 4.8. Furthermore, the LLS performance under the IPL can be compatible with the LLS performance under the OPL which utilizes one more measurement. For example, the RMSE of the $4BSs$ case under the IPL is 10.7 m while the RMSE of the $5BSs$ case under the OPL is 10.65 m. The more number of BSs utilized in a location estimate requires more communication overheads. As a consequence, from the study of geometric effect of LLS estimator, it is suggested that the OPL should be avoided for increasing the precision of MS's location estimation. This conclusion will be valuable for either cellular networks or WSNs while conducting the deployment of BSs or implementing a BS selection algorithm. ◇

4.5 Concluding Remarks

This chapter derives the linearized location estimation problem based Cramèr-Rao lower bound (L-CRLB) which provides the analytical form to discuss the geometric effect for the linear least

square (LLS) estimator. The geometric properties and the relationships between the L-CRLB and conventional CRLB are obtained with theoretical proofs. It is validated in the simulations that the L-CRLB can provide the tight lower bound for the LLS estimator, especially under the situations with smaller measurement noises. Moreover, the proposed L-CRLB can be utilized to describe the performance difference of an LLS estimator under different geometric layouts. The MS locates inside a BS-constrained geometry will provide higher estimation accuracy comparing with the case that the MS is situated outside of the BS-confined geometry layout.

Chapter 5

Geometry-Assisted Linearized Localization Algorithms for Wireless Networks

- The geometric analysis with the proposed L-CRLB in Chapter 4 motivates the design of geometry-assisted linearized localization (GALL) algorithm in order to consider the geometric effect associated with the linearization lost. Two different implementations, including the GALL with two-step LS estimator (GALL-TSLS) and the GALL with Kalman filter (GALL-KF), are proposed to consider the situations with and without the adoption of MS's historical estimation.

5.1 Introduction

The objective of Chapter 4 is to formulate the theoretic lower bound for the geometric analysis of the linearized location estimation problem (L-LEP). Since the location estimation problem (LEP) is inherently nonlinear, the original LEP is often transformed into an L-LEP by introducing an additional variable to transfer the nonlinear equation into a linear equation for the computation of mobile station's (MS's) position. This transformation leads to a different parameterization and the analysis of the L-LEP has not been fully addressed in previous research work. Based on the concept of Cramer-Rao lower bound (CRLB), the theoretic lower bound of the L-LEP is derived as the L-LEP based CRLB (L-CRLB). The closed-form formulation of the FIM for the derived L-CRLB provides a comparison between the L-LEP and the conventional LEP.

A key contribution of Chapter 4 is obtained from Lemma 4.3 that the proposed L-CRLB can describe the geometric relationship between the MS and its corresponding BSs, i.e., either the MS is located inside or outside the geometry constrained by the BSs; while the conventional CRLB criterion observes the same value for both cases. It is found in Lemma 4.3 that the L-CRLB for MS

to locate inside the BS polygon will be smaller than that for MS situated outside the BS polygon. This result implicitly indicates that the estimation accuracy from a linearized location estimator will be higher for the inside polygon layout (IPL) compared to the outside polygon layout (OPL) case. Based on this fact, the objective of the chapter is to propose a geometry-assisted linearized localization (GALL) algorithm algorithm to enhance the estimation accuracy of the linearized location estimator for the OPL.

In this chapter, the GALL scheme is proposed to enhance the estimation precision by incorporating the geometric information within the conventional two-step least squares (TSLS) algorithm [17]. Note that the LLS method is one of the methods to solve the L-LEP; while the TSLS is an performance enhancing estimator based on the LLS method. Since the linearization lost exists in the first step of the TSLS estimator, the properties derived for the L-LEP can be utilized to describe the geometric effect of the TSLS estimator. Based on an initial estimate of the MS's location, the GALL algorithm is proposed to fictitiously rotate (i.e., not to physically relocate) different BSs locations according to the L-CRLB criterion in order to achieve enhanced MSs location estimate. Reasonable location estimation can be acquired by adopting the GALL algorithm, especially feasible for the cases with poor geometric circumstances of the L-LEP, e.g., if the MS is located outside of the geometric layout confined by the BSs. Two different types of implementations are proposed for the GALL scheme, including the GALL with TSLS estimator (GALL-TSLS) and the GALL with Kalman filter (GALL-KF) schemes. The GALL-TSLS can directly provide enhanced MS's location estimate compared to the conventional TSLS method, which will be validated in the simulation results. The GALL-KF approach further utilizes the Kalman filter to provide smoothing effect on the initial estimate with a two-stage location estimation architecture. Simulation results illustrate that the proposed GALL-KF scheme can achieve higher accuracy for the MS's estimated location compared to the other existing methods in both line-of-sight (LOS) and none-line-of-sight (NLOS) environments.

The remainder of this chapter is organized as follows. The determination of fictitious BS's locations based on the proposed GALL algorithm is explained in Section 5.2; while Section 5.3 demonstrates the GALL-TSLS and the GALL-KF schemes as the implementation of the GALL algorithm. Section 5.4 shows the performance evaluation of the proposed schemes. The conclusions are drawn in Section 5.5.

5.2 Proposed Geometry-Assisted Linearized Localization (GALL) Algorithm

The main objective of the proposed GALL scheme is to enhance the LLS-based algorithms by considering the geometric effect to the location estimation accuracy. The signal model for the TOA measurements in a synchronous network is utilized for two-dimension (2-D) location estimation,

which can be referred to Section 2.1.1. The core component of the GALL scheme is to acquire the positions of the *fictitious* BSs such as to achieve the minimum L-CRLB value with respect to the MS's initial location estimate $\hat{\boldsymbol{x}}^o$. Note that the position of the i-th fictitious BS with respect to the MS's initial location estimate can be represented based on the measurement distance r_i and the BS's orientation α_i. Since r_i is available as the measured information, the determination of *fictitious* BS's position corresponds to the adjustment of the BS's orientation α_i. The position information of these *fictitious* BSs will be utilized to replace that of the original BSs in order to achieve better geometric layout for location estimation, which will be discussed as the implementation of the GALL scheme in Section 5.3. In this section, the core mechanism of the GALL algorithm to identify which BSs should be fictitiously rotated will be demonstrated. The sub-schemes of the GALL algorithm with different numbers of fictitious BSs will be stated, i.e., the GALL with one fictitiously movable BS scheme (GALL(1BS)) and the GALL with two fictitiously movable BSs scheme (GALL(2BS)) in Subsections 5.2.1 and 5.2.2 respectively. Subsection 5.2.3 describes the combined schemes of the GALL algorithm by selecting among different numbers of fictitious BSs based on the minimum L-CRLB requirement.

5.2.1 GALL with One Fictitiously Movable BS (GALL(1BS)) scheme

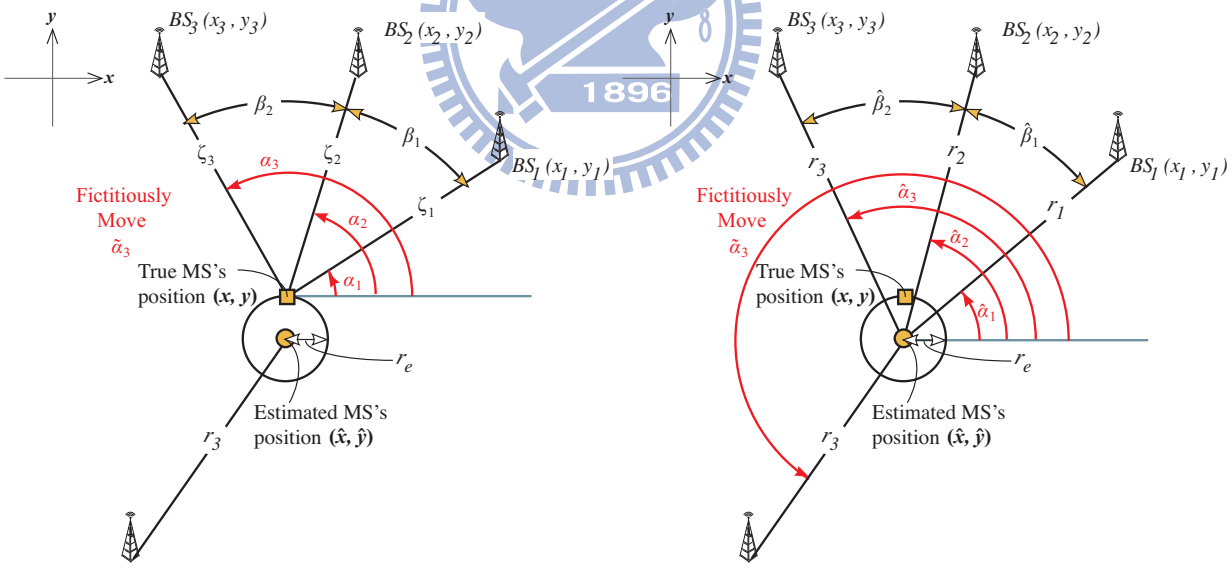

(a) An example of one fictitiously movable BS centered at the true MS's position.

(b) An example of one fictitiously movable BS centered at the estimated MS's position.

Figure 5.1: Schematic diagrams of GALL with one fictitiously movable BS scheme.

The GALL(1BS) scheme is designed to fictitiously relocate the position of one BS according to the criterion for achieving the optimal geometric layout, i.e., the minimum L-CRLB. Note that

only one BS is allowed to be fictitiously movable and the others remain fixed in this case. The objective of the GALL(1BS) scheme is to decide which BS should be fictitiously moved in order to obtain the minimum L-CRLB. The *GALL(1BS) problem* is defined as

$$j^m = \arg \min_{\substack{\mathcal{C}_L(\tilde{\alpha}_j^m)<\mathcal{C}_L \\ j=1,\ldots,N}} \mathcal{C}_L(\tilde{\alpha}_j^m), \tag{5.1}$$

where $\tilde{\alpha}_j^m$ represents the orientation of the j^m-th fictitiously moveable BS that achieves the minimum L-CRLB. Providing that all the BSs within GALL(1BS) scheme cannot result in lowered L-CRLB values compared to the original C_L, the constraint defined in (5.1) will not be satisfied. In other words, the original L-CRLB has already been the lowest under the given measurement conditions, where none of the BSs is required to be fictitiously moved and the initial MS's location estimate will become the final estimate. By observing from the problem defined in (5.1), the optimal rotated angle $\tilde{\alpha}_j^m$ of a single BS should be determined first. The *one fictitiously movable BS problem* is defined to obtain the optimal rotated angle of the j-th BS as

$$\tilde{\alpha}_j^m = \arg \min_{\forall \tilde{\alpha}_j} \mathcal{C}_L(\tilde{\alpha}_j), \quad \forall \tilde{\alpha}_j = [0°, 360°). \tag{5.2}$$

Note that the original $\mathbf{H}$ matrix in (4.15) for the computation of $\mathcal{C}_L$ cannot be obtained owing to the required true MS's position and noiseless relative distances. The estimated matrix $\hat{\mathbf{H}}$ can be calculated based on the initial estimate $\hat{\boldsymbol{x}}^o$ and the measurement distance r as

$$\begin{aligned} \hat{\mathbf{H}} &= \begin{bmatrix} \frac{x_1-\hat{x}^o}{r_1} & \cdots & \frac{x_i-\hat{x}^o}{r_i} & \cdots & \frac{\tilde{x}_j-\hat{x}^o}{r_j} & \cdots & \frac{x_N-\hat{x}^o}{r_N} \\ \frac{y_1-\hat{y}^o}{r_1} & \cdots & \frac{y_i-\hat{y}^o}{r_i} & \cdots & \frac{\tilde{y}_j-\hat{y}^o}{r_j} & \cdots & \frac{y_N-\hat{y}^o}{r_N} \\ \frac{1}{2r_1} & \cdots & \frac{1}{2r_i} & \cdots & \frac{1}{2r_j} & \cdots & \frac{1}{2r_N} \end{bmatrix} \\ &= \begin{bmatrix} \cos\hat{\alpha}_1 & \cdots & \cos\hat{\alpha}_i & \cdots & \cos\tilde{\alpha}_j & \cdots & \cos\hat{\alpha}_N \\ \sin\hat{\alpha}_1 & \cdots & \sin\hat{\alpha}_i & \cdots & \sin\tilde{\alpha}_j & \cdots & \sin\hat{\alpha}_N \\ \frac{1}{2r_1} & \cdots & \frac{1}{2r_i} & \cdots & \frac{1}{2r_j} & \cdots & \frac{1}{2r_N} \end{bmatrix}, \end{aligned} \tag{5.3}$$

where $\hat{\alpha}_i$ in (5.3) represents the i-th BS's estimated orientation based on the initial estimate $\hat{\boldsymbol{x}}^o$. The parameters $\tilde{\boldsymbol{b}}_j = (\tilde{x}_j, \tilde{y}_j)$ and $\tilde{\alpha}_j$ in (5.3) denote the position and orientation of the j-th fictitiously moveable BS, respectively. It is noticed that the design of proposed GALL scheme also considers the effect coming from the approximation of matrix $\hat{\mathbf{H}}$. As shown in Fig. 5.1(b), the orientation of the fictitiously moved BS is considered to center at the MS's estimated position instead of the true MS's position as in Fig. 5.1(a). It can be observed that the selection of fictitiously moveable BS may induce additional error since it is designed based on the imperfect initial estimate even though it can provide better geometry for location estimation. This demonstrates the situation that the fictitiously moveable BS may not always result in lowered L-CRLB value than the original network layout as stated in the constraint of problem (5.1). Note that the initial estimation error

can be approximated as a Gaussian noise distribution with the standard deviation of the initial estimation error σ_{r_e}, i.e., $\mathcal{N}(0, \sigma_{r_e}^2)$ where σ_{r_e} depends on the precision of the initial estimate $\hat{\boldsymbol{x}}^o$. Providing that the LLS-based estimation is utilized for the initial estimation, the matrix $\mathbf{I}_{\boldsymbol{\zeta}}$ for the computation of $\mathcal{C}_L$ can be derived based on the precision of MS's initial estimate σ_{r_e} as $\mathbf{I}_{\boldsymbol{\zeta}} = \text{diag}\{[\sigma_{r_1}^{-2}, \ldots, \sigma_{r_i}^{-2}, \ldots, (\sigma_{r_j}^2 + \sigma_{r_e}^2)^{-1}, \ldots, \sigma_{r_N}^{-2}]\}$. The L-CRLB $\mathcal{C}_L(\tilde{\alpha}_j)$ in (5.2) can thus be derived as

$$\mathcal{C}_L(\tilde{\alpha}_j) = \frac{1}{D_\theta}[(\sum_{\substack{i=1\\(i\neq j)}}^{N} \frac{\sin\hat{\alpha}_i}{2\sigma_{r_i}^2 \cdot r_i} + \frac{\sin\tilde{\alpha}_j}{2(\sigma_{r_j}^2 + \sigma_{r_e}^2)\cdot r_j})^2 + (\sum_{\substack{i=1\\(i\neq j)}}^{N} \frac{\cos\hat{\alpha}_i}{2\sigma_{r_i}^2 \cdot r_i} + \frac{\cos\tilde{\alpha}_j}{2(\sigma_{r_j}^2 + \sigma_{r_e}^2)\cdot r_j})^2 + \sum_{i=1}^{N} \frac{N}{4\cdot r_i^2}], \tag{5.4}$$

where D_θ denotes for the determinant of FIM matrix $\mathbf{I}_{\boldsymbol{\theta}}$. By neglecting the terms in (5.4) that are not related to the parameter $\tilde{\alpha}_j$, the *equivalent one fictitiously movable BS problem* as presented in problem (5.2) can be obtained as

$$\begin{aligned} \tilde{\alpha}_j^m &= \arg\min_{\forall\tilde{\alpha}_j} f_1(\tilde{\alpha}_j) \qquad (5.5)\\ &= \arg\min_{\forall\tilde{\alpha}_j} \frac{1}{D_\theta}[(\sum_{\substack{i=1\\(i\neq j)}}^{N} \frac{\sin\hat{\alpha}_i}{2\sigma_{r_i}^2 \cdot r_i} + \frac{\sin\tilde{\alpha}_j}{2(\sigma_{r_j}^2 + \sigma_{r_e}^2)\cdot r_j})^2 + (\sum_{\substack{i=1\\(i\neq j)}}^{N} \frac{\cos\hat{\alpha}_i}{2\sigma_{r_i}^2 \cdot r_i} + \frac{\cos\tilde{\alpha}_j}{2(\sigma_{r_j}^2 + \sigma_{r_e}^2)\cdot r_j})^2], \end{aligned}$$

where $f_1(\tilde{\alpha}_j)$ can be regarded as the cost function of the considered problem. It can be observed that the solution of problem (5.5) can be acquired if the following conditions on the first and second derivatives of $f_1(\tilde{\alpha}_j)$ are satisfied, i.e.,

$$\left[\frac{\partial f_1(\tilde{\alpha}_j)}{\partial\tilde{\alpha}_j}\right]_{\tilde{\alpha}_j=\tilde{\alpha}_j^m} = 0, \tag{5.6}$$

$$\left[\frac{\partial^2 f_1(\tilde{\alpha}_j)}{\partial^2\tilde{\alpha}_j}\right]_{\tilde{\alpha}_j=\tilde{\alpha}_j^m} > 0. \tag{5.7}$$

Due to the complex formulation of (5.5) - (5.7), there does not exist closed form for obtaining the optimal value of $\tilde{\alpha}_j^m$. In order to solve the optimum rotated angle $\tilde{\alpha}_j^m$, root-finding algorithms can be utilized to find suitable solution candidates between $[0, 360°)$ in (5.6), and these solutions will further be examined to satisfy the requirement of (5.7). If there are still multiple candidates that fits all the requirements, i.e., there are multiple local minimums for problem (5.2), the angle $\tilde{\alpha}_j^m$ that possesses with the global minimum L-CRLB value will be chosen from (5.4) among those solution candidates.

Furthermore, in order to reduce the computation complexity, a cost function $g_1(\tilde{\alpha}_j)$ is defined

to simplify the original problem (5.2) without the consideration of D_θ in (5.5). An *approximate one fictitiously movable BS problem* can therefore be obtained as

$$\begin{aligned}\tilde{\alpha}_j^m &= \arg\min_{\forall\tilde{\alpha}_j} g_1(\tilde{\alpha}_j) \qquad (5.8)\\ &= \arg\min_{\forall\tilde{\alpha}_j}[(\sum_{\substack{i=1\\(i\neq j)}}^{N}\frac{\sin\hat{\alpha}_i}{2\sigma_{r_i}^2\cdot r_i}+\frac{\sin\tilde{\alpha}_j}{2(\sigma_{r_j}^2+\sigma_{r_e}^2)\cdot r_j})^2+(\sum_{\substack{i=1\\(i\neq j)}}^{N}\frac{\cos\hat{\alpha}_i}{2\sigma_{r_i}^2\cdot r_i}+\frac{\cos\tilde{\alpha}_j}{2(\sigma_{r_j}^2+\sigma_{r_e}^2)\cdot r_j})^2].\end{aligned}$$

It is interesting to notice that the cost function $g_1(\tilde{\alpha}_j)$ can be closely related to the conditions stated in (4.18) for Corollary 4.1. Providing that the minimum value of $g_1(\tilde{\alpha}_j)$ approaches zero, the two conditions in (4.18) can be satisfied by solving problem (5.8). In other words, by fictitiously moving the j-th BS via angle $\tilde{\alpha}_j^m$ with the consideration of σ_{r_e} for initial estimate, the layout with the smallest linearization lost can possibly be achieved where the L-CRLB is equivalent to the CRLB. Therefore, based on the design of fictitious movable BS, the two square terms within $g_1(\tilde{\alpha}_j)$ can be treated as the extension of the two error terms ε_1 and ε_2 as described after Corollary 4.1 that affect the precision of linearized location estimators. By considering the first derivative of $g_1(\tilde{\alpha}_j)$ equal to zero, the rotated angle $\tilde{\alpha}_j^m$ for this problem can be derived as

$$\tilde{\alpha}_j^m = \tan^{-1}(\sum_{\substack{i=1\\(i\neq j)}}^{N}\frac{\cos\hat{\alpha}_i}{2\sigma_{r_i}^2\cdot r_i})/(\sum_{\substack{i=1\\(i\neq j)}}^{N}\frac{\sin\hat{\alpha}_i}{2\sigma_{r_i}^2\cdot r_i}). \qquad (5.9)$$

Note that the angle $\tilde{\alpha}_j^m$ does not depend on any information from the j-th BS, i.e., the measurement of the j-th BS. The angle $\tilde{\alpha}_j^m$ lies in the domain of arc tangent function between $(-90°, 90°)$ which is half of the domain of $[0, 360°)$. Since both angles $\tilde{\alpha}_j^m$ and $\tilde{\alpha}_j^m + 180°$ can be the local minimum of the subproblem (5.8), these two angles will be further substituted into (5.4) to choose the angle with smaller L-CRLB value. Following the procedures as stated above, all the BSs can be fictitiously moved and the associated rotated angle $\tilde{\alpha}_j^m$ can be obtained. The j^m-th BS with the minimum L-CRLB value will be selected to be the fictitiously moveable BS for the GALL(1BS) scheme in problem (5.1). For example as shown in Fig. 5.1, only the third BS, i.e., $j^m = 3$, is fictitiously adjusted and the other two BSs remain at the same position. The j^m-th fictitiously moved BS will be relocated to the coordinate as

$$\begin{cases}\tilde{x}_{j^m} = r_{j^m}\cos(\tilde{\alpha}_j^m)\\ \tilde{y}_{j^m} = r_{j^m}\sin(\tilde{\alpha}_j^m)\end{cases}. \qquad (5.10)$$

Note that the measurement of the j^m-th BS remains the same as r_{j^m}. The noise variance of this measurement is recalculated as $\sigma_{r_j^m}^2 + \sigma_{r_e}^2$. Based on the new set of BSs adjusted by the proposed GALL(1BS) scheme, the LLS-based estimation can be adopted to obtain the final estimation of

MS's position.

5.2.2 GALL with Two Fictitiously Movable BSs (GALL(2BSs)) Scheme

The GALL(2BSs) scheme is designed to fictitiously relocate the position of two BSs according to the minimal L-CRLB layout criterion. Under this condition, two BSs are defined to be fictitiously movable and the others are fixed. The objective of the GALL(2BSs) scheme is to select the specific two BSs that should be fictitiously moved in order to achieve the layout with the minimum L-CRLB. The *GALL(2BSs) problem* is defined as

$$\{j^m, k^m\} = \arg \min_{\substack{\mathcal{C}_L(\tilde{\alpha}_j^m, \tilde{\alpha}_k^m) < \mathcal{C}_L \\ j=1,\ldots,N, k=1,\ldots,N, j\neq k}} \mathcal{C}_L(\tilde{\alpha}_j^m, \tilde{\alpha}_k^m), \tag{5.11}$$

where $\tilde{\alpha}_j^m$ and $\tilde{\alpha}_k^m$ represent the orientation of two fictitiously moveable BSs. The constraint in (5.11) is to verify if the original L-CRLB has already been the lowest under the given measurement conditions. Before solving problem (5.11), the optimum rotated angles $\tilde{\alpha}_j^m$ and $\tilde{\alpha}_k^m$ of the two fictitiously movable BSs should be decided first. The *two fictitiously movable BSs problem* is defined to find the optimum rotated angles as

$$\{\tilde{\alpha}_j^m, \tilde{\alpha}_k^m\} = \arg \min_{\forall \tilde{\alpha}_j, \tilde{\alpha}_k, j\neq k} \mathcal{C}_L(\tilde{\alpha}_j, \tilde{\alpha}_k), \quad \forall \tilde{\alpha}_j, \tilde{\alpha}_k = [0°, 360°). \tag{5.12}$$

Note that the matrix $\mathbf{I}_{\boldsymbol{\zeta}}$ in $\mathcal{C}_L(\tilde{\alpha}_j, \tilde{\alpha}_k)$ can be obtained as $\mathbf{I}_{\boldsymbol{\zeta}} = \text{diag}\{[\sigma_{r_1}^{-2}, \ldots, (\sigma_{r_j}^2 + \sigma_{r_e}^2)^{-1}, \ldots, (\sigma_{r_k}^2 + \sigma_{r_e}^2)^{-1}, \ldots, \sigma_{r_N}^{-2}]\}$, where the standard deviation σ_{r_e} of MS's initial estimate is considered in both the j-th and k-th fictitiously movable BSs. Therefore, the L-CRLB can be derived as

$$\begin{aligned}\mathcal{C}_L(\tilde{\alpha}_j, \tilde{\alpha}_k) = \frac{1}{D_\theta}[(\sum_{\substack{i=1 \\ (i\neq j,k)}}^{N} \frac{\sin\hat{\alpha}_i}{2\sigma_{r_i}^2 \cdot r_i} + \frac{\sin\tilde{\alpha}_j}{2(\sigma_{r_j}^2 + \sigma_{r_e}^2) \cdot r_j} + \frac{\sin\tilde{\alpha}_k}{2(\sigma_{r_k}^2 + \sigma_{r_e}^2) \cdot r_k})^2 \\ +(\sum_{\substack{i=1 \\ (i\neq j,k)}}^{N} \frac{\cos\hat{\alpha}_i}{2\sigma_{r_i}^2 \cdot r_i} + \frac{\cos\tilde{\alpha}_j}{2(\sigma_{r_j}^2 + \sigma_{r_e}^2) \cdot r_j} + \frac{\cos\tilde{\alpha}_k}{2(\sigma_{r_k}^2 + \sigma_{r_e}^2) \cdot r_k})^2 + \sum_{i=1}^{N} \frac{N}{4 \cdot r_i^2}].\end{aligned} \tag{5.13}$$

Similar to the GALL(1BS) scheme, the *equivalent two fictitiously movable BSs problem* for problem (5.12) can also be acquired as

$$\{\tilde{\alpha}_j^m, \tilde{\alpha}_k^m\} = \arg \min_{\forall \tilde{\alpha}_j, \tilde{\alpha}_k, j\neq k} f_2(\tilde{\alpha}_j, \tilde{\alpha}_k), \tag{5.14}$$

where $f_2(\tilde{\alpha}_j, \tilde{\alpha}_k)$ is regarded as the cost function of problem (5.14) as

$$\begin{aligned} f_2(\tilde{\alpha}_j, \tilde{\alpha}_k) &= \frac{1}{D_\theta}\Big(\sum_{\substack{i=1 \\ (i\neq j,k)}}^{N} \frac{\sin\hat{\alpha}_i}{2\sigma_{r_i}^2 \cdot r_i} + \frac{\sin\tilde{\alpha}_j}{2(\sigma_{r_j}^2+\sigma_{r_e}^2)\cdot r_j} + \frac{\sin\tilde{\alpha}_k}{2(\sigma_{r_k}^2+\sigma_{r_e}^2)\cdot r_k}\Big)^2 \\ &\quad + \Big(\sum_{\substack{i=1 \\ (i\neq j,k)}}^{N} \frac{\cos\hat{\alpha}_i}{2\sigma_{r_i}^2 \cdot r_i} + \frac{\cos\tilde{\alpha}_j}{2(\sigma_{r_j}^2+\sigma_{r_e}^2)\cdot r_j} + \frac{\cos\tilde{\alpha}_k}{2(\sigma_{r_k}^2+\sigma_{r_e}^2)\cdot r_k}\Big)^2. \end{aligned} \tag{5.15}$$

It can be observed that problem (5.14) can be solved if the following conditions on the first derivatives of $f_2(\tilde{\alpha}_j, \tilde{\alpha}_k)$ are satisfied, i.e.,

$$\left[\frac{\partial f_2(\tilde{\alpha}_j, \tilde{\alpha}_k)}{\partial \tilde{\alpha}_j}\right]_{\substack{\tilde{\alpha}_j=\tilde{\alpha}_j^m \\ \tilde{\alpha}_k=\tilde{\alpha}_k^m}} = 0, \left[\frac{\partial f_2(\tilde{\alpha}_j, \tilde{\alpha}_k)}{\partial \tilde{\alpha}_k}\right]_{\substack{\tilde{\alpha}_j=\tilde{\alpha}_j^m \\ \tilde{\alpha}_k=\tilde{\alpha}_k^m}} = 0, \tag{5.16}$$

and the conditions on the second derivatives of $f_2(\tilde{\alpha}_j, \tilde{\alpha}_k)$ are also fulfilled, i.e., $a > 0$ and $ac - b^2 > 0$, where

$$a = \left[\frac{\partial^2 f_2(\tilde{\alpha}_j, \tilde{\alpha}_k)}{\partial^2 \tilde{\alpha}_j}\right]_{\substack{\tilde{\alpha}_j=\tilde{\alpha}_j^m \\ \tilde{\alpha}_k=\tilde{\alpha}_k^m}}, b = \left[\frac{\partial^2 f_2(\tilde{\alpha}_j, \tilde{\alpha}_k)}{\partial \tilde{\alpha}_j \partial \tilde{\alpha}_k}\right]_{\substack{\tilde{\alpha}_j=\tilde{\alpha}_j^m \\ \tilde{\alpha}_k=\tilde{\alpha}_k^m}}, c = \left[\frac{\partial^2 f_2(\tilde{\alpha}_j, \tilde{\alpha}_k)}{\partial^2 \tilde{\alpha}_k}\right]_{\substack{\tilde{\alpha}_j=\tilde{\alpha}_j^m \\ \tilde{\alpha}_k=\tilde{\alpha}_k^m}}. \tag{5.17}$$

Since the closed form solution of $\tilde{\alpha}_j^m$ and $\tilde{\alpha}_k^m$ can not be obtained in this case, numerical methods can be utilized to acquire the optimal angles $\tilde{\alpha}_j^m$ and $\tilde{\alpha}_k^m$ for achieving minimum L-CRLB for problem (5.14). To reduce the computation complexity, a cost function $g_2(\tilde{\alpha}_j, \tilde{\alpha}_k)$ is defined to simplify the original problem (5.12) into an *approximate two fictitiously movable BSs problem*

$$\{\tilde{\alpha}_j^m, \tilde{\alpha}_k^m\} = \arg \min_{\forall \tilde{\alpha}_j, \tilde{\alpha}_k, j\neq k} g_2(\tilde{\alpha}_j, \tilde{\alpha}_k), \tag{5.18}$$

where

$$\begin{aligned} g_2(\tilde{\alpha}_j, \tilde{\alpha}_k) &= \Big(\sum_{\substack{i=1 \\ (i\neq j,k)}}^{N} \frac{\sin\hat{\alpha}_i}{2\sigma_{r_i}^2 \cdot r_i} + \frac{\sin\tilde{\alpha}_j}{2(\sigma_{r_j}^2+\sigma_{r_e}^2)\cdot r_j} + \frac{\sin\tilde{\alpha}_k}{2(\sigma_{r_k}^2+\sigma_{r_e}^2)\cdot r_k}\Big)^2 \\ &\quad + \Big(\sum_{\substack{i=1 \\ (i\neq j,k)}}^{N} \frac{\cos\hat{\alpha}_i}{2\sigma_{r_i}^2 \cdot r_i} + \frac{\cos\tilde{\alpha}_j}{2(\sigma_{r_j}^2+\sigma_{r_e}^2)\cdot r_j} + \frac{\cos\tilde{\alpha}_k}{2(\sigma_{r_k}^2+\sigma_{r_e}^2)\cdot r_k}\Big)^2. \end{aligned} \tag{5.19}$$

The closed form solution of (5.18) for the $N = 3$ case is illustrated as follows. For ease of computation, the three BSs' orientation can be represented by their adjacent included angles as $\hat{\boldsymbol{\alpha}} = \{\hat{\alpha}_1 = \hat{\alpha}_2 - \hat{\beta}_1, \hat{\alpha}_2, \hat{\alpha}_3 = \hat{\alpha}_2 + \hat{\beta}_2\}$ as shown in Fig. 5.1. The GALL(2BSs) scheme fictitiously relocates the positions of two BSs among the three which can be denoted as $\tilde{\boldsymbol{\alpha}} = \{\hat{\alpha}_2 - \tilde{\beta}_1, \hat{\alpha}_2, \hat{\alpha}_2 - \tilde{\beta}_2\}$.

Furthermore, according to the rotation property, the orientation of the fictitiously moved BSs can be transformed as $\tilde{\boldsymbol{\alpha}} = \{-\tilde{\beta}_1, 0°, -\tilde{\beta}_2\}$. By considering the first derivative equation in (5.16), the BSs' adjacent included angles for achieving the minimum CRLB are calculated as

$$\tilde{\beta}_1^m = \cos^{-1} \frac{\sigma_{r_1}^4 r_1^2 \sigma_{r_2}^4 r_2^2 - \sigma_{r_2}^4 r_2^2 \sigma_{r_3}^4 r_3^2 - \sigma_{r_1}^4 r_1^2 \sigma_{r_3}^4 r_3^2}{2\sigma_{r_1}^2 r_1 \cdot \sigma_{r_2}^2 r_2 \cdot \sigma_{r_3}^4 r_3^2}, \tag{5.20}$$

$$\tilde{\beta}_2^m = \cos^{-1} \frac{\sigma_{r_2}^4 r_2^2 \sigma_{r_3}^4 r_3^2 - \sigma_{r_1}^4 r_1^2 \sigma_{r_3}^4 r_3^2 - \sigma_{r_1}^4 r_1^2 \sigma_{r_2}^4 r_2^2}{2\sigma_{r_1}^4 r_1^2 \cdot \sigma_{r_2}^2 r_2 \cdot \sigma_{r_3}^2 r_3}, \tag{5.21}$$

where the angle $\tilde{\beta}_j^m$ for $j = 1$ and 2 lies in the domain of arc cosine function from $[0, 180°]$ which is half of the domain $[0, 360°)$. Both angles $\tilde{\beta}_j^m$ and $\tilde{\beta}_j^m + 180°$ are considered the local minimums of subproblem (5.18). Therefore, these angles will be substituted into (5.13) to determine the angle with smaller L-CRLB value. After the adjacent included angles are calculated, the BSs' orientation of the GALL(2BSs) scheme can be acquired as $\tilde{\boldsymbol{\alpha}}^m = \{\tilde{\alpha}_1^m = \hat{\alpha}_2 - \tilde{\beta}_1^m, \hat{\alpha}_2, \tilde{\alpha}_3^m = \hat{\alpha}_2 + \tilde{\beta}_2^m\}$. Accordingly, all the BSs can be fictitiously moved and the associated rotated angle $\tilde{\alpha}_j^m$ and $\tilde{\alpha}_k^m$ will be obtained. The j^m-th and k^m-th BSs with the minimum L-CRLB value are decided to be the fictitiously moveable BS for the GALL(2BSs) scheme in problem (5.11). The positions of j^m-th and k^m-th BSs can be fictitiously relocated and computed based on (5.10). Note that the measurement remains the same while the noise variance of the measurement is recalculated by considering the initial estimation error. With the new set of BSs obtained from the GALL(2BSs) scheme, the LLS-based estimation algorithms can be adopted to obtain the final MS's location estimation. Based on the derivation of proposed GALL(2BSs) scheme, the number of fictitiously movable BSs can also be increased by extending the GALL scheme with multivariable optimization, i.e., GALL(3BSs), GALL(4BSs).

5.2.3 GALL Scheme

Based on Subsections 5.2.1 and 5.2.2, it can be observed that the GALL(2BSs) scheme provides one more degree of freedom compared to the GALL(1BS) scheme, which should increase the precision of location estimation owing to the enhancement from the geometric effect. However, the two fictitiously moveable BSs associate with the initial MS's estimation error may degrade the performance for location estimation. Therefore, the GALL scheme is designed to select between the two sub-schemes, i.e., GALL(1BS) and GALL(2BSs), in order to achieve minimum L-CRLB value among all different cases. The *GALL problem* can be defined as

$$\tilde{\boldsymbol{\alpha}}^m = \arg \min_{\substack{\tilde{\boldsymbol{\alpha}}_{1BS}^m, \tilde{\boldsymbol{\alpha}}_{2BS}^m \\ \mathcal{C}_L(\tilde{\boldsymbol{\alpha}}_{1BS}^m), \mathcal{C}_L(\tilde{\boldsymbol{\alpha}}_{2BS}^m) < \mathcal{C}_L}} [\mathcal{C}_L(\tilde{\boldsymbol{\alpha}}_{1BS}^m), \mathcal{C}_L(\tilde{\boldsymbol{\alpha}}_{2BS}^m)], \tag{5.22}$$

where $\tilde{\boldsymbol{\alpha}}_{1BS}^m$ and $\tilde{\boldsymbol{\alpha}}_{2BS}^m$ represent the sets of BS's orientation with the lowest L-CRLB by adopting the GALL(1BS) and GALL(2BSs) schemes, respectively. Each of the fictitiously moved BS set

is selected according to the minimum L-CRLB criteria. Note that if both the GALL(1BS) and GALL(2BSs) schemes cannot provide a lower L-CRLB scenario compared to the original unmoved version, the GALL scheme will choose the original BS's positions for MS's location estimation according to the constraint in (5.22).

5.3 Implementations of Geometry-Assisted Linearized Location (GALL) Algorithm

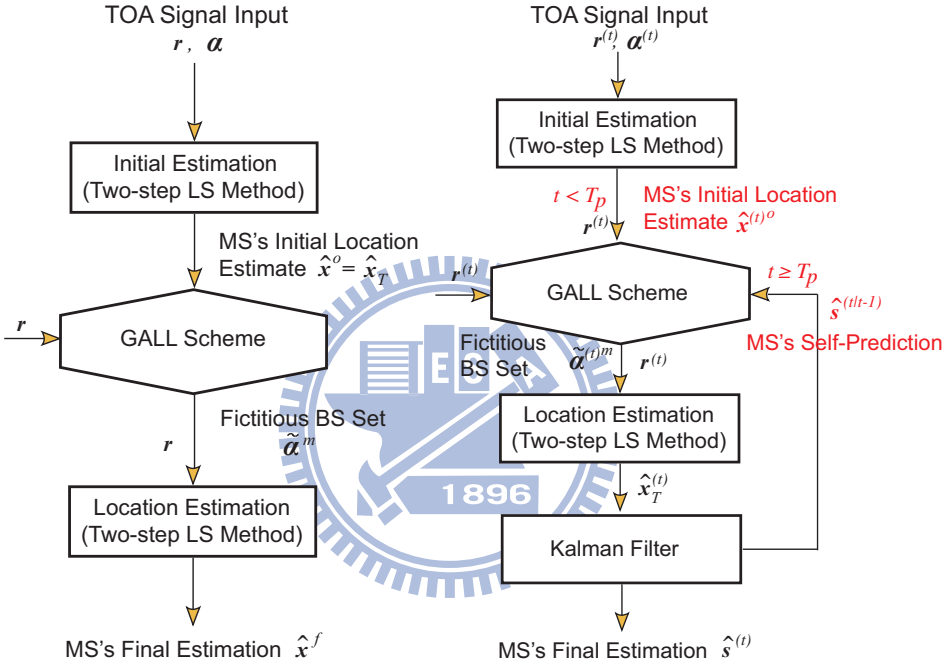

(a) Proposed GALL-TSLS scheme. (b) Proposed GALL-KF scheme.

Figure 5.2: Implementations of proposed GALL algorithm.

As described in previous section, the main objective of the proposed GALL scheme is to acquire the positions of fictitiously movable BSs in order to provide better geometric layout for MS's location estimation. Since the GALL scheme is designed based on the initial estimate of the MS, there can be different implementations to adopt the GALL scheme for location estimation. Fig. 5.2 illustrates the schematic diagrams for the implementations of the proposed GALL algorithm. The GALL-TSLS scheme as shown in Fig. 5.2(a) is proposed to calculate both the initial and final estimates of the MS's position based on the TSLS estimator [17]. On the other hand, a two-stage architecture named GALL-KF scheme as shown in Fig. 5.2(b), i.e., TSLS estimator with Kalman filter, is proposed to enhance the initial estimate with the historical information from Kalman filter. These two types of implementations of GALL scheme are explained in the following two subsections.

5.3.1 GALL with TSLS estimator (GALL-TSLS)

As shown in Fig. 5.2(a), the MS's initial estimate $\hat{\boldsymbol{x}}^o$ can be obtained by performing the TSLS method (i.e., $\hat{\boldsymbol{x}}^o = \hat{\boldsymbol{x}}_T$). The formulation and concept of the TSLS method can be found in Section 2.4. With the initial estimate, the fictitious BS set can be calculated based on the proposed GALL scheme targeting on achieving the minimum L-CRLB requirement. The TSLS is performed for the second time with the adjusted BSs and the received measurements to obtain the MS's location estimate for the GALL-TSLS scheme.

5.3.2 GALL with Kalman Filter (GALL-KF)

In order to provide enhanced location estimate, the proposed GALL-KF scheme as shown in Fig. 5.2(b) is suggested to estimate the MS's position using a two-stage estimator, i.e., a TSLS estimator with a Kalman filter. The measurements are collected in different time instants to obtain a better initial estimate, the notation in this section is considered with the time instant t in Section 2.1.1. The Kalman filter is employed to estimate the MS's position based on its previously estimated data. Note that the formulation and concept can be referred to Section 2.5. Note that for the two-stage location estimation, the input of the Kalman filter is obtained from the result of the GALL scheme as $\boldsymbol{z}^{(t)} = \hat{\boldsymbol{x}}_T^{(t)}$ in Fig. 5.2(b). The estimated output/state $\hat{\boldsymbol{s}}^{(t)}$ is the 2-dimensional MS's position. The variables $\boldsymbol{m}^{(t)}$ and $\boldsymbol{p}^{(t)}$ denote the measurement and the process noises associated with the covariance matrices $\mathbf{R}$ and $\mathbf{Q}$ within the Kalman filtering formulation. Note that the matrix $\mathbf{R}$ can be determined by the FIM of L-CRLB and $\mathbf{Q}$ is set to be an identity matrix. Furthermore, the matrix $\mathbf{E}$ and the state transition matrix $\mathbf{F}$ in (2.16) and (2.17) respectively can be obtained as $\mathbf{E} = \mathbf{F} = \mathbf{I}_{2\times 2}$.

As shown in Fig. 5.2(b), the execution process of the proposed GALL-KF scheme consists of two phases, including the transition period (T_p) and the stable period. During the transient period $t < T_p$, the GALL-KF scheme adopts the TSLS method to provide the initial estimate of the MS. After the tracking time is longer than T_p, the GALL-KF scheme starts to adopt the prediction from the output of the Kalman filter, i.e., $\hat{\boldsymbol{s}}^{(t|t-1)}$, which serves as the updated initial MS's estimate for the GALL scheme. By adopting the Kalman filter, it can be observed that the GALL-KF scheme only requires to perform a single round of location estimation compared to the GALL-TSLS scheme after the system is executed in the stable state. The Kalman filter can refine the MS's position estimation with the historical measurements based on the initial estimate, which should provide better estimation accuracy by adopting the GALL-KF scheme compared to the GALL-TSLS method.

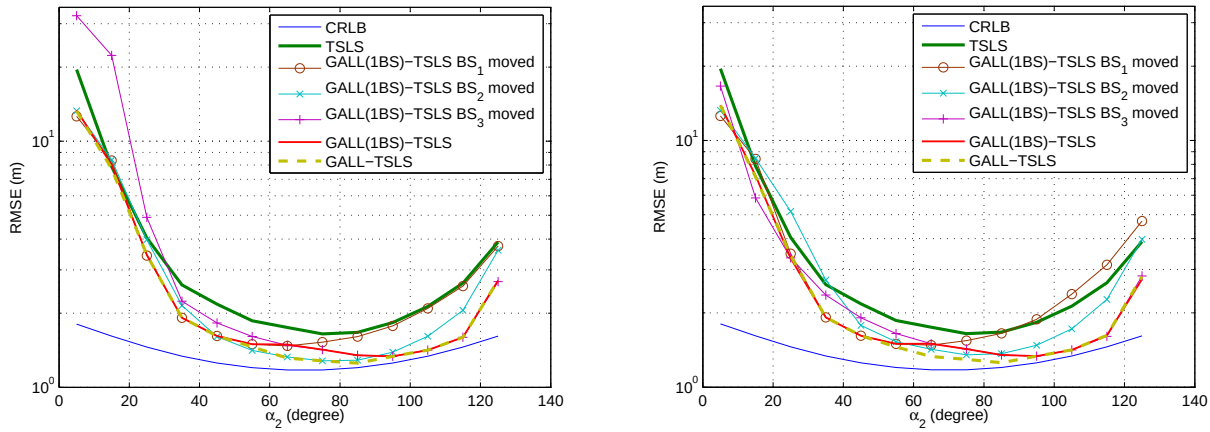

(a) GALL-TSLS with original one fictitiously movable BS problem.

(b) GALL-TSLS with approximate one fictitiously movable BS problem.

Figure 5.3: Validation on GALL-TSLS scheme with one fictitiously movable BS problem.

5.4 Performance Evaluation

Simulations are performed to show the effectiveness of the GALL algorithms (i.e., GALL-TSLS and GALL-KF) under different network topologies and the MS's positions. The number of BSs is considered as three in the examples since three BSs is the minimum sufficient number for the localization problem. The model for the LOS measurement noise of the TOA signals is considered as in Section 2.2.1.1 as the Gaussian distribution with zero mean and standard deviation as σ_n meters in different cases. In the following examples 5.1 and 5.2, the GALL-TSLS algorithm is simulated to validate the effectiveness of the fictitiously movable BS schemes on the TSLS based estimation.

Example 5.1 (Validation on approximate one fictitiously movable BS problem)**.** The purpose of this example is to compare and validate the difference between the original and approximate one fictitiously movable BS problems. Consider three sensors whose coordinates are $\boldsymbol{b}_1 = [50\cos 0°,\ 50\sin 0°]^T$, $\boldsymbol{b}_2 = [30\cos\alpha_2, 30\sin\alpha_2]^T$, and $\boldsymbol{b}_3 = [20\cos 140°,\ 20\sin 140°]^T$ where $\boldsymbol{b}_2$ is function of α_2 with its range as indicated in the x-axis of Fig. 5.3. The MS's true position is assumed to be placed at the origin, i.e., $\boldsymbol{x} = [0, 0]^T$. Note that all the layouts formed by the three sensors with the change of α_2 are designed to be OPLs for validation purpose. More realistic network scenarios will be considered in the following examples. The standard deviation of the Gaussian noises is chosen as $\sigma_n = 1$ in this example. The root mean square error (RMSE) is defined as $\text{RMSE} = \sqrt{\sum_{i=1}^{M} \|\hat{\boldsymbol{x}} - \boldsymbol{x}\|^2 / M}$ where M denotes the number of trials as 1000. Fig. 5.3(a) shows the original one fictitiously movable BS problem obtained by exhaustively solving (5.2); while Fig. 5.3(b) illustrates the approximate one fictitiously movable BS problem acquired from (5.8) and

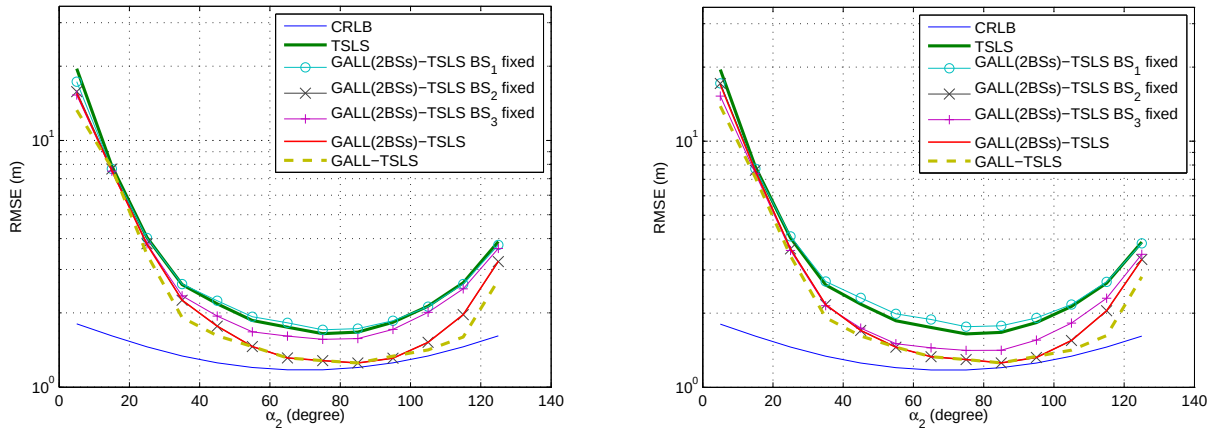

(a) GALL-TSLS with original two fictitiously movable BSs problem.

(b) GALL-TSLS with approximate two fictitiously movable BSs problem.

Figure 5.4: Validation on GALL-TSLS scheme with two fictitiously movable BSs problem.

(5.9), which are respectively denoted as "GALL(1BS)-TSLS BS$_i$ moved" in both plots, for $i = 1$, 2, and 3. In each of the three cases, i.e., $i = 1$, 2 and 3, BS$_i$ is fictitiously moved for obtaining the optimal angle $\tilde{\alpha}_i^m$ that can achieve the minimum value of L-CRLB. Moreover, the "GALL(1BS)-TSLS" curves in both plots respectively denote the GALL(1BS) problem as defined in (5.1) by selecting among different fictitiously movable angles from the original problem (5.2) in Fig. 5.3(a) and approximate problem (5.8) in Fig. 5.3(b). Since the "GALL(1BS)-TSLS" acquire the positions of the fictitious BSs such as to achieve the minimum L-CRLB value with respect to the MSs initial location instead of the MS's true position, the RMSE performance is not necessarily the lowest compared to the "GALL(1BS)-TSLS BS$_i$ moved" scheme for $i = 1$, 2, and 3. Note that both the CRLB and the conventional TSLS scheme are also illustrated in both plots for comparison purpose. It can be observed that even though the approximate problem will be differ from the original problem by individually moving one of the three BSs fictitiously, the resulting problem (5.1), i.e., the GALL(1BS)-TSLS scheme, obtained from (5.8) will be closely match with (5.2) as shown in both plots. Furthermore, it can be seen that the GALL(1BS)-TSLS scheme can provide better RMSE performance compared to the conventional TSLS scheme. ◇

Example 5.2 (Validation on approximate two fictitiously movable BSs problem)**.** This example is to compare and validate the difference between the original and approximate two fictitiously movable BSs problems in Fig. 5.4(a) and Fig. 5.4(b), respectively. Same network layout and noise variance as in example 5.1 are utilized in this example. The curves named "GALL(2BSs)-TSLS BS$_i$ fixed" refer to the problems that the i-th BS is fixed while the other two BSs are movable, i.e., the angle set $\{\tilde{\alpha}_2^m, \tilde{\alpha}_3^m\}$ of the curve "GALL(2BSs)-TSLS BS$_1$ fixed" are obtained via (5.12) and (5.18)

for the original (Fig. 5.4(a)) and approximate (Fig. 5.4(b)) problems respectively. Moreover, the curve "GALL(2BSs)-TSLS" denotes for the problem in (5.11) to select among different movable angles from the original problem (5.12) in Fig. 5.4(a) and the approximate problem (5.18) in Fig. 5.4(b). Similar to the previous example, the final GALL(2BSs)-TSLS scheme of both problems are observed to be consistent with each other from the simulation results. Meanwhile, the effectiveness of problem (5.22) for the GALL scheme is also validated by selecting among the GALL(1BS)-TSLS and the GALL(2BSs)-TSLS schemes. By observing both Figs. 5.3 and 5.4, the GALL-TSLS scheme with the problem (5.22) can achieve the lowest RMSE compared to the other methods. ◇

It is intuitive that the closed form property of the approximate problem can provide efficiency in computational complexity compared to the original problem. Therefore, the approximate problem with the GALL scheme will be adopted in the rest of the examples for performance comparison. In order to provide better estimation precision for MS's location estimate, the GALL-KF algorithm is simulated to compare with the existing TSLS [17], Beck [40], and SDR [41] algorithms, which are named as TSLS-KF, Beck-KF, and SDR-KF respectively. Note that these three algorithms are also cascaded with the Kalman filters to perform two-stage estimation in order to provide fair comparison.

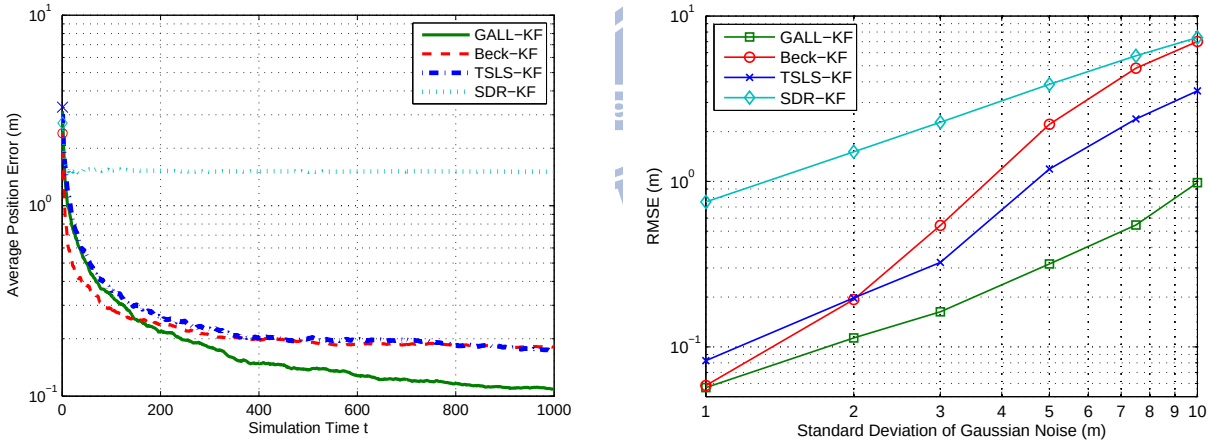

(a) Average position error versus simulation time under $\sigma_n = 2$.

(b) RMSE versus different σ_n.

Figure 5.5: Performance comparison of example 5.3.

Example 5.3 (A special case of GALL-KF scheme)**.** In this example, a special network scenario is simulated to provide performance comparison for the GALL-KF scheme. Consider an array of three sensors in the OPL whose coordinates are $\boldsymbol{b}_1 = [20\cos 0°,\ 20\sin 0°]^T$, $\boldsymbol{b}_2 = [30\cos 80°,\ 30\sin 80°]^T$, and $\boldsymbol{b}_3 = [50\cos 140°,\ 50\sin 140°]^T$; while the MS's true position is fixed at $\boldsymbol{x} = [0,\ 0]^T$. Fig. 5.5(a) demonstrates the performance comparison of average position error for the simulation time

instant $t = 1000$, where each time instant is run with 1000 simulation samples. Note that the average position error at the time instant t is defined as $\sum_{i=1}^{M} \|\hat{\boldsymbol{s}}^{(t)} - \boldsymbol{x}^{(t)}\|/M$. The transient period T_p is chosen as 20 which means that the GALL-KF scheme starts to adopt the prediction from the Kalman filter at the time instant $t = 21$. The standard deviation of Gaussian noises σ_n is chosen as 2 in Fig. 5.5(a). Since the Kalman filter is effective in smoothing the estimation result, it can be observed that the average position error is decreased and converges with the increment of time instant t for all the schemes in Fig. 5.5(a). With the consideration of the L-CRLB in the algorithm design, the proposed GALL-KF implementation can achieve lowered average position error compared to the other schemes; while the SDR-KF has the worst performance among all the algorithms. Since the two-stage architecture does not provide smoothing gain to the SDR-KF method, the SDR-KF scheme will not be further considered in the rest of the simulation examples.

Fig. 5.5(b) illustrates the performance comparison of RMSE at the simulation time instant $t = 1000$ under different standard deviations of the Gaussian noises. It can be observed that the GALL-KF scheme can provide a significant gain over the other methods under different noise values. Note that the Beck-KF scheme is observed to be sensitive to the noise which results in higher RMSE compared to the TSLS-KF scheme under larger noise condition. For example, compared to the TSLS-KF and Beck-KF methods, the proposed GALL-KF scheme will result in 2.8 meter and 6 meter less of RMSE respectively under $\sigma_n = 10$ meter as shown in Fig. 5.5. ◇

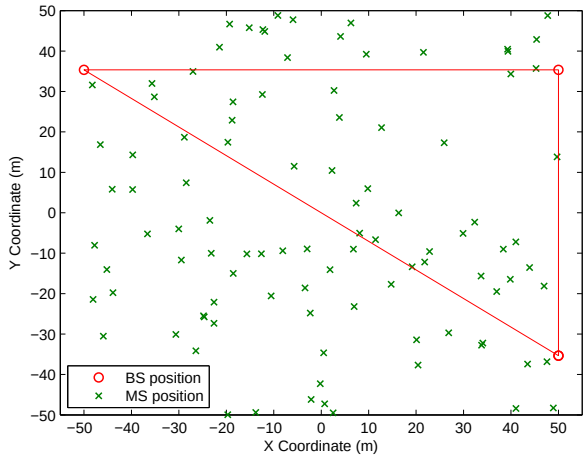

Figure 5.6: Network layout of example 5.4.

Example 5.4 (A general case of GALL-KF scheme under LOS environment)**.** This example illustrates a general scenario of wireless sensor network as shown in Fig. 5.6 for performance comparison under LOS environment. The BSs' coordinates are selected as $\boldsymbol{b}_1 = [50,\ -35.36]^T$, $\boldsymbol{b}_2 = [50,\ 35.36]^T$, and $\boldsymbol{b}_3 = [-50,\ 35.36]^T$, and there are 100 MSs randomly deployed in a 100×100

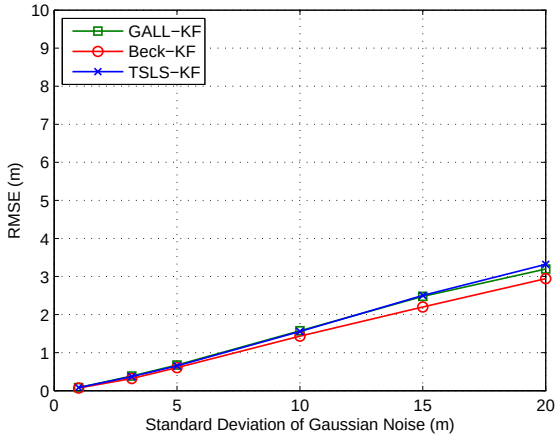

(a) MSs in the IPL.

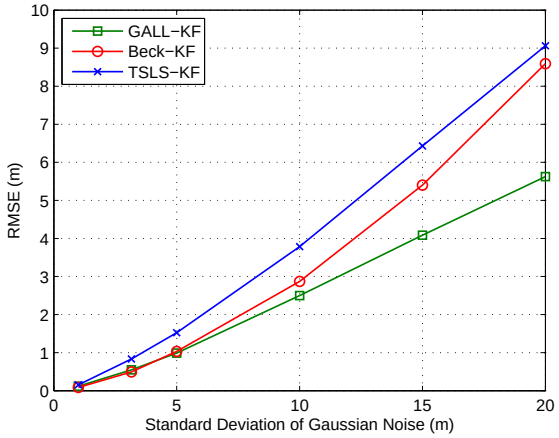

(b) MSs in the OPL.

Figure 5.7: RMSE performance verus different standard deviations of Gaussian noise with network layout in Fig. 5.6.

meter square space. Note that the number of MSs located in the OPL is larger than that in the IPL in this example in order to demonstrate that the OPL may frequently occur in a sensor network environment. The performance of the IPL and the OPL under the LOS condition are separately examined udner different noise standard deviation in Fig. 5.7(a) and (b), respectively. Since the difference between the L-CRLB and the CRLB is considered small in the IPL case, similar RMSE performance is observed among the three compared schemes as illustrated in Fig. 8(a). On the other hand, with the OPL scenario as shown in Fig. 8(b), the GALL-KF scheme can outperform the other two methods under different noise environments, e.g., the GALL-KF approach will result in 2.9 and 3.4 meters less of RMSE compared to the Beck-KF and TSLS-KF schemes respectively under $\sigma_n = 20$ meter in Fig. 5.7(b), which is considered the major contribution of the proposed GALL-KF scheme. ◇

Example 5.5 (A general case of GALL-KF scheme under realistic environment)**.** In this example, the performance comparison is conducted for the GALL-KF scheme under the realistic environment. The same network layout setting as example 5.4 is adopted; while the noise setting is different by considering the NLOS in this example. In order to include the influence from the NLOS noise, the TOA model in cellular network as in Section 2.2.1.2 is adopted. τ_m represents the median value of τ_i, which is utilized as the x-axis in Figs. 5.8(a) and 5.8(b).

Fig. 5.8(a) illustrates the performance comparison for the three schemes in the IPL under NLOS environment. It can be observed that the proposed GALL-KF approach can provide the smallest RMSE compared to the other two schemes, e.g., the GALL-KF scheme will result in 3.1 and 5.2 meters less of RMSE respectively under $\tau_m = 0.2$ μs compared to the Beck-KF and TSLS-

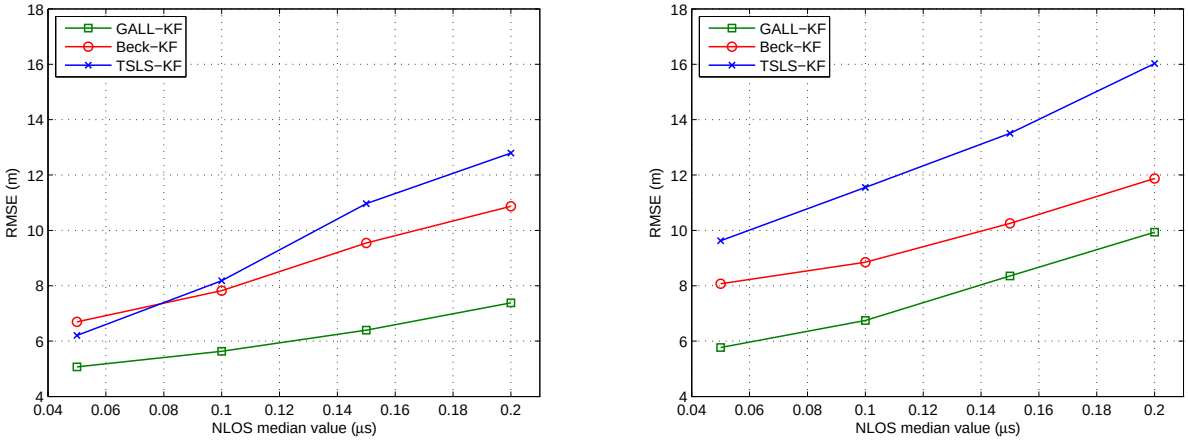

(a) MSs in the IPL.

(b) MSs in the OPL.

Figure 5.8: RMSE performance versus different NLOS median values with network layout in Fig. 5.6.

KF methods. The reason is that the GALL-KF scheme is designed based on the minimization of L-CRLB by fictitiously adjusting the locations of BS. As mentioned in Subsection II.C, the value of L-CRLB is affected by the distance between the BS and MS, which will be greatly influenced by the NLOS noises. Therefore, the effect from the NLOS noises has been implicitly considered in the design of GALL-KF scheme, which improves the location estimation performance. Moreover, Fig. 5.8(b) illustrates the performance comparison for the OPL scenario under NLOS environment. The proposed GALL-KF scheme can still outperform the other two methods, e.g., around 1.9 and 6 meters less of RMSE in comparison with the Beck-KF and TSLS-KF schemes under $\tau_m = 0.2$ μs in Fig. 5.7(b). The merits of proposed GALL-KF scheme can therefore be observed. ◇

5.5 Concluding Remarks

The properties of linearized location estimation algorithms by introducing an additional variable are analyzed from the geometric point of view. By proposing the linearized location estimation problem based CRLB (L-CRLB), the linearization lost from the linearized location estimation algorithms can be observed. In order to minimize the linearization lost, the geometry-assisted linearized localization (GALL) algorithm is proposed in the chapter by fictitiously moving the base stations (BSs) in order to achieve the new geometric layout with minimum L-CRLB value. The GALL with two-step least squares (GALL-TSLS) implementation can enhance the estimation performance of the conventional TSLS estimator. By improving the initial estimation with the adoption of historical information, the GALL with Kalman filter (GALL-KF) scheme further outperforms the other location estimators with similar two-stage estimation structure.

Chapter 6

Hybrid Network/Satellite-Based Location Estimation and Tracking Systems

- The location algorithms for the mobile stations in the telecommunication system can generally be categorized into the network-based and the satellite-based systems. Hybrid location estimation architectures, which have not been fully addressed in the literature, are proposed in this chapter to combine various satellite-based and the cellular-based signals for location estimation and tracking, i.e., TOA, TDOA, and AOA. [1]

6.1 Introduction

The quality-of-service of the positioning accuracy has been announced after the issue of the emergency 911 (E911) subscriber safety service [42], which makes the location based service become a necessary functionality in the telecommunication systems. Location-based service would be covered in telecommunication standards in order to meet the E911 requirement and for the resource management purposes such as location-based handover [43]. A variety of wireless location techniques have been studied and investigated [44, 45]. These schemes can be classified into (*i*) the network-based and (*ii*) the satellite-based location estimation algorithms. The representative systems for the network-based location techniques include the cellular-based networks, which adopt the time difference-of-arrival (TDOA) and the angle-of-arrival (AOA) information for location estimation. The well-adapted technology for the satellite-based location estimation method is to utilize the global positioning systems (GPSs), which measures the time-of-arrival (TOA) of the

[1] The chapter is based on [J-2] Po-Hsuan Tseng and Kai-Ten Feng, "Hybrid Network/Satellite-Based Location Estimation and Tracking Systems for Wireless Network," *IEEE Trans. on Vehicular Technology*, Vol.58, Issue 9, pp. 5174 - 5189, Nov. 2009.

signals coming from different satellites. It has been studied in several researches [46, 34] that the performance of the location estimation techniques listed above varies under different environments. Due to shortage of signal sources (e.g., at rural area) or severe none-line-of-sight (NLOS) situation (e.g., at urban area), the network-based (i.e., TDOA, AOA) methods result in degraded performance for the location determination of the MS [47, 48]. On the other hand, the major problem for the satellite-based method [49] is that the performance is considerably degraded while the satellite signals are severely blocked (e.g., at urban or indoor area).

In order to achieve better accuracy for location estimation, a hybrid approach should be considered to satisfy the requirements under different environments. However, most of the existing research work does not explicitly design location estimation algorithms that are targeted for heterogeneous circumstances. The assisted GPS (A-GPS) system is considered a well-known technique that fuses the network-based signals in order to enhance the startup performance of a GPS-based positioning system. With the availability of different types of signal sources, the accuracy for location estimation can be improved. The practical system that provides the implementation of the A-GPS system is contributed to the GpsOne [50] chipset solution. Nevertheless, only high-level description is available that explains how the GpsOne system conducts hybrid location estimation. There is lack of detail information regarding the hybrid architecture and performance evaluation for location estimation under different environments.

The main objective of this chapter is to propose hybrid architectures and algorithms for location estimation under heterogeneous networks. Two different types of hybrid location estimation and tracking systems are proposed in this chapter. The first scheme, called the fusion-based hybrid (FH) architecture, determines the MS's location by combining the separate outcomes from both the network-based and the satellite-based techniques (e.g., by integrating the location information obtained from the cellular network and the GPS receiver). Within each of the two separate channels, the two-step least squares (TSLS) method [17] is utilized to estimate the MS's position based on the measurement inputs. The Bayesian inference model [51, 52] is adopted as the fusion mechanism to acquire the final position estimate from both the satellite system and the cellular networks. On the other hand, the unified hybrid (UH) architecture is proposed as the second scheme. The hybrid signal selection (HSS) scheme is proposed to restrict the number of heterogeneous incoming sources based on their signal qualities. Moreover, the hybrid least squares (HLS) estimator is employed to provide location estimation of the MS from the selected signal inputs (i.e., the combination of the TOA, the TDOA, and the AOA measurements). The source deficiency problem, which may occur either within the cell-based or the satellite-based system, can effectively be mitigated by adopting the proposed UH architecture. Furthermore, the Kalman filtering technique [18] is exploited within the two proposed hybrid architectures, which is capable of providing noise smoothing and location tracking while the MS is dynamically moving within the network. The performance of the proposed hybrid location estimation and tracking schemes are evaluated via simulations under different environments.

From implementation perspective, both hybrid architectures can be employed depending on the flexibility of hardware unit within an MS. Two types of signal selection schemes are employed in these hybrid architectures, including the fixed-set of signal inputs (FSI) and the selective-set of signal inputs (SSI) methods. The FSI algorithm can be utilized by a standardized hardware platform, which consists of the GPS receiver and the radio baseband. It is noted that two fixed-set of signal inputs are acquired from each of the two channels within the hardware platform. This type of architecture is beneficial for its standardized cost and implementation. On the other hand, the SSI scheme can be employed in an MS via software implementation or flexible hardware design. The scheme can provide both flexible system upgrade and effective location estimation of the MS under different circumstances. It is noted that both signal selection schemes can be implemented with the FH architecture; while the UH architecture adopts the SSI approach.

The remainder of the chapter is organized as follows. Section 6.2 presents the system architectures and the modeling of the signal sources for the the proposed schemes. The signal selection algorithms adopted within the proposed schemes are explained in Section 6.3. Section 6.4 describes the proposed HLS estimator associated with the conventional TSLS method. Section 6.5 illustrates the performance evaluation and the implementation assessment of the proposed hybrid schemes. Section 6.6 draws the conclusions.

6.2 System Architecture and Modeling

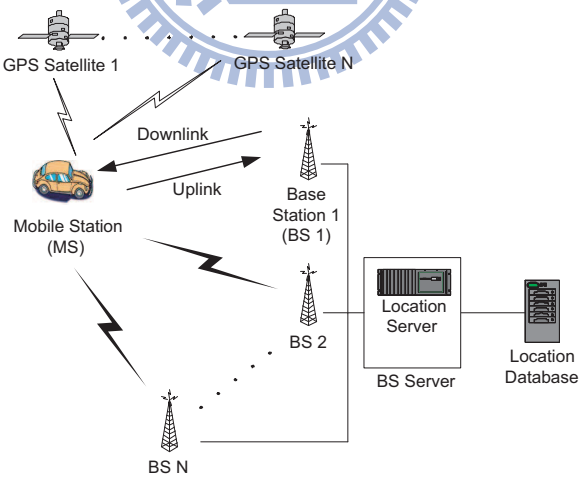

Figure 6.1: Schematic diagram of hybrid mobile location estimation.

6.2.1 System Architecture

Fig. 6.1 shows the schematic diagram of the system architecture for the hybrid location estimation. The hybrid system combines the signals coming from both the satellites and the cellular networks.

In order to obtain the TOA measurements from the satellites, it is assumed that the MS should be equipped with a GPS receiver (for the FH scheme) or merely a GPS front-end (for the UH scheme). On the other hand, the network-based system adopts the following features from the 3GPP [53] and the WiMax standards [54]: (*i*) Each Base Station (BS) has a downlink (forward-link) pilot channel that continuously broadcast its pilot signal in order to provide timing and phase information for all the MS in this cellular network. (*ii*) Each BS has a dedicated uplink (reverse-link) pilot channel from the MS to provide initial acquisition, time tracking, and power control measurements. (*iii*) Each BS is equipped with antenna arrays for adaptive beam steering in order to facilitate the AOA measurements. As shown in Fig. 6.1, the TDOA measurements are conducted at the MS by obtaining the signals via the downlink pilot channels from the BSs. The AOA signals are transmitted from the MS to the BSs using the uplink pilot channel. The AOA measurements are performed at the BS using its antenna arrays for 3-D adaptive beam steering. In order to avoid signal degradation due to the near-far effect, it is assumed that only the home BS provides the capability of the AOA measurements.

As stated in the 3GPP standard, the location determination of the MS can either be MS-Based or MS-Assisted. The choice between these two types of system depends on the requirement of the communication bandwidth and the computation power of the MS. The FH and the UH schemes as proposed in this chapter can be applied to either the MS-Assisted or the MS-Based system. The following two subsections describe the proposed system architectures based on these two types of system:

6.2.1.1 Mobile-Assisted System

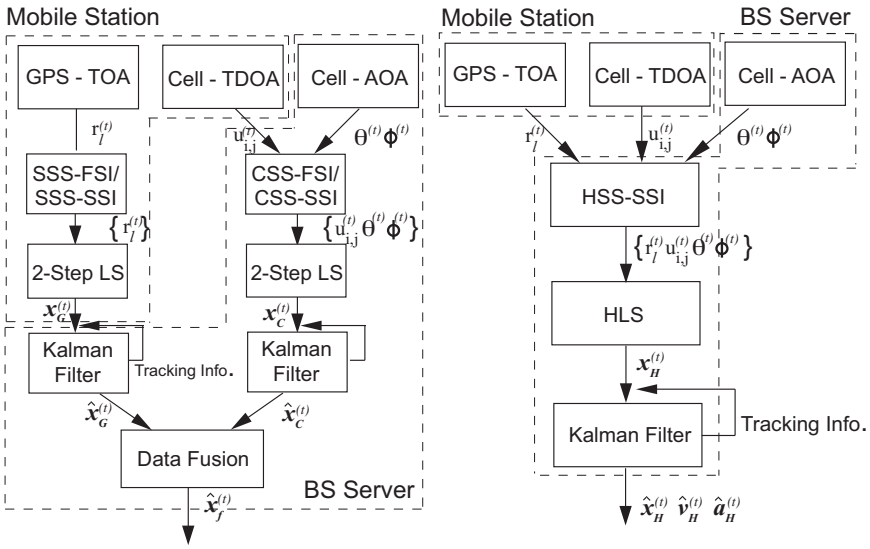

Figure 6.2: Mobile-assisted system using the FH architecture (left diagram) and the UH architecture (right diagram).

This type of architecture is suitable for the MS with insufficient computation capability. The left schematic diagram of Fig. 6.2 illustrates the FH scheme that implements on the MS-Assisted positioning system. The following steps describe the procedures of the FH scheme for the MS-Assisted system:

(i) The GPS-equipped MS receives signals from the satellites and conducts TOA pseudo-range measurement ($r_i^{(t)}$). The GPS receiver either selects five TOA measurements via the satellite-based signal selection with fixed-set of signal inputs (SSS-FSI) scheme or a flexible number of measurements via the satellite-based signal selection with selective-set of signal inputs (SSS-SSI) scheme. The MS's three-dimensional position (i.e., $\boldsymbol{x}_G^{(t)} = [x_G^{(t)}, y_G^{(t)}, z_G^{(t)}]^T$) can therefore be estimated using the TSLS method. On the other hand, the TDOA signals are measured at the MS by obtaining signals from its home BS and the neighboring BSs via the downlink pilot channel.

(ii) These two sets of information, the location estimation ($\boldsymbol{x}_G^{(t)}$) and the TDOA measurements ($u_{i,j}^{(t)}$), are transmitted back to the home BS via the uplink pilot channel.

(iii) The AOA measurement ($\theta_1^{(t)}$, $\phi_1^{(t)}$) is conducted at the home BS by receiving the signals from the MS via the uplink channel.

(iv) The location server at the home BS performs either the cell-based signal selection for fixed-set of signal inputs (CSS-FSI) or the cell-based signal selection for selective-set of signal inputs (CSS-SSI) scheme from the network-based signal sources, and the TSLS method is utilized to estimate the three-dimensional position ($\boldsymbol{x}_C^{(t)}$) of the MS.

(v) The BS location server performs Kalman filtering technique to smooth out the measurement noises and to track the position data both from the TOA and the TDOA/AOA channels (i.e., $\hat{\boldsymbol{x}}_G^{(t)}$ and $\hat{\boldsymbol{x}}_C^{(t)}$). The formulation of Kalman filter can be referred to Section 2.5. Note that the position ($\hat{\boldsymbol{x}}^{(t)}$), velocity ($\hat{\boldsymbol{v}}^{(t)}$), and acceleration ($\hat{\boldsymbol{a}}^{(t)}$) tracking are considered in the Kalman

filter formulation. The matrix $\mathbf{E}$ and the state transition matrix $\mathbf{F}$ can be obtained as

$$\mathbf{E} = \begin{bmatrix} 1 & 0 & 0 & 0 & 0 & 0 & 0 & 0 & 0 \\ 0 & 1 & 0 & 0 & 0 & 0 & 0 & 0 & 0 \\ 0 & 0 & 1 & 0 & 0 & 0 & 0 & 0 & 0 \end{bmatrix}, \tag{6.1a}$$

$$\mathbf{F} = \begin{bmatrix} 1 & 0 & 0 & \Delta t & 0 & 0 & \frac{1}{2}\Delta t^2 & 0 & 0 \\ 0 & 1 & 0 & 0 & \Delta t & 0 & 0 & \frac{1}{2}\Delta t^2 & 0 \\ 0 & 0 & 1 & 0 & 0 & \Delta t & 0 & 0 & \frac{1}{2}\Delta t^2 \\ 0 & 0 & 0 & 1 & 0 & 0 & \Delta t & 0 & 0 \\ 0 & 0 & 0 & 0 & 1 & 0 & 0 & \Delta t & 0 \\ 0 & 0 & 0 & 0 & 0 & 1 & 0 & 0 & \Delta t \\ 0 & 0 & 0 & 0 & 0 & 0 & 1 & 0 & 0 \\ 0 & 0 & 0 & 0 & 0 & 0 & 0 & 1 & 0 \\ 0 & 0 & 0 & 0 & 0 & 0 & 0 & 0 & 1 \end{bmatrix}, \tag{6.1b}$$

where Δt denotes the sample time interval. For the FH architecture (as in the left diagrams of Figs. 6.2 and 6.3), the output of the Kalman filter corresponds to either $\hat{\boldsymbol{s}}_C^{(t)} = [[\hat{\boldsymbol{x}}_C^{(t)}]^T, [\hat{\boldsymbol{v}}_C^{(t)}]^T, [\hat{\boldsymbol{a}}_C^{(t)}]^T]^T$ or $\hat{\boldsymbol{s}}_G^{(t)} = [[\hat{\boldsymbol{x}}_G^{(t)}]^T, [\hat{\boldsymbol{v}}_G^{(t)}]^T, [\hat{\boldsymbol{a}}_G^{(t)}]^T]^T$, while the measurement input $\boldsymbol{z}^{(t)} = \boldsymbol{x}_C^{(t)}$ or $\boldsymbol{z}^{(t)} = \boldsymbol{x}_G^{(t)}$ is obtained from the outputs of the TSLS estimator at the time instant t. Based on both the prediction and updating processes within the Kalman filtering formulation, the trajectory of MS can be predicted and traced in reasonable estimation accuracy. Note that the Kalman tracking will conduct linear prediction (with constant acceleration) for obtaining the MS's position while the number of signal inputs becomes insufficient in each of the two channels.

(*vi*) Data Fusion is performed to merge disparate types of information in order to enhance the position accuracy. The Bayesian inference model [51, 52] is adopted to incorporate both the means ($\underline{\hat{\boldsymbol{x}}}_G^{(t)}$ and $\underline{\hat{\boldsymbol{x}}}_C^{(t)}$) of the filtered estimations ($\hat{\boldsymbol{x}}_G^{(t)}$ and $\hat{\boldsymbol{x}}_C^{(t)}$) from the TOA and the TDOA/AOA measurements based on their signal variations as

$$\hat{\boldsymbol{x}}_f^{(t)} = \begin{bmatrix} \hat{x}_f^{(t)} \\ \hat{y}_f^{(t)} \\ \hat{z}_f^{(t)} \end{bmatrix} \tag{6.2}$$

$$= \begin{bmatrix} \frac{\sigma_{G,x}^2}{\sigma_{G,x}^2+\sigma_{C,x}^2} & 0 & 0 \\ 0 & \frac{\sigma_{G,y}^2}{\sigma_{G,y}^2+\sigma_{C,y}^2} & 0 \\ 0 & 0 & \frac{\sigma_{G,z}^2}{\sigma_{G,z}^2+\sigma_{C,z}^2} \end{bmatrix} \begin{bmatrix} \underline{\hat{x}}_C^{(t)} \\ \underline{\hat{y}}_C^{(t)} \\ \underline{\hat{z}}_C^{(t)} \end{bmatrix} + \begin{bmatrix} \frac{\sigma_{C,x}^2}{\sigma_{G,x}^2+\sigma_{C,x}^2} & 0 & 0 \\ 0 & \frac{\sigma_{C,y}^2}{\sigma_{G,y}^2+\sigma_{C,y}^2} & 0 \\ 0 & 0 & \frac{\sigma_{C,z}^2}{\sigma_{G,z}^2+\sigma_{C,z}^2} \end{bmatrix} \begin{bmatrix} \underline{\hat{x}}_G^{(t)} \\ \underline{\hat{y}}_G^{(t)} \\ \underline{\hat{z}}_G^{(t)} \end{bmatrix}.$$

It is noted that the parameters $\boldsymbol{\sigma}_C = [\sigma_{C,x},\ \sigma_{C,y},\ \sigma_{C,z}]^T$ and $\boldsymbol{\sigma}_G = [\sigma_{G,x},\ \sigma_{G,y},\ \sigma_{G,z}]^T$

represent the corresponding standard deviations of $\hat{\boldsymbol{x}}_C^{(t)}$ and $\hat{\boldsymbol{x}}_G^{(t)}$, respectively. The fused position estimate ($\hat{\boldsymbol{x}}_f^{(t)}$) of the MS can therefore be obtained.

The right schematic diagram of Fig. 6.2 shows the proposed UH scheme that is adopted on the MS-Assisted system. Comparing with the FH scheme, one of the major differences in the UH architecture is that the TOA measurements (obtained via the the GPS front-end within the MS) is transmitted to the BS instead of the estimated MS's position ($\boldsymbol{x}_G^{(t)}$). After acquiring the three different types of signal inputs (i.e., the TOA, the TDOA, and the AOA measurements), the location server at the home BS will start to perform signal selection via the proposed hybrid signal selection with selective-set of signal inputs (HSS-SSI) scheme. The selection scheme will guarantee the availability of sufficient signal inputs for the HLS estimator and also eliminate severely interfered signals. The HLS estimator will therefore be conducted to combine the various types of measurement inputs for the estimation of the MS's three-dimensional position ($\boldsymbol{x}_H^{(t)}$). For the UH architecture (as in the right diagrams of Figs. 6.2 and 6.3), the output of the Kalman filter corresponds to $\hat{\boldsymbol{s}}_H^{(t)} = [[\hat{\boldsymbol{x}}_H^{(t)}]^T,\ [\hat{\boldsymbol{v}}_H^{(t)}]^T,\ [\hat{\boldsymbol{a}}_H^{(t)}]^T]^T$; while the measurement input $\boldsymbol{z}^{(t)} = \boldsymbol{x}_H^{(t)}$ can be acquired from the proposed HLS estimator. The matrix E and the state transition matrix F can be obtained as (6.1a) and (6.1b)).

6.2.1.2 Mobile-Based System

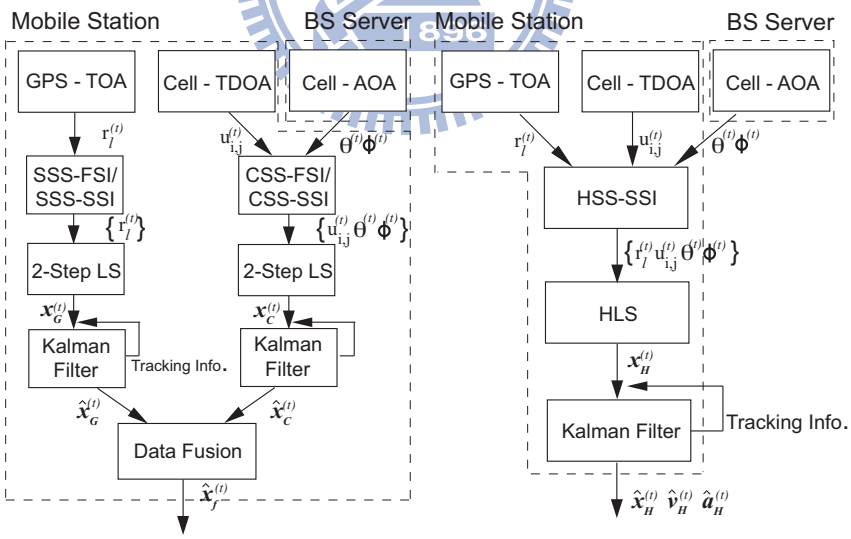

Figure 6.3: Mobile-based system using the FH architecture (left diagram) and the UH architecture (right diagram).

This type of architecture is suitable for the MS that possesses adequate computation capability. The left schematic diagram of Fig. 6.3 shows the proposed FH scheme for the MS-Based positioning system. Comparing with the left diagram of Fig. 6.2, the AOA measurement ($\theta_1^{(t)}$, $\phi_1^{(t)}$) is obtained

from the home BS and is transmitted to the MS via the downlink pilot channel. All the remaining functionalities (i.e., signal selection, location estimation, Kalman filtering, and data fusion) are performed at the MS in order to obtain the final location estimate ($\hat{\boldsymbol{x}}_f^{(t)}$). On the other hand, the proposed UH scheme for the MS-Based positioning system is illustrated in the right diagram of Fig. 6.3. Similarly, the only function conducted by the BS server is to measure the AOA signal ($\theta_1^{(t)}$, $\phi_1^{(t)}$), and is consequently transmitted back to the MS via the downlink pilot channel. All the other tasks that are accomplished by the MS can be referred to the UH method for the MS-Assisted system (as in the right diagram of Fig. 6.2), excepting that those are performed within the MS in this case.

6.2.2 Problem Description

Consider a network of transmitting satellites and cellular BSs. Our goal is to estimate the unknown positions of an MS at time instant t which are denoted by a set of 3-dimensional vectors $\mathbf{x}^{(t)} = [x^{(t)},\ y^{(t)},\ z^{(t)}]^T$. In other words, based on the known positions of the transmitting satellites and BSs, the mobile units wish to estimate their positions at different time instants. When the ℓ-th satellite broadcasts its signal, the MS receives an effective TOA measurement $r_\ell^{(t)}$. Note that the clock bias b caused by the clock offset between the MS and the satellite should be estimated. Meanwhile, the cellular BS also broadcasts its signal. The effective TDOA signal $u_{i,j}^{(t)}$ can be measured from the i-th and j-th BSs by eliminated the clock offset. Meanwhile, the horizontal and vertical AOA (i.e., $\theta_1^{(t)}$ and $\phi_1^{(t)}$) signals can be measured by the home BSs. By collecting the TOA, TDOA and AOA measurements from the satellite and cellular BS, the goal is for the MS to generate an estimate $\hat{\boldsymbol{x}}^{(t)} = [\hat{x}^{(t)},\ \hat{y}^{(t)},\ \hat{z}^{(t)}]^T$ of its position.

6.2.3 Mathematical Modeling of Signal Sources

The 3-D coordinates of the MS are exploited in the proposed hybrid location estimation schemes. The mathematical models for the TOA, the TDOA, and the AOA measurements can be referred to Section 2.1.1, 2.1.2, and 2.1.3, respectively.

6.3 Signal Selection Schemes for Proposed Hybrid Architectures

Conventional studies [36] indicate that all of the signal inputs should be utilized for location estimation such as to achieve better performance under the situation that the measurements are Line-Of-Sight (LOS) signals. Specifically, the Cramér-Rao Lower Bound (i.e., the error lower bound) under LOS environment is monotonically decreasing as the number of the BS is augmented. However, in realistic environments, it is expected to encounter situations with different error distributions [55, 38, 56], e.g., with environment containing both the NLOS and the LOS measurements. In other words, providing that the NLOS measurement exists, the strategy of adopting all of the

signal measurements will not be considered an optimal method. As a result, it is required to exploit signal selection scheme among the various signal sources.

The signal selection schemes are considered as the post-processing after the front-end hardware transceiver has pre-filtered the input signals, e.g., by eliminating the interferences from the fading effects. Different types of signal selection algorithms have been proposed. It has been studied [57, 58] to be an NP-hard problem for obtaining the optimal set of signal sources (out of exhaustive search on the sample space) in order to achieve the minimum estimation error for the MS's position. Therefore, approximate solutions for achieving the optimal set of signal sources are proposed in the next subsections. The selection strategy for both FSI and SSI scheme are proposed based on different criterion under the satellite-based (Subsection 6.3.1) and the cell-based (Subsection 6.3.2) networks respectively. In Subsection 6.3.3, the SSI scheme is exploited to sort out the available sources based on their signal qualities under the heterogeneous environments. It is noticed that whether to choose a fixed-set or a selective-set of signal inputs depends on the tradeoffs between the hardware cost and the implementation flexibility. Without severe degradation on the estimation accuracy, the proposed FSI scheme can be implemented in a standardized hardware platform for the purpose of reducing the hardware cost and increasing the computation speed. On the other hand, by considering the software implementation, the proposed SSI scheme can achieve better estimation accuracy without being constrained by a fixed number of signal sources.

6.3.1 Satellite-based Signal Selection (SSS) Scheme

The SSS-FSI and the SSS-SSI schemes within the FH architecture (as shown in the left diagrams of Figs. 6.2 and 6.3) are presented in this subsection. The procedure of the SSS approach is to first utilize the Receiver Autonomous Integrity Monitoring (RAIM) [59] technique for the elimination of possible faulty satellites. The remaining satellites will further be distinguished with either good or bad signal quality according to both their elevation angles and SNR values. Moreover, in the SSS-FSI scheme, the total number of signals is further constrained to be a fixed number for ease of implementation. In general, four measurement inputs will be sufficient for the estimation of four state variables. However, due to the nonlinear behavior (i.e., terms with square root) associated with the equations, additional TOA measurement will be required for the closed-form location estimator [60, 61], e.g., TSLS estimator. For achieving higher estimation accuracy, there are also literatures [49] seeking for solutions with more available signal sources. Therefore, the minimum number of the satellites required for the SSS-FSI scheme is chosen as five.

Several factors [60] can degrade the satellite signals and consequently affect the accuracy for MS's location estimation algorithm, e.g. the number of visible satellites and the satellite geometry. In order to effectively consider these inferior effects to the accuracy for location estimation, three parameters are considered in the proposed SSS scheme, including the elevation angle of satellite, the SNR value [62], and the Geometric Dilution of Position (GDOP) metric. In general, severe

multi-path effect will be incurred with comparably smaller satellite elevation angle; while the SNR value can be utilized as an index to remove weak signal sources. Meanwhile, it is noted that GDOP [63] is a well-adopted metric for justifying the accuracy of location estimation based on the geometric layouts between the MS and its associated satellites. Furthermore, the RAIM technique is also adopted to examine the integrity of GPS psuedo-range measurements. Within the scheme of RAIM Fault Detection and Exclusion (RAIM-FDE) [64], the GPS receiver can both detect and isolate the erroneous channels from those that can be utilized for location estimation.

Algorithm 6.1 SSS-FSI Scheme

Ensure: $\mathbf{S}_s$.

for $S_i \in \mathbf{S}_t$ **do**
  $\mathbf{S}_b \leftarrow$ RAIM-FDE($\mathbf{S}_i$) % Isolate the possible fault satellites with RAIM-FDE scheme
  if $S_i.\phi_i^{(t)} > \phi_{th}$ and $S_i.\gamma_i^{(t)} > \gamma_{th}$ **then**
    $\mathbf{S}_g \leftarrow \{\ \mathbf{S}_g,\ S_i\ \}$;
  else
    $\mathbf{S}_b \leftarrow \{\ \mathbf{S}_b,\ S_i\ \}$;
  end if
end for
$\mathbf{S}_s \leftarrow$ Optimum5($\mathbf{S}_g$) % Optimize based on the GDOP metric and result in $N(\mathbf{S}_s) = 5$

The proposed SSS-FSI scheme is first illustrated in Algorithm 6.1; while the difference between the SSS-SSI and SSS-FSI schemes will be described afterwards. In Algorithm 6.1, the entire set of available satellites is defined as $\mathbf{S}_t = \{\mathbf{S}_g, \mathbf{S}_b\} = \{S_i \,|\, \forall i,\ 1 \leq i \leq n\}$, where $\mathbf{S}_g$ and $\mathbf{S}_b$ are represented as the sets of satellites with good and bad signal qualities. $\mathbf{S}_s \in \mathbf{S}_t$ is the satellite set that is selected by the SSS-FSI scheme. It is also noted $N(\Phi)$ denotes the number of elements within the Φ set. Initially, the proposed scheme utilizes the RAIM-FDE scheme to detect and isolate the satellites S_i that are detected to cause the fault. It is noted that the RAIM-FDE technique will only eliminate those satellites that fail to pass the detection. The proposed SSS-FSI scheme continues to construct the remaining $\mathbf{S}_g$ set by verifying if the elevation angle ($\phi_i^{(t)}$) and the SNR value ($\gamma_i^{(t)}$) of the satellite S_i are larger than their pre-specified thresholds, ϕ_{th} and γ_{th}. Furthermore, the minimal required number of satellites for the proposed SSS-FSI scheme can be acquired with the exploitation of the Optimum5 scheme as in Algorithm 6.1. Basically, this technique is adopted from [65] in order to obtain the optimal set of satellites $\mathbf{S}_s$ (which is chosen as five) based on the minimal GDOP criterion. However, the computation of minimum GDOP value involves a series of matrix operations, which is considered inapplicable for implementation. In order to compute the GDOP value in the real-time manner, matrix inversion lemma is utilized to approximate the complex matrix calculation into a recursive computation with single order operations, i.e., to reduce the computation cost from $O(n^3)$ to $O(n)$. Moreover, by adopting the revolving door method, the previous calculation can further be reused instead of conducting entire matrix calculation. With

the recursive computation, this scheme is also feasible to be employed under the situations that visible satellites are changing from time to time.

On the other hand, compared to the SSS-FSI approach, the proposed SSS-SSI scheme removes the constraint that total the number of satellites in the selected set $\mathbf{S}_s$ should be five. In other words, Optimum5 function as implemented in Line 7 of Algorithm 6.1 is removed which consequently results in $\mathbf{S}_s = \mathbf{S}_g$. Furthermore, it is noted that the SSS-FSI and SSS-SSI schemes become the same algorithm providing that the $N(\mathbf{S}_g)$ is smaller or equal to the number of five. In Section 6.5, the performance comparisons between these two signal selection schemes will further be evaluated from both the computation cost and estimation accuracy.

6.3.2 Cell-based Signal Selection (CSS) Scheme

Algorithm 6.2 CSS-FSI Scheme

Ensure: $\mathbf{B}_s$.

1: $\mathbf{B}_t \leftarrow$ SortMin ($\mathbf{B}_t$, $\mathbf{B}_t.\hat{\sigma}^2$); % Sort $\mathbf{B}_t$ based on $\mathbf{B}_t.\hat{\sigma}^2$ with monotonic increasing order
2: $[\hat{\boldsymbol{x}}_C^{(t)}]^{(0)} \leftarrow$ TwoStepLS ($\{B_1, \ldots, B_4\}$); % Any location estimator could be utilized for initial estimation
3: $\mathbf{B}_t.\lambda^{(t)} \leftarrow$ ResidualTest ($\mathbf{B}_t$, $[\hat{\boldsymbol{x}}_C^{(t)}]^{(0)}$);
4: **for** $B_i \in \mathbf{B}_t$ **do**
5: **if** $B_i.\lambda_i^{(t)} < \lambda_{th}$ **then**
6: $\mathbf{B}_l \leftarrow \{ \mathbf{B}_l, B_i \}$; % LOS condition;
7: SortMin($\mathbf{B}_l$, $\mathbf{B}_l.\lambda^{(t)}$); % Sort $\mathbf{B}_l$ based on $\mathbf{B}_l.\lambda^{(t)}$ with monotonic increasing order
8: **else**
9: $\mathbf{B}_n \leftarrow \{ \mathbf{B}_n, B_i \}$; % NLOS condition
10: SortMin($\mathbf{B}_n$, $\mathbf{B}_n.\lambda^{(t)}$); % Sort $\mathbf{B}_n$ based on $\mathbf{B}_n.\lambda^{(t)}$ with monotonic increasing order
11: **end if**
12: **end for**
13: **if** $N(\mathbf{B}_l) \geq 4$ **then**
14: $\mathbf{B}_s \leftarrow \{ B_{l,1}, ..., B_{l,4} \}$;
15: **else**
16: j $\leftarrow \{ 4 - N(\mathbf{B}_l) \}$;
17: $\mathbf{B}_s \leftarrow \{ \mathbf{B}_l, B_{n,1}, ..., B_{n,j} \}$;
18: **end if**

This subsection describes the CSS-FSI and CSS-SSI scheme within the FH architecture (as shown in the left diagrams of Figs. 6.2 and 6.3). As indicated in (3.6), the range measurement $u_{i,j}^{(t)}$ is contaminated with the measurement errors ($n_i^{(t)}$ and $n_j^{(t)}$) and the NLOS errors ($e_i^{(t)}$ and $e_j^{(t)}$). The NLOS error, which represents the additional propagation time (i.e., with positive value), has been observed as a dominate issue for the time-based location estimation [55, 38, 66, 67, 56, 68] and is hard to be removed from the front end signal processing. It has been investigated that the NLOS error can be exceeded to 589 meters within the IS-95 Code Division Multiple Access (CDMA)

networks [67]. The large bias in the range measurement will severely decrease the accuracy of the network-based location estimation algorithms. Consequently, the proposed CSS scheme will primarily focus on selecting the measurement inputs that are less corrupted by the NLOS errors.

The concept of the CSS-FSI approach will first be explained in Algorithm 6.2; while the difference between the CSS-SSI and CSS-FSI schemes will be described afterwards. In Algorithm 6.2, the set of available BSs is defined as $\mathbf{B}_t = \{\mathbf{B}_l, \mathbf{B}_n\} = \{B_i \,|\, \forall i, 1 \leq i \leq m\}$, where $\mathbf{B}_l$ and $\mathbf{B}_n$ are represented as the sets of BSs that belong to the LOS and the NLOS measurements. $\mathbf{B}_s \in \mathbf{B}_t$ is denoted as the BS set that is selected by the proposed CSS-FSI scheme. Initially, the set of available BSs $\mathbf{B}_t$ is sorted with monotonic increasing order based on the signal variance from its corresponding BS. Based on the selected four BSs (i.e., B_1 to B_4) with comparably smaller signal variances, an initial MS's estimated position $[\hat{\boldsymbol{x}}_C^{(t)}]^{(0)}$ can be acquired by adopting a conventional location estimation method, e.g., the TSLS method [69] in our case. It is noted that four measurement inputs, which result in three TDOA signals (as in (3.6)), will compose the minimal required number of BSs for the estimation of the MS's 3-D position.

In order to identify the NLOS errors from the TDOA range measurements, a residual-test modified from [55] is exploited after the initial location estimation. It is noted that the main concept of the residual test is to distinguish potential NLOS measurement based on the existence of LOS signal sources for location estimation. The outcome of the residual-test $\lambda_i^{(t)}$ for the BS B_i can be represented as

$$\lambda_i^{(t)} = F(u_{i,j}^{(t)} - d_{i,j}^{(t)}([\hat{\boldsymbol{x}}_C^{(t)}]^{(0)}) | \hat{e}_i^{(t)} = 0, \hat{e}_j^{(t)} = 0) = \frac{1}{2} + \frac{1}{2}\,\mathrm{erf}\left(\frac{(u_{i,j}^{(t)} - d_{i,j}^{(t)}([\hat{\boldsymbol{x}}_C^{(t)}]^{(0)}))}{\sqrt{2}\hat{\sigma}_i}\right), \tag{6.3}$$

where $d_{i,j}^{(t)}([\hat{\boldsymbol{x}}_C^{(t)}]^{(0)})$ denotes the difference between the distances (i.e., $d_i^{(t)}([\hat{\boldsymbol{x}}_C^{(t)}]^{(0)})$ and $d_j^{(t)}([\hat{\boldsymbol{x}}_C^{(t)}]^{(0)})$) from the initial estimated position $[\hat{\boldsymbol{x}}_C^{(t)}]^{(0)}$ to the positions of B_i and B_j. The main concept of the residual-test in (6.3) is to determine the residual $\lambda_i^{(t)}$ based on the observation from the difference between the measured and the reference distances. Since the noiseless relative distance $\zeta_{i,j}^{(t)}$ is considered unattainable, $d_{i,j}^{(t)}([\hat{\boldsymbol{x}}_C^{(t)}]^{(0)})$ is utilized to approximately represent the reference relative distance. Since the error function lies between [-1,1], the outcome of the residual-test $\lambda_i^{(t)}$ will be within the range of [0,1]. Providing that the measurement $u_{i,j}^{(t)}$ contains the NLOS error, the measurement distance $u_{i,j}^{(t)}$ should be larger than the reference distance $d_{i,j}([\hat{\boldsymbol{x}}_C^{(t)}]^{(0)})$. It is noted that even with the possibility to encounter a poor initial estimate $[\hat{\boldsymbol{x}}_C^{(t)}]^{(0)}$, $u_{i,j}^{(t)}$ will still be larger than $d_{i,j}^{(t)}([\hat{\boldsymbol{x}}_C^{(t)}]^{(0)})$ since $d_{i,j}^{(t)}([\hat{\boldsymbol{x}}_C^{(t)}]^{(0)})$ should always fall within area that is confined by its corresponding BSs. Consequently, the residual value $\lambda_i^{(t)}$ will be resulted in a larger value, i.e., in general lies between 0.5 and 1. On the other hand, the $\lambda_i^{(t)}$ value will resides between 0 and 0.5 under the situations with LOS environments. The $\lambda_i^{(t)}$ value for each B_i will be compared with a pre-determined threshold λ_{th}, which is assigned around 0.5, in order to identify the existence of the NLOS error

from the LOS measurement inputs. After acquiring both the $\mathbf{B}_l$ and $\mathbf{B}_n$ sets, the CSS-FSI scheme will obtain the set with the minimal required number of BSs (i.e., $\mathbf{B}_s$) that is associated with comparably smaller NLOS errors. It is noted that the residual test can become ineffective under the condition that all the signals in the $\mathbf{B}_t$ set are with NLOS errors. In such case, the NLOS BSs within $\mathbf{B}_n$ set will be selected for location estimation as illustrated in Algorithm 6.2. In the performance evaluation section (i.e., Section 6.5), both the identification rate for NLOS signals and the estimation accuracy that incorporates the potential failure of residual test are considered in the simulations.

Similarly, compared to the CSS-FSI approach, the proposed CSS-SSI scheme removes the constraint of fixed number of measurement inputs. All the LOS signal inputs will be utilized in the CSS-SSI scheme for location estimation of the MS. Performance comparison between these two selection schemes will be addressed in Section 6.5.

6.3.3 Hybrid Signal Selection for Selective-set of Signal Inputs (HSS-SSI) Scheme

Algorithm 6.3 HSS-SSI Scheme

Ensure: $\mathbf{H}_s$.

if $N(\mathbf{B}_l) + N(\mathbf{S}_g) \geq 6$ **then**
    $\mathbf{H}_s \leftarrow \{ \mathbf{S}_g, \mathbf{B}_l \}$;
else if $N(\mathbf{B}_l) + N(\mathbf{S}_g) + N(\mathbf{S}_b) \geq 6$ **then**
    $\mathbf{H}_s \leftarrow \{ \mathbf{S}_g, \mathbf{B}_l, \mathbf{S}_b \}$;
else
    $\mathbf{H}_s \leftarrow \{ \mathbf{S}_g, \mathbf{B}_l, \mathbf{S}_b, \mathbf{B}_n \}$;
end if

As shown in the right diagrams of Figs. 6.2 and 6.3, the HSS scheme for the UH is presented in this subsection. Unlike the previous two selection schemes for the FSI case with fixed number of signal inputs (i.e., $N(\mathbf{S}_s) = 5, N(\mathbf{B}_s) = 4$), the number of selected signal sources (i.e., $N(\mathbf{H}_s)$) are flexibly within the HSS-SSI scheme, i.e., $6 \leq N(\mathbf{H}_s) \leq N(\mathbf{S}_t) + N(\mathbf{B}_t)$. It is noted that the smallest number for the scheme (i.e., $N(\mathbf{H}_s) = 6$) is considered as the minimal number of input requirement by using the HLS estimator, which will be addressed in the Subsection 6.4.2. The objective of the proposed HSS-SSI scheme is primarily based on choosing the sources with better signal qualities. As illustrated in Algorithm 6.3, the selection strategy is based on prioritizing the following three categories: (i) the Satellites with good signal quality ($\mathbf{S}_g$) and the BSs with LOS measurement ($\mathbf{B}_l$); (ii) the Satellite with bad signal quality ($\mathbf{S}_b$); and (iii) the BSs with NLOS measurement ($\mathbf{B}_n$). Categories (ii) and (iii) will not be chosen as long as there is sufficient number of signal inputs available in (i). Moreover, the number of signal inputs obtained from the HSS-SSI scheme will not be confined as that in the FSI scheme.

6.4 Hybrid Least Squares (HLS) Location Estimation Algorithm

In this section, the HLS location estimation scheme is proposed for the UH system; while the TSLS method that extended from the conventional algorithm will be utilized in the FH system.

6.4.1 Two-Step LS (TSLS) Location Algorithm

The TSLS estimator was adopted to solve the location estimation problem from the TOA [34], the TDOA [17], and the TDOA/AOA measurements [69]. Note that the formulation of the TSLS method can be referred to Section 2.4. In addition to estimating the two-dimensional position of the MS as in the previous research, the TSLS method is applied in the proposed FH system to calculate the 3-D location of the MS. Specifically, the clock bias is also included within the FH system. The following two subsections describe the 3-D TOA location estimation for the satellite-based system, and the 3-D TDOA/AOA location estimation algorithm for the cellular network.

6.4.1.1 3-D TOA Location Estimation

In order to estimate the MS's 3-D position (i.e., $x^{(t)}$, $y^{(t)}$, $z^{(t)}$) at time instant t and the clock bias (i.e., b) within the TSLS formulation from the TOA measurements, it is assumed that signals coming from at least five satellites are available. The 3-D TOA measurements as described in (2.1) can be rewritten as in matrix format as $\mathbf{M}_1\boldsymbol{\theta}^{(t)} = \mathbf{J}_1$ as

$$\mathbf{M}_1 = \begin{bmatrix} -2x_1 & -2y_1 & -2z_1 & 2r_1 & 1 \\ -2x_2 & -2y_2 & -2z_2 & 2r_2 & 1 \\ . & . & . & . & . \\ -2x_N & -2y_N & -2z_N & 2r_N & 1 \end{bmatrix}, \quad \mathbf{J}_1 = \begin{bmatrix} r_1^{(t)^2} - \kappa_1 \\ r_2^{(t)^2} - \kappa_2 \\ . \\ r_N^{(t)^2} - \kappa_N \end{bmatrix}, \tag{6.4}$$

with $\boldsymbol{\theta}^{(t)} = [x^{(t)},\ y^{(t)},\ z^{(t)},\ b,\ \beta^{(t)}]^T$. It is noted that $\beta^{(t)} = (x^{(t)})^2 + (y^(t))^2 + (z^(t))^2 - b^2$ and $\kappa_\ell = x_\ell^2 + y_\ell^2 + z_\ell^2$. The concept of the TSLS method is to acquire an intermediate location estimate in the first step by assuming that $\{x^{(t)},\ y^{(t)},\ z^{(t)},\ b\}$ and $\beta^{(t)}$ are not correlated. The second step of the method releases this assumption by adjusting the intermediate result to obtain an improved location estimate, $\boldsymbol{x}_G^{(t)} = [x_G^{(t)},\ y_G^{(t)},\ z_G^{(t)}]^T$.

6.4.1.2 3-D TDOA/AOA Location Estimation

To solve for the TSLS problem for the cellular-based system, the home BS should provide both the TOA and AOA measurements, while three additional TOA measurements are assumed to be obtainable from other BSs. The 3-D TDOA and AOA measurements as in (3.6) and (2.4) - (2.5)

can also be rewritten in the form of $\mathbf{M}_1\boldsymbol{\theta}^{(t)} = \mathbf{J}_1$ as

$$\mathbf{M} = -2 \cdot \begin{bmatrix} x_2 - x_1 & y_2 - y_1 & z_2 - z_1 & u_{2,1}^{(t)} \\ x_3 - x_1 & y_3 - y_1 & z_3 - z_1 & u_{3,1}^{(t)} \\ \vdots & \cdots & \cdots & \vdots \\ x_N - x_1 & y_N - y_1 & z_N - z_1 & u_{N^{(t)},1}^{(t)} \\ -\sin\theta_1^{(t)} & \cos\theta_1^{(t)} & 0 & 0 \\ 0 & 0 & \cos\phi_1^{(t)} & -\cos\phi_1^{(t)}\sin\phi_1^{(t)} \end{bmatrix}, \quad \mathbf{J} = \begin{bmatrix} (u_{2,1}^{(t)})^2 - \kappa_2 + \kappa_1 \\ (u_{3,1}^{(t)})^2 - \kappa_3 + \kappa_1 \\ \cdots \\ (u_{N,1}^{(t)})^2 - \kappa_N + \kappa_1 \\ 2x_1\sin\theta_1^{(t)} - 2y_1\cos\theta_1^{(t)} \\ -2z_1\cos\phi_1^{(t)} \end{bmatrix} \tag{6.5}$$

with $\boldsymbol{\theta}^{(t)} = [x^{(t)}, y^{(t)}, z^{(t)}, r_1^{(t)}]^T$. In both matrices, the AOA components are computed based on the geometric approximation as described in [69]. The TSLS method can therefore be applied to obtain the location estimates from the TDOA/AOA measurements to obtain an improved location estimate, $\boldsymbol{x}_C^{(t)} = [x_C^{(t)}, y_C^{(t)}, z_C^{(t)}]^T$.

6.4.2 HLS Location Estimation Algorithm

In the UH system, the MS is capable of utilizing different types of signal sources for acquiring the location information. The HLS location estimator is proposed in this subsection in order to facilitate the MS's location estimation with heterogeneous signal inputs. It is especially noticed that the combination of the TOA and the TDOA/AOA channels within the TSLS formulation is nontrivial. Within the formulation of the conventional TSLS location algorithm, the variables introduced in the TOA-based scheme include $\{x^{(t)}, y^{(t)}, z^{(t)}, b, \beta^{(t)}\}$ (in Subsection 6.4.1.1); while that for the TDOA/AOA-based approach comprise $\{x^{(t)}, y^{(t)}, z^{(t)}, r_1^{(t)}\}$ (in Subsection 6.4.1.2). In order to eliminate the nonlinear terms in both schemes, the intermediate variables $\beta^{(t)}$ and $r_1^{(t)}$ are utilized along with the desired estimated parameters $\{x^{(t)}, y^{(t)}, z^{(t)}, b\}$. Consequently, the total number of required measurement inputs for the proposed HLS estimator will become six, i.e., for the estimation of the variables $\{x^{(t)}, y^{(t)}, z^{(t)}, b, \beta^{(t)}, r_1^{(t)}\}$. Due to the resulting two intermediate variables, an additional step will be required within the HLS location estimator.

Within the TOA-based TSLS formation, the circular equation $r_\ell^{(t)} = \zeta_\ell^{(t)} + b$ for the TOA measurement $r_\ell^{(t)}$ is represented as

$$(r_\ell^{(t)} - b)^2 = (\zeta_\ell^{(t)})^2 = (x_\ell - x^{(t)})^2 + (y_\ell - y^{(t)})^2 + (z_\ell - z^{(t)})^2, \tag{6.6}$$

which can further be expanded as

$$(r_\ell^{(t)})^2 = \beta^{(t)} - 2x_\ell \cdot x^{(t)} - 2y_\ell \cdot y^{(t)} - 2z_\ell \cdot z^{(t)} + 2r_\ell^{(t)} \cdot b + \kappa_\ell, \tag{6.7}$$

with $\beta^{(t)} = (x^{(t)})^2 + (y^{(t)})^2 + (z^{(t)})^2 - b^2$ and $\kappa_\ell = x_\ell^2 + y_\ell^2 + z_\ell^2$. The first step of the TSLS scheme is to solve the weighted LS problem via the linear equation with variables $\{x^{(t)}, y^{(t)}, z^{(t)}, b, \beta^{(t)}\}$. On the other hand, the TDOA/AOA-based TSLS problem considers the hyperbolic equation for

the TDOA measurement $(u_{i,1}^{(t)})$ considering from the i-th BS with respect to the home BS as

$$(u_{i,1}^{(t)})^2 \;=\; 2u_{i,1}^{(t)} \cdot r_1^{(t)} - 2x_{i,1} \cdot x^{(t)} - 2y_{i,1} \cdot y^{(t)} - 2z_{i,1} \cdot z^{(t)} + (\kappa_i - \kappa_1), \tag{6.8}$$

where the four variables $\{x^{(t)}, y^{(t)}, z^{(t)}, r_1^{(t)}\}$ are considered to be solved within the TSLS formulation. It is noted that the variables $r_1^{(t)}$ and $\beta^{(t)}$ are functions of the $x^{(t)}$, $y^{(t)}$, and $z^{(t)}$ variables. By combining (6.7) and (6.8), the elements within the matrix formulation (i.e., $\mathbf{M}_1[\boldsymbol{x}_H^{(t)}]^{(1)} = \mathbf{J}_1$) for the first step of the proposed HLS estimator can be obtained as

$$\mathbf{M}_1 = \begin{bmatrix} \mathbf{M}_{TDOA}^{N(\mathbf{B}_l)\times 6} \\ \mathbf{M}_{AOA}^{2\times 6} \\ \mathbf{M}_{TOA}^{N(\mathbf{S}_g)\times 6} \end{bmatrix} = \begin{bmatrix} -2(x_2-x_1) & -2(y_2-y_1) & -2(z_2-z_1) & 0 & 0 & -2u_{2,1}^{(t)} \\ -2(x_3-x_1) & -2(y_3-y_1) & -2(z_3-z_1) & 0 & 0 & -2u_{3,1}^{(t)} \\ \vdots & \cdots & \cdots & \cdots & \cdots & \vdots \\ -2(x_{N(\mathbf{B}_l)}-x_1) & -2(y_{N(\mathbf{B}_l)}-y_1) & -2(z_{N(\mathbf{B}_l)}-z_1) & 0 & 0 & -2u_{N(\mathbf{B}_l),1}^{(t)} \\ -\sin\theta_1^{(t)} & \cos\theta_1^{(t)} & 0 & 0 & 0 & 0 \\ 0 & 0 & \cos\phi_1^{(t)} & 0 & 0 & -\cos\phi_1^{(t)}\sin\phi_1^{(t)} \\ -2\tilde{x}_1 & -2\tilde{y}_1 & -2\tilde{z}_1 & 2\tilde{r}_1^{(t)} & 1 & 0 \\ \vdots & \cdots & \cdots & \cdots & \cdots & \vdots \\ -2\tilde{x}_{N(\mathbf{S}_g)} & -2\tilde{y}_{N(\mathbf{S}_g)} & -2\tilde{z}_{N(\mathbf{S}_g)} & 2\tilde{r}_{N(\mathbf{S}_g)}^{(t)} & 1 & 0 \end{bmatrix}, \tag{6.9}$$

$$\mathbf{J}_1 = \begin{bmatrix} \mathbf{J}_{TDOA}^{N(\mathbf{B}_l)\times 1} \\ \mathbf{J}_{AOA}^{2\times 1} \\ \mathbf{J}_{TOA}^{N(\mathbf{S}_g)\times 1} \end{bmatrix} = \begin{bmatrix} (u_{2,1}^{(t)})^2 - \kappa_2 + \kappa_1 \\ (u_{3,1}^{(t)})^2 - \kappa_3 + \kappa_1 \\ \cdots \\ (u_{N(\mathbf{B}_l),1}^{(t)})^2 - \kappa_{N(\mathbf{B}_l)} + \kappa_1 \\ -x_1\sin\theta_1^{(t)} + y_1\cos\theta_1^{(t)} \\ z_1\cos\phi_1^{(t)} \\ (\tilde{r}_1^{(t)})^2 - \tilde{\kappa}_1 \\ \cdots \\ (\tilde{r}_{N(\mathbf{S}_g)}^{(t)})^2 - \tilde{\kappa}_{N(\mathbf{S}_g)} \end{bmatrix}, \tag{6.10}$$

[1] with $[\boldsymbol{x}_H^{(t)}]^{(1)} = [[x^{(t)}]^{(1)}, [y^{(t)}]^{(1)}, [z^{(t)}]^{(1)}, b^{(1)}, [\beta^{(t)}]^{(1)}, [r_1^{(t)}]^{(1)}]^T$ as

$$[\boldsymbol{x}_H^{(t)}]^{(1)} = (\mathbf{M}_1^T \boldsymbol{\Psi}_1^{-1} \mathbf{M}_1)^{-1} \mathbf{M}_1^T \boldsymbol{\Psi}_1^{-1} \mathbf{J}_1. \tag{6.11}$$

Since the error of the first step estimation is obtained as $\psi_1 = \mathbf{M}_1[\boldsymbol{x}_H^{(t)}]^{(1)} - \mathbf{J}_1 = 2c\mathbf{B}_1\mathbf{n}_1 + c^2\mathbf{n}_1^2$, the weighting matrix $\boldsymbol{\Psi}_1$ can be acquired by neglecting the square term $c^2\mathbf{n}_1^2$ as

$$\boldsymbol{\Psi}_1 = E[\psi_1\psi_1^T] = 4c^2\mathbf{B}_1\, E[\mathbf{n}_1\mathbf{n}_1^T]\, \mathbf{B}_1 = 4c^2\mathbf{B}_1\mathbf{Q}_1\mathbf{B}_1, \tag{6.12}$$

[1] For notation convenience, the variables with a tilde are denoted for the satellite-based variables, e.g., $\tilde{r}_1$; while variables without the tilde (e.g., r_1) are utilized as network-based variables.

where

$$\mathbf{B}_1 = \text{diag}\left\{ \zeta_2^{(t)}, \cdots, \zeta_{N(\mathbf{B}_l)}^{(t)}, \zeta_1^{(t)} \cos\phi_1^{(t)}, \zeta_1^{(t)}, \tilde{\zeta}_1^{(t)}, \cdots, \tilde{\zeta}_{N(\mathbf{S}_g)}^{(t)} \right\},$$

$$\mathbf{Q}_1 = \text{diag}\left\{ \sigma_{r_{2,1}}^2, \cdots, \sigma_{r_{N(\mathbf{B}_l),1}}^2, \sigma_{r_\theta}^2, \sigma_{r_\phi}^2, \sigma_{\tilde{r}_1}^2, \cdots, \sigma_{\tilde{r}_{N(\mathbf{S}_g)}}^2 \right\}.$$

The weighted LS formulation can therefore be performed to acquire the approximate values of the variables within $[\boldsymbol{x}_H^{(t)}]^{(1)}$. By assigning $\ell = 1$ in (6.7), it can be obtained that $r_1^{(t)} = ((x^{(t)})^2 + (y^{(t)})^2 + (z^{(t)})^2 - 2x_1x^{(t)} - 2y_1y^{(t)} - 2z_1z^{(t)} + \kappa_1)^{1/2}$. In order to provide hybrid location estimation for both the TOA and the TDOA/AOA measurements, the relationship between (6.7) and (6.8) should be established (i.e., between $\beta^{(t)}$ and $r_1^{(t)}$). With coordinate transformation, it is feasible to assume that the home BS is located at the origin, i.e., $[x_1,\ y_1,\ z_1]^T = [0, 0, 0]^T$. The variable $(r_1^{(t)})^2$ becomes $(r_1^{(t)})^2 = (x^{(t)})^2 + (y^{(t)})^2 + (z^{(t)})^2$ within (6.8), which can consequently result in the relationship of $\beta^{(t)} = (r_1^{(t)})^2 - b^2$ from (6.7). Therefore, the relationship could be applied and the elements within the 2-nd step of the HLS estimator formulation (i.e., $\mathbf{M}_2[\boldsymbol{x}_H^{(t)}]^{(2)} = \mathbf{J}_2$) can be obtained as

$$\mathbf{M}_2 = \left[\begin{array}{ccccc} 1 & 0 & 0 & 0 & 0 \\ 0 & 1 & 0 & 0 & 0 \\ 0 & 0 & 1 & 0 & 0 \\ 0 & 0 & 0 & 1 & 0 \\ 0 & 0 & 0 & -1 & 1 \\ 0 & 0 & 0 & 0 & 1 \end{array}\right], \mathbf{J}_2 = \left[\begin{array}{c} ([x^{(t)}]^{(1)})^2 \\ ([y^{(t)}]^{(1)})^2 \\ ([z^{(t)}]^{(1)})^2 \\ (b^{(1)})^2 \\ ([\beta^{(t)}]^{(1)}) \\ ([r_1^{(t)}]^{(1)})^2 \end{array}\right], \tag{6.13}$$

with $[\boldsymbol{x}_H^{(t)}]^{(2)} = [\ ([x^{(t)}]^{(2)})^2, ([y^{(t)}]^{(2)})^2, ([z^{(t)}]^{(2)})^2, (b^{(2)})^2, ([r_1^{(t)}]^{(2)})^2]^T$, which can also be solved by the weighted LS formulation with the weighting matrix $\boldsymbol{\Psi}_2$ of the 2-nd step as

$$\boldsymbol{\Psi}_2 = 4\mathbf{B}_2\text{cov}([\boldsymbol{x}_H^{(t)}]^{(1)})\mathbf{B}_2 = 4\mathbf{B}_2(\mathbf{M}_1{}^T\boldsymbol{\Psi}_1{}^{-1}\mathbf{M}_1)^{-1}\mathbf{B}_2, \tag{6.14}$$

where $\mathbf{B}_2 = \text{diag}\{[x^{(t)}]^{(1)},\ [y^{(t)}]^{(1)},\ [z^{(t)}]^{(1)},\ b^{(1)},\ 1/2,\ [r_1^{(t)}]^{(1)}\}$. With the relationship of $\beta^{(t)} = (r_1^{(t)})^2 - b^2$, it can be observed that the variable β is removed from $[\boldsymbol{x}_H^{(t)}]^{(1)}$ such as to formed the reduced dimension vector of $[\boldsymbol{x}_H^{(t)}]^{(2)}$. Furthermore, the 3-rd step of the HLS estimator is again to incorporate the relationship with $([r_1^{(t)}]^{(2)})^2 = ([x^{(t)}]^{(3)})^2 + ([y^{(t)}]^{(3)})^2 + ([z^{(t)}]^{(3)})^2$ into the matrix

formulation (i.e., $\mathbf{M}_3[\boldsymbol{x}_H^{(t)}]^{(3)} = \mathbf{J}_3$) as

$$\mathbf{M}_3 = \begin{bmatrix} 1 & 0 & 0 & 0 \\ 0 & 1 & 0 & 0 \\ 0 & 0 & 1 & 0 \\ 0 & 0 & 0 & 1 \\ 1 & 1 & 1 & 0 \end{bmatrix}, \quad \mathbf{J}_3 = \begin{bmatrix} ([x^{(t)}]^{(2)})^2 \\ ([y^{(t)}]^{(2)})^2 \\ ([z^{(t)}]^{(2)})^2 \\ ([b^{(t)}]^{(2)})^2 \\ ([r_1^{(t)}]^{(2)})^2 \end{bmatrix}, \tag{6.15}$$

with $[\boldsymbol{x}_H^{(t)}]^{(3)} = [([x^{(t)}]^{(3)})^2, ([y^{(t)}]^{(3)})^2, ([z^{(t)}]^{(3)})^2, (b^{(3)})^2]^T$. The associated weighting matrix $\boldsymbol{\Psi}_3$ of the 3-rd step becomes

$$\boldsymbol{\Psi}_3 = \mathbf{B}_3 \text{cov}([\boldsymbol{x}^{(t)}]_H^{(2)})\mathbf{B}_3 = \mathbf{B}_3(\mathbf{M}_2{}^T\boldsymbol{\Psi}_2{}^{-1}\mathbf{M}_2)^{-1}\mathbf{B}_3, \tag{6.16}$$

where $\mathbf{B}_3$ is an identical matrix, which indicates that the 3-rd step of the HLS estimator is exploited as the tuning process based on the 2-nd step's covariance matrix $\text{cov}([\boldsymbol{x}_H^{(t)}]^{(2)})$. The final estimated MS's position by using the proposed HLS estimator can be obtained as $\boldsymbol{x}_H^{(t)} = \mathbf{T} \cdot ([\boldsymbol{x}_H^{(t)}]^{(3)})^{1/2}$, where $\mathbf{T} = \text{diag}(1, 1, 1, 0)$. The effectiveness of the HLS estimator will be evaluated in the simulations.

6.5 Performance Evaluation

The performance of the proposed hybrid architectures is evaluated via simulations and is described the following subsections. The noise models of TOA from the satellites, TDOA, and AOA from the cellular networks can be referred to Sections 2.2.1.3, 2.2.1.2, and 2.2.2, respectively. Subsection 6.5.1 addresses the assessments on the proposed schemes according to time complexity. Subsection 6.5.2 describes the validation of the hybrid architectures and the associated HLS estimator under the circumstance with pure measurement noises. Subsection 6.5.3 illustrates the performance evaluation of the proposed schemes under the NLOS environments. Two cases are considered: (*i*) the different circumstances with fixed-set of available signal inputs, and (*ii*) the realistic environments with either a stationary MS or a moving MS.

6.5.1 Assessments on Proposed Architectures and Schemes

In order to illustrate the feasibility of proposed architectures, the assessments for corresponding approaches are discussed in this subsection in view of time complexity. It is noted that both FH and UH architectures can be implemented as either the Mobile-Assisted or the Mobile-Based system. In the Mobile-Based system, except for the AOA information needs to be delivered from the BS to the MS, all the required information for location estimation and tracking are calculated and processed within the MS. On the other hand, considerable message transmissions between the MS and BS should be conducted by adopting the Mobile-Assisted system such as to provide the BS for

Table 6.1: Number of required computations of the FH architecture

	Value p	Value q	Computation costs
Satellite-based 1-st step	5	5	1400
Satellite-based 2-nd step	5	4	1214
Cell-based 1-st step	4	4	720
Cell-based 2-nd step	4	3	603
Total			3937

obtaining the MS's position. Therefore, providing that the MS is possessed with sufficient processing capability, the Mobile-Based system is considered a favorable architecture for location estimation of the MS. However, due to the huge processing load within the MS by adopting the Mobile-Based system, efficient power management should be considered to reduce power consumption within the MS.

Moreover, the assessment between the FH and UH architectures is discussed. Basically, two pairs of location estimators and Kalman filters are adopted for the FH scheme; while an integrated technique is exploited in the UH architecture. In order to illustrate the comparison between the FH and UH structures, an example is given under the situation with $N(\mathbf{S}_g) = 5$ and $N(\mathbf{B}_l) = 4$, which corresponds to $N(\mathbf{H}_s) = 9$. First of all, the time complexity of TSLS method and proposed HLS scheme can be obtained by considering both matrix multiplication and matrix inversion within the LS estimator. It is noted that the multiplication between an $i \times j$ matrix and an $j \times k$ matrix runs in $O(i \cdot j \cdot k)$; while the computation cost of matrix inversion for an $i \times i$ matrix can be approximated as $O(i^3)$ [70]. Providing that the number of measurement inputs is p and the number of variables to be solved is q, the computation cost for each LS iteration step becomes $O(6p^3) + O(q^3) + O(3p^2q) + O(pq^2) + O(pq)$ by evaluating the complexity on (6.11) and (6.12). Therefore, the total number of computations for the FH and UH architectures can be obtained as listed in Tables 6.1 and 6.2, respectively. On the other hand, providing that the number of measurement inputs is u and the number of state vector is w, the computation cost for the Kalman filter can be acquired as $O(u^3) + O(w^3) + O(2u^2w) + O(2uw^2)$ for each iteration [19]. Considering the case that $u = 3$ and $w = 9$, the computation costs for the FH and UH can be obtained as 2808 and 1404 respectively since two separate Kalman filters are required for the FH scheme. Therefore, the total computation costs from both the Location estimator and the Kalman filter for the FH and UH architectures become 6745 and 11185, respectively. With smaller size of measurement input by adopting separate estimation paths, the FH architecture will possess less amount of computation load comparing with the UH structure.

Furthermore, the complexity of both fixed-set and selective-set of signal selection methods is compared within the FH architecture. An example is considered with the GPS-SSI and GPS-FSI schemes under the situation while $N(\mathbf{S}_g) = 7$. Compared with the GPS-SSI scheme, the GPS-

Table 6.2: Number of required computations of the UH architecture

	Value p	Value q	Computation costs
HLS 1-st step	9	6	6426
HLS 2-nd step	6	5	2141
HLS 3-rd step	5	4	1214
Total			9781

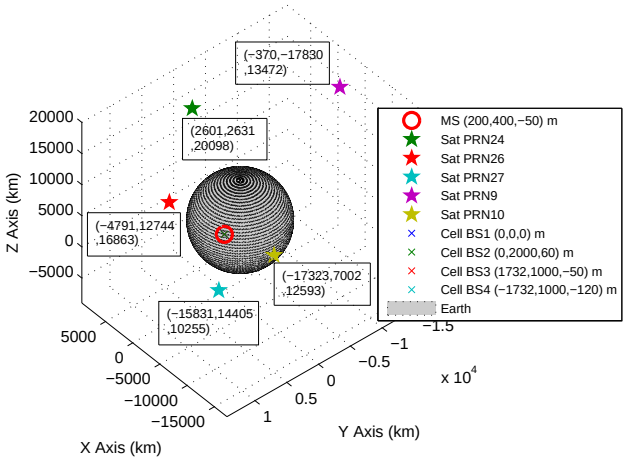

Figure 6.4: Simulation parameters for Subsections 6.5.2, 6.5.3.1, and 6.5.3.2: graphical representation for the coordinates of satellites marked in textbox (km), cell BSs (m), and MS (m).

FSI method additionally performs the Optimum5 algorithm in order to restrict the number of measurement input to 5. It is required for the optimum5 function to search $C_5^{N(\mathbf{S}_g)}$ times for signal selection, i.e., $C_5^7 = 21$ times of computation. On the other hand, considering the computation cost for implementing the TSLS method, the GPS-FSI scheme will conserve $3128 - 1400 = 1728$ times of calculation comparing with the GPS-SSI approach. As a result, the FSI scheme can conserve the computation cost by reducing the number of measurement inputs; while the SSI approach will in general provide better estimation performance with its additional usage of signal sources. Performance comparisons between these proposed architectures and approaches will be conducted and validated in the following subsections.

6.5.2 Validation of Proposed Algorithms with Pure Measurement Noises

Example 6.1 (Validation on Proposed HLS estimator with Pure Measurement Noises)**.** The HLS estimator as proposed in the Subsection 6.4.2 is validated under the environment with pure measurement noises, i.e., only $n_\xi^{(t)}$ (for $\xi = \ell$, i, and j), $n_\theta^{(t)}$, and $n_\phi^{(t)}$ are considered. Fig. 6.4 shows the simulation parameters for performance validation. Fig. 6.5 illustrates the comparison of the

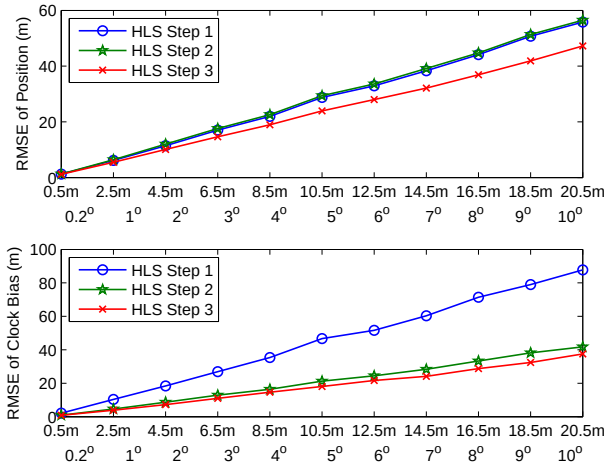

Figure 6.5: Performance comparison between each step of the HLS estimator under pure measurement noises: RMSE of position (upper plot) and RMSE of clock bias (lower plot) vs. standard deviation of measurement noises (σ_n, σ_{n_θ}, and σ_{n_ϕ}).

RMSE for the MS's estimated position (upper plot) and the clock bias (lower plot) between the three steps of the HLS estimator under different standard deviations of the measurement noises σ_{n_ξ}, σ_{n_θ}, and σ_{n_ϕ}. It is noted that the Root Mean Square Error (RMSE) is computed as: RMSE $= \left[\sum_{i=1}^{N_r} \|\boldsymbol{x}^{(t)} - \hat{\boldsymbol{x}}^{(t)}(i)\|^2 / N_r\right]^{1/2}$, where $N_r = 10{,}000$ indicates the number of simulation runs. It is noted that $\boldsymbol{x}^{(t)}$ represents the true position of MS; while $\hat{\boldsymbol{x}}^{(t)}(i)$ denotes for the MS's estimated position in the upper plot of Fig. 6.5. On the other hand, $\boldsymbol{x}^{(t)}$ indicates the clock bias (chosen as 50,000 m in this case) and $\hat{\boldsymbol{x}}^{(t)}(i)$ corresponds to the estimated clock bias in the lower plot of Fig. 6.5. It can be observed that the RMSEs of MS's estimated position are significantly decreased from step 2 to 3; while that of the clock bias are considerably reduced from step 1 to 2. The reason can be attributed to the implicit different weights that are imposed by the distinctive steps within the proposed HLS estimator. The mechanism within the second step of the HLS estimator removes the clock bias b by adopting the relationship between the intermediate variables $\beta^{(t)}$ and $r_1^{(t)}$, i.e., $\beta^{(t)} = (r_1^{(t)})^2 - b^2$. On the other hand, the association between $r_1^{(t)}$ and the MS's position is constructed within the third step of the HLS scheme, i.e., $(r_1^{(t)})^2 = (x^{(t)})^2 + (y^{(t)})^2 + (z^{(t)})^2$. Consequently, the results obtained from Fig. 6.5 validates the effectiveness of the proposed HLS estimator for location estimation of the MS. ◇

Example 6.2 (Validation on Proposed FH and UH Architectures with Pure Measurement Noises)**.** Fig. 6.6 shows the performance comparison between the proposed FH ($\hat{\boldsymbol{x}}_f^{(t)}$) and UH ($\hat{\boldsymbol{x}}_H^{(t)}$) schemes, associated with the Cell-FH ($\hat{\boldsymbol{x}}_C^{(t)}$) and the GPS-FH ($\hat{\boldsymbol{x}}_G^{(t)}$) methods. It is noted that the Cell-FH and the GPS-FH schemes are denoted as the separate channels within the FH architecture without the implementation of the data fusion. For example, the Cell-FH scheme includes the building

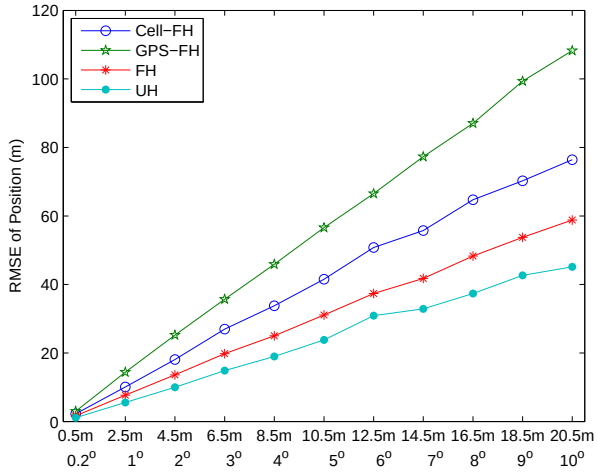

Figure 6.6: Performance comparison between the location estimation schemes under pure measurement noises: RMSE of position vs standard deviation of measurement noises (σ_n, σ_{n_θ}, and σ_{n_ϕ}).

Table 6.3: NLOS BS identification rate for FH scheme under urban environment.

Number of NLOS BSs: $N(\mathbf{B}_n)$	Number of NLOS BS Correctly Detected	Number of BS $N(\mathbf{B}_t)$ $[N(\mathbf{S}_t)]$ 4 [5]	5 [5]	6 [5]
1BS	1BS	0.778	0.852	0.898
2BSs	2BSs	0.443	0.678	0.839
	1BS	0.084	0.054	0.003
3BSs	3BSs		0.459	0.645
	2BSs		0.115	0.051
	1BS		0.016	0.137

blocks of the CSS, the TSLS method, and the Kalman Filter as shown in the left diagram of Fig. 6.2. Both schemes are utilized in this and the remaining subsections to illustrate the performance for location estimation while only a single type of channel (either the cellular or the satellite-based network) is exploited. It is also noted that both FSI and SSI schemes are considered the same since minimum number of required signal inputs is adopted in this case. Moreover, online adaption for the data fusion mechanism as in (6.3) is performed in the simulations. The signal means and variances, i.e., ($\underline{\hat{\boldsymbol{x}}}_G^{(t)}$, $\boldsymbol{\sigma}_G$) and ($\underline{\hat{\boldsymbol{x}}}_C^{(t)}$, $\boldsymbol{\sigma}_C$), are obtained based on the acquisition of the previous ten estimated data points of $\hat{\boldsymbol{x}}_G^{(t)}$ and $\hat{\boldsymbol{x}}_C^{(t)}$, respectively. It can be observed that the proposed UH and the FH architectures outperform the other two schemes under various noise environments. The effectiveness of the data fusion within the FH scheme is validated. With the incorporation of the HLS estimator, the UH scheme can provide better performance comparing with the FH method, especially with larger standard deviation of the measurement noises. ◇

Table 6.4: NLOS BS identification rate for UH scheme under urban environment.

Number of NLOS BSs: $N(\mathbf{B}_n)$	Number of NLOS BS Correctly Detected	Number of BS $N(\mathbf{B}_t)$ $[N(\mathbf{S}_t)]$ 4 [5]	5 [5]	6 [5]
1BS	1BS	0.862	0.907	0.945
2BSs	2BSs	0.732	0.800	0.890
	1BS	0.246	0.050	0.006
3BSs	3BSs		0.634	0.728
	2BSs		0.321	0.050
	1BS		0.034	0.049

6.5.3 Simulation Results Under NLOS environments

6.5.3.1 Identification of BSs with NLOS Errors

Example 6.3 (Identification of BSs with NLOS Errors)**.** As explained in Subsection 6.3.2, a residual-test is performed for the identification of the BSs with NLOS errors. Tables 6.3 and 6.4 show the identification rates (i.e., the rates to correctly detect the BS(s) with NLOS error) for both the FH and the UH schemes under urban environment. The test threshold $\lambda_{th} = 0.9$ is chosen to achieve low false alarm rate associated with 10,000 trials of the residual-test. For instance, the identification rate for correctly obtain 2 NLOS BSs under the situation of 2 NLOS BSs (with $N(\mathbf{B}_t)[N(\mathbf{S}_t)] = 5[5]$) is 0.678 for the FH scheme and 0.800 for the UH method. It can be observed from Tables 6.3 and 6.4 that the UH scheme can provide higher identification rate comparing with that from the FH method. The reason can be attributed to the better initial location estimate of the MS ($[\hat{\boldsymbol{x}}_H^{(t)}]^{(0)}$) acquired from the UH structure. ◇

6.5.3.2 Environments with Fixed-Set of Available Signal Inputs

Example 6.4 (Environments with Fixed-Set of Available Signal Inputs)**.** In this scenario, fixed-set of available signal inputs are considered, i.e., five satellites ($N(\mathbf{S}_t) = 5$) and four BSs ($N(\mathbf{B}_t) = 4$) are accessible. The signal inputs that are adopted within the FH scheme is considered fixed; while the signal selection scheme within the UH scheme (i.e., the HSS-SSI in Algorithm 3) chooses signals with better quality, which may result in smaller number of signal sources (i.e., in the case that $N(\mathbf{S}_g) < 5$ or $N(\mathbf{B}_l) < 4$). The simulation parameters are shown in Fig. 6.4. Fig. 6.7 illustrates the performance comparison between the four schemes under the urban (left plot) and the rural (right plot) environments. It is noted that the position error (Δx) are computed as: $\Delta x = \left[\sum_{i=1}^{N_r} \|\boldsymbol{x}^{(t)} - \hat{\boldsymbol{x}}^{(t)}(i)\|\right] / N_r$, where $N_r = 1{,}000$ indicates the number of simulation runs. Different signal qualities of the satellites and the NLOS errors in the cellular signals are considered as shown in the captions of Fig. 6.7. In both environments, it can be observed that the proposed UH scheme can provide better performance comparing with the other three methods under different percentages of position errors. It is expected to observe that the Cell-FH scheme is shown to have worse performance comparing with the GPS-FH method under the urban environment and the

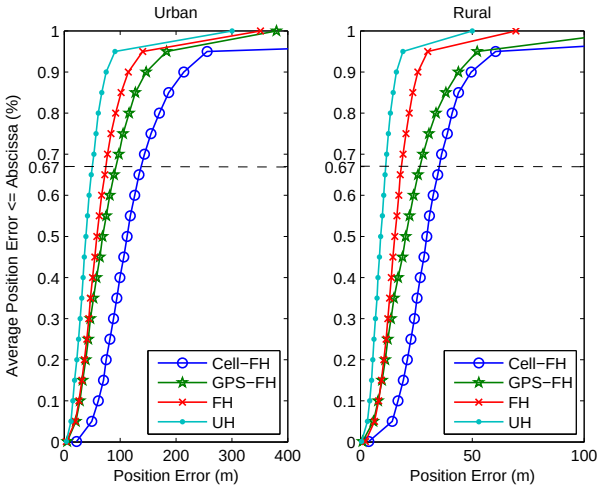

Figure 6.7: Left plot: performance comparison under urban environment with 50% of NLOS BSs and 20% of bad satellites; right plot: performance comparison under rural environment with 50% of NLOS BSs and 0% of bad satellites.

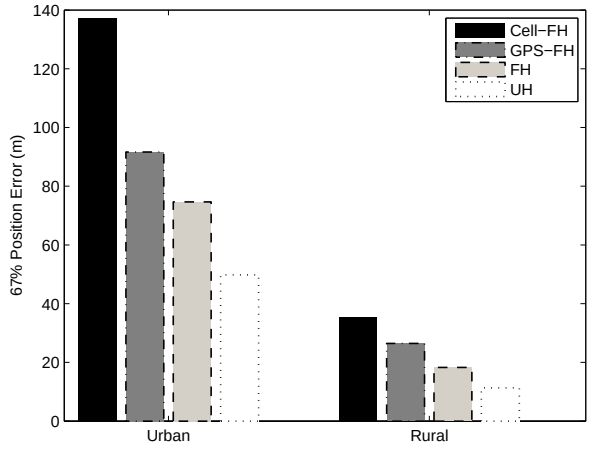

Figure 6.8: Performance comparison with 67% position error under urban and rural environments: the bars from left to right indicate Cell-FH, GPS-FH, FH, and UH schemes.

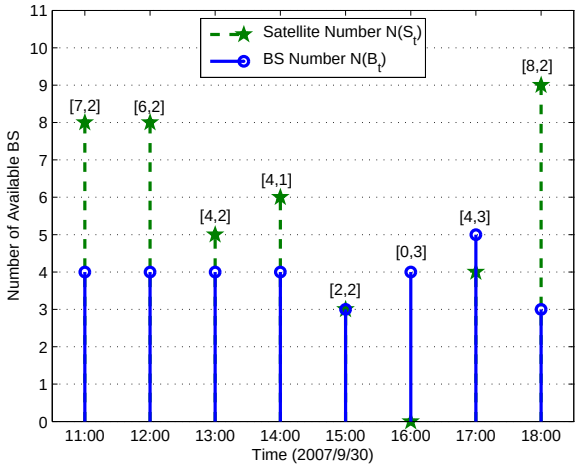

Figure 6.9: Number of available satellites and BSs at different time instants for stationary MS: the set $[N(\mathbf{S}_g), N(\mathbf{B}_l)]$ on the graph indicates the numbers of satellites with good signal quality and BSs with LOS measurement.

rural area as in Fig. 6.7. Fig. 6.8 shows the performance comparison of these four schemes within the two environments under 67% of position error. It is expected to find that smaller position errors are obtained by using the proposed UH scheme. ◇

6.5.3.3 Realistic Environments with a Stationary MS

Example 6.5 (Realistic Environments with a Stationary MS)**.** This scenario demonstrates how the proposed algorithms work in the realistic situations while a MS is stationary at a specific location (i.e., in the urban area) for a certain time interval. Fig. 6.9 shows the total available satellites ($N(\mathbf{S}_t)$) and BSs ($N(\mathbf{B}_t)$) that are considered every hour between 11:00 to 18:00 on 2007/9/30 at $(N24.47, E120.59, 91m)$ in Hsinchu, Taiwan. The coordinates of satellites are collected from the Satscape software [71], which calculates satellite positions using NORAD SGP4 orbital models. The sets of satellites with good signal quality and the BSs with LOS measurements (i.e., $[N(\mathbf{S}_g)$, $N(\mathbf{B}_l)]$) are denoted on the plot. It is noted that incorrect identification for both types of signal sources are also considered in the simulations.

By adopting the scenario as in Fig. 6.9, the performance comparison between the four different schemes can be obtained as shown in Fig. 6.10 (under 67% of position error). In general, the proposed UH algorithm outperforms the other four schemes in most cases. At the time instant of 14:00, the large estimation error (i.e., 125 m as in Fig. 6.10) acquired from the Cell-FH-FSI scheme can be attributed to the weak NLOS identification as shown in Fig. 6.9, where $N(\mathbf{B}_t) = 4$ and $N(\mathbf{B}_l) = 1$. The fusion algorithm within the FH-SSI scheme can overcome excessive NLOS errors, which results in better location estimation comparing with the other methods. At time 15:00 where $[N(\mathbf{S}_t), N(\mathbf{B}_t)] = [3, 3]$, all the four schemes (i.e., the GPS-FH-FSI, the Cell-FH-FSI, the FH-FSI,

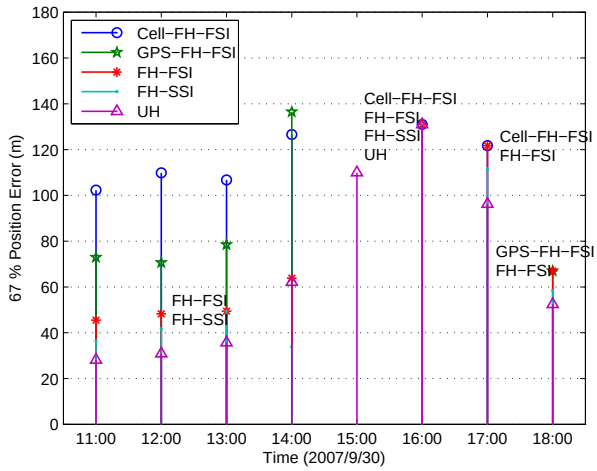

Figure 6.10: Performance comparison under 67% of position error at different time instants: At 13:00, FH-FSI and FH-SSI schemes achieve the same performance; At 16:00, Cell-FH-FSI, FH-FSI, FH-SSI, and UH schemes achieve the same performance; At 17:00, Cell-FH-FSI and FH-FSI Schemes achieve the same performance; At 18:00, GPS-FH-FSI and FH-FSI achieve the same performance.

and the FH-SSI methods) fail to perform location estimation for the MS due to the deficiency of signal sources. However, the UH scheme still can effectively provide consistent location estimation with the position error equal to 108 m as shown in Fig. 6.10. At the time instant of 16:00 where the number of available satellite is zero, both the FH and the UH schemes are transformed into the Cell-FH-FSI method, which utilizes the TSLS method for location estimation. It can be observed that same estimation error (i.e., around 130 m) is obtained as shown in Fig. 6.10. On the other hand, the GPS-FH-FSI scheme apparently will not be able to conducted location estimation for the MS. At the time instant of 17:00 where the number of available satellite is four, the GPS-FH-FSI scheme will not be able to provide location estimation neither. The FH-FSI schemes is transformed into the Cell-FH-FSI method, while the FH-SSI still adopts signal sources from both sides to achieve lower estimation error equal to 111 m. At time 18:00 with $[N(\mathbf{S}_g), N(\mathbf{B}_l)] = [8, 2]$, the FH algorithm will perform the same as the GPS-FH-FSI method due to the insufficient signals within the cell-based network. However, the UH algorithm can still provide feasible location estimation (around 15 m less in position error) comparing with the FH-FSI scheme even with insufficient signal inputs. ◇

6.5.3.4 Realistic Environments with a Moving MS

Example 6.6 (Realistic Environments with a Moving MS)**.** In this scenario, the proposed schemes are compared under the environment with a moving MS, where the urban area with 50% of NLOS BSs condition is considered. It is noted that the trajectories of satellites adopted from Satscape software [71] are approximated with NORAD SGP4 model. The trajectories start from 13:30 on 2007/9/30 for the duration of 100 sec. The simulation parameters and scenarios are shown in

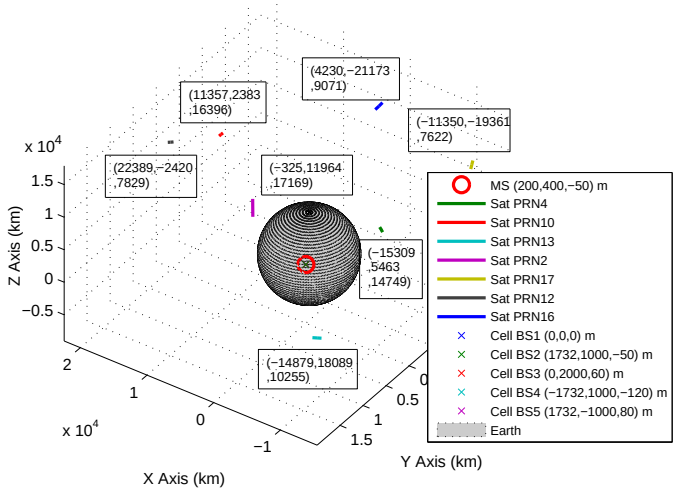

Figure 6.11: Simulation parameters for Subsection 6.5.3.4: graphical representation for the coordinates of moving satellites (solid line: satellites trajectory during 100 sec; textbox: coordinates of satellite at time instant of 13:30 in km), cell BSs (m), and MS (m).

Fig. 6.11 for the starting coordinates and the trajectories of moving satellites during this period. Moreover, the trajectory of MS is also illustrated in Fig. 6.14(a). The total available satellites ($N(\mathbf{S}_t)$) and BSs ($N(\mathbf{B}_t)$) are illustrated in Fig. 6.12 with the sets of [$N(\mathbf{S}_g)$, $N(\mathbf{B}_l)$] indicated on the plot.

Fig. 6.13 shows the position errors between the four schemes under the topology as in Fig. 6.12 (with time duration of 100 sec). It can be observed that the proposed UH algorithm is able to provide better performance for location estimation and tracking comparing with the other four methods. It is noticed that the Kalman filter within all the four algorithms become effective for MS's location tracking in this case. In region I, excessive position errors are observed in all five schemes due to the transient state of their Kalman filters. However, the error convergent rates are tolerable due to the sufficient signal sources that are available for location estimation. On the other hand, signal deficiency happens within the cellular channel in the region IV, VI, and VII. The GPS-FH-FSI, the FH-FSI, the FH-SSI, and the UH algorithms can still conduct persistent location estimation using the sources from the satellite signals. The Cell-FH-FSI method can only perform linear prediction within its Kalman filtering technique, which results in comparably worse performance for location tracking.

Figs. 6.14(a) to 6.14(c) show the trajectory tracking for the MS's position, velocity, and acceleration between the two selective-set of signal selection schemes, i.e., the FH-SSI and UH approaches. The MS is considered to be tracked in a two-dimensional x-y plane setting. It can be shown that the UH scheme outperforms the FH-SSI method for location tracking of the MS. The performance problem within the FH-SSI scheme primarily comes from the variations on the number of available signal inputs; while the UH algorithm can provide satisfactory performance for location estimation

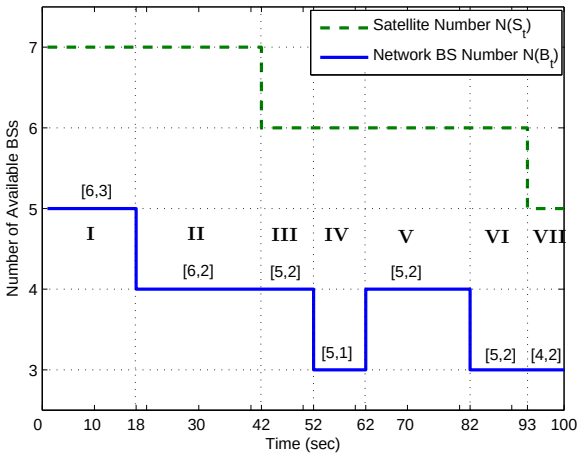

Figure 6.12: Number of available satellites and BSs at different time instants (for moving MS): the set $[N(\mathbf{S}_g), N(\mathbf{B}_l)]$ on the graph indicates the numbers of satellites with good signal quality and BSs with LOS measurement.

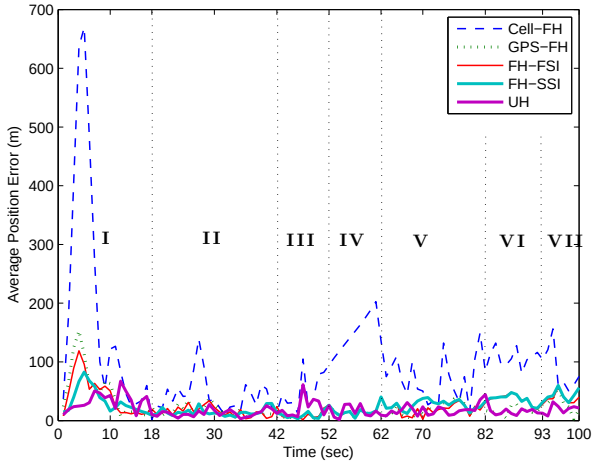

Figure 6.13: Performance comparison for location estimation and tracking: position error vs time (the region indexes correspond to the indexes as in Fig. 6.12).

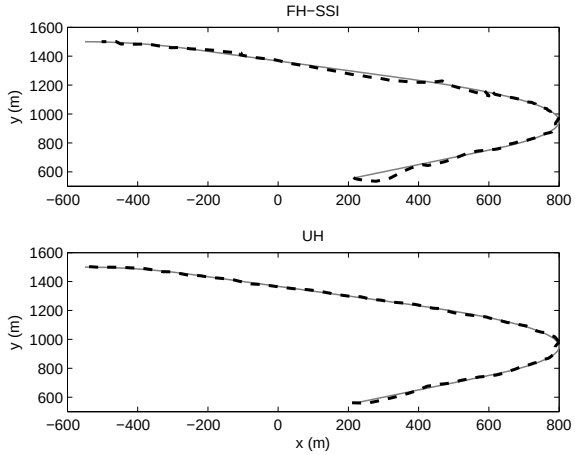

(a) Trajectory.

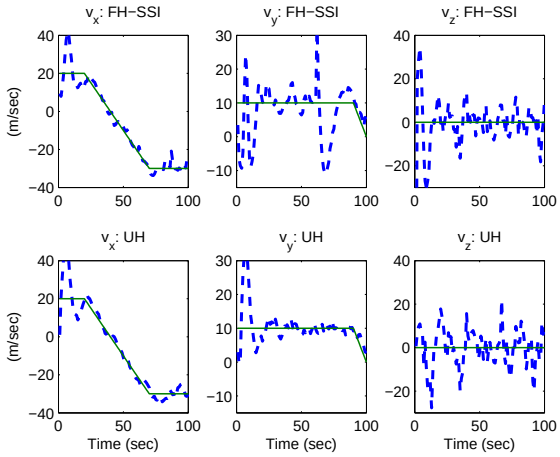

(b) Velocity.

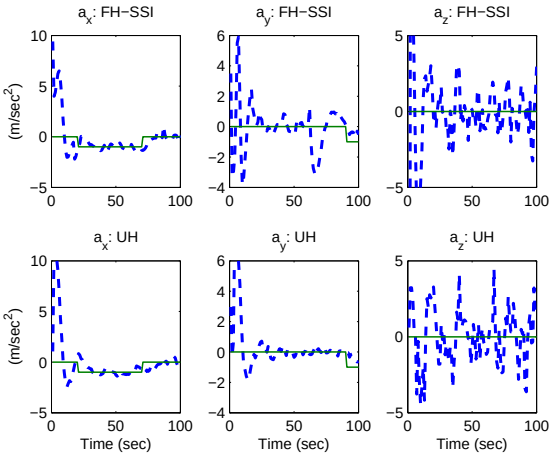

(c) Acceleration.

Figure 6.14: Performance comparison of MS tracking using the FH-SSI (upper plots) and the UH (lower plots). (Solid lines: true value; dotted lines: estimated trajectories).

by adjusting itself under a diverse range of available signal sources. ◇

6.6 Concluding Remarks

In this chapter, two different hybrid architectures for location estimation and tracking of mobile stations are proposed. By combining the satellite and the network-based systems, the proposed Fusion-based Hybrid architecture with Fixed-set of Signal Inputs (FH-FSI) can provide adequate precision for location estimation within existing infrastructure. Moreover, the Fusion-based Hybrid architecture with Selective-set of Signal Inputs (FH-SSI) further improves the estimation accuracy, especially under Non-Line-of-Sight environments. On the other hand, the Unified Hybrid (UH) architecture can achieve higher reliability for location estimation and tracking with its flexible architecture in most of the cases, even with deficient signal sources from the heterogeneous networks. It is shown in the simulation results that the proposed hybrid schemes can provide consistent location estimation accuracy under different environments.

Chapter 7

Location Tracking Algorithms for Environments with Insufficient Signal Sources

- The location estimators associated with the Kalman filtering techniques, a.k.a. two-stage location tracking architecture, are exploited to both acquire location estimation and trajectory tracking for the mobile devices. However, most of the existing schemes become inapplicable for location tracking due to the deficiency of signal sources. Two predictive location tracking algorithms are proposed to alleviate this problem, by utilizing the predictive information obtained from the Kalman filter in order to provide the additional geometric constraints for the location estimator. [1]

7.1 Introduction

In addition to the estimation of a MS's position, trajectory tracking of a moving MS has been studied [72, 73, 74, 75, 76, 77, 18, 21]. The Extended Kalman Filter (EKF) scheme [72, 73, 74] is considered the well-adopted method for location tracking. The EKF algorithm estimates the MS's position, speed, and acceleration via the linearization of measurement inputs. The technique by combining the Kalman filter with the Weighted Least Square (WLS) method is exploited in [75]. The Kalman Tracking (KT) scheme [76, 77] distinguishes the linear part from the originally nonlinear equations for location estimation. The linear aspect is exploited within the Kalman filtering formulation; while the nonlinear term is served as an external measurement input to the Kalman filter. The technique utilized in [18] adopted the Kalman filters for both pre-processing and post-processing in order to both mitigate the Non-Line-of-Sight (NLOS) noises and track the

[1] This chapter is mainly based on [J-3] Po-Hsuan Tseng, Kai-Ten Feng, Yu-Chiun Lin, and Chao-Lin Chen , "Wireless Location Tracking Algorithms for Environments with Insufficient Signal Sources," in *IEEE Trans. on Mobile Computing*, vol.8, issue 12, pp. 1676 - 1689, Dec. 2009.

MS's trajectory. The Cascade Location Tracking (CLT) scheme as proposed in [21] utilizes the two-step least squares (TSLS) method for initial location estimation of the MS. The Kalman filtering technique is employed to smooth out and to trace the position of the MS based on its previously estimated data.

The Geometric Dilution of Precision (GDOP) [63, 36] and the Cramér-Rao Lower Bound (CRLB) [38] are the well-adopted metrics for justifying the accuracy of location estimation based on the geometric layouts between the MS and its associated BSs. It has been indicated in [78] that the environments with ill-conditioned layouts will result in relatively larger GDOP and CRLB values. In general, the ill-conditioned situations can be classified into two categories: (*i*) insufficient number of available neighborhood BSs around the MS; and (*ii*) the occurrence of collinearity or coplanarity between the BSs and the MS. It is noticed that the problem caused by case (*ii*) can be resolved with well-planned locations of the BSs. Nevertheless, the scenarios with insufficient signal sources (i.e., case (*i*)) can happen in real circumstances, e.g., under rural environments or city valley with blocking buildings. It will be beneficial to provide consistent accuracy for location tracking under various environments. However, the wireless location tracking problem with deficient signal sources has not been extensively addressed in previous studies. In the cellular-based networks, three BSs are required in order to provide three signal sources for the TOA-based location estimation. The scheme as proposed in [79] considers the location tracking problem under the circumstances with short periods of signal deficiency, i.e., occasionally with only two signal sources available. The linear predictive information obtained from the Kalman filter is injected into its original LS scheme while one of the BSs is not observable. However, this algorithm is regarded as a preliminary design for signal deficient scenarios, which does not consider the cases while only one BS is available for location estimation. Insufficient accuracy for location estimation and tracking of the MS is therefore perceived.

Definition 7.1 (Insufficient Signal Sources)**.** When the available number of measurements from the neighborhood BSs is less than three, the case is defined as insufficient signal source for 2-D the location estimation problem.

In this chapter, a Predictive Location Tracking (PLT) algorithm is proposed to improve the problem with insufficient measurement inputs, i.e., with only two BSs or a single BS available to be exploited. The predictive information obtained from the Kalman filter is adopted as the virtual signal sources, which are incorporated into the TSLS method for location estimation and tracking. Moreover, a Geometry-assisted Predictive Location Tracking (GPLT) scheme is proposed by adopting the GDOP concept into its formulation in order to further enhance the performance of the original PLT algorithm. The position of the virtual signal source is relocated for the purpose of achieving the minimum GDOP value with respect to the MS's position. Consistent precision for location tracking of a MS is observed by exploiting the GPLT algorithm. Comparing with the existing techniques, the simulation results show that the proposed GPLT scheme can acquire

higher accuracy for location estimation and tracking even under the situations with inadequate signal sources.

The remainder of this chapter is organized as follows. Section 7.2 briefly describes the modeling of the signal sources, the TSLS estimator, and the GDOP metric. The concepts and motivations of the proposed PLT and GPLT schemes are explained in Section 7.3. Section 7.4 presents the PLT algorithm with two different scenarios; while the formulation of the GPLT scheme is exploited in Section 7.5. Section 7.6 illustrates the performance evaluation of the proposed PLT and the GPLT schemes in comparison with the existing location tracking techniques. Section 7.7 draws the conclusions.

7.2 Preliminaries

7.2.1 Problem Description

Consider a synchronous network of $N^{(t)}$ transmitting BSs fixed at the known positions at time instant t. Our goal is to estimate the unknown positions of an MS at time instant t which are denoted by a set of 2-dimensional vectors $\boldsymbol{x}^{(t)} = [x^{(t)}, y^{(t)}]^T$. In other words, based on the known positions of the transmitting BSs, the mobile units wish to estimate their positions at different time instants. There are typically movement of MS between the sampling time instant t and $t+1$. When the i-th BS $\boldsymbol{b}_i^{(t)} = [x_i^{(t)}, y_i^{(t)}]^T$ broadcasts its signal at time instant t, the MS receives a TOA measurement $r_i^{(t)}$. Note that the number of available BSs $N^{(t)}$ varies at different time instant, which results in a variable receivable BS set and receivable measurement set. By collecting measurements from time instant 1 to t from the BSs to the MS (i.e., $\boldsymbol{r}^{(1:t)} = [\boldsymbol{r}_1^{(1:t)}, ..., \boldsymbol{r}_{N^{(t)}}^{(1:t)}]$), the goal is for the MS to generate an estimate $\hat{\boldsymbol{x}}^{(t)}$ of its position under different number of measurements, even under the insufficient signal sources cases.

7.2.2 Mathematical Modeling of Signal Sources

In order to facilitate the design of the proposed PLT and the GPLT algorithms, the signal model for the 2-dimensional TOA measurements is utilized. The detail of TOA model can be referred to Section 2.1.1.

7.2.3 Geometric Dilution of Precision (GDOP)

The GDOP [63] associated with the position error is utilized as an index for observing the location precision of the MS under different geometric location within the networks, e.g., the cellular or the satellite networks. In general, a larger GDOP value corresponds to a comparably worse geometric layout (established by the MS and its associated BSs), which consequently results in augmented errors for location estimation. Considering the MS's location under the two-dimensional

coordinate, the GDOP value (G) obtained at the position $\boldsymbol{x}^{(t)}$ can be represented as

$$\mathrm{G}_{\boldsymbol{x}^{(t)}} = \left\{\mathrm{trace}\left[(\mathbf{H}_{\boldsymbol{x}^{(t)}}^{T}\mathbf{H}_{\boldsymbol{x}^{(t)}})^{-1}\right]\right\}^{\frac{1}{2}}, \tag{7.1}$$

where

$$\mathbf{H}_{\boldsymbol{x}^{(t)}} = \begin{bmatrix} \frac{x^{(t)}-x_1^{(t)}}{\zeta_1^{(t)}} & \frac{y^{(t)}-y_1^{(t)}}{\zeta_1^{(t)}} \\ \cdots & \cdots \\ \frac{x^{(t)}-x_i^{(t)}}{\zeta_i^{(t)}} & \frac{y^{(t)}-y_i^{(t)}}{\zeta_i^{(t)}} \\ \cdots & \cdots \\ \frac{x^{(t)}-x_{N^{(t)}}}{\zeta_{N^{(t)}}^{(t)}} & \frac{y^{(t)}-y_{N^{(t)}}}{\zeta_{N^{(t)}}^{(t)}} \end{bmatrix}. \tag{7.2}$$

It is noted that the elements within the matrix $\mathbf{H}_{\boldsymbol{x}^{(t)}}$ can be acquired from (2.2). It has been shown in [63] that the minimum GDOP value frequently occurs around the center of the network layout, e.g., the minimum GDOP inside a K-side ($K \geq 3$) regular polygon is shown to take place at the center of the layout and the value is obtained as $\mathrm{G} = \frac{2}{\sqrt{K}}$. Moreover, the GDOP value and the CRLB value are demonstrated to be identical given a Gaussian-distributed noise model [36].

7.3 Architecture Overview of Proposed PLT and GPLT Algorithms

The objective of the proposed PLT and the GPLT algorithms is to utilize the predictive information acquired from the Kalman filter to serve as the assisted measurement inputs while the environments are deficient with signal sources. Fig. 7.1 illustrates the system architectures of the KT [76], the CLT [21] and the proposed PLT/GPLT schemes. The TOA signals ($\boldsymbol{r}^{(t)}$ as in (2.1)) associated with the corresponding location set of the BSs ($\boldsymbol{P}_{BS}^{(t)}$) are obtained as the signal inputs to each of the system, which result in the estimated state vector of the MS, i.e., $\hat{\boldsymbol{s}}^{(t)} = [[\hat{\boldsymbol{x}}^{(t)}]^T, [\hat{\boldsymbol{v}}^{(t)}]^T, [\hat{\boldsymbol{a}}^{(t)}]^T]^T$ where $\hat{\boldsymbol{x}}^{(t)} = [\hat{x}^{(t)}, \hat{y}^{(t)}]^T$ represents the MS's estimated position, $\hat{\boldsymbol{v}}^{(t)} = [\hat{v}_x^{(t)}, \hat{v}_y^{(t)}]^T$ is the estimated velocity, and $\hat{\boldsymbol{a}}^{(t)} = [\hat{a}_x^{(t)}, \hat{a}_y^{(t)}]^T$ denotes the estimated acceleration.

Since the equations (i.e., (2.1) and (2.2)) associated with the network-based location estimation are intrinsically nonlinear, different mechanisms are considered within the existing algorithms for location tracking. The KT scheme [76] (as shown in Fig. 7.1.(a)) explores the linear aspect of location estimation within the Kalman filtering formulation; while the nonlinear term (i.e., $\hat{R}^{(t)} = (\hat{x}^{(t)})^2 + (\hat{y}^{(t)})^2$) is treated as an additional measurement input to the Kalman filter. It is stated within the KT scheme that the value of the nonlinear term can be obtained from an external location estimator, e.g., via the TSLS method. Consequently, the estimation accuracy of the KT algorithm greatly depends on the precision of the additional location estimator. On

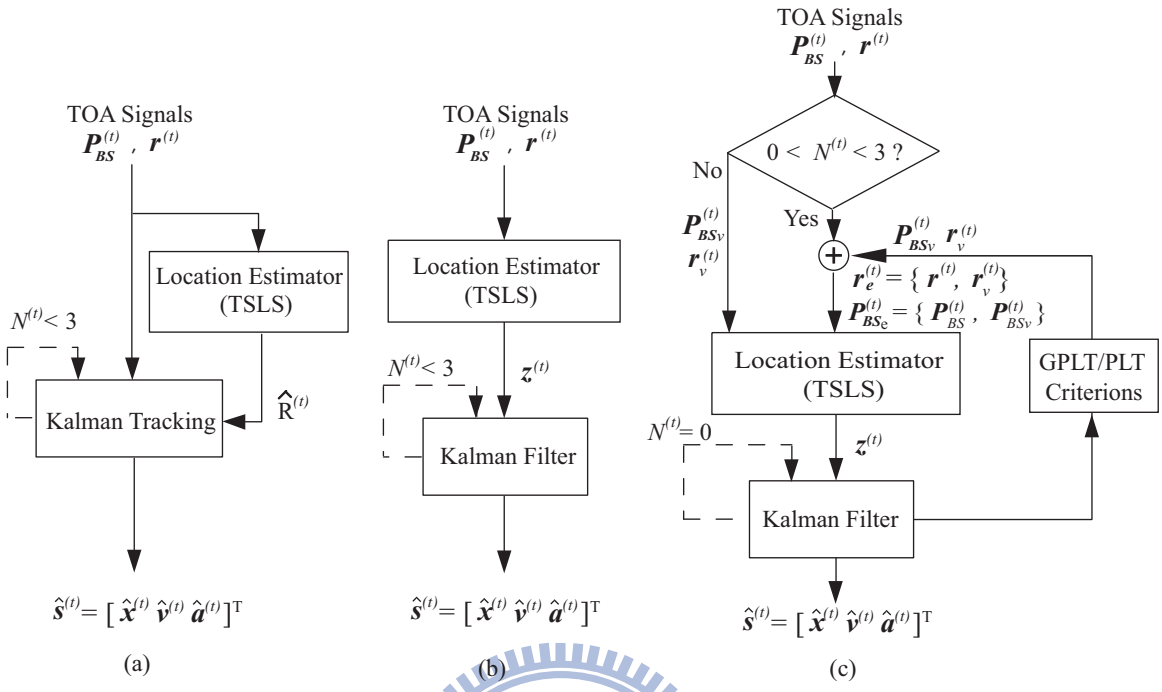

Figure 7.1: The architecture diagrams of (a) the Kalman Tracking (KT) scheme; (b) the Cascade Location Tracking (CLT) scheme; and (c) the proposed Predictive Location Tracking (PLT) and Geometry-assisted Predictive Location Tracking (GPLT) schemes

the other hand, the CLT scheme [21] (as illustrated in Fig. 7.1.(b)) adopts the TSLS method to acquire the preliminary location estimate of the MS. The Kalman Filter is utilized to smooth out the estimation error by tracing the estimated state vector $\hat{\boldsymbol{s}}^{(t)}$ of the MS.

The architecture of the proposed PLT and GPLT schemes is illustrated in Fig. 7.1.(c). It is noticed that the GPLT algorithm involves additional transformation via the GDOP calculation comparing with the PLT scheme. It can be seen that the PLT/GPLT algorithms will be the same as the CLT scheme while $N^{(t)} \geq 3$, i.e., the number of available BSs is greater than or equal to three. However, the effectiveness of the PLT/GPLT schemes is revealed as $1 \leq N^{(t)} < 3$, i.e., with deficient measurement inputs. The predictive state information obtained from the Kalman filter is utilized for acquiring the assisted information, which will be fed back into the location estimator. The extended sets for the locations of the BSs (i.e., $\boldsymbol{P}_{BS_e}^{(t)} = \{\boldsymbol{P}_{BS}^{(t)}, \boldsymbol{P}_{BS_v}^{(t)}\}$) and the measured relative distances (i.e., $\boldsymbol{r}_e^{(t)} = [\boldsymbol{r}^{(t)}, \boldsymbol{r}_v^{(t)}]$) will be utilized as the inputs to the location estimator. The sets of the virtual BS's locations $\boldsymbol{P}_{BS_v}^{(t)}$ and the virtual measurements $\boldsymbol{r}_v^{(t)}$ are defined as follows.

Definition 7.2 (Virtual Base Stations)**.** Within the PLT/GPLT formulation, the virtual Base Stations are considered as the designed locations for assisting the location tracking of the MS under the environments with deficient signal sources. The set of virtual BSs $\mathbf{P}_{BS_v}^{(t)}$ is defined under

two different numbers of $N^{(t)}$ as

$$\mathbf{P}_{BS_v}^{(t)} = \begin{cases} \{\boldsymbol{b}_{v_1}^{(t)}\} & \text{for } N^{(t)} = 2 \\ \{\boldsymbol{b}_{v_1}^{(t)},\ \boldsymbol{b}_{v_2}^{(t)}\} & \text{for } N^{(t)} = 1 \end{cases} . \tag{7.3}$$

Definition 7.3 (Virtual Measurements)**.** Within the PLT/GPLT formulation, the virtual measurements are utilized to provide assisted measurement inputs while the signal sources are insufficient. Associating with the designed set of virtual BSs $\mathbf{P}_{BS_v}^{(t)}$, the corresponding set of virtual measurements $\mathbf{r}_v^{(t)}$ is defined as

$$\mathbf{r}_v^{(t)} = \begin{cases} \{r_{v_1}^{(t)}\} & \text{for } N^{(t)} = 2 \\ \{r_{v_1}^{(t)},\ r_{v_2}^{(t)}\} & \text{for } N^{(t)} = 1 \end{cases} . \tag{7.4}$$

It is noticed that the major tasks of both the PLT and GPLT schemes are to design and to acquire the values of $\boldsymbol{P}_{BS_v}^{(t)}$ and $\boldsymbol{r}_v^{(t)}$ for the two cases (i.e., $N^{(t)} = 1$ and 2) with inadequate signal sources. In both the KT and the CLT schemes, the estimated state vector $\hat{\boldsymbol{s}}^{(t)}$ can only be updated by the internal prediction mechanism of the Kalman filter while there are insufficient numbers of BSs (i.e., $N^{(t)} < 3$ as shown in Fig. 7.1.(a) and 7.1.(b) with the dashed lines). The location estimator (i.e., the TSLS method) is consequently disabled owing to the inadequate number of the signal sources. The tracking capabilities of both schemes significantly depend on the correctness of the Kalman filter's prediction mechanism. Therefore, the performance for location tracking can be severely degraded due to the changing behavior of the MS, i.e., with the variations from the MS's acceleration.

On the other hand, the proposed PLT/GPLT algorithms can still provide satisfactory tracking performance with deficient measurement inputs, i.e., with $N^{(t)} = 1$ and 2. Under these circumstances, the location estimator is still effective with the additional virtual BSs $\boldsymbol{P}_{BS_v}^{(t)}$ and the virtual measurements $\boldsymbol{r}_v^{(t)}$, which are imposed from the predictive output of the Kalman filter (as shown in Fig. 7.1.(c)). It is also noted that the PLT/GPLT schemes will perform the same as the CLT method under the case with no signal input, i.e., under $N^{(t)} = 0$. Furthermore, the GPLT algorithm enhances the precision and the robustness of the location estimation from the PLT scheme by considering the GDOP effect, i.e., the geographic relationship between the locations of the BSs and the MS. By adopting the GPLT scheme, the locations of the virtual BSs $\boldsymbol{P}_{BS_{v,PLT}}^{(t)}$ obtained from the PLT method are adjusted into $\boldsymbol{P}_{BS_{v,GPLT}}^{(t)}$ in order to make the predicted MS possess with a minimal GDOP value. Consequently, smaller estimation errors can be acquired by exploiting the GPLT algorithm comparing with the PLT scheme. The virtual BS's location set $\boldsymbol{P}_{BS_{v,PLT}}^{(t)}$ and the virtual measurements $\boldsymbol{r}_{v,PLT}^{(t)}$ by exploiting the PLT formulation is presented in the next section; while the adjusted location set of the virtual BSs $\boldsymbol{P}_{BS_{v,GPLT}}^{(t)}$ adopting from the GPLT algorithm will be derived in Section 7.5.

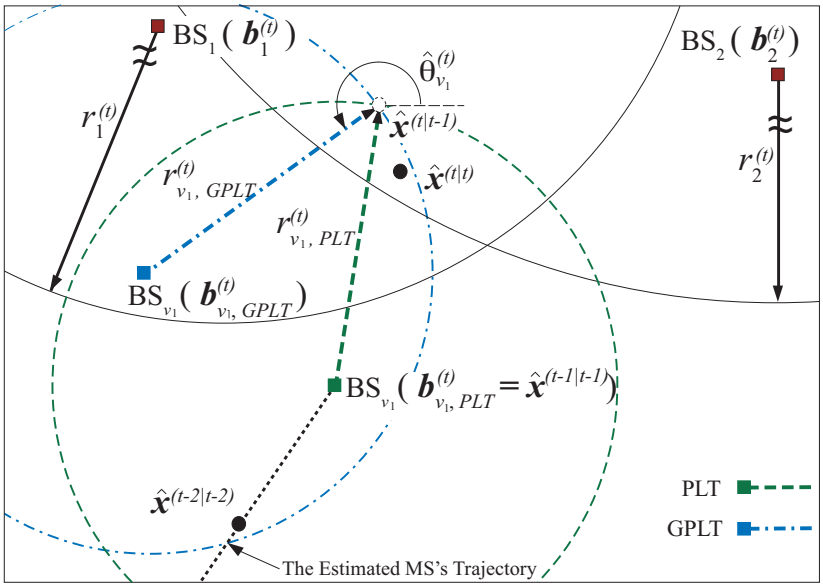

Figure 7.2: The schematic diagram of the two-BSs case for the proposed PLT and GPLT schemes

7.4 Formulation of PLT Algorithm

The proposed PLT scheme will be explained in this section. The formulation of Kalman filter can be referred to Section 2.5. Note that the position ($\hat{\boldsymbol{x}}^{(t)}$), velocity ($\hat{\boldsymbol{v}}^{(t)}$), and acceleration ($\hat{\boldsymbol{a}}^{(t)}$) tracking are considered in the Kalman filter formulation. The estimated output/state corresponds to $\hat{\boldsymbol{s}}^{(t)} = [[\hat{\boldsymbol{x}}^{(t)}]^T, [\hat{\boldsymbol{v}}^{(t)}]^T, [\hat{\boldsymbol{a}}^{(t)}]^T]^T$. The measurement vector $\boldsymbol{z}^{(t)} = [\hat{x}_T^{(t)}, \hat{y}_T^{(t)}]^T$ represents the measurement input which is obtained from the output of the TSLS estimator at the time instant t (as in Fig. 7.1.(c)). Therefore, the matrix $\mathbf{E}$ and the state transition matrix $\mathbf{F}$ can be obtained as

$$\mathbf{E} = \begin{bmatrix} 1 & 0 & 0 & 0 & 0 & 0 \\ 0 & 1 & 0 & 0 & 0 & 0 \end{bmatrix}, \tag{7.5}$$

$$\mathbf{F} = \begin{bmatrix} 1 & 0 & \Delta t & 0 & \frac{1}{2}\Delta t^2 & 0 \\ 0 & 1 & 0 & \Delta t & 0 & \frac{1}{2}\Delta t^2 \\ 0 & 0 & 1 & 0 & \Delta t & 0 \\ 0 & 0 & 0 & 1 & 0 & \Delta t \\ 0 & 0 & 0 & 0 & 1 & 0 \\ 0 & 0 & 0 & 0 & 0 & 1 \end{bmatrix}, \tag{7.6}$$

where Δt denotes the sample time interval.

7.4.1 Two-BSs Case

As shown in Fig. 7.2, it is assumed that only two BSs (i.e., BS_1 and BS_2) associated with two TOA measurements are available at the time instant t in consideration. The main target is to introduce an additional virtual BS along with its virtual measurement (i.e., $\boldsymbol{P}^{(t)}_{BS_v,PLT} = \{\boldsymbol{b}^{(t)}_{v_1,PLT}\}$ and $\boldsymbol{r}^{(t)}_{v,PLT} = \{r^{(t)}_{v_1,PLT}\}$) by acquiring the predictive output information from the Kalman filter. Knowing that there are predicting and correcting phases within the Kalman filtering formulation, the predictive state can therefore be utilized to compute the supplementary virtual measurement $r^{(t)}_{v_1,PLT}$ as

$$\begin{aligned} r^{(t)}_{v_1,PLT} &= \|\hat{\boldsymbol{x}}^{(t|t-1)} - \hat{\boldsymbol{x}}^{(t-1|t-1)}\| \\ &= \|\mathbf{E}\,\mathbf{F}\,\hat{\boldsymbol{s}}^{(t-1|t-1)} - \hat{\boldsymbol{x}}^{(t-1|t-1)}\|, \end{aligned} \tag{7.7}$$

where $\hat{\boldsymbol{x}}^{(t|t-1)}$ denotes the predicted MS's position at time instant t; while $\hat{\boldsymbol{x}}^{(t-1|t-1)}$ is the corrected (i.e., estimated) MS's position obtained at the $(t-1)$-th time instant. It is noticed that both values are available at the $(t-1)$-th time instant. The virtual measurement $r^{(t)}_{v_1,PLT}$ is defined as the distance between the previous location estimate ($\hat{\boldsymbol{x}}^{(t-1|t-1)}$) as the position of the virtual BS (i.e., BS_{v_1}: $\boldsymbol{b}^{(t)}_{v_1,PLT} \triangleq \hat{\boldsymbol{x}}^{(t-1|t-1)}$) and the predicted MS's position ($\hat{\boldsymbol{x}}^{(t|t-1)}$) as the possible position of the MS (as shown in Fig. 7.2). It is also noted that the corrected state vector $\hat{\boldsymbol{s}}^{(t-1|t-1)}$ is available at the current time instant t. However, due to the insufficient measurement input, the state vector $\hat{\boldsymbol{s}}^{(t|t)}$ is unobtainable at the t-th time instant while adopting the conventional TSLS estimator. By exploiting $r^{(t)}_{v_1,PLT}$ (in (7.7)) as the additional signal input, the measurement vector $\boldsymbol{z}^{(t)}$ can be acquired after the three measurement inputs $\boldsymbol{r}^{(t)}_e = \{r^{(t)}_1, r^{(t)}_2, r^{(t)}_{v_1,PLT}\}$ and the locations of the BSs $\boldsymbol{P}^{(t)}_{BS,e} = \{\boldsymbol{b}^{(t)}_1, \boldsymbol{b}^{(t)}_2, \boldsymbol{b}^{(t)}_{v_1,PLT}\}$ have been imposed into the TSLS estimator. As $\boldsymbol{z}^{(t)}$ has been obtained, the corrected state vector $\hat{\boldsymbol{s}}^{(t|t)}$ can be updated with the implementation of the correcting phase of the Kalman filter at the time instant t as

$$\hat{\boldsymbol{s}}^{(t|t)} = \hat{\boldsymbol{s}}^{(t|t-1)} + \mathbf{P}_{(t|t-1)}\mathbf{E}^T[\mathbf{E}\mathbf{P}^{(t|t-1)}\mathbf{E}^T + \mathbf{R}]^{-1} \cdot (\boldsymbol{z}^t - \mathbf{E}\hat{\boldsymbol{s}}^{(t|t-1)}), \tag{7.8}$$

where

$$\mathbf{P}^{(t|t-1)} = \mathbf{F}\mathbf{P}^{(t-1|t-1)}\mathbf{F}^T + \mathbf{Q}, \tag{7.9}$$

and

$$\mathbf{P}^{(t-1|t-1)} = [\,\mathbf{I} - \mathbf{P}^{(t-1|t-2)}\mathbf{E}^T\,(\mathbf{E}\mathbf{P}^{(t-1|t-2)}\mathbf{E}^T + \mathbf{R})^{-1}\mathbf{E}\,] \cdot \mathbf{P}^{(t-1|t-2)}. \tag{7.10}$$

It is noted that $\mathbf{P}^{(t|t-1)}$ and $\mathbf{P}^{(t-1|t-1)}$represent the predicted and the corrected estimation covariance within the Kalman filter. $\mathbf{I}$ in (7.10) is denoted as an identity matrix. As can been observed

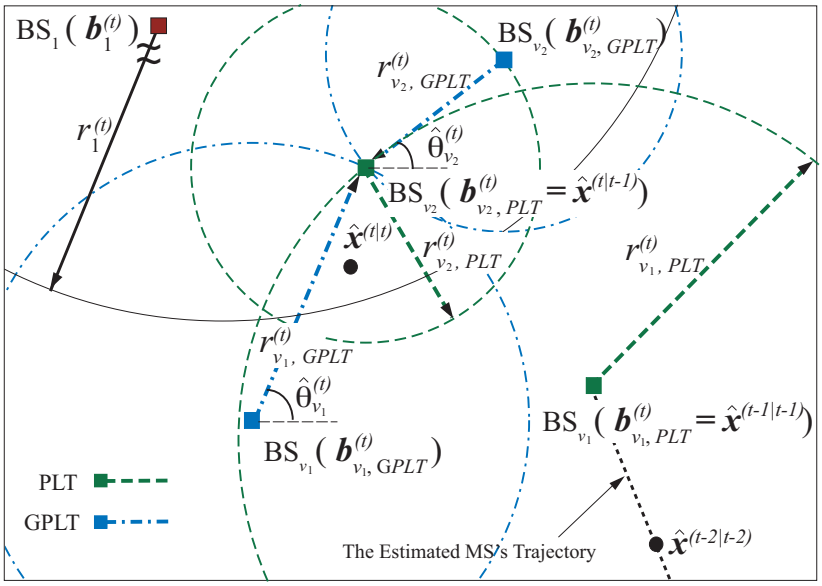

Figure 7.3: The schematic diagram of the single-BS case for the proposed PLT and GPLT schemes

from Fig. 7.2, the virtual measurement $r^{(t)}_{v_1,PLT}$ associating with the other two existing measurements $r^{(t)}_1$ and $r^{(t)}_2$ provide a confined region for the estimation of the MS's location at the time instant t, i.e., $\hat{\boldsymbol{x}}^{(t|t)}$.

7.4.2 Single-BS Case

In this case, only one BS (i.e., BS_1) with one TOA measurement input is available at the time instant t (as shown in Fig. 7.3). Two additional virtual BSs and measurements are required for the computation of the TSLS estimator, i.e., $\boldsymbol{P}^{(t)}_{BS_v,PLT} = \{\boldsymbol{b}^{(t)}_{v_1,PLT}, \boldsymbol{b}^{(t)}_{v_2,PLT}\}$ and $\boldsymbol{r}^{(t)}_{v,PLT} = \{r^{(t)}_{v_1,PLT}, r^{(t)}_{v_2,PLT}\}$. Similar to the previous case, the first virtual measurement $r^{(t)}_{v_1,PLT}$ is acquired as in (7.7) by considering $\hat{\boldsymbol{x}}^{(t-1|t-1)}$ as the position of the first virtual BS (i.e., $\boldsymbol{b}^{(t)}_{v_1,PLT} = \hat{\boldsymbol{x}}^{(t-1|t-1)}$) with the predicted MS's position (i.e., $\hat{\boldsymbol{x}}_{(t|t-1)}$) as the possible position of the MS. On the other hand, the second virtual BS's position is assumed to locate at the predicted MS's position (i.e., $\boldsymbol{b}^{(t)}_{v_2,PLT} \triangleq \hat{\boldsymbol{x}}^{(t|t-1)}$) as illustrated in Fig. 7.3. The corresponding second virtual measurement $r^{(t)}_{v_2,PLT}$ is defined as the average prediction error obtained from the Kalman filtering formulation by accumulating the previous time steps as

$$r^{(t)}_{v_2,PLT} = \frac{1}{t-1}\sum_{i=1}^{t-1} \|\hat{\boldsymbol{x}}^{(i|i)} - \hat{\boldsymbol{x}}^{(i|i-1)}\|. \tag{7.11}$$

It is noted that $r^{(t)}_{v_2,PLT}$ is obtained as the mean prediction error until the $(t-1)$-th time instant. In the case while the Kalman filter is capable of providing sufficient accuracy in its prediction phase,

the virtual measurement $r_{v_2,PLT}^{(t)}$ may approach zero value. Associating with the single measurement $r_1^{(t)}$ from BS_1, the two additional virtual measurements $r_{v_1,PLT}^{(t)}$ (centered at $\hat{\boldsymbol{x}}^{(t-1|t-1)}$) and $r_{v_2,PLT}^{(t)}$ (centered at $\hat{\boldsymbol{x}}^{(t|t-1)}$) result in a constrained region (as in Fig. 7.3) for location estimation of the MS under the environments with insufficient signal sources.

It is also noticed that the variations of the measurement inputs are the required information for adopting the TSLS estimator. It utilizes the signal variation as an indicator to consider the weighting factor for a specific signal source, i.e., smaller weighting coefficient should be assigned to a measurement input if it encompasses comparably larger signal variations. The weighted least square algorithm can therefore be performed within the TSLS estimator according to the designated weighting values associated with the signal sources. Similar concept can be exploited to assign the weighting coefficients for the virtual measurements. The virtual measurements can be represented as

$$r_{v_i}^{(t)} = \zeta_{v_i}^{(t)} + n_{v_i}^{(t)}, \qquad \text{for } i = 1,\ 2, \tag{7.12}$$

where $\zeta_{v_i}^{(t)}$ is denoted as the deterministic noiseless virtual measurement; while $n_{v_i}^{(t)}$ represents the *virtual noise* (i.e., the component with randomness) associated with the virtual measurement $r_{v_i}^{(t)}$. The following Lemma illustrates that the resulted virtual noises $n_{v_i}^{(t)}$ are considered zero-mean random variables.

Lemma 7.1. *Based on the definition of the virtual measurements $r_{v_i,PLT}^{(t)}$ as in (7.7) and (7.11), the corresponding virtual noises become zero-mean random variables.*

Proof. The first virtual measurement $r_{v_1,PLT}^{(t)}$ as proposed in (7.7) is considered first. Based on (7.12), the virtual noise $n_{v_1,PLT}^{(t)}$ associated with $r_{v_1,PLT}^{(t)}$ can be written as

$$\begin{aligned} n_{v_1,PLT}^{(t)} &= r_{v_i,PLT}^{(t)} - \zeta_{v_i,PLT}^{(t)} \\ &= \|\hat{\boldsymbol{x}}^{(t|t-1)} - \hat{\boldsymbol{x}}^{(t-1|t-1)}\| - \|\boldsymbol{x}^{(t)} - \hat{\boldsymbol{x}}^{(t-1|t-1)}\|. \end{aligned} \tag{7.13}$$

It is noted that that both the variables $\hat{\boldsymbol{x}}^{(t|t-1)}$ and $\hat{\boldsymbol{x}}^{(t-1|t-1)}$ are acquired from the Kalman filtering formulation. The primary target of the Kalman filter is to achieve zero mean estimation errors, i.e., $E[\boldsymbol{x}^{(t)} - \hat{\boldsymbol{x}}^{(t|t)}] = E[\boldsymbol{x}^{(t)} - \hat{\boldsymbol{x}}^{(t|t-1)}] = 0$. It can consequently be obtained that $E[\boldsymbol{x}^{(t)}] = E[\hat{\boldsymbol{x}}^{(t|t)}] = E[\hat{\boldsymbol{x}}^{(t|t-1)}]$ as the estimation errors are converged. Considering that the variables $\boldsymbol{x}^{(t)}$, $\hat{\boldsymbol{x}}^{(t|t)}$, and $\hat{\boldsymbol{x}}^{(t|t-1)}$ possess the same probability distribution, the expected value of the first virtual noise can therefore be rewritten as $E[n_{v_1,PLT}^{(t)}] = E[\|\hat{\boldsymbol{x}}^{(t|t-1)} - \hat{\boldsymbol{x}}^{(t-1|t-1)}\|] - E[\|\boldsymbol{x}^{(t)} - \hat{\boldsymbol{x}}^{(t-1|t-1)}\|] = \|E[\hat{\boldsymbol{x}}^{(t|t-1)}] - E[\hat{\boldsymbol{x}}^{(t-1|t-1)}]\| - \|E[\boldsymbol{x}^{(t)}] - E[\hat{\boldsymbol{x}}^{(t-1|t-1)}]\| = \|E[\boldsymbol{x}^{(t)}] - E[\hat{\boldsymbol{x}}^{(t-1|t-1)}]\| - \|E[\boldsymbol{x}^{(t)}] - E[\hat{\boldsymbol{x}}_{(t-1|t-1)}]\| = 0$. The result shows that the first virtual measurement $r_{v_i,PLT}^{(t)}$ is possessed with the virtual noise $n_{v_1,PLT}^{(t)}$ with zero mean value.

Similarly, the virtual noise $n_{v_2,PLT}^{(t)}$ associated with the second virtual measurement $r_{v_2,PLT}^{(t)}$ (in

(7.11)) can be expressed as

$$\begin{aligned} n_{v_2,PLT}^{(t)} &= r_{v_2,PLT}^{(t)} - \zeta_{v_2,PLT}^{(t)} \\ &= \left[\frac{1}{t-1}\sum_{i=1}^{t-1}\|\hat{\boldsymbol{x}}^{(i|i)} - \hat{\boldsymbol{x}}^{(i|i-1)}\|\right] - \|\boldsymbol{x}^{(t)} - \hat{\boldsymbol{x}}^{(t|t-1)}\| \end{aligned} \tag{7.14}$$

Based on the same estimation objective by adopting the Kalman filter, the expected value of the virtual noise $n_{v_2,PLT}^{(t)}$ is obtained as $E[n_{v_2,PLT}^{(t)}] = \frac{1}{t-1}\sum_{i=1}^{t-1}E[\|\hat{\boldsymbol{x}}^{(i|i)} - \hat{\boldsymbol{x}}^{(i|i-1)}\|] - E[\|\boldsymbol{x}^{(t)} - \hat{\boldsymbol{x}}^{(t|t-1)}\|] = \frac{1}{t-1}\sum_{i=1}^{t-1}\|E[\hat{\boldsymbol{x}}^{(t|t)}] - E[\hat{\boldsymbol{x}}^{(t|t-1)}]\| - \|E[\boldsymbol{x}^{(t)}] - E[\hat{\boldsymbol{x}}^{(t|t-1)}]\| = 0$. The result indicates that the virtual noise $n_{v_2,PLT}^{(t)}$ associated with the second virtual measurement is acquired as a zero mean random variable. This completes the proof. □

It is noticed that the zero-mean characteristics of the virtual noises (as was proved in Lemma 7.1) will be utilized as a property for Lemma 7.2 in the next section. Based on (7.7), the signal variation of $r_{v_1,PLT}^{(t)}$ is considered as the variance of the predicted distance $\|\hat{\boldsymbol{x}}^{(t|t-1)} - \hat{\boldsymbol{x}}^{(t-1|t-1)}\|$ between the previous $(t-1)$ time instants. Associated with the result obtained from Lemma 7.1, the virtual noise $n_{v_1}^{(t)}$ is regarded as zero mean with variance $\sigma^2_{n_{v_1}^{(t)}} = \mathrm{Var}(r_{v_1,PLT}^{(t)}) = \mathrm{Var}(\|\hat{\boldsymbol{x}}^{(t|t-1)} - \hat{\boldsymbol{x}}^{(t-1|t-1)}\|)$. Similarly, since the signal variation of the second virtual measurement $r_{v_2,PLT}^{(t)}$ is obtained as the variance of the averaged prediction errors (as in (7.11)), the associated virtual noise $n_{v_2,k}$ can also be considered as zero mean with variance $\sigma^2_{n_{v_2}^{(t)}} = \mathrm{Var}(r_{v_2,PLT}^{(t)})$. Consequently, the variances of the virtual noises (i.e., $\sigma^2_{n_{v_1}^{(t)}}$ and $\sigma^2_{n_{v_2}^{(t)}}$) will be exploited as the weighting coefficients within the formulation of the TSLS estimator.

7.5 Formulation of GPLT Algorithm

As was explained in Subsection 7.2.3, the geometric relationship between the MS and its associated BSs (i.e., indicated by the corresponding GDOP value) will affect the precision for location estimation and tracking. The concept of the proposed GPLT scheme is to adjust the positions of the virtual BSs such that the predicted MS will consequently be possessed with a smaller GDOP value based on the newly formed geometric layout. The modified positions of the virtual BSs will therefore be adopted associated with the existing BSs for location estimation. Similarly, the two-BSs and the single-BS cases are considered for the GPLT algorithm as follows.

7.5.1 Two-BSs Case

In this case, the primary target for the GPLT scheme is to design the location of the virtual BS, i.e., BS_{v_1}: $\boldsymbol{b}_{v_1,GPLT}^{(t)}$. As shown in Fig. 7.2, two parameters (i.e., the distance $r_{v_1,GPLT}^{(t)}$ and the angle $\theta_{v_1}^{(t)}$) with respect to the predicted MS's position $\hat{\boldsymbol{x}}^{(t|t-1)}$ are introduced to represent the

designed virtual BS's position $\boldsymbol{b}_{v_1,GPLT}^{(t)}$. The selection of these two parameters within the GPLT algorithm is explained in the following subsections.

7.5.1.1 Computation of Angle

The main objective of the GPLT scheme is to acquire the angle $\theta_{v_1}^{(t)}$ of $\boldsymbol{b}_{v_1,GPLT}^{(t)}$ such that the predicted MS ($\hat{\boldsymbol{x}}^{(t|t-1)}$) will possess a minimal GDOP value within its network topology for location estimation. As illustrated in Fig. 7.2, the following equality can be obtained based on the geometric relationship

$$\hat{\boldsymbol{x}}^{(t|t-1)} - \boldsymbol{b}_{v_1,GPLT}^{(t)} = (-r_{v_1,GPLT}^{(t)} \cdot \cos\theta_{v_1}^{(t)},\ -r_{v_1,GPLT}^{(t)} \cdot \sin\theta_{v_1}^{(t)}). \tag{7.15}$$

It is noticed that the angle θ_k is rotated from the positive x-axis based on the predicted MS ($\hat{\boldsymbol{x}}^{(t|t-1)}$). As mentioned above, the position of the virtual BS ($\boldsymbol{b}_{v_1,GPLT}^{(t)}$) is designed such that the predicted MS ($\hat{\boldsymbol{x}}^{(t|t-1)}$) will be located at a minimal GDOP position based on the extended geometric set $\boldsymbol{P}_{BS_e}^{(t)} = \{\boldsymbol{b}_1^{(t)},\ \boldsymbol{b}_2^{(t)},\ \boldsymbol{b}_{v_1,GPLT}^{(t)}\}$. By incorporating (7.15) into (7.1) and (7.2), the GDOP value (i.e., $\mathrm{G}_{\hat{\boldsymbol{x}}^{(t|t-1)}}$) computed at the predicted MS's position $\hat{\boldsymbol{x}}^{(t|t-1)} = (\hat{x}^{(t|t-1)},\ \hat{y}^{(t|t-1)})$ can be obtained. The associated matrix $\mathbf{H}_{\hat{\boldsymbol{x}}^{(t|t-1)}}$ becomes

$$\mathbf{H}_{\hat{\boldsymbol{x}}^{(t|t-1)}} = \begin{bmatrix} \frac{\hat{x}^{(t|t-1)}-x_1^{(t)}}{r_1^{(t)}} & \frac{\hat{y}^{(t|t-1)}-y_1^{(t)}}{r_1^{(t)}} \\ \frac{\hat{x}^{(t|t-1)}-x_2^{(t)}}{r_2^{(t)}} & \frac{\hat{y}^{(t|t-1)}-y_2^{(t)}}{r_2^{(t)}} \\ \frac{\hat{x}^{(t|t-1)}-x_{v_1,GPLT}^{(t)}}{r_{v_1,GPLT}^{(t)}} & \frac{\hat{y}^{(t|t-1)}-y_{v_1,GPLT}^{(t)}}{r_{v_1,GPLT}^{(t)}} \end{bmatrix} = \begin{bmatrix} \frac{\hat{x}^{(t|t-1)}-x_1^{(t)}}{r_1^{(t)}} & \frac{\hat{y}^{(t|t-1)}-y_1^{(t)}}{r_1^{(t)}} \\ \frac{\hat{x}^{(t|t-1)}-x_2^{(t)}}{r_2^{(t)}} & \frac{\hat{y}^{(t|t-1)}-y_2^{(t)}}{r_2^{(t)}} \\ -\cos\theta_{v_1}^{(t)} & -\sin\theta_{v_1}^{(t)} \end{bmatrix}. \tag{7.16}$$

It is noted that the noiseless relative distances $\zeta_i^{(t)}$ in (7.1) are approximately replaced by $r_i^{(t)}$ in (7.16) since $\zeta_i^{(t)}$ are considered unattainable. It can be observed from (7.16) that the matrix $\mathbf{H}_{\hat{\boldsymbol{x}}^{(t|t-1)}}$ associated with the resulting $\mathrm{G}_{\hat{\boldsymbol{x}}^{(t|t-1)}}$ value are regarded as functions of the angle $\theta_{v_1}^{(t)}$, i.e., $\mathbf{H}_{\hat{\boldsymbol{x}}^{(t|t-1)}}(\theta_{v_1}^{(t)})$ and $\mathrm{G}_{\hat{\boldsymbol{x}}^{(t|t-1)}}(\theta_{v_1}^{(t)})$. Based on the objective of the GPLT scheme, the angle $\hat{\theta}_{v_1}^{(t)}$ which results in the minimal GDOP value can therefore be acquired as

$$\hat{\theta}_{v_1}^{(t)} = \arg \min_{\forall\theta_{v_1}^{(t)}} \mathrm{G}_{\hat{\boldsymbol{x}}^{(t|t-1)}}(\theta_{v_1}^{(t)}). \tag{7.17}$$

It is intuitive to observed that (7.17) can be achieved if the following conditions on the first and second derivatives of $\mathrm{G}_{\hat{\boldsymbol{x}}^{(t|t-1)}}(\theta_{v_1}^{(t)})$ are satisfied:

$$\left[\frac{\partial \mathrm{G}_{\hat{\boldsymbol{x}}^{(t|t-1)}}(\theta_{v_1}^{(t)})}{\partial\theta_{v_1}^{(t)}}\right]_{\theta_{v_1}^{(t)}=\hat{\theta}_{v_1}^{(t)}} = 0 \tag{7.18}$$

$$\left[\frac{\partial^2 \mathrm{G}_{\hat{\boldsymbol{x}}^{(t|t-1)}}(\theta_{v_1}^{(t)})}{\partial(\theta_{v_1}^{(t)})^2}\right]_{\theta_{v_1}^{(t)}=\hat{\theta}_{v_1}^{(t)}} > 0 \tag{7.19}$$

By substituting (7.16) and (7.1) into (7.18), the angle $\hat{\theta}_{v_1}^{(t)}$ can be computed as

$$\hat{\theta}_{v_1}^{(t)} = \tan^{-1}\left(\frac{1 \pm \sqrt{1+\Gamma^2}}{\Gamma}\right), \tag{7.20}$$

where Γ is derived as

$$\Gamma = \frac{2[(r_2^{(t)})^2(\hat{x}^{(t|t-1)} - x_1^{(t)})(\hat{y}^{(t|t-1)} - y_1^{(t)}) + (r_1^{(t)})^2(\hat{x}^{(t|t-1)} - x_2^{(t)})(\hat{y}^{(t|t-1)} - y_2^{(t)})]}{(r_2^{(t)})^2(\hat{x}^{(t|t-1)} - x_1^{(t)})^2 - (r_2^{(t)})^2(\hat{y}_{(t|t-1)} - y_1^{(t)})^2 + (r_1^{(t)})^2(\hat{x}_{(t|t-1)} - x_2^{(t)})^2 - (r_1^{(t)})^2(\hat{y}^{(t|t-1)} - y_2^{(t)})^2}. \tag{7.21}$$

It is noted that the selection for either the positive or the negative value of $\hat{\theta}_{v_1}^{(t)}$ is determined by (7.19). At each time instant t, the relative angle $\hat{\theta}_{v_1}^{(t)}$ between $\hat{\boldsymbol{x}}^{(t|t-1)}$ and $\boldsymbol{b}_{v_1,GPLT}^{(t)}$ can therefore be obtained such that $\hat{\boldsymbol{x}}^{(t|t-1)}$ is located at the position with a minimal GDOP value based on its current network layout.

Moreover, it is important to observe from (7.20) and (7.21) that the angle $\hat{\theta}_{v_1}^{(t)}$ is independent to the virtual measurement $r_{v_1,GPLT}^{(t)}$. In other words, considering the two-BS case with one adjustable virtual BS, the distance $r_{v_1,GPLT}^{(t)}$ can arbitrarily be chosen along the direction with angle $\hat{\theta}_{v_1}^{(t)}$ and consequently the minimal GDOP for $\hat{\boldsymbol{x}}^{(t|t-1)}$ is still attained. However, this result does not guarantee the independency between the virtual distance $r_{v_1,GPLT}^{(t)}$ and the estimation errors. In the next subsection, the distance effect to the location estimation errors will further be evaluated.

7.5.1.2 Selection of Distance

In this subsection, the virtual measurement $r_{v_1,GPLT}^{(t)}$ will be determined, which can be utilized for acquiring the position of the virtual BS $\boldsymbol{b}_{v_1,GPLT}^{(t)}$. It is observed in (7.16) that the GDOP value at the predicted MS's position is primarily dominated by the relative angle (i.e., $\theta_{v_1}^{(t)}$) between the MS and the BSs; while the distance information (i.e., $r_{v_1,GPLT}^{(t)}$) is considered uninfluential to the GDOP value. This uncorrelated relationship between the GDOP value and the relative distance has also been observed as in [63]. The following Lemma shows that the selection of the virtual distance $r_{v_1,GPLT}^{(t)}$ becomes insignificant for the WLS-based location estimation.

Lemma 7.2. *A time-based location estimation problem is considered for the MS using the Weighted Least Square (WLS) algorithm. Assuming that a measurement input obtained from a specific BS is associated with zero mean random noises, the expected value of the location estimation error is independent to the distance between the specific BS and the MS.*

Proof. Considering three TOA measurements are available for estimating the MS's position (as described in (2.1) with $N^{(t)} = 3$), it is assumed that the third TOA measurement $r_3^{(t)}$ is only

contaminated by random noises with zero mean value, i.e., $E[n_3^{(t)}] = 0$ and $e_3^{(t)} = 0$ in (2.1). The target of this proof is to illustrate that the expected value of the estimation error resulting from the WLS method is independent to the magnitude of the measurement input $r_3^{(t)}$. Note that the detail formulation of the WLS can be referred to Section 2.3. The primary concern of this proof is to acquire the expected value of the estimation error $\Delta\hat{\boldsymbol{x}}^{(t)} = [\Delta\hat{x}^{(t)},\, \Delta\hat{y}^{(t)}]^T$, which can be obtained as

$$\Delta\hat{\boldsymbol{x}}^{(t)} = \mathbf{C}([\mathbf{M}_1^{(t)}]^T\boldsymbol{\Psi}_1^{-1}\mathbf{M}_1^{(t)})^{-1}[\mathbf{M}_1^{(t)}]^T\boldsymbol{\Psi}_1^{-1}\Delta\mathbf{J}_1^{(t)} \tag{7.22}$$

Note that (7.22) indicates that the estimation error vector $\Delta\hat{\boldsymbol{x}}^{(t)}$ is incurred by the variation within the vector $\mathbf{J}^{(t)}$. The value of $\Delta\mathbf{J}^{(t)}$ is obtained by considering the variations from the measurement inputs as in (2.1))

$$\Delta\mathbf{J}^{(t)} = \begin{bmatrix} 2\zeta_1^{(t)}\,(n_1^{(t)} + e_1^{(t)}) + (n_1^{(t)} + e_1^{(t)})^2 \\ 2\zeta_2^{(t)}\,(n_2^{(t)} + e_2^{(t)}) + (n_2^{(t)} + e_2^{(t)})^2 \\ 2\zeta_3^{(t)}\,n_3^{(t)} + (n_3^{(t)})^2 \end{bmatrix} \simeq \begin{bmatrix} 2\zeta_1^{(t)}\,(n_1^{(t)} + e_1^{(t)}) \\ 2\zeta_2^{(t)}\,(n_2^{(t)} + e_2^{(t)}) \\ 2\zeta_3^{(t)}\,n_3^{(t)} \end{bmatrix}, \tag{7.23}$$

where $e_3^{(t)}$ equals to zero as mentioned at the beginning of this proof. It is noted that the approximation from the second equality within (7.23) is valid by considering that the noiseless distance $\zeta_i^{(t)}$ is in general larger than the combined noise effect $(n_i^{(t)} + e_i^{(t)})$. For simplicity and without lose of generality, coordinate transformation can be adopted within (7.22) such that $[x_1^{(t)},\, y_1^{(t)}]^T = [0, 0]^T$. The expected value of the estimation error (i.e., $\Delta\hat{\boldsymbol{x}}^{(t)} = [\Delta\hat{x}^{(t)},\, \Delta\hat{y}^{(t)}]^T$) can therefore be acquired by expanding (7.22) as (7.24) and (7.25)

$$\begin{aligned} E[\Delta\hat{x}^{(t)}] &= E\left[\frac{\zeta_1^{(t)}(n_1^{(t)} + e_1^{(t)})(y_2^{(t)} - y_3^{(t)}) + \zeta_2^{(t)}(n_2^{(t)} + e_2^{(t)})y_3^{(t)} - \zeta_3^{(t)}n_3^{(t)}y_2^{(t)}}{x_3^{(t)}y_2^{(t)} - x_2^{(t)}y_3^{(t)}}\right] \\ &= E\left[\frac{\zeta_1^{(t)}(n_1^{(t)} + e_1^{(t)})(y_2^{(t)} - y_3^{(t)}) + \zeta_2^{(t)}(n_2^{(t)} + e_2^{(t)})y_3^{(t)}}{x_3^{(t)}y_2^{(t)} - x_2^{(t)}y_3^{(t)}}\right] \end{aligned} \tag{7.24}$$

$$\begin{aligned} E[\Delta\hat{y}^{(t)}] &= E\left[\frac{\zeta_1^{(t)}(n_1^{(t)} + e_1^{(t)})(x_2^{(t)} - x_3^{(t)}) + \zeta_{2^{(t)}}(n_2^{(t)} + e_2^{(t)})x_3^{(t)} - \zeta_3^{(t)}n_3^{(t)}x_2^{(t)}}{y_3^{(t)}x_2^{(t)} - y_2^{(t)}x_3^{(t)}}\right] \\ &= E\left[\frac{\zeta_1^{(t)}(n_1^{(t)} + e_1^{(t)})(x_2^{(t)} - x_3^{(t)}) + \zeta_2^{(t)}(n_2^{(t)} + e_2^{(t)})x_3^{(t)}}{y_3^{(t)}x_2^{(t)} - y_2^{(t)}x_3^{(t)}}\right] \end{aligned} \tag{7.25}$$

It is noted that the second equalities for both (7.24) and (7.25) are attained based on the assumption that $E[n_{3,k}] = 0$. From (7.24) and (7.25), it can clearly be observed that the expected value of the estimation error (i.e., $E[\Delta\hat{\boldsymbol{x}}^{(t)}] = \left[E[\Delta\hat{x}^{(t)}],\, E[\Delta\hat{y}^{(t)}]\right]^T$) is independent to the measured distance $r_3^{(t)}$ under the assumption that its associated measurement noise $n_3^{(t)}$ is considered a zero mean

random variable, i.e., $E[r_3^{(t)}] = E[\zeta_3^{(t)}] + E[n_3^{(t)}] = E[\zeta_3^{(t)}]$. This completes the proof. □

This lemma states that the expected value of the location estimation error is independent to the distance between a specific BS to the MS if the noises associated with the measurement inputs are statistically distributed with a zero mean value. In generic time-based location estimation, the phenomenon stated in Lemma 7.2 does not usually exist since most of the measurement inputs are contaminated with NLOS noises, i.e., $e_i^{(t)}$ in (2.1) is randomly distributed with positive mean value. The NLOS error is augmented as the distance between the specific BS and the MS is increased, which causes the corresponding measurement input to become unreliable comparing with the other signal sources. This result is consistent with the intuition that BSs with closer distances to the MS are always selected for location estimation. In the proposed GPLT scheme, however, the virtual measurement $r_{v_1,GPLT}^{(t)}$ is considered as a designed distance which is infected by its corresponding virtual noise $n_{v_1,GPLT}^{(t)}$ with zero mean value (as can be obtained from Lemma 7.1). Based on Lemma 7.2, the selection of the distance $r_{v_1,GPLT}^{(t)}$ becomes uninfluential to the estimation error while exploiting the WLS algorithm for location estimation. This result is similar to the derived GDOP value that is unrelated to the distance information between the BSs and the MS (as can be observed from (7.16)). In the simulation section, the uncorrelated relationship between $r_{v_1,GPLT}^{(t)}$ and the estimation error will further be validated by exploiting the TSLS estimator, which is considered one of the the WLS-based algorithms for location estimation. It will be demonstrated via the simulation results that the influence from the length of the virtual measurement to the estimation error is considered insignificant.

The procedures of the proposed GPLT scheme under the two-BSs case is explained as follows. The target is to obtain the position of the MS at the time instant t (i.e., $\hat{\boldsymbol{x}}^{(t|t)}$) based on the available information, including the measurement and location information acquired from both BS_1 and BS_2 along with the predicted position of the MS (i.e., $\hat{\boldsymbol{x}}^{(t|t-1)}$). Two steps are involved within the proposed GPLT scheme: (i) the determination of the virtual BS's position and the virtual measurement; and (ii) the estimation and tracking of the MS's position. As shown in Fig. 7.2, the orientation of the virtual BS ($\hat{\theta}_{v_1}^{(t)}$) relative to the predicted MS's position $\hat{\boldsymbol{x}}^{(t|t-1)}$ is determined based on the criterion of minimizing the GDOP value on $\hat{\boldsymbol{x}}^{(t|t-1)}$ (as obtained from (7.17) and (7.20)). As was indicated by Lemma 7.2, the selection of the virtual distance $r_{v_1,GPLT}^{(t)}$ with respect to the predicted MS's position $\hat{\boldsymbol{x}}^{(t|t-1)}$ is considered insignificant to the estimation errors. Therefore, the distance is selected the same value as was designed in the PLT algorithm, i.e., $r_{v_1,GPLT}^{(t)} = r_{v_1,PLT}^{(t)}$ as in (7.7). The location of the virtual BS ($\boldsymbol{b}_{v_1,GPLT}^{(t)}$) and the length of the virtual measurement ($r_{v_1,GPLT}^{(t)}$) can consequently be acquired. It is also noticed that the design of the virtual noise can therefore be selected the same as that in the PLT scheme, i.e., zero mean random distributed with variance $\sigma^2_{n_{v_1}^{(t)}} = \mathrm{Var}(r_{v_1,PLT}^{(t)}) = \mathrm{Var}(\|\hat{\boldsymbol{x}}^{(t|t-1)} - \hat{\boldsymbol{x}}^{(t-1|t-1)}\|)$.

After acquiring the information of the virtual BS as the additional signal source, the extended sets of the BSs and the measurement inputs can be established as $\boldsymbol{P}_{BS_e}^{(t)} = \{\boldsymbol{b}_1^{(t)}, \boldsymbol{b}_2^{(t)}, \boldsymbol{b}_{v_1,GPLT}^{(t)}\}$

and $\boldsymbol{r}_e^{(t)} = \{r_1^{(t)}, r_2^{(t)}, r_{v_1,GPLT}^{(t)}\}$. As illustrated in Fig. 7.1.(c), the extended set of signal sources are utilized as the inputs to the TSLS estimator. The estimated MS's position $\hat{\boldsymbol{x}}^{(t|t)}$ can therefore be obtained by adopting the correcting phase of the Kalman filter, which completes the location estimation and tracking processes at the t-th time instant.

7.5.2 Single-BS Case

As illustrated in Fig. 7.3, only one BS ($\boldsymbol{b}_1^{(t)}$) associated with the measurement input $r_1^{(t)}$ is available at the considered t-th time instant. Additional two virtual BSs associated with their virtual measurements are required as the inputs for the TSLS estimator, i.e., $\boldsymbol{P}_{BS_v,GPLT}^{(t)} = \{\boldsymbol{b}_{v_1,GPLT}^{(t)}, \boldsymbol{b}_{v_2,GPLT}^{(t)}\}$ and $\boldsymbol{r}_{v,GPLT}^{(t)} = \{r_{v_1,GPLT}^{(t)}, r_{v_2,GPLT}^{(t)}\}$. By adopting similar concept as stated in Section 7.5.1, the following equations can be obtained based on the geometric relationships from Fig. 7.3,

$$\hat{\boldsymbol{x}}^{(t|t-1)} - \boldsymbol{b}_{v_1,GPLT}^{(t)} = (-r_{v_1,GPLT}^{(t)} \cdot \cos\theta_{v_1}^{(t)}, -r_{v_1,GPLT}^{(t)} \cdot \sin\theta_{v_1}^{(t)}), \tag{7.26}$$

$$\hat{\boldsymbol{x}}^{(t|t-1)} - \boldsymbol{b}_{v_2,GPLT}^{(t)} = (-r_{v_2,GPLT}^{(t)} \cdot \cos\theta_{v_2}^{(t)}, -r_{v_2,GPLT}^{(t)} \cdot \sin\theta_{v_2}^{(t)}). \tag{7.27}$$

Based on (7.26) and (7.27), it can be observed that the design concept of the GPLT scheme for the single-BS case is to obtain the feasible locations for both $\boldsymbol{b}_{v_1,GPLT}^{(t)}$ and $\boldsymbol{b}_{v_2,GPLT}^{(t)}$ by rotating around the predicted MS's location $\hat{\boldsymbol{x}}^{(t|t-1)}$. For fair comparison, the two virtual measurements are designed to be the same as that utilized in the PLT scheme, i.e., $\boldsymbol{r}_{v,GPLT}^{(t)} = \{r_{v_1,PLT}^{(t)}, r_{v_2,PLT}^{(t)}\}$ as in (7.7) and (7.11). The two rotating angles $\theta_{v_1}^{(t)}$ and $\theta_{v_2}^{(t)}$ that are designed to be hinged at the predicted MS's location $\hat{\boldsymbol{x}}^{(t|t-1)}$ will be sequentially determined as follows. First of all, as shown in Fig. 7.3, the position of the second virtual BS ($\boldsymbol{b}_{v_2,GPLT}^{(t)}$) is designed at a location with distance $r_{v_2,GPLT}^{(t)}$ relative to the predicted MS's position $\hat{\boldsymbol{x}}^{(t|t-1)}$. It is noted that the position of the first virtual BS that is designed from the PLT scheme (i.e., $\boldsymbol{b}_{v_1,PLT}^{(t)} = \hat{\boldsymbol{x}}^{(t-1|t-1)}$) is assigned as the preliminary position for the first virtual BS, i.e., $\boldsymbol{b}_{v_1,GPLT}^{(t)} = \boldsymbol{b}_{v_1,PLT}^{(t)}$. Based on the information acquired from $\text{BS}_1(\boldsymbol{b}_1^{(t)})$ and $\boldsymbol{b}_{v_1,PLT}^{(t)}$ associated with the predicted MS's position $\hat{\boldsymbol{x}}^{(t|t-1)}$, the rotating angle $\hat{\theta}_{v_2}^{(t)}$ for the second virtual BS can be acquired as in (7.20). After the angle $\hat{\theta}_{v_2}^{(t)}$ has been obtained, the position of the second virtual BS ($\boldsymbol{b}_{v_2,GPLT}^{(t)}$) becomes available as in (7.27). Same procedure based on (7.20) can be adopted to obtained the rotating angle $\hat{\theta}_{v_1}^{(t)}$ of the first virtual BS, where the available information includes $\boldsymbol{b}_1^{(t)}$ and $\boldsymbol{b}_{v_2,GPLT}^{(t)}$ associated with the predicted MS's position $\hat{\boldsymbol{x}}^{(t|t-1)}$. Consequently, the positions for both of the virtual measurements $\boldsymbol{b}_{v_1,GPLT}^{(t)}$ and $\boldsymbol{b}_{v_2,GPLT}^{(t)}$ can be determined.

Based on intuitive observation and the computation of GDOP value from (7.1), a comparable larger GDOP occurs if the geometric layout formed by the three BSs is approximately collinear, i.e., less than 5° in one of the triangular angle. This situation in general happens by adopting the PLT scheme under the single-BS case, especially under the situation while the MS is moving along

the same direction for a certain time interval. As shown in Fig. 7.3, the designed positions of the virtual BSs, i.e., $\boldsymbol{b}_{v_1,PLT}^{(t)}$ and $\boldsymbol{b}_{v_2,PLT}^{(t)}$, are observed to be collinear with the measurement input $\text{BS}_1(\boldsymbol{b}_1^{(t)})$. The benefits for exploiting the GPLT scheme can be revealed in consideration of the collinearity problem. With the computation of the angle $\hat{\theta}_{v_2}^{(t)}$ from the GPLT scheme, the collinear situation between BS_1 and BS_{v_2} can be avoided; while the rotated angle $\hat{\theta}_{v_1}^{(t)}$ alleviates potential small angle between BS_1 and BS_{v_1}. By considering the geometric layout within the design of the GPLT scheme, the situations with worse GDOP value can be improved. The precision for location estimation and tracking of the MS can consequently be enhanced.

7.6 Performance Evaluation

Simulations are performed to show the effectiveness of the proposed PLT and GPLT schemes under different numbers of BSs, including the scenarios with deficient signal sources. The noise models and the simulation parameters are illustrated in Subsection 7.6.1. Subsection 7.6.2 validates the GPLT scheme according to the variations from the relative angle and the distance between the MS and the designed virtual BS. The performance comparison between the proposed PLT and GPLT algorithms with the other existing location tracking schemes, i.e., the KT and the CLT techniques, are conducted in Subsection 7.6.3.

7.6.1 Noise Models and Simulation Parameters

In order to include the influence from the NLOS noise, the TOA model in cellular network as in Section 2.2.1.2 is adopted. The model for the measurement noise of the TOA signals is selected as the Gaussian distribution with zero mean and 10 meters of standard deviation, i.e., $n_i^{(t)} \sim \mathcal{N}(0, 100)$. The median value of the root mean square delay spread τ_m is chosen as 0.1 μs in this subsection primarily fulfill the environment while the MS is located within the rural area. It is noticed that the reason for selecting the rural area as the simulation scenario is due to its higher probability to suffer from deficiency of signal sources. Moreover, the sampling time Δt is chosen as 1 sec in the simulations.

7.6.2 Validation of GPLT Scheme

In this subsection, the proposed GPLT scheme is validated with the angle and distance effects. Since the static MS case is considered in the subsection, the time instant t is removed for the notational simplicity.

7.6.2.1 Validation with Angle Effect

As mentioned in Subsection 7.5.1.1, the primary objective of the proposed GPLT algorithm is to adjust the position of the virtual BS such that the predicted MS can be situated at a location

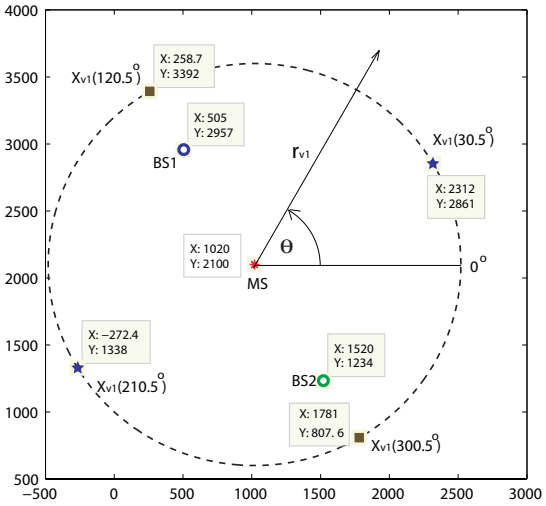

Figure 7.4: An exemplify diagram for the scenarios with the two-BSs layout. Stars ($\boldsymbol{x}_{v_1}(30.5^o)$ and $\boldsymbol{x}_{v_1}(210.5^o)$): the positions of the virtual BS cause the minimal GDOP value of the MS; Squares ($\boldsymbol{x}_{v_1}(120.5^o)$ and $\boldsymbol{x}_{v_1}(300.5^o)$): the positions of the virtual BS cause the maximal GDOP value of the MS

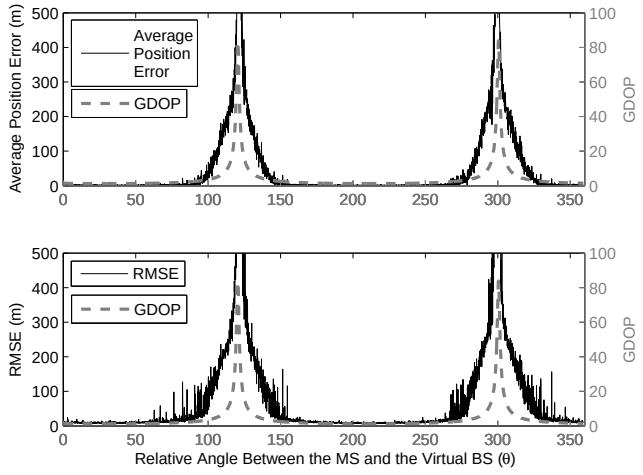

Figure 7.5: Upper plot: the average position error (solid line) and the GDOP value (dashed line) vs the relative angle between the MS and the virtual BS (θ); Lower plot: the RMSE (solid line) and the GDOP value (dashed line) vs the relative angle between the MS and the virtual BS (θ)

with minimal GDOP value. The design concept implicitly indicates that the estimation error can be reduced if the MS is possessed with a smaller GDOP value formed by its geometric layout. In the following example, the relationship between the estimation errors and the GDOP values will be verified via simulations.

Example 7.1 (Validation with Angle Effect)**.** As shown in Fig. 7.4, the two-BS case is considered associated with the locations of the BSs are $\text{BS}_1 = [505,\ 2957]^T$ and $\text{BS}_2 = [1520,\ 1234]^T$ in meters. The MS's true position is located at $\boldsymbol{x} = [1020, 2100]^T$ m. The position of the virtual BS is assumed at $\boldsymbol{x}_{v_1}(\theta) = [1020 + 1500\cos\theta,\ 2100 + 1500\sin\theta]^T$ m with $\theta = [0°, 359°)$. It can be seen that the potential positions of the virtual BS are considered to be located at a distance 1500 meters away from the MS's true position along with different relative angles θ.

Fig. 7.5 illustrates the comparison between the average position error (upper plot), the root mean square error (RMSE, lower plot), and the GDOP value versus the relative angle (θ) between the true MS and the virtual BS. It is noted that the average position error (Δx) and the RMSE are computed as: $\Delta x = \left[\sum_{i=1}^{N} \|\boldsymbol{x} - \hat{\boldsymbol{x}}(i)\|\right]/N$ and $\text{RMSE} = \left[\sum_{i=1}^{N} \|\boldsymbol{x} - \hat{\boldsymbol{x}}(i)\|^2/N\right]^{1/2}$ where $N = 50$ indicates the number of simulation runs. It is also noticed that the GDOP value ($\text{G}_{\boldsymbol{x}}$) is evaluated at the MS's true position; while the estimated MS's position $\hat{\boldsymbol{x}}(i)$ is obtained by the TSLS estimator employing the various positions of the virtual BS, i.e., $\boldsymbol{x}_{v_1}(\theta)$ for $\theta = [0°, 359°)$. It can be observed from both plots in Fig. 7.5 that the average position error and the RMSE follow the similar trend as the computed GDOP value. Both the minimal average estimation error (associated with the RMSE) and the minimal GDOP value occur at the locations of $\boldsymbol{x}_{v_1}(30.5^o) = [2312,\ 2861]^T$ m and $\boldsymbol{x}_{v_1}(210.5^o) = [-272.4,\ 1338]^T$ m. It is noted that the angle $\hat{\theta}_1$ for the minimal GDOP value can also be directly computed and verified from (7.20). Moreover, the maximal GDOP values and the maximal estimation errors (including both the average estimation error and the RMSE) happen around the locations of $\boldsymbol{x}_{v_1}(120.5^o) = [258.7,\ 3392]^T$ m and $\boldsymbol{x}_{v_1}(300.5^o) = [1781, 807.6]^T$ m. The results can further be validated by observing the geometric layout as in Fig. 7.4. The minimal GDOP values of the true MS occur as the three BSs form a equilateral triangle; while the maximal GDOP values happen as the three BSs are situated along a straight line. The above observations validate the effectiveness of the proposed GPLT scheme by obtaining a position of the virtual BS with a smaller GDOP value, which consequently reduces the corresponding estimation error. On the other hand, the estimation errors can be severely augmented if the MS happens to be located at a position with the maximum GDOP value by adopting other schemes. It can therefore be concluded that the results obtained from the simulations comply with the design objectives of the GPLT algorithm. ◇

7.6.2.2 Validation with Distance Effect

In this subsection, the results obtained from Lemma 7.2 will be validated via simulations. It is stated in Lemma 7.2 that the expected value of the estimation error is independent to the distance

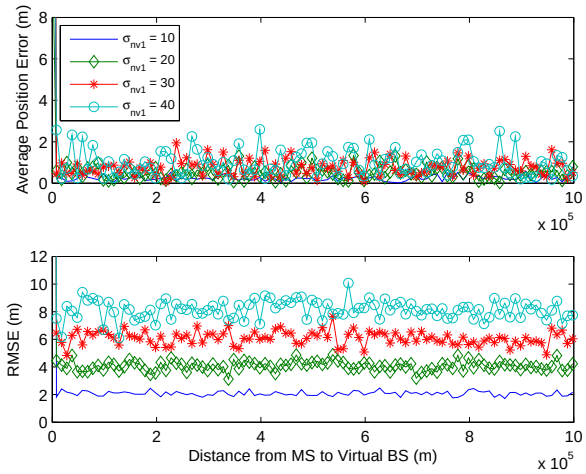

Figure 7.6: Upper plot: the average position errors vs the relative distance between the MS and the virtual BS (r_{v_1}); Lower plot: the RMSE vs the relative distance between the MS and the virtual BS (r_{v_1}) (with $\sigma_{n_{v_1}} = 10, 20, 30, 40$)

between the MS and a specific BS (which is associated with the measurement input contaminating zero mean random noises) by adopting the WLS location estimation algorithm. In order to validate Lemma 7.2 by the simulation data, the estimation errors induced by adopting the TSLS estimator will be obtained for the evaluation of the distance effect.

Example 7.2 (Validation with Distance Effect)**.** Fig. 7.6 illustrates the average position error (upper plot) and the RMSE (lower plot) acquired from the TSLS method under different relative distances between the MS and the virtual BS (i.e., r_{v_1}). It is noted that the distance r_{v_1} is simulated from 1 to 10^6 m along the angle $\theta = 60^o$ as shown in Fig. 7.4. The four simulated results are conducted under different signal standard deviations (i.e., $\sigma_{n_{v_1}} = 10, 20, 30, 40$) in order to exam the potential effect from the signal variances. As can be expected, the estimation errors are observed to be independent to the relative distance between the MS and the virtual BS, which are similar to the results as concluded from Lemma 7.2. Moreover, it is also reasonable to perceive that the increases on the signal standard deviation $\sigma_{n_{v_1}}$ will induce proportional augmentation on the RMSE (in the lower plot of Fig. 7.6); while the average position error is considered not related to the changes due to the signal variations (in the upper plot of Fig. 7.6). From the above observations via the simulation data, the uncorrelated relationship between the distance r_{v_1} and the estimation error is found to be consistent with the results as acquired from Lemma 7.2. However, a feasible value of r_{v_1} should be selected in the simulations in order not to exceed the limitation of computation, e.g., matrix inversion can result in singular value as an extremely large value of r_{v_1} is exploited. For fair comparison purpose, the distance r_{v_1} for the GPLT scheme is chosen to be the same as that in the PLT scheme in the following subsection. ◇

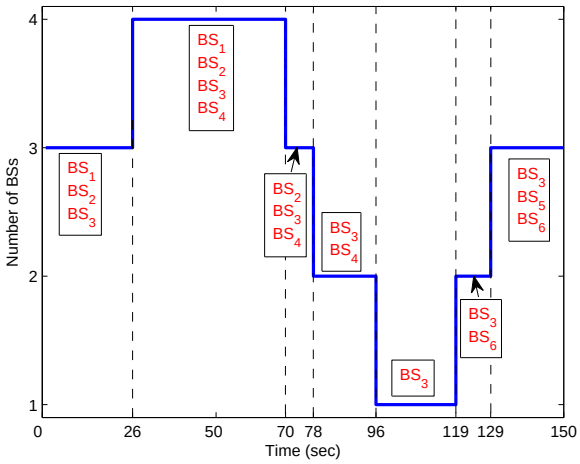

Figure 7.7: Total number of available BSs ($N^{(t)}$) vs. simulation time (sec); Black textbox: available BSs ($P_{BS}^{(t)}$) during each time interval

TABLE I
Performance Comparison between the Location Tracking Algorithms
(Average Position Error (m))

	10%	20%	30%	40%	50%	60%	70%	80%	90%	100%
EKF	33.83	37.65	42.60	417.11	968.97	1430.33	2029.04	2698.13	3161.70	3344.07
KT	37.33	46.86	50.70	67.85	110.01	139.53	246.45	474.13	926.54	2026.95
CLT	19.34	26.05	27.21	46.53	72.86	198.88	327.65	671.46	1184.14	1949.06
PLT	19.34	26.05	27.21	48.58	63.07	70.90	86.13	117.44	188.14	268.89
GPLT	19.34	26.05	27.21	48.58	64.12	77.51	99.50	113.70	143.69	196.51

7.6.3 Simulation Results

The performance comparisons between the EKF scheme, KT scheme, the CLT scheme, and the proposed PLT and GPLT algorithms are conducted under the rural environment.

Example 7.3 (A Trajectory Moving Case with Insufficient Signal Sources)**.** Fig. 7.7 illustrates the scenario with various numbers of BSs (i.e., the $N^{(t)}$ values) that are available at different time intervals, where $P_{BS}^{(t)}$ denotes the set of available BSs (as indicated in Fig. 7.8(a)) that are visible during each time interval. It can be seen that the number of BSs becomes insufficient (i.e., $N^{(t)} < 3$) from the time interval of $t = 78$ to 129 sec. The total simulation interval is set as 150 seconds.

Figs. 7.8(a) to 7.8(c) illustrate the performance comparisons of the trajectory, the velocity, and the acceleration tracking using the four algorithms. The estimated values obtained from these schemes are illustrated via the dashed lines; while the true values are denoted by the solid lines. The locations of the BSs are represented by the red empty circles as in Fig. 7.8(a). The acceleration is designed to vary at time $t = 40$, 55, 100, and 120 sec from $\boldsymbol{a}^{(t)} = [a_x^{(t)},\ a_y^{(t)}]^T = [0.5,\ 0]^T, [-1,\ 1.5]^T, [0,\ 0]^T, [0.5,\ 0]^T$, to $[1,\ -2]^T$ m/sec^2 (as shown in Fig. 7.8(c)). It is noted

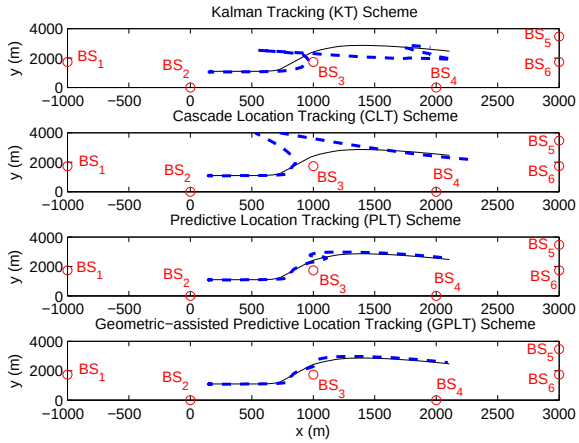

(a) Trajectory.

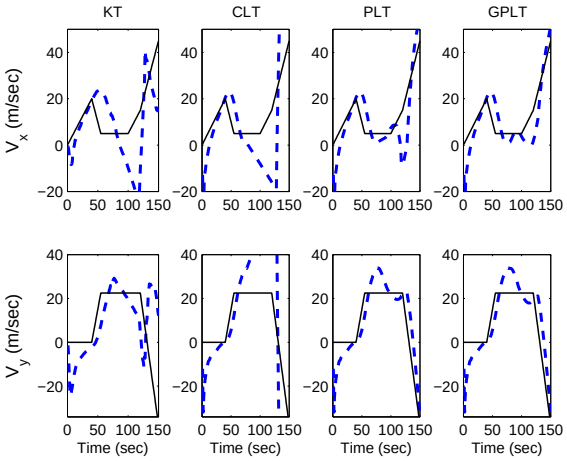

(b) Velocity.

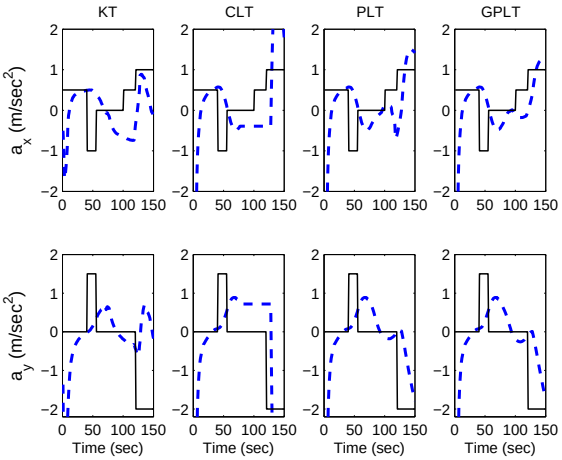

(c) Acceleration.

Figure 7.8: Performance comparison of MS tracking. (Dashed lines: estimated value; Solid lines: true value; Red empty circles in Fig. 7.8(a): the position of the BSs).

that the number of BSs becomes insufficient during the second acceleration change (i.e., at $t = 78$ sec). Table I illustrates the performance comparison between the five location tracking algorithms under different percentages of average position errors, i.e., by sorting the estimation errors during the entire simulation interval. It can be observed that both the proposed GPLT and the PLT schemes provide better performance comparing with the other existing algorithms owing to their consideration of insufficient signal sources, e.g., the GPLT algorithm outperform the CLT scheme with around 560 m of estimation error under 80% of average position error. It is also noticed that the EKF scheme possesses the worst performance comparing with the other algorithms under different percentages of estimation errors. Therefore, only the KT, the CLT, the PLT, and the GPLT schemes are further compared for performance evaluation.

By observing the starting time interval between $t = 0$ and 77 sec (where the number of BSs is sufficient), the four algorithms provide similar performance on location tracking as shown in the x-y plots in Fig. 7.8(a). As illustrated in Figs. 7.8(b) and 7.8(c), it can be seen that the KT scheme can provide better performance on the velocity and acceleration tracking during the transient phase (i.e from $t = 0$ to 10 sec) comparing with the other schemes. The reason can be attributed to the inherent architecture difference as shown in Fig. 7.1. The KT scheme is designed to be a unified scheme which compromises between the estimated state variables, $\hat{\boldsymbol{x}}^{(t)}$, $\hat{\boldsymbol{v}}^{(t)}$, and $\hat{\boldsymbol{a}}^{(t)}$. On the other hand, the CLT algorithm associated with the PLT/GPLT schemes are designed to be a cascaded structure, where the measurement input of the Kalman filter is the resulting estimated MS's position from the TSLS method. The estimated position of the MS dominates the update of the state variables; while both the velocity and the acceleration are considered less essential comparing with the update of the position $\hat{\boldsymbol{x}}^{(t)}$. Consequently, comparable better velocity and acceleration updates are observed by adopting the KT scheme during the transient response as in Figs. 7.8(b) and 7.8(c). However, the KT scheme results in the worst performance among the four schemes after the transient phase (as shown in Figs. 7.8(b) and 7.8(c)). Owing to the utilization of an external location estimator within the KT scheme, the estimation errors are increasingly accumulated caused by the potential inaccuracy of the estimator.

During the time interval between $t = 78$ and 129 sec with inadequate signal sources, it can be observed that only the proposed GPLT scheme can achieve satisfactory performance in the trajectory, the velocity, and the acceleration tracking. The estimated trajectories obtained from both the KT and the CLT schemes diverge from the true trajectories due to the inadequate number of measurement inputs. It is noticed that the inaccuracy within the PLT scheme is primarily resulted from the implicitly worse geometric layout at certain time instants, which will further be explained by the GDOP plot as in Fig. 7.10.

Moreover, Fig. 7.9 illustrate the average position error (upper plot) and the RMSE (lower plot) (i.e., characterizing the signal variances) for location estimation and tracking of the MS. The four location tracking schemes are compared based on the same simulation scenario as shown in Fig. 7.7. It can be observed from both plots that the proposed GPLT and PLT algorithms outperform

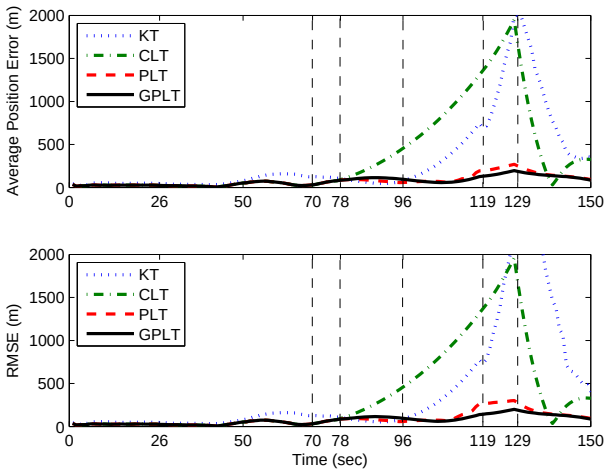

Figure 7.9: Upper plot: the average position error vs. the simulation time (sec); Lower plot: the RMSE vs. the simulation time (sec)

the conventional KT and CLT schemes. The main differences between these algorithms occur while the signal sources become insufficient within the time interval between $t = 78$ and 129 sec. The proposed GPLT and PLT schemes can still provide consistent location estimation and tracking; while the other two algorithms result in significantly augmented estimation errors. The major reason is attributed to the assisted information that is fed back into the location estimator while the signal sources are deficient. Furthermore, the GPLT algorithm outperforms the PLT scheme primarily due to its exploitation of the GDOP criterion.

The comparison of the average GDOP values (associated with their confident intervals) between the PLT and the GPLT schemes is illustrated in Fig. 7.10. It is noted that the averaged GDOP values are computed based on 25 simulation runs. The average GDOP values are compared only during the time interval with deficient signal sources, i.e., while the virtual BSs and the virtual measurements are exploited in both schemes. It can be observed that the GDOP values obtained from the GPLT algorithm are consistent during the simulation period with reasonable variations. On the other hand, the GDOP values acquired from the PLT scheme result in larger variations, especially during the time interval of $t = 96$ to 119 sec. The results are consistent with those estimation errors as acquired from Fig. 7.9 that worse GDOP value will result in incorrect location estimation of the MS. During the time interval of $t = 78$ to 95 sec, the GDOP values obtained from both schemes are considered similar, which represent that comparable geometric topology are formed by their individual virtual BSs. The geometric effect will not be an influential factor to the estimation error for the MS. On the other hand, during the time interval of $t = 110$ to 119, sudden deviates in the GDOP values are observed by using the PLT scheme. The larger average position error and the RMSE within the PLT algorithm (as seen from Fig. 7.9 at around $t = 120$ sec) can therefore be attributed to the corresponding increased GDOP values and variations.

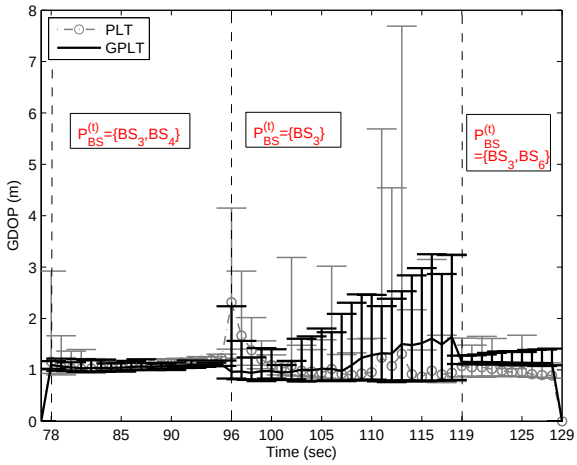

Figure 7.10: Comparison of the average GDOP values (associated with their confident intervals) between the PLT and the GPLT schemes during the time interval with deficient signal sources

Nevertheless, with the adoption of the minimal GDOP criterion, the proposed GPLT scheme can still maintain consistent GDOP values under different numbers of available signal inputs. The resulting estimation error and RMSE can consequently be controlled within a reliable interval. ◇

Example 7.4 (PLT and GPLT under NLOS environment). In order to evaluate the effect of the NLOS errors to the estimation performance, the average position error and the RMSE as depicted in Fig. 7.11 are utilized to compare the three schemes under different NLOS errors, where the median value of the NLOS noises τ_m = 0.1, 0.3, and 0.4 corresponds to the rural, suburban, and urban environments. It is noted that both the estimation error and the RMSE are obtained as the average values acquired from the trajectory as designed in Fig. 7.8(a). Moreover, the performance obtained from the KT scheme is not illustrated in Fig. 7.11 due to its drastically degraded performance as the NLOS noises τ_m is increased. Owing to the consideration of the geometric layout, it can be observed from Fig. 7.11 that the proposed GPLT scheme possesses better performance comparing with the other two algorithms under different NLOS errors. Furthermore, the performance obtained from the PLT scheme is severely degraded with the increase of the NLOS errors. As a result, the effectiveness of the GPLT algorithm is perceived, especially under insufficient signal sources (i.e., $N^{(t)}$ = 1 and 2). ◇

7.7 Concluding Remarks

In this chapter, the Predictive Location Tracking (PLT) and the Geometry-assisted Predictive Location Tracking (GPLT) schemes are proposed. The predictive information obtained from the Kalman filtering formulation is exploited as the additional measurement inputs for the location

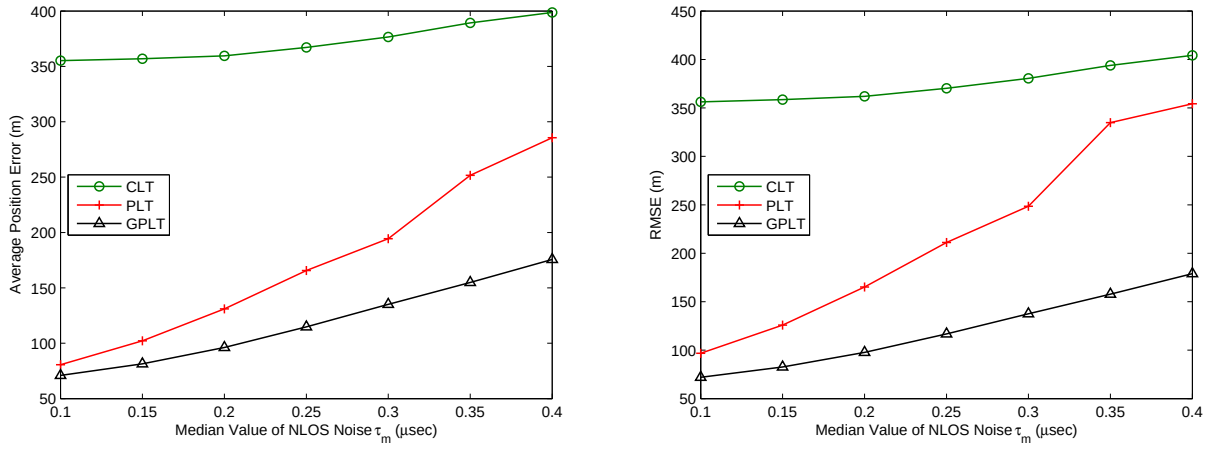

Figure 7.11: Left Plot: the Average Position Error vs the Median value of NLOS noise (τ_m); Right Plot: the RMSE vs the Median value of NLOS noise (τ_m)

estimator. With the feedback information, sufficient signal sources become available for location estimation and tracking of a mobile device. Moreover, the GPLT algorithm adjusts the locations of its virtual Base Stations based on the GDOP criterion. It is shown in the simulation results that the proposed GPLT algorithm can provide consistent accuracy for location estimation and tracking even under the environments with insufficient signal sources.

Chapter 8

Cooperative Self-Navigation in a Mixed LOS and NLOS Environment

- The problem of cooperative self-navigation for mobile sensors in the mixed LOS/NLOS environment is first investigated in this chapter based on measuring time-of-arrival from the cooperative sensing. The proposed cooperative self-navigation (CSN) with joint position and channel tracking takes advantage over the noncooperative methods with the extra cooperative measurements and over the methods without channel tracking.

8.1 Introduction

For self-navigation, a mobile unit needs to determine its own coordinate position based on its reception of signals *from* multiple radio stations of known positions. These radio stations are known as anchors. In fact, the self-navigation problem is equivalent to the source localization problem whose goal is to estimate source location based on signals received *by* multiple sensors [80]. A number of wireless positioning methods have been widely studied with various signal measurements. Representative signal models for wireless positioning includes distance measurements [13], time-of-arrival (TOA) [9], time difference-of-arrival (TDOA) [10], angle-of-arrival (AOA) [12], and the received signal strength (RSS) [11]. Because AOA and RSS measurements can be highly inaccurate under complex indoor environment in practice, we focus on TOA measurement for self-navigation in this work. For mobile self-navigation, the mobile sensor (MS) unit moves dynamically. The TOA measurement is made sequentially and the mobile state is estimated or updated to facilitate location estimate for next instant.

We note that the measurement error (noise) model of the TOA depends on whether the path between a radio anchor and the mobile receiver is a direct line-of-sight (LOS) path or non-line-of-sight (NLOS) path. NLOS refers to a transmission path obstructed by structures which cause substantial bias to the signal travel time/distance. Traditional schemes locate the position of a

mobile sensor based on its received radio signals from the anchors only. Instead, we study the problem of cooperative navigation, in which multiple sensors can exchange their received signals or their estimated positions in order to jointly improve the accuracy of their individual positions. Despite the lack of accurate position information at all the sensors, cooperative navigation and positioning have been shown to improve the estimation results from the perspective of Fisher information matrix or Cramer-Rao bound [81].

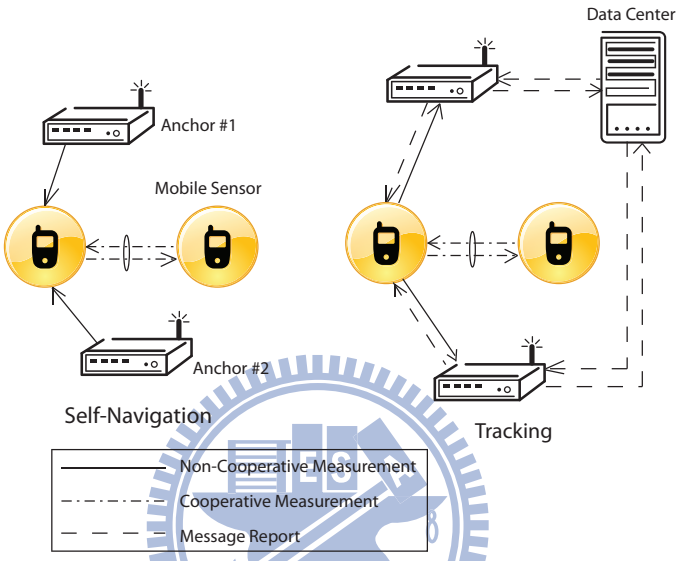

Figure 8.1: Transmission and measurement procedure of (a) cooperative self-navigation (CSN) (b) cooperative tracking.

Fig. 8.1 further illustrates the concept of cooperative self-navigation (CSN). Each MS listens to the signal broadcast by the anchors and estimates its position from the downlink TOA measurement. Each MS should exchange some belief information with others for CSN. In particular, each MS can re-estimate its own position after receiving signals from the anchors and beliefs from other MSs. Cooperative self-navigation keeps the transmission overhead low by only sending the belief of its position. In fact, a known work on cooperative localization using *sum-product algorithm* is the so-called SPAWN of [82] which adopted non-parametric belief propagation [83] for information exchange among mobile sensors of unknown positions. The authors of [82] demonstrated superior performance of SPAWN with a recursive Bayesian estimation over both the non-cooperative scheme and the cooperative least-squares scheme. However, the assumption that either the channels are known to be LOS or NLOS limits the practical applicability of SPAWN. Specifically, in a dynamic system, channels would switch between LOS or NLOS over time because of MS movement and other moving objects. Hence, we do not know a priori whether a given channel is LOS or NLOS at a particular time.

To model the channel evolution in time and space, a Markov model has been proposed in [84]. Several papers deal this problem by introducing an interacting multiple model (IMM) [85, 86, 87].

The IMM method estimates all possible modes in parallel and mixes the estimation result according to mode probability. The authors of [85, 86] utilized the IMM method on the signal models, where each distance measurement consists two modes including LOS and NLOS. One IMM and two Kalman filters are utilized to smooth each TOA [85] measurement, thereby leading to better position estimate. The authors of [86] further proposed an extended Kalman filter based IMM to smooth the RSS that combines with the TOA via data fusion. Instead of applying an IMM on each measurement, the authors of [87] used one IMM on the position estimate. Assuming that there are total N anchors, there are 2^N modes which capture all the combinations of LOS/NLOS conditions, e.g., $N = 3$ with 8 modes containing {LOS, LOS, LOS},{LOS, LOS, NLOS},...,{NLOS, NLOS, NLOS}. The position is estimated according to LOS/NLOS combinations in different modes. The integration of position estimates for different modes enhances the performance at the expense of computational complexity. On the other hand, the authors of [88, 89] considered a joint channel condition and position tracking problem based on the hidden Markov model. The grid based [88] and particle filter [89] are employed for the problem. The authors of [90] considered a Rao-Blackwell particle filter method by estimating the channel condition with particle filter and then applying extended Kalman filter for the position estimation. As is clear from the literature survey, there are a number of researches on the location estimation in mixed LOS/NLOS environment. Still, no study based on cooperative sensing has been investigated.

In the chapter, we investigate how cooperative measurement sensing can improve self-navigation in a mixed LOS/NLOS channel condition. The **major contribution of the chapter** is the derivation of an optimized recursive Bayesian solution for CSN, which has not been done before. Since the channel condition is non-deterministic and is obviously non-Gaussian, we adopt the use of multiple model SIR particle filter [91] to approximate the associated non-linear and non-Gaussian recursive Bayesian problem and to develop a CSN method. The chapter consists of five sections. In Section 8.2, we describe our problem formulation by presenting our measurement model and a model of channel state transition in self-navigation. In Section 8.3, we propose a joint channel condition and position estimation for the CSN. Section 8.4 presents numerical simulation results that are followed by the conclusion in Section 8.5.

8.2 Problem Formulation

Unlike the single MS estimation problems in Chapter 4 to 7, the cooperative localization considering multiple MSs are presented in this chapter. Therefore, different notations are adopted in this chapter.

8.2.1 Problem Description

Consider a synchronous network of N transmitting anchors fixed at the known positions. Their positions are denoted by a set of m-dimensional vectors $\mathbf{a} = [\mathbf{a}_1\ \mathbf{a}_2\ ...\ \mathbf{a}_N]^T$, respectively. Although $m = 2$ and $m = 3$ are both possible, without loss of generality, we consider $m = 2$ in this chapter. Our goal is to estimate the unknown positions of M mobile sensors at time instant t which are denoted by a set of m-dimensional vectors $\mathbf{x}^{(t)} = [\mathbf{x}_1^{(t)}\ \mathbf{x}_2^{(t)}\ ...\ \mathbf{x}_M^{(t)}]^T$. In other words, based on the known positions of the transmitting anchors, the mobile units wish to estimate their positions at different time instants. There are typically movement of sensors between the sampling time instants t and $t+1$.

When the i-th anchor broadcasts its signal, the j-th sensor receives a measurement $y_{i,j}^{(t)}$. Meanwhile, the MS cooperates with each other by transmitting its belief position to others. Hence, the j-th sensor also receives cooperative measurement $z_{\ell,j}^{(t)}$ from the ℓ-th MS to the j-th MS. We assume that the two types of signals are orthogonally multiplexed possibly in frequency or in code such that of $y_{i,j}^{(t)}$ and $z_{\ell,j}^{(t)}$ do not interfere with each other's reception by the j-th sensor.

By collecting measurements from time index 1 to t from the sources to the j-th MS (i.e., $\mathbf{y}_j^{(1:t)} = [y_{1,j}^{(1:t)}\ ...\ y_{N,j}^{(1:t)}]^T$) and the cooperative measurements from the other mobiles to the j-th MS (i.e., $\mathbf{z}_j^{(1:t)} = [z_{1,j}^{(1:t)}\ ...\ z_{j-1,j}^{(1:t)}\ z_{j+1,1}^{(1:t)}\ ...\ z_{M,j}^{(1:t)}]^T$), the goal is for the j-th MS to generate an estimate $\mathbf{x}_j^{(t)}$ of its position and channel condition jointly for the self-navigation.

8.2.2 Measurement Model

As explained earlier, we focus on the TOA measurement model. For notational simplicity, the TOA measurement from the anchor to the MS is multiplied by the speed of light c. Thus, the effective TOA measurement is

$$y_{i,j}^{(t)} = \|\mathbf{a}_i - \mathbf{x}_j^{(t)}\| + v_{i,j}^{(t)}(s_{i,j}^{(t)}), \quad i = 1, 2, ..., N, j = 1, 2, ..., M, \tag{8.1}$$

where $\|\cdot\|$ denotes the Euclidean distance and $v_{i,j}^{(t)}$ is the measurement noise at time t. Similarly, the TOA measurement between mobile stations are

$$z_{i,j}^{(t)} = \|\mathbf{x}_i^{(t)} - \mathbf{x}_j^{(t)}\| + w_{i,j}^{(t)}(l_{i,j}^{(t)}), \quad i = 1, 2, ..., j-1, j+1, ..., M, j = 1, 2, ..., M, \tag{8.2}$$

where $w_{i,j}^{(t)}$ represents the additive measurement error/noise.

The difference between LOS and NLOS models lies in the noise distributions. In the chapter, both LOS and NLOS situations are considered. Thus, the noise distribution of each link can be either LOS or NLOS distribution. The channel condition is hidden in the measurement. Though we are primarily interested in estimating the position of the MS, the estimation of the channel condition is necessary to identify different noise distributions.

We therefore denote the channel state between the i-th anchor and the j-th MS as $s_{i,j}^{(t)} \in \{0,1\}$ and denote the cooperative channel condition from the ℓ-th MS to the j-th MS is as $l_{\ell,j}^{(t)} \in \{0,1\}$. LOS corresponds to state 0 whereas NLOS is denoted by state 1. For the convenience, we denote all the noncooperative channel states to the j-th MS as a N-dimensional vector $\mathbf{s}_j = [s_{1,j} \ ... \ s_{N,j}]$. We also denote all the cooperative channel states to the j-th MS as a vector of $\mathbf{l}_j = [l_{1,j} \ ...l_{j-1,j} \ l_{j+1,j} \ ...l_{M,j}]$.

8.2.3 State Transition Model

For a self-navigation problem, both the position and the channel condition of the MS change from time to time in a period from time index 1 to T. In order to model the correlation of the position and the channel condition between different time instant, a hidden Markov process of order one is adopted as the state model. The position of the j-th MS is considered as a Markov process from time index $t-1$ to t,

$$\mathbf{x}_j^{(t)} = \mathbf{x}_j^{(t-1)} + T_s \cdot \mathbf{v}_j^{(t)}, \tag{8.3}$$

where $\mathbf{v}_j^{(t)}$ denotes the $m \times 1$ vector of the j-th MS velocity at time t. T_s represents the sampling interval. We assume $\mathbf{v}_j^{(t)}$ as a continuous random distribution. Meanwhile, the channel condition is modeled as a Markov chain with the LOS and the NLOS states. The transition probability is modeled as

$$P(l_{i,j}^{(t)} = a \mid l_{i,j}^{(t-1)} = b) = P(s_{i,j}^{(t)} = a \mid s_{i,j}^{(t-1)} = b) = \begin{cases} p_0 & a=0 \quad b=0 \\ 1-p_0 & a=1 \quad b=0 \\ 1-p_1 & a=0 \quad b=1 \\ p_1 & a=1 \quad b=1 \end{cases}. \tag{8.4}$$

8.3 Proposed Cooperative Self-Navigation (CSN) Method

The proposed CSN method is first presented in the optimal recursive Bayesian estimation representation in subsection 8.3.1. The subsection 8.3.2 describes how the particle filter approximates the probability density function of the Bayesian estimation in practice and how the MS collects the measurement with the proposed CSN method.

8.3.1 Optimal Recursive Bayesian Estimation

In this recursive Bayesian estimation problem, the important process is to calculate the joint position and channel condition posteriori distribution,

$$P(\mathbf{x}_j^{(t)}, \mathbf{s}_j^{(t)}, \mathbf{l}_j^{(t)} \mid \mathbf{y}_j^{(1:t)}, \mathbf{z}_j^{(1:t)}) = \frac{1}{\zeta} \underbrace{P(\mathbf{y}_j^{(t)}, \mathbf{z}_j^{(t)} \mid \mathbf{x}_j^{(t)}, \mathbf{s}_j^{(t)}, \mathbf{l}_j^{(t)})}_{likelihood} \cdot \underbrace{P(\mathbf{x}_j^{(t)}, \mathbf{s}_j^{(t)}, \mathbf{l}_j^{(t)} \mid \mathbf{y}_j^{(1:t-1)}, \mathbf{z}_j^{(1:t-1)})}_{prior}, \tag{8.5}$$

where the denominator acts like a normalizing constant as

$$\begin{aligned} \zeta &= P(\mathbf{y}_j^{(t)}, \mathbf{z}_j^{(t)} \mid \mathbf{y}_j^{(1:t-1)}, \mathbf{z}_j^{(1:t-1)}) \\ &= \sum_{\mathbf{s}_j^{(t)}} \sum_{\mathbf{l}_j^{(t)}} \int P(\mathbf{y}_j^{(t)}, \mathbf{z}_j^{(t)} \mid \mathbf{x}_j^{(t)}, \mathbf{s}_j^{(t)}, \mathbf{l}_j^{(t)}) P(\mathbf{x}_j^{(t)}, \mathbf{s}_j^{(t)}, \mathbf{l}_j^{(t)} \mid \mathbf{y}_j^{(1:t-1)}, \mathbf{z}_j^{(1:t-1)}) \, d\mathbf{x}_j^{(t)}. \end{aligned} \tag{8.6}$$

The prediction information in (8.5) can be derived as

$$\begin{aligned} & P(\mathbf{x}_j^{(t)}, \mathbf{s}_j^{(t)}, \mathbf{l}_j^{(t)} \mid \mathbf{y}_j^{(1:t-1)}, \mathbf{z}_j^{(1:t-1)}) \\ &= \sum_{\mathbf{s}_j^{(t-1)}} P(\mathbf{s}_j^{(t)} \mid \mathbf{s}_j^{(t-1)}) \sum_{\mathbf{l}_j^{(t-1)}} P(\mathbf{l}_j^{(t)} \mid \mathbf{l}_j^{(t-1)}) \int P(\mathbf{x}_j^{(t)} \mid \mathbf{x}_j^{(t-1)}) P(\mathbf{x}_j^{(t-1)}, \mathbf{s}_j^{(t-1)}, \mathbf{l}_j^{(t-1)} \mid \mathbf{y}_j^{(1:t-1)}, \mathbf{z}_j^{(1:t-1)}) \, d\mathbf{x}_j^{(t-1)} \\ &= \underbrace{\sum_{\mathbf{s}_j^{(t-1)}} P(\mathbf{s}_j^{(t)} \mid \mathbf{s}_j^{(t-1)}) P(\mathbf{s}_j^{(t-1)} \mid \mathbf{y}_j^{(1:t-1)}, \mathbf{z}_j^{(1:t-1)})}_{noncooperative\ channel\ condition\ prediction} \cdot \underbrace{\sum_{\mathbf{l}_j^{(t-1)}} P(\mathbf{l}_j^{(t)} \mid \mathbf{l}_j^{(t-1)}) P(\mathbf{l}_j^{(t-1)} \mid \mathbf{y}_j^{(1:t-1)}, \mathbf{z}_j^{(1:t-1)})}_{cooperative\ channel\ condition\ prediction} \\ & \underbrace{\int P(\mathbf{x}_j^{(t)} \mid \mathbf{x}_j^{(t-1)}) P(\mathbf{x}_j^{(t-1)} \mid \mathbf{y}_j^{(1:t-1)}, \mathbf{z}_j^{(1:t-1)}) \, d\mathbf{x}_j^{(t-1)}}_{position\ prediction\ P(\mathbf{x}_j^{(t)} \mid \mathbf{y}_j^{(1:t-1)}, \mathbf{z}_j^{(1:t-1)})}. \end{aligned} \tag{8.7}$$

In the chapter, the position and channel condition are assumed to be independent, and the prediction can be performed separately. (8.7) can be calculated through the known initial condition and the known state model in (8.3) and (8.4). Note that all links including the noncooperative measurements $\mathbf{y}_j^{(t)}$ and the cooperative measurements $\mathbf{z}_j^{(t)}$ are considered independent. The likelihood in (8.5) can be written as

$$P(\mathbf{y}_j^{(t)}, \mathbf{z}_j^{(t)} \mid \mathbf{x}_j^{(t)}, \mathbf{s}_j^{(t)}, \mathbf{l}_j^{(t)}) = \underbrace{\prod_k P(y_{k,j}^{(t)} \mid \mathbf{x}_j^{(t)}, s_{k,j}^{(t)})}_{noncooperative\ likelihood} \cdot \underbrace{\prod_i P(z_{i,j}^{(t)} \mid \mathbf{x}_j^{(t)}, l_{i,j}^{(t)})}_{cooperative\ likelihood}. \tag{8.8}$$

From (8.5)-(8.8), the posterior function in (8.5) can be rewritten as

$$P(\mathbf{x}_j^{(t)}, \mathbf{s}_j^{(t)}, \mathbf{l}_j^{(t)} \mid \mathbf{y}_j^{(1:t)}, \mathbf{z}_j^{(1:t)}) = \frac{1}{\zeta} \underbrace{[\int P(\mathbf{x}_j^{(t)} \mid \mathbf{x}_j^{(t-1)}) P(\mathbf{x}_j^{(t-1)} \mid \mathbf{y}_j^{(1:t-1)}, \mathbf{z}_j^{(1:t-1)})\, d\mathbf{x}_j^{(t-1)}]}_{position\ prediction\ P(\mathbf{x}_j^{(t)} \mid \mathbf{y}_j^{(1:t-1)}, \mathbf{z}_j^{(1:t-1)})} [B][C]. \tag{8.9}$$

B refers to the terms related to the noncooperative likelihood and channel condition prediction, while C refers to the terms related to the cooperative likelihood and channel condition prediction. For the noncooperative term, the TOA measurement is affected by the MS position and the channel condition.

$$B = \prod_k \sum_{s_{k,j}^{(t-1)}} P(y_{k,j}^{(t)} \mid \mathbf{x}_j^{(t)}, s_{k,j}^{(t)}) P(s_{k,j}^{(t)} \mid s_{k,j}^{(t-1)}) P(s_{k,j}^{(t-1)} \mid \mathbf{y}_j^{(1:t-1)}, \mathbf{z}_j^{(1:t-1)}). \tag{8.10}$$

For the cooperative term, the TOA measurement is affected by the source position, the MS position, and the channel condition, i.e.,

$$C = \prod_i \sum_{l_{i,j}^{(t-1)}} [\int P(z_{i,j}^{(t)} \mid \mathbf{x}_i^{(t)}, \mathbf{x}_j^{(t)}, l_{i,j}^{(t)}) P(\mathbf{x}_i^{(t)})\, d\mathbf{x}_i^{(t)}] P(l_{i,j}^{(t)} \mid l_{i,j}^{(t-1)}) P(l_{k,j}^{(t-1)} \mid \mathbf{y}_j^{(1:t-1)}, \mathbf{z}_j^{(1:t-1)}). \tag{8.11}$$

The extra integration in (8.11) is required for the cooperative measurement which also increases the computational complexity. Note that for the noncooperative term in (8.10), we already know the source position. However, for the cooperative term in (8.11), we can only calculate $P(\mathbf{x}_i^{(t)})$ through the belief of the i-th MS based on the measurement from time 1 to $t-1$ as

$$P(\mathbf{x}_i^{(t)}) \simeq b(\mathbf{x}_i^{(t)}) = P(\mathbf{x}_i^{(t)} \mid \mathbf{y}_i^{(1:t-1)}, \mathbf{z}_i^{(1:t-1)}). \tag{8.12}$$

Therefore, the coordinates of the anchors and each mobile's belief record are available for all mobile stations to jointly estimate their positions. Note that the belief transmission is chosen as the prediction information before the measurement update at time t. With the measured TOA and belief information from cooperating mobiles, each MS can estimate its own position according to the recorded channel condition. The MS can update the belief to its posterior information as $b(\mathbf{x}_i^{(t)}) = P(\mathbf{x}_i^{(t)} \mid \mathbf{y}_i^{(1:t)}, \mathbf{z}_i^{(1:t)})$ with (8.5)−(8.11). Following the belief propagation concept in [83], the MS refines its estimate and broadcasts its own belief information iteratively to further enhance the joint location accuracy.

The second consideration is how the recorded channel condition affects the estimate. We take the channel condition of the cooperative link for example. In order to demonstrate the effectiveness of joint position and channel condition estimation, the channel condition can be classified as the following cases:

(A1) *Joint Position and Channel Condition Tracking:* The self-navigation unit keeps recording the channel condition of each links $P(l_{i,j}^{(t-1)} \mid \mathbf{z}_j^{(t-1)})$. Therefore, by adopting the state model in (8.4) to calculate $P(l_{i,j}^{(t)} \mid l_{i,j}^{(t-1)})$, the posterior distribution in (8.5) can be calculated.

(A2) *No Knowledge of Channel Condition:* In this case, the original CSN method does not take the channel condition into account. In other words, there is no information about $P(l_{i,j}^{(t)} \mid l_{i,j}^{(t-1)})$ and $P(l_{i,j}^{(t-1)} \mid \mathbf{z}_j^{(t-1)})$. The likelihood function becomes

$$P(z_{i,j}^{(t)} \mid \mathbf{x}_j^{(t)}) = \sum_{l_{i,j}^{(t)}} P(z_{i,j}^{(t)} \mid \mathbf{x}_j^{(t)}, l_{i,j}^{(t)}) P(l_{i,j}^{(t)}). \tag{8.13}$$

Therefore, we can only assume that the LOS or the NLOS happens with the same probability $P(l_{i,j}^{(t)}) = \frac{1}{2}$.

(A3) *Perfect Knowledge of Channel Condition:* In this situation, the channel condition is known at every time instant, i.e., $P(l_{i,j}^{(t)})$ is a dirac delta function in (8.13). Note that the knowledge of channel condition can be obtained through the LOS/NLOS classification. In order to achieve accurate classification, there is an extra overhead needed for LOS/NLOS detection. This situation can serve as an upper bound for the proposed method.

8.3.2 Particle Filter Representation

8.3.2.1 Fundamental Concepts of Particle Filter

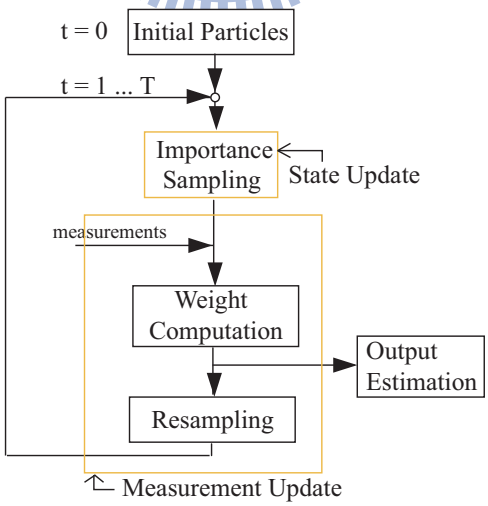

Figure 8.2: A flow chart about the sampling importance resampling (SIR) particle filter.

The concept of the particle filter is to use a set of particles $\{[\mathbf{x}_j^{(t)}]_q, [\mathbf{s}_j^{(t)}]_q, [\mathbf{l}_j^{(t)}]_q\}_{q=1}^{N_q}$ associated

with its weighting $[w_j^{(t)}]_q$ to denote a random measure of the posterior distribution

$$P(\mathbf{x}_j^{(t)}, \mathbf{s}_j^{(t)}, \mathbf{l}_j^{(t)} \mid \mathbf{y}_j^{(1:t)}, \mathbf{z}_j^{(1:t)}) \simeq \sum_{q=1}^{N_q} [w_j^{(t)}]_q \cdot \delta(\mathbf{x}_j^{(t)} - [\mathbf{x}_j^{(t)}]_q) \cdot \delta(\mathbf{s}_j^{(t)} - [\mathbf{s}_j^{(t)}]_q) \cdot \delta(\mathbf{l}_j^{(t)} - [\mathbf{l}_j^{(t)}]_q). \quad (8.14)$$

Here N_q denotes for the number of particles, $[\mathbf{x}_j^{(t)}]_q$ represents the q-th particle of the j-th m-dimensional MS position $\mathbf{x}_j^{(t)}$ at time t, and $[\mathbf{s}_j^{(t)}]_q$ represents the q-th particle of the noncooperative link condition $\mathbf{s}_j^{(t)}$ received by the j-th MS. Furthermore, $[\mathbf{l}_j^{(t)}]_q$ represents the q-th particle of the cooperative link condition $\mathbf{l}_j^{(t)}$ received by the j-th MS, and $[w_j^{(t)}]_q$ denotes the importance weights associated to the q-th particle.

The multiple model sampling importance resampling (SIR) particle filter [91, 92] is one of the represented method and is adopted in our method as shown in Fig. 8.2. Note that the Bayesian recursive estimation can be classified as the state update and the measurement update. In the state update stage, the importance density of SIR filter is chosen to be the transition prior to draw samples (i.e., particles). Note that there are two likelihood functions, one for LOS channel and one for NLOS channel condition, respectively. By substituting the position samples into the likelihood function according to channel condition samples, the weights of the corresponding particles can be obtained. The associated weights are regarded as the approximations to the posterior probabilities of the particles such that $\sum_{q=1}^{N_q} [w_j^{(t)}]_q = 1$. Therefore, for importance sampling, the minimum mean square error estimation (e.g., position) can be obtained from a weighted average as

$$E[\mathbf{x}_j^{(t)} \mid \mathbf{y}_j^{(1:t)}, \mathbf{z}_j^{(1:t)}] = \int P(\mathbf{x}_j^{(t)} \mid \mathbf{y}_j^{(1:t)}, \mathbf{z}_j^{(1:t)}) \cdot \mathbf{x}_j^{(t)} d\mathbf{x}_j^{(t)} \simeq \sum_{q=1}^{N_q} [w_j^{(t)}]_q \cdot [\mathbf{x}_j^{(t)}]_q. \quad (8.15)$$

In order to overcome the degeneracy problem, which denotes particles with negligible weights after iterations, the resampling of the particles is necessary. The idea of the resampling algorithm is to remove the particles with small weights and increase the particles with large weights by making several copies to fill the place of the deleted particles. Therefore, the weights would be adjusted to $1/N_q$, which means there is no need to record the weights for every time instant.

8.3.2.2 Particle Filter for CSN

Fig. 8.3 and Algorithm 8.1 illustrate how to update the particles and the associated weights recursively with the proposed CSN method for the j-th MS. We assume prior knowledge (or estimate) on the starting position and channel condition $P(\mathbf{x}_j^{(0)})$, $P(\mathbf{s}_j^{(0)})$, and $P(\mathbf{l}_j^{(0)})$ and draw particles $\{[\mathbf{x}_j^{(0)}]_q, [\mathbf{s}_j^{(0)}]_q, [\mathbf{l}_j^{(0)}]_q\}_{q=1}^{N_q}$ accordingly. At every sample time t, the SIR particle filter draws the important density using the transition prior, i.e., $[\mathbf{x}_j^{(t)}]_q \sim P(\mathbf{x}_j^{(t)} \mid [\mathbf{x}_j^{(t-1)}]_q)$, $[\mathbf{s}_j^{(t)}]_q \sim P(\mathbf{s}_j^{(t)} \mid [\mathbf{s}_j^{(t-1)}]_q)$, and $[\mathbf{l}_j^{(t)}]_q \sim P(\mathbf{l}_j^{(t)} \mid [\mathbf{l}_j^{(t-1)}]_q)$ $\forall q$. The noncooperative source broadcasts its coordinates. At the

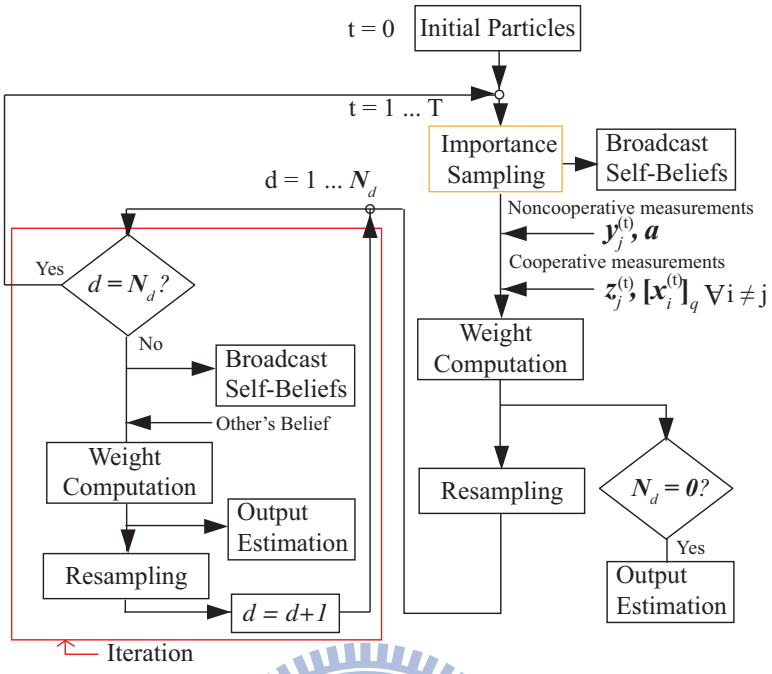

Figure 8.3: A flow chart about the particle filter for CSN.

same time, the cooperative nodes transmit their position belief with the particle representation $\{[\mathbf{x}_j^{(t)}]_q^{(0)}\}_{q=1}^{N_q}$ in parallel. Both the noncooperative and cooperative channel condition are only recorded by local MS. After the MS receives the noncooperative measurements, the anchors' coordinates, the cooperative measurements, and the particles from the cooperative nodes, we can then calculate the weights as

$$[\tilde{w}_j^{(t)}]_q = P(\mathbf{y}_j^{(t)}, \mathbf{z}_j^{(t)} \mid [\mathbf{x}_j^{(t)}]_q, [\mathbf{s}_j^{(t)}]_q, [\mathbf{l}_j^{(t)}]_q) = \prod_k P(y_{k,j}^{(t)} \mid [\mathbf{x}_j^{(t)}]_q, [s_{k,j}^{(t)}]_q) \prod_i P(z_{i,j}^{(t)} \mid [\mathbf{x}_j^{(t)}]_q, [l_{i,j}^{(t)}]_q), \tag{8.16}$$

where the weights should be normalized by $[w_j^{(t)}]_q = [\tilde{w}_j^{(t)}]_q / \Sigma_{q=1}^{N_q} [\tilde{w}_j^{(t)}]_q$. Therefore, the minimum mean square error estimate can be generated with

$$\begin{cases} \hat{\mathbf{x}}_j^{(t)} = \Sigma_{q=1}^{N_q} [w_j^{(t)}]_q \cdot [\mathbf{x}_j^{(t)}]_q \\ \hat{\mathbf{s}}_j^{(t)} = round(\Sigma_{q=1}^{N_q} [w_j^{(t)}]_q \cdot [\mathbf{s}_j^{(t)}]_q) \\ \hat{\mathbf{l}}_j^{(t)} = round(\Sigma_{q=1}^{N_q} [w_j^{(t)}]_q \cdot [\mathbf{l}_j^{(t)}]_q) \end{cases} . \tag{8.17}$$

Note that the entries of vectors $\hat{\mathbf{s}}_j^{(t)}$ and $\hat{\mathbf{l}}_j^{(t)}$ are either 0 or 1. Hence, we include rounding to the nearest 0 or 1 to serve as an estimation output after the summarization of the weighting associated to the particles. The channel condition particles are maintained as the probability that the corresponding link was in LOS or NLOS. The systematic resampling algorithm [93] is performed

to adjust the particles into an equal weight set.

Since there is uncertainty about the coordinates of the mobiles, the iterative calculation between the cooperative mobiles is adopted. We let cooperative MS to transmit its belief N_d times between the time t to $t+1$. $[\mathbf{x}_j^{(t)}]_q^{(d)}$ denotes the q-th particles of the j-th MS position calculated at the d-th iteration which happens between the time t to $t+1$. For notation convenience, $[.]_q^{(d)}$ represents the q-th particle of the unknown variable at the d-th iteration. In each iteration, the MS first broadcasts its own belief. After receiving the others' beliefs, the whole measurement process is performed to update its belief. Before the noncooperative source broadcasts the signal at next time $t+1$, the cooperative MS can exchange their updated belief, recalculate the $[w_j^{(t)}]_q^{(d)}$ and resampling iteratively to refine the estimation.

Algorithm 8.1 Proposed CSN Method for j-th MS

initial state $[\mathbf{x}_j^{(0)}]_q$, $[\mathbf{s}_j^{(0)}]_q$, $[\mathbf{l}_j^{(0)}]_q$ $\forall q$
for $t = 1$ to T **do**
  for $q = 1$ to N_q **do**
    importance sampling: $[\mathbf{x}_j^{(t)}]_q^{(0)} \sim P(\mathbf{x}_j^{(t)} \mid [\mathbf{x}_j^{(t-1)}]_q)$, $[\mathbf{s}_j^{(t)}]_q^{(0)} \sim P(\mathbf{s}_j^{(t)} \mid [\mathbf{s}_j^{(t-1)}]_q)$, $[\mathbf{l}_j^{(t)}]_q^{(0)} \sim P(\mathbf{l}_j^{(t)} \mid [\mathbf{l}_j^{(t-1)}]_q)$
  end for
  broadcast self-belief $\{[\mathbf{x}_j^{(t)}]_q^{(0)}\}_{q=1}^{N_q}$ *%Quantization in Section 8.4.3*
  receive noncooperative measurement $\mathbf{y}_j^{(t)}$ and associated coordinates $\mathbf{a}_j$
  receive cooperative measurement $\mathbf{z}_j^{(t)}$ and associated beliefs $\{[\mathbf{x}_i^{(t)}]_q^{(0)}\}_{q=1}^{N_q}$ $(i = 1, ..., j, j+1, ...N)$
  weights computation according to (8.16)
  calculate $[\hat{\mathbf{x}}_j^{(t)}]^{(0)}$, $[\hat{\mathbf{s}}_j^{(t)}]^{(0)}$, $[\hat{\mathbf{l}}_j^{(t)}]^{(0)}$ according to (8.17)
  update self-belief $\{[\mathbf{x}_j^{(t)}]_q^{(1)}, [\mathbf{s}_j^{(t)}]_q^{(1)}, [\mathbf{l}_j^{(t)}]_q^{(1)}\}_{q=1}^{N_q} = resample(\{[\mathbf{x}_j^{(t)}]_q^{(0)}, [\mathbf{s}_j^{(t)}]_q^{(0)}, [\mathbf{l}_j^{(t)}]_q^{(0)}, [w_j^{(t)}]_q^{(0)}\}_{q=1}^{N_q})$
  for $d = 1$ to N_d **do**
    broadcast self-belief $\{[\mathbf{x}_j^{(t)}]_q^{(d)}\}_{q=1}^{N_q}$ *%Quantization in Section 8.4.3*
    receive beliefs from other MSs $\{[\mathbf{x}_i^{(t)}]_q^{(d)}\}_{q=1}^{N_q}$ $(i = 1, ..., j, j+1, ...N)$
    weights computation according to (8.16)
    calculate $[\hat{\mathbf{x}}_j^{(t)}]^{(d)}$, $[\hat{\mathbf{s}}_j^{(t)}]^{(d)}$, $[\hat{\mathbf{l}}_j^{(t)}]^{(d)}$ according to (8.17)
    update self-belief $\{[\mathbf{x}_j^{(t)}]_q^{(d+1)}, [\mathbf{s}_j^{(t)}]_q^{(d+1)}, [\mathbf{l}_j^{(t)}]_q^{(d+1)}\}_{q=1}^{N_q} = resample(\{[\mathbf{x}_j^{(t)}]_q^{(d)}, [\mathbf{s}_j^{(t)}]_q^{(d)}, [\mathbf{l}_j^{(t)}]_q^{(d)}, [w_j^{(t)}]_q^{(d)}\}_{q=1}^{N_q})$
  end for
  update estimation at time t: $\hat{\mathbf{x}}_j^{(t)} = [\hat{\mathbf{x}}_j^{(t)}]^{(N_d)}$, $\hat{\mathbf{s}}_j^{(t)} = [\hat{\mathbf{s}}_j^{(t)}]^{(N_d)}$, $\hat{\mathbf{l}}_j^{(t)} = [\hat{\mathbf{l}}_j^{(t)}]^{(N_d)}$ in (8.17)
  for $q = 1$ to N_q **do**
    update particles: $[\mathbf{x}_j^{(t)}]_q = [\mathbf{x}_j^{(t)}]_q^{(N_d+1)}$, $[\mathbf{s}_j^{(t)}]_q = [\mathbf{s}_j^{(t)}]_q^{(N_d+1)}$, $[\mathbf{l}_j^{(t)}]_q = [\mathbf{l}_j^{(t)}]_q^{(N_d+1)}$
  end for
end for

8.4 Simulations and Results

In this section, we provide several examples to illustrate the performance and effectiveness of the proposed cooperative navigation strategies. We name the proposed cooperative navigation method as CSN. We will test the three different strategies (A1), (A2), and (A3) described in Section 8.3.1 to deal with channel conditions. In addition, as a comparison, we also test the JMS-PF given by [89] as the noncooperative self-navigation method in conjunction with joint channel condition estimation.

We set $N_q = 500$ particles and iteration number $N_d = 0$. Recall that zero iteration number represents only prediction information exchanged between the MSs, where the noncooperative and cooperative measurements update once per sampling interval. We will further examine the iterative refinement effect in Example 8.4. We consider a random initialization in our simulation examples. We partition the area of consider into grids of $5m \times 5m$. At the start $t = 0$, we assume to know which grid the MSs are but not their exact positions. Thus, we draw initial position particles uniformly within the grid. We assume to know channel conditions within a 90% confidence interval, i.e., $P(\mathbf{s}_j^{(0)}) = P(\mathbf{l}_j^{(0)}) = 0.9$, where we draw particles uniformly with 90% of channel condition particles in the true channel state. We will further examine the imperfect knowledge of initial position and channel condition in Examples 8.5 and 8.6. We model MS movement as random walks in the simulations. We also assume to know the speed of the MS movement based on a pedometer but not its direction. This leads to the state equation in (8.3)

$$\mathbf{x}_j^{(t)} = \mathbf{x}_j^{(t-1)} + T_s \cdot v_j^{(t)} \cdot \begin{bmatrix} \cos\theta_j^{(t)} & \sin\theta_j^{(t)} \end{bmatrix}^T, \tag{8.18}$$

where the sampling interval is chosen as $T_s = 1$ second. The velocity $v_j^{(t)}$ is a truncated Gaussian distribution $v_j^{(t)} \sim \mathcal{N}(0,1)$ over interval $0 \le v_j^{(t)} \le \infty$. With the moving direction unknown, it is assumed to be uniformly distributed with $\theta_j^{(t)} \sim \mathcal{U}[0, 2\pi)$. Therefore, the particles of MS position are uniformly generated on the circle centered at $\mathbf{x}_j^{(t-1)}$ with the known radius of $v_j^{(t)}$.

We adopt the measurement model of [82], where the mean and variance of the Gaussian distribution are parameterized in the form of $\alpha d^2 + \beta d + \delta$ based on the true distance d. The noise distribution $P(y_{i,j}^{(t)}|s_{i,j}^{(t)})$ depends on the distance $d = \|\mathbf{a}_i - \mathbf{x}_j^{(t)}\|$ as in

$$P(y_{i,j}^{(t)}|s_{i,j}^{(t)}) = \begin{cases} \mathcal{N}(-0.003d^2 + 1.0075d - 0.0298, 0.0007) & s_{i,j}^{(t)} = 0 \\ \mathcal{N}(0.0099d^2 + 0.8263d + 0.6908, 0.0001d^2 - 0.0015d + 0.0056) & s_{i,j}^{(t)} = 1 \end{cases}. \tag{8.19}$$

Note that $P(z_{i,j}^{(t)}|l_{i,j}^{(t)})$ also possesses the same distribution as $P(y_{i,j}^{(t)}|s_{i,j}^{(t)})$ though it depends on the true distance between $\mathbf{x}_i^{(t)}$ and $\mathbf{x}_j^{(t)}$, i.e., $d = \|\mathbf{x}_i^{(t)} - \mathbf{x}_j^{(t)}\|$.

We use the *outage probability of the MS position error* [82] as the performance measure. In other words, we calculate the average probability that the MS position error exceeds a threshold

e_{th}:

$$P_{out}^{(t)}(e_{th}) = \sum_{i=1}^{P}\sum_{j=1}^{M} I(\|\mathbf{x}_j^{(t)} - \hat{\mathbf{x}}_j^{(t)}\| > e_{th})/(M \cdot P), \tag{8.20}$$

where $I(.)$ denotes the indicator function. Note that the outage probability averages over M mobiles in P trials. At the same time, we also adopt the root mean square error (RMSE) to assess the performance of proposed strategies as

$$RMSE^{(t)} = \left[\sum_{i=1}^{P}\sum_{j=1}^{M} \|\mathbf{x}_j^{(t)} - \hat{\mathbf{x}}_j^{(t)}\|^2/(M \cdot P)\right]^{1/2}. \tag{8.21}$$

Each simulation example lasts $T = 20$ seconds.

8.4.1 Fixed Number of Non-cooperative Measurements

In this subsection, we place three anchors as the fixed non-cooperative nodes in a two-dimensional network topology at $\mathbf{a}_1 = [5\ 50]$, $\mathbf{a}_2 = [50\ 50]$, and $\mathbf{a}_3 = [50\ 5]$. Four mobiles are located at $\mathbf{x}_1 = [20\ 25]$, $\mathbf{x}_2 = [25\ 20]$, $\mathbf{x}_3 = [25\ 30]$, and $\mathbf{x}_4 = [30\ 25]$. The number of simulation trials is $P = 1000$. The non-cooperative channel condition follows a Markov chain according to (8.4) with $p_0 = p_1 = 0.9$. On the other hand, the cooperative channel condition is modeled as LOS throughout the simulation period. Recall that the LOS/NLOS setting in the simulation is to examine how LOS cooperative measurements can provide assistance in the cooperative localization problem.

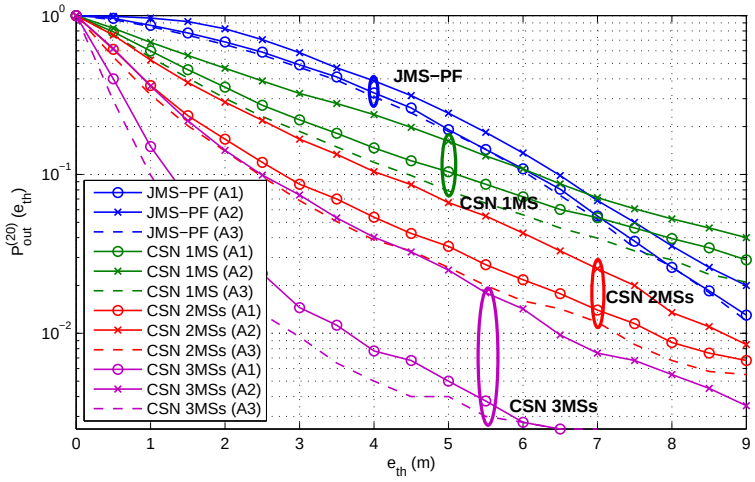

Figure 8.4: Performance of the location estimation in terms of outage probability for Example 8.1.

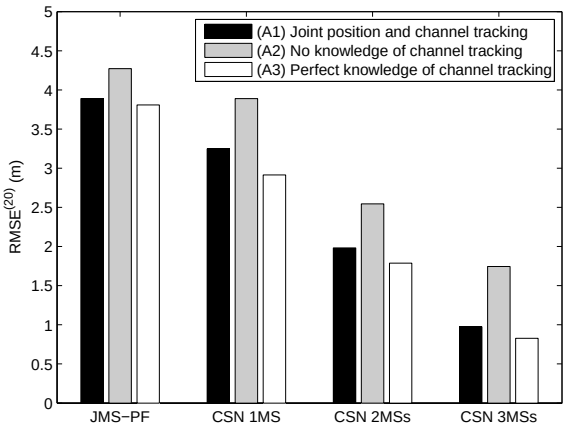

Figure 8.5: Performance of the location estimation in terms of RMSE for Example 8.1 with strategies (A1), (A2), and (A3).

Example 8.1 (1 noncooperative measurement)**.** In this example, each MS only receives one non-cooperative measurement from the anchor which is insufficient measurement in traditional localization problem. The numbers of cooperative measurements for the MSs are selected as one, two, and three in the simulations, respectively, and are labeled as 1MS, 2MSs, and 3MSs. At $t = 20$, Figs. 8.4 and 8.5, respectively, illustrate the outage probability and the RMSE of the JMS-PF, CSN with 1MS, CSN with 2MSs, and CSN with 3MSs based on three different strategies (A1), (A2), and (A3). Note that the outage probability increases with time owing to the random walk by the MS and the transition of channel conditions between LOS and NLOS. We observe that since strategy A2 has no knowledge on the channel state, it results in the worst performance given the same number of cooperative measurements. The reason is that, without the knowledge of channel state, we can only assume that LOS or NLOS occurs with 1/2 probability. Therefore, method A2 can provide as an upper bound of the outage probability for the proposed joint position and channel estimation scheme A1. On the other hand, strategy A3 is based on known channel, thereby providing a lower bound for the performance of A1. Our proposed joint position and channel estimation scheme A1 is a compromise between accurate position estimate and channel state estimate.

The simulation results illustrate little difference among the three strategies of the JMS-PF scheme. The reason is that a single non-cooperative measurement is sufficient for estimating mobile positions even with the available channel state information. On the other hand, joint CSN schemes can provide additional channel information which effectively reduce the RMSE of the MS. For example, as shown in Fig. 8.5, strategy A1 of the proposed CSN 3MS scheme can reduce the RMSE by about $0.9m$ versus that of strategy A2. Furthermore, there is a crossover between the JMS-PF and the CSN 1MS schemes as observed from Fig. 8.4, which indicates that the CSN 1MS scheme leads to higher outage probability under larger MS's position error. The reason is that

Table 8.1: The error percentage of channel tracking with strategy (A1) in Examples 8.1 and 8.2

	JMS-PF	CSN 1 MS	CSN 2MSs	CSN 3MSs
Example 8.1	22.94%	1.23%	0.57%	0.41%
Example 8.2	1.51%	0.66%	0.53%	-

the belief exchange among mobiles on estimated position can become inefficient in cases when the estimates are poor. With the increasing number of cooperative measurements, the diversity of measurement inputs can lower the effect of effect of poor MS location estimation. As illustrated in Fig. 8.4, compared to other schemes, CSN 3MS achieves better outage performance especially under larger MS's position error. Similar results can be observed from the RMSE performance of Fig. 8.5. The proposed CSN 3MS scheme in A1 can provide around $2.9m$ lower RMSE compared to JMS-PF.

On the other hand, the tracking performance of channel state should also be observed. For fair comparison between JMS-PF and CSN, we only consider the tracking performance of channel state for the noncooperative measurements, i.e., between the anchor and MS. The error percentage of channel tracking (P_c) is defined as the error between the actual channel state and its estimate:

$$P_c^{(t)} = \sum_{i=1}^{P}\sum_{t=1}^{T}\sum_{j=1}^{M}\frac{\|\mathbf{s}_j^{(t)} - \hat{\mathbf{s}}_j^{(t)}\|_1}{N \cdot M \cdot T \cdot P} \cdot 100(\%) \tag{8.22}$$

where $\|.\|_1$ denotes the ℓ_1 norm. Note that the number of anchors in this example is $N = 1$ and the total number of MSs is $M = 4$. As shown in Table 8.1, increasing the number of cooperative measurements can reduce the error of channel tracking, which validates the effectiveness of joint estimation for position and channel condition.

Example 8.2 (2 noncooperative measurements)**.** In this case, each MS receives measurement from two anchors. The number of cooperative mobile signals is 1 and 2, respectively, denoted as 1MS and 2 MS in Figs. 8.6 and 8.7. Under known channel condition, the performance difference between the noncooperative and cooperative cases is insignificant in this example compared to that in Example 8.1. This is because the extra noncooperative measurement in this example can provide additional information for estimating mobile locations. As shown in Fig. 8.7, similar RMSE performance is obtained for strategy A3 in all three schemes while significant performance difference is acquired in the schemes with strategy A1. The proposed CSN scheme can still provider better performance compared to the JMS-PF method, e.g., the CSN 2MSs case will provide around $0.3m$ less in RMSE in comparison with the JMS-PF scheme as in Fig. 8.7. Moreover, Table 8.1 shows better channel tracking by CSN over that of JMS-PF.

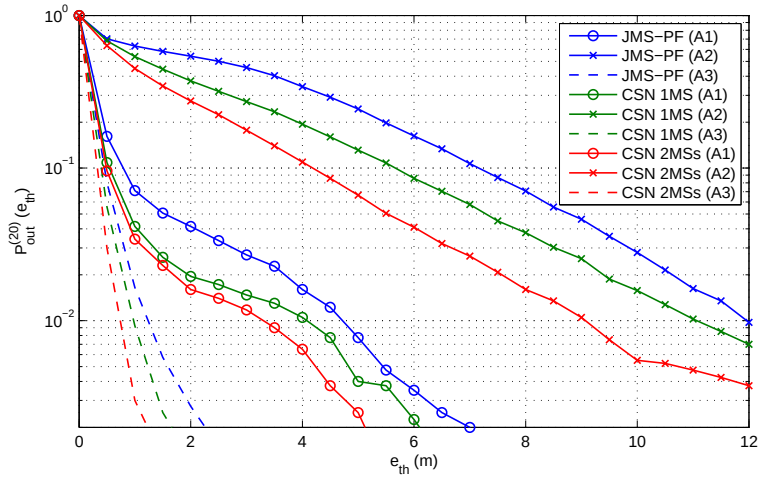

Figure 8.6: Performance of the location estimation in terms of outage Probability for Example 8.2

8.4.2 A Sensor Network Scenario

Example 8.3. In this example, a sensor network topology is confined in a $100m \times 100m$ space as shown in Fig. 8.8. There are 13 fixed anchors randomly distributed with known position and 50 dynamically moving mobiles during the simulation period. The transmission ranges for all the anchors and mobiles are limited to $20m$. For this topology, distributions of the average available numbers of noncooperative and cooperative measurements for the 50 mobiles are shown, respectively, in top and bottom plots of Fig. 8.9. Note that both the noncooperative and the cooperative measurements can be LOS or NLOS according to the Markov model. All other conditions remain the same as in previous examples.

As shown in Figs. 8.10 and 8.11, the proposed CSN can achieve lower outage probability and smaller RMSE in comparison with JMS-PF. For example, compared to JMS-PF, the CSN-A1 reduces outage probability by 0.27 for $e_{th} = 3m$ in Fig. 8.10 and lowers the RMSE by $2.3m$ in Fig. 8.11. From Fig. 8.10, we can conclude that the CSN results in substantial improvement over the noncooperative scheme in sensor networks. As indicated in Example 8.1, the cooperative scheme provides improvement over the insufficient measurement case. Even with the possibility of NLOS cooperative measurements in this example, CSN can still provide effective channel tracking, resulting in better location estimation performance.

Example 8.4. In this example, we study the number of iterations of belief propagation within each sampling interval. The test scenario in Example 8.3 is reconsidered. Recall that MSs only exchange their predictive beliefs when $N_d = 0$. If $N_d = 1$ or $N_d > 1$, the MSs exchange the posterior beliefs to further refine the belief. In Table 8.2, the improvement achieved by going from the zero to one iterative refinement is obvious. However, even larger iteration number does not appear to further improve the performance over $N_d = 1$, which demonstrates that one or two iterations would be

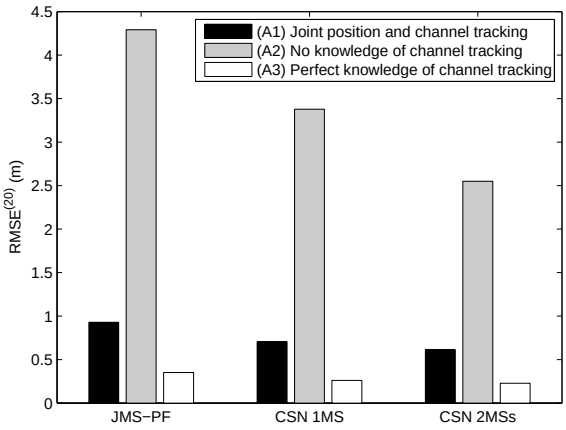

Figure 8.7: Performance of the location estimation in terms of RMSE for Example 8.2 with strategies (A1), (A2), and (A3).

Table 8.2: Iterative Belief Propagation Impact in Example 8.3

CSN(A1): Number of Iterations	$N_d = 0$	$N_d = 1$	$N_d = 2$	$N_d = 3$	JMS-PF(A1)
RMSE (m)	1.039	0.974	0.985	0.971	3.31

sufficient.

Example 8.5. We test the effect of initial position in this example. The test scenario in Example 8.3 is reconsidered, except for changes of initial position. In Table 8.3, we assign the initial particles as the true MS's position in the ideal case, e.g., $[\mathbf{x}_j^{(0)}]_q = \delta(\mathbf{x}_j^{(0)})\ \forall q$. We draw initial particles uniformly with a larger grid in a $10m \times 10m$ layout partition. As expected, the RMSE error increases for the noncooperative and cooperative case as the initial estimation error increases.

Example 8.6. In this example, we test the impact of initial channel condition. The test scenario in Example 8.3 is re-tested, except for the change of initial channel condition. In Table 8.4, we assign the initial particles as the true MS's position in the perfect case, e.g., $[\mathbf{s}_j^{(0)}]_q = \delta(\mathbf{s}_j^{(0)})\ \forall q$. The RMSE error increases for the noncooperative and cooperative case as the channel condition error increases.

Table 8.3: Initial Position Impact in Example 8.3

Knowledge of MS's Initial Position	Perfect	$5m \times 5m$ Region in Ex 8.3	$10m \times 10m$ Region
CSN(A1): RMSE$^{(20)}$ (m)	0.83	1.039	1.70
JMS-PF(A1): RMSE$^{(20)}$ (m)	3.14	3.31	3.84

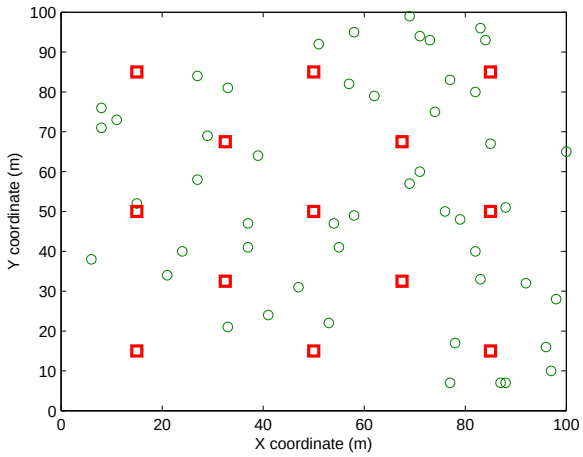

Figure 8.8: Network topology of Example 8.3: red squares represent the positions of the anchor; green circles represent the positions of the MS.

Table 8.4: Initial Channel Condition Impact in Example 8.3

Knowledge of MS's Initial Position	Perfect	$P(\mathbf{s}_j^{(0)}) = P(\mathbf{l}_j^{(0)}) = 0.9$ in Ex 8.3	$P(\mathbf{s}_j^{(0)}) = P(\mathbf{l}_j^{(0)}) = 0.5$
CSN(A1): RMSE (m)	0.89	1.039	1.22
JMS-PF(A1): RMSE (m)	3.23	3.31	3.42

8.4.3 Signaling of Cooperative Navigation

Recall that cooperative navigation requires additional information exchange among mobiles by letting mobiles broadcast their beliefs. Unlike the case involving only anchored nodes, MS moves and should broadcast its belief to other mobiles in each time instant. This signaling requires communication overhead. To lower the required bandwidth for belief broadcasting, we assume in this section that the mobile beliefs are quantized into finite bits before broadcasting. This is incorporated into Algorithm 8.1.

To demonstrate the effect of such quantization on mobile navigation, the test scenario in Example 8.3 is reconsidered using quantized beliefs. Note that there is no belief propagation and hence

Table 8.5: Communication Overhead for Quantized Belief Sharing and Estimation Accuracy in Example 8.3

CSN(A1): Number of Quantized Bits	$Q = 4$	$Q = 5$	$Q = 6$	$Q = 7$	$Q = 8$	CSN(A1)	JMS-PF(A1)
RMSE (m)	5.116	3.832	2.209	1.403	1.047	1.039	3.31
Quantization Error Standard Deviation (m)	1.804	0.902	0.451	0.226	0.113	0	0
Communication Overhead ($kbps$)	4	5	6	7	8	∞	0

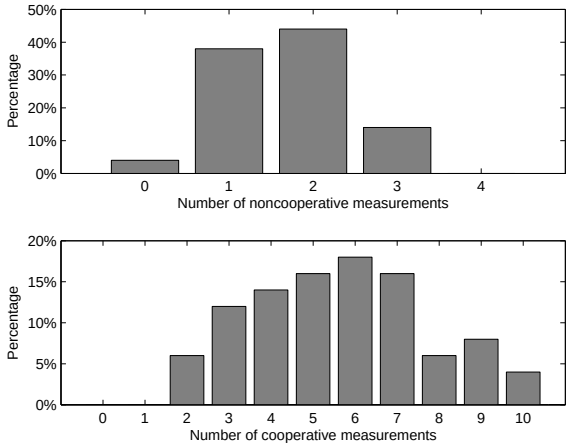

Figure 8.9: The distributions for the average available numbers of noncooperative and cooperative measurements for the 50 MSs in Example 8.3.

no quantization error for the noncooperative JMS-PF scheme. On the other hand, the full CSN algorithm broadcasts the full belief message without quantization, hence using infinite bandwidth. Quantizing the position particles results in the quantization error which degrades the performance of the proposed CSN scheme. But quantization of beliefs will be better than no belief exchange at all. Thus, the RMSE results of CSN and JMS schemes with strategy (A1) in Example 8.3 are provided in Table 8.5 as benchmarks for the quantized CSN performance.

In Example 8.3, the x- and y- coordinates lie in $[0, 100]$. We adopt the measure of "relative resolution" for a fixed-size layout to investigate the tradeoff between bandwidth requirement and estimation accuracy. Therefore, the quantized unit (δ) for the number of quantized bits (Q) is chosen according to the size of grid partition as $\delta = 100/2^Q$, e.g., the quantization unit is $\delta = 0.39$ for $Q = 8$. The quantization is performed by rounding, which causes the quantization error to be uniformly distributed. Thus, the quantization error has standard deviation of $\sqrt{\delta^2/12} = 0.1128$ for $Q = 8$. The communication overhead (T_o) is calculated according to the number of position particles and their quantized bits transmitted per second as $T_o = N_q \cdot m \cdot Q \cdot (N_d + 1)$, e.g., the communication overhead for a 2-dimensional position vector with 500 particles for $Q = 8$ is $T_o = 500 \cdot 2 \cdot 8 \cdot 2 = 16(kbps)$. As shown in Table 8.5, cooperative estimation is better than the noncooperative (JMS) scheme when more than 5 quantization bits are assigned. In fact, the performance of CSN with strategy (A1) given $Q = 8$ quantization bits can achieve the nearly identical performance to the non-quantization result. According to [94], IEEE 802.15.4 can be supported data rate up to $250(kbps)$. If $Q = 8$, a small communication overhead of $16(kbps)$ is feasible even for low rate sensor networks. This example reaffirms the practicality of the proposed cooperative navigation under limited sensor node bandwidth.

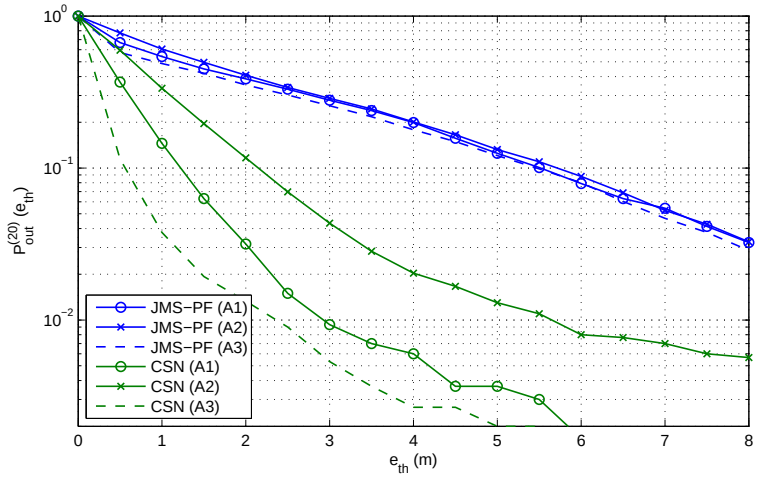

Figure 8.10: Performance of the location estimation in terms of outage probability for Example 8.3.

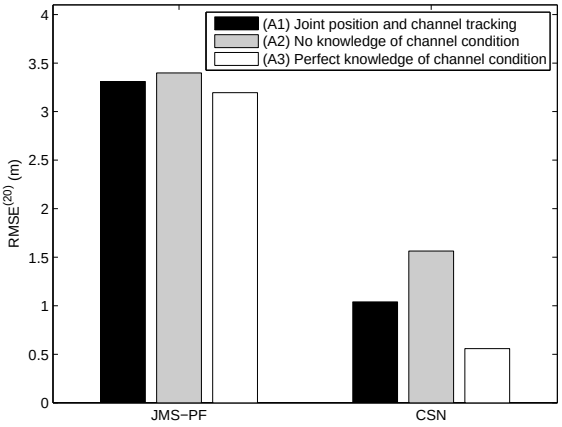

Figure 8.11: Performance of the location estimation in terms of RMSE for Example 8.3 with strategies (A1), (A2), and (A3).

8.5 Concluding Remarks

In this work, we investigate the problem of CSN in a mixed LOS/NLOS environment. We develop a method for CSN for a team of mobile units. We propose to apply multiple model SIR particle filter for joint estimation of mobile position and their channel conditions. We show the importance of channel condition tracking in a mixed LOS/NLOS environment for cooperative self-navigation. Our results demonstrate the significant performance advantage of CSN over noncooperative methods, especially in environment where LOS cooperative measurement can complement NLOS noncooperative measurements. Without a complex LOS/NLOS identification algorithm, our proposed scheme can provide feasible location estimation performance for mobile sensors in a highly dynamic sensor network scenario.

Chapter 9

Conclusions

The dissertation first illustrates an example on how to enable location based service (LBS) in the wireless network. We have studies the LBS of the fourth generation cellular network candidate, e.g., IEEE 802.16m system,

- Chapter 3 describes cellular-based location estimation using timing estimates for next generation telecommunication networks. Different ranging techniques are introduced and simulated with the standard LBS evolution methodology. By studying the performance of the downlink (DL) preamble measurement, inter-cell interference is found to be the limiting factor. On the other hand, uplink (UL) ranging measurement suffers hearability problem. Neither DL nor UL basic LBS support can achieve the performance requirement of emergency 911 (E-911). In DL measurements, the mobile station (MS) measures the secondary advanced preamble from the BSs which results in less network information exchange between base stations (BSs) and less power consumption. The properties provide the feasibility for DL LBS to be implemented in practice. Furthermore, the performance of the basic LBS support can be enhanced by adopting inter-cell cancellation methods at the physical layer or interference avoidance at the media access control (MAC) layer. The former approach utilizes signal processing techniques to cancel the interference with channel estimation. The performance for location estimation can be enhanced at the cost of increasing complexity at the receiver. On the other hand, the latter approach groups the preamble location groups (PLGs) to schedule concurrent transmission of BSs located within two cell-to-cell distances. The simulation results confirm that enhanced LBS support satisfies the requirement for E-911 positioning accuracy.

The dissertation second studies the behavior and fundamental limits of location estimation problem.

- Chapter 4 derives the linearized location estimation problem based Cramèr-Rao lower bound (L-CRLB) which provides the analytical form to discuss the geometric effect for the linear least square (LLS) estimator. The geometric properties and the relationships between the

L-CRLB and conventional CRLB are obtained with theoretical proofs. It is validated in the simulations that the L-CRLB can provide the tight lower bound for the LLS estimator, especially under the situations with smaller measurement noises. Moreover, the proposed L-CRLB can be utilized to describe the performance difference of an LLS estimator under different geometric layouts. The MS locates inside a BS-constrained geometry will provide higher estimation accuracy comparing with the case that the MS is situated outside of the BS-confined geometry layout.

Through the study of CRLB as shown in Remark 1, the limiting factors affect the estimation accuracy as: 1) geometric effect; 2) signal model or noise variance; 3) number of signal sources. The remaining dissertation has investigated and solved the limiting factors by utilizing the real-time statistical signal processing techniques.

- In Chapter 5, the geometry-assisted linearized localization (GALL) algorithm is proposed by fictitiously moving the base stations (BSs) in order to achieve the new geometric layout with minimum L-CRLB value in order to minimize the linearization lost. The GALL with two-step least squares (GALL-TSLS) implementation can enhance the estimation performance of the conventional TSLS estimator. By improving the initial estimation with the adoption of historical information, the GALL with Kalman filter (GALL-KF) scheme further outperforms the other location estimators with similar two-stage estimation structure.

- In Chapter 6, two different hybrid architectures for location estimation and tracking of mobile stations are proposed. By combining the satellite and the network-based systems, the proposed Fusion-based Hybrid architecture with Fixed-set of Signal Inputs (FH-FSI) can provide adequate precision for location estimation within existing infrastructure. Moreover, the Fusion-based Hybrid architecture with Selective-set of Signal Inputs (FH-SSI) further improves the estimation accuracy, especially under Non-Line-of-Sight environments. On the other hand, the Unified Hybrid (UH) architecture can achieve higher reliability for location estimation and tracking with its flexible architecture in most of the cases, even with deficient signal sources from the heterogeneous networks. It is shown in the simulation results that the proposed hybrid schemes can provide consistent location estimation accuracy under different environments.

- In Chapter 7, the Predictive Location Tracking (PLT) and the Geometric-assisted Predictive Location Tracking (GPLT) schemes are proposed. The predictive information obtained from the Kalman filtering formulation is exploited as the additional measurement inputs for the location estimator. With the feedback information, sufficient signal sources become available for location estimation and tracking of a mobile device. Moreover, the GPLT algorithm adjusts the locations of its virtual Base Stations based on the GDOP criterion. It is shown in

the simulation results that the proposed GPLT algorithm can provide consistent accuracy for location estimation and tracking even under the environments with insufficient signal sources.

- In Chapter 8, the problem of cooperative self-navigation in a mixed LOS/NLOS environment is investigated. We develop a method for cooperative self-navigation for a team of mobile units. We propose to apply particle filter for joint estimation of mobile position and their channel conditions. We show the importance of channel condition tracking in a mixed LOS/NLOS environment for cooperative self-navigation. Our results demonstrate the significant performance advantage of cooperative self-navigation over noncooperative methods, especially in environment where LOS cooperative measurement can complement NLOS noncooperative measurements. Without a complex LOS/NLOS identification algorithm, our proposed scheme can provide feasible location estimation performance for mobile sensors in a highly dynamic sensor network scenario.

9.1 Future Works

In this dissertation, we develop several mobile location estimation and tracking methods under various wireless networks. It is a challenging task to make the estimation accuracy approach to the performance limits. Given the measurements from the known position BSs in the location estimation problem, the performance is bounded by CRLB. There are two different directions to further improve the performance. Mobile location tracking enhances the performance by considering the time diversity and the movement model of the MS. Cooperative localization enhances the performance by considering the spatial diversity and the distributed. Therefore, cooperative location tracking or cooperative self-navigation (CSN) which combines the time and space diversity is regarded as a more accurate scheme compared to traditional location estimation scheme. There are still rich research topics in this field. For example,

- What is the tradeoff between the computational complexity and performance tradeoff for the CSN methods, i.e., reducing the computation complexity for the CSN methods?
- We consider a synchronous network for the CSN. What will happen if the CSN is employed in the asynchronous network?
- CSN requires extra communication overhead between MSs. Besides wireless sensor network, is the concept of cooperative localization acceptable by any other commercial standardized networks?

Besides mobile location estimation and tracking algorithms, one other important issue is to determine how many distance-related signals MSs should collect. This would refer to resource allocation problem for the mobile location estimation and tracking. For example, in a dedicated

location estimation system, such as globe positioning system (GPS) or wireless sensor network (WSN) deployed for the location estimation purpose,

- How many noncooperative or cooperative measurements are required to achieve the tradeoff between the signaling overhead and performance?
- In the geometric point of view, where should we place the anchors and which MSs should we cooperate to?

The resource allocation problem becomes more complicated in a general network system, which has been illustrated in Chapter 3. We know that at least three measurements orthogonally multiplexed possibly in frequency or in code should be collected in the location estimation problem. However, the purpose of the general network system is to increase the system throughput, i.e., utilizing as much bandwidth as possible. Although the frequency reuse concept can be utilized to avoid bandwidth waste in different region, the location estimation in a general network system occupies system resource which can be regarded as a system overhead. This arises an interesting resource allocation problem, e.g.,

- Given the position accuracy constraint, how many noncooperative or cooperative measurements are required to minimize the usage of resource?

References

[1] *Enhanced 911 - Wireless Services.* Federal Communication Commission. [Online]. Available: http://www.fcc.gov/pshs/services/911-services/(visitonFeb.2010)

[2] N. Patwari, J. N. Ash, S. Kyperountas, A. O. Hero III, R. L. Moses, and N. S. Correal, "Locating the Nodes: Cooperative Localization in Wireless Sensor Networks," *IEEE Signal Processing Mag.*, vol. 22, pp. 54–69, Jul. 2005.

[3] S. Gezici, Z. Tian, G. B. Giannakis, H. Kobayashi, A. F. Molisch, H. V. Poor, and Z. Sahinoglu, "Localization via Ultra-Wideband Radios: A Look at Positioning Aspects for Future Sensor Networks," *IEEE Signal Processing Mag.*, vol. 22, pp. 70–84, Jul. 2005.

[4] S. Hara, D. Zhao, K. Yanagihara, J. Taketsugu, K. Fukui, S. Fukunaga, and K. Kitayama, "Propagation Characteristics of IEEE 802.15.4 Radio Signal and Their Application for Location Estimation," in *IEEE Vehicular Technology Conference*, Jun. 2005, pp. 97–101.

[5] L.-W. Yeh, M.-S. Hsu, Y.-F. Lee, and Y.-C. Tseng, "Indoor localization: Automatically Constructing Today's Radio Map by iRobot and RFIDs," in *IEEE Sensors*, Oct. 2009, pp. 1463 –1466.

[6] S. Feng and C. L. Law, "Assisted GPS and Its Impact on Navigation in Intelligent Transportation Systems," in *Proc. IEEE 5th International Conference on Intelligent Transportation Systems*, 2002, pp. 926–931.

[7] P. Farradyne, *Vehicle Infrastructure Integration (VII) - Architecture and Functional Requirements*, draft version 1.0 ed., Apr. 2005.

[8] L. Perusco and K. Michael, "Control, Trust, Privacy, and Security: Evaluating Location-based Services," *IEEE Technol. Soc. Mag.*, vol. 26, pp. 4–16, Jul. 2007.

[9] J.-Y. Lee and R. Scholtz, "Ranging in a Dense Multipath Environment Using an UWB Radio Link," *IEEE J. Select. Areas Commun.*, vol. 20, no. 9, pp. 1677–1683, Dec. 2002.

[10] E. Xu, Z. Ding, and S. Dasgupta, "Reduced Complexity Semidefinite Relaxation Algorithms for Source Localization based on Time Difference of Arrival," *IEEE Trans. Mobile Comput.*, accepted in 2011.

[11] C. Meng, Z. Ding, and S. Dasgupta, "A Semidefinite Programming Approach to Source Localization in Wireless Sensor Networks," *IEEE Signal Processing Lett.*, vol. 15, pp. 253–256, 2008.

[12] D. Niculescu and B. Nath, "Ad Hoc Positioning System (APS) Using AOA," in *Proc. Conference on Computer Communications (INFOCOM 2003)*, vol. 3, Mar. 2003, pp. 1734–1743.

[13] C. Wang and L. Xiao, "Sensor Localization under Limited Measurement Capabilities," *IEEE Network*, vol. 21, no. 3, pp. 16–23, May 2007.

[14] C. Y. Lee, *Mobile Communications Engineering: Theory and Applications.* McGraw-Hall, 1998.

[15] H. Kuusniemi, A. Wieser, G. Lachapellea, and J. Takala, "User-level reliability monitoring in urban personal satellite-navigation," *IEEE Trans. Aerosp. Electron. Syst.*, vol. 43, pp. 1305–1318, Oct. 2007.

[16] J. J. Caffery, Jr., "A New Approach to the Geometry of TOA Location," in *IEEE Proc. Vehicular Technology Conf.*, Sep. 2000, pp. 1943–1949.

[17] Y. T. Chen and K. C. Ho, "A Simple and Efficient Estimator for Hyperbolic Location," *IEEE Trans. Signal Processing*, vol. 42, pp. 1905–1915, Aug. 1994.

[18] B. L. Le, K. Ahmed, and H. Tsuji, "Mobile Location Estimator with NLOS Mitigation Using Kalman Filtering," in *Proc. IEEE Wireless Communications and Networking Conference*, vol. 3, Mar. 2003, pp. 1969–1973.

[19] M. J. Goris, D. A. Gray, and I. M. Y. Mareels, "Reducing the computational load of a Kalman filter," *IEE Electronics Letters*, vol. 18, pp. 1539–1541, Aug. 1997.

[20] IEEE Std 802.16m-2011(Amendment to IEEE Std 802.16-2009), *IEEE Standard for Local and metropolitan area networks Part 16: Air Interface for Broadband Wireless Access Systems Amendment 3: Advanced Air Interface*, May 2011.

[21] C. L. Chen and K. F. Feng, "Hybrid Location Estimation and Tracking System for Mobile Devices," in *IEEE Vehicular Technology Conference*, Jun. 2005, pp. 2648–2652.

[22] W. H. Foy, "Position-Location Solutions by Taylor-Series Estimation," *IEEE Trans. Aerosp. Electron. Syst.*, vol. 12, pp. 187–194, Mar. 1976.

[23] C. Mensing, S. Sand, A. Dammann, and W. Utschick, "Interference-aware location estimation in cellular ofdm communications systems," in *IEEE International Conference on Communications, 2009 (ICC '09.)*, 14-18 2009, pp. 1–6.

[24] IEEE C802.16m-09/2314r2, "Proposed Text for Enhanced LBS Support (15.8.3)," Nov. 2009.

[25] IEEE C802.16m-09/2515, "Proposed Text on Enhanced LBS Support in Downlink," Nov. 2009.

[26] IEEE C802.16m-09/2202, "System Level Evaluation Assumptions for LBS Performance Analysis," Sep. 2009.

[27] IEEE 802.16m-08/004r5, "IEEE 802.16m Evaluation Methodology Document (EMD)," Jan. 2009.

[28] P. Bahl and V. N. Padmanabhan, "RADAR: an in-building RF-based user location and tracking system," in *IEEE INFOCOM*, 2000, pp. 775 –784.

[29] S.-P. Kuo and Y.-C. Tseng, "A Scrambling Method for Fingerprint Positioning Based on Temporal Diversity and Spatial Dependency," *IEEE Trans. Knowledge Data Eng.*, vol. 20, no. 5, pp. 678–684, May 2008.

[30] C.-L. Wang, D.-S. Wu, and F.-F. Shu, "Design and Implementation of a Decentralized Positioning System for Wireless Sensor Networks," in *IEEE Wireless Communications and Networking Conference (WCNC)*, Apr. 2010, pp. 1–6.

[31] D.-S. Wu and C.-L. Wang, "Decentralized Cooperative Positioning and Tracking Based on a Weighted Sign Algorithm for Wireless Sensor Networks," in *IEEE Global Telecommunications Conference (GLOBECOM)*, Dec. 2009, pp. 1–6.

[32] N. B. Priyantha, "The Cricket Indoor Location System," Ph.D. dissertation, Massachusetts Institute of Technology, Jun. 2005.

[33] K. W. Cheung, H. C. So, W. K. Ma, and Y. T. Chan, "Least Squares Algorithms for Time-of-arrival-based Mobile Location," *IEEE Trans. Signal Processing*, vol. 52, pp. 1121–1128, Apr. 2004.

[34] X. Wang, Z. Wang, and B. O'Dea, "A TOA-Based Location Algorithm Reducing the Errors Due to Non-Line-of-Sight (NLOS) Propagation," *IEEE Trans. Veh. Technol.*, vol. 52, pp. 112–116, Jan. 2003.

[35] K. Yu, "3-D Localization Error Analysis in Wireless Networks," *IEEE Trans. Wireless Commun.*, vol. 6, pp. 3473–3481, Oct. 2007.

[36] J. Chaffee and J. Abel, "GDOP and the Cramer-Rao Bound," in *IEEE Position Location and Navigation System (PLANS) Conference*, Apr. 1994, pp. 663–668.

[37] C. Chang and A. Sahai, "Estimation Bounds for Localization," in *IEEE Sensor and Ad Hoc Communications and Networks (SECON)*, Oct. 2004, pp. 415–424.

[38] Y. Qi, H. Kobayashi, and H. Suda, "Analysis of Wireless Geolocation in a Non-Line-of-Sight Environment," *IEEE Trans. Wireless Commun.*, vol. 5, pp. 672–681, Mar. 2006.

[39] Steven M. Kay, *Fundamentals of Statistical Signal Processing: Estimation Theory.* Prentice Hall, 1993.

[40] A. Beck, P. Stoica, and L. Jian, "Exact and Approximate Solutions of Source Localization Problems," *IEEE Trans. Signal Processing*, vol. 56, no. 5, pp. 1770–1778, May 2008.

[41] K. W. Cheung, W. K. Ma, and H. C. So, "Accurate approximation algorithm for TOA-based maximum likelihood mobile location using semidefinite programming," in *IEEE International Conference on Acoustics, Speech, and Signal Processing (ICASSP '04)*, vol. 2, May 2004, pp. 145–148.

[42] *Enhanced 911 - Wireless Services.* Federal Communication Commission. [Online]. Available: http://www.fcc.gov/911/enhanced/

[43] H.-P. Lin, R.-T. Juang, and D.-B. Lin, "Validation of an Improved Location-based Handover Algorithm using GSM Measurement Data," *Mobile Computing, IEEE Transactions on*, vol. 4, no. 5, pp. 530–536, Sep. 2005.

[44] Y. Zhao, "Standardization of Mobile Phone Positioning for 3G Systems," *IEEE Commun. Mag.*, vol. 40, pp. 108–116, Jul. 2002.

[45] J. H. Reed, K. J. Krizman, B. D. Woerner, and T. S. Rappaport, "An Overview of the Challenges and Progress in Meeting the E-911 Requirement for Location Service," *IEEE Commun. Mag.*, vol. 36, pp. 30–37, Apr. 1998.

[46] Y. T. Chan, C. H. Yau, and P. C. Yau, "Linear and Approximate Maximum Likelihood Localization from TOA Measurements," in *Proc. IEEE 7th International Symposium on Signal Processing and Its Applications*, vol. 2, Jul. 2003, pp. 295–298.

[47] D. Porcino, "Performance of a OTDOA-IPDL Positioning Receiver for 3GPP-FDD Mode," in *Proc. IEE 3G Mobile Communication Technologies*, Mar. 2001, pp. 221–225.

[48] *Location Technologies for GSM, GPRS, and UMTS Network.* SnapTrack Inc. [Online]. Available: http://www.snaptrack.com/

[49] *GPS Guide: for beginners.* Garmin Corporation. [Online]. Available: http://www.garmin.com/aboutGPS/manual.html

[50] K. Wang, L. Yan, H. Wen, and K. He, "GpsOne: A New Solution to Vehicle Navigation," in *Proc. IEEE Position Location and Navigation Symposium*, Apr. 2004, pp. 341–346.

[51] G. R. Iverson, *Bayesian Statistical Inference.* Beverly Hills, 1984.

[52] T. K-Ostmann and A. E. Bell, "A Data Fusion Architecture for Enhanced Position Estimation in Wireless Networks," *IEEE Commun. Lett.*, vol. 5, pp. 343–345, Aug. 2001.

[53] *3rd Generation Partnership Project (3GPP) Specifications Release 8.* 3GPP TS 21.101. [Online]. Available: http://www.3gpp.org/specs/releases.htm

[54] *Draft Standard for Local and Metropolitan Area Networks Part 16: Air Interface for Broadband Wireless Access Systems*, IEEE Std 802.16 Rev3 (Revision of IEEE Std 802.16-2004), 2008.

[55] L. Cong and W. Zhuang, "Nonline-of-Sight Error Mitigation in Mobile Location," *IEEE Trans. Wireless Commun.*, vol. 4, pp. 560–573, Mar. 2005.

[56] Y.-T. Chan, W.-Y. Tsui, H.-C. So, and P.-C. Ching, "Time-of-Arrival Based Localization Under NLOS Conditions," *IEEE Trans. Veh. Technol.*, vol. 55, pp. 17–23, Jan. 2006.

[57] L. M. Kaplan, "Global Node Selection for Localization in a Distributed Sensor Network," *IEEE Trans. Aerosp. Electron. Syst.*, vol. 42, pp. 114–135, Jan. 2006.

[58] ——, "Local Node Selection for Localization in a Distributed Sensor Network," *IEEE Trans. Aerosp. Electron. Syst.*, vol. 42, pp. 136–146, Jan. 2006.

[59] J. Liu, M. Lu, X. Cui, and Z. Feng, "Theoretical Analysis of RAIM in the Occurrence of Simultaneous Two-Satellite Faults," *IET Trans. Radar Sonar Navig.*, vol. 1, pp. 92–97, Apr. 2007.

[60] J. B.-Y. Tsui, *Fundamentals of Global Positioning System Receivers: A Software Approach.* John Wiley & Sons Inc.

[61] K.-T. Feng, C.-L. Chen, and C.-H. Chen, "GALE: An Enhanced Geometry-Assisted Location Estimation Algorithm for NLOS Environments," *IEEE Trans. Mobile Comput.*, vol. 7, pp. 199–213, Feb. 2008.

[62] Y. Yong and M. Lingjuan, "GDOP Results in All-in-view Positioning and in Four Optimum Satellites Positioning with GPS PRN Codes Ranging," in *Proc. IEEE Position Location and Navigation Symposium*, Apr. 2004, pp. 723–727.

[63] N. Levanon, "Lowest GDOP in 2-D scenarios," in *Proc. IEE Radar, Sonar and Navigation*, Jun. 2000, pp. 149–153.

[64] B. S. Pervan, D. G. Lawrence, C. E. Cohen, and B. W. Parkinson, "Parity Space Methods for Autonomous Fault Detection and Exclusion Using GPS Carrier Phase," in *Proc. IEEE Position Location and Navigation Symposium*, Apr. 1996, pp. 649–656.

[65] M. S. Phatak, "Recursive Method for Optimum GPS Satellite Selection," *IEEE Trans. Aerosp. Electron. Syst.*, vol. 37, pp. 751–754, Apr. 2001.

[66] S. A. Jazzar, J. C. Jr., and H. R. You, "A Scattering Model Based Approach to NLOS Mitigation in TOA Location Systems," in *Proc. IEEE Vehicular Technology Conference*, May 2002, pp. 861–865.

[67] S.-S. Woo, H.-R. You, and J.-S. Koh, "The NLOS Mitigation Technique for Position Location Using IS-95 CDMA Networks," in *Proc. IEEE Vehicular Technology Conference*, Sep. 2000, pp. 2556–2560.

[68] P. C. Chen, "A Non-Line-of-Sight Error Mitigation Algorithm in Location Estimation," in *Proc. IEEE Wireless Communications and Networking Conference*, Sep. 1999, pp. 316–320.

[69] L. Cong and W. Zhuang, "Hybrid TDOA/AOA Mobile User Location for Wideband CDMA Cellular Systems," *IEEE Trans. Wireless Commun.*, vol. 1, pp. 439–447, Jul. 2002.

[70] T. H. Cormen, C. E. Leiserson, R. L. Rivest, and C. Stein, *Introduction to Algorithms*. The MIT Press, 2001.

[71] *Satscape Homepage - Freeware Satellite Tracker*. [Online]. Available: http://www.satscape.co.uk

[72] T. Liu, P. Bahl, and I. Chlamtac, "Mobility Modeling, Location Tracking, and Trajectory Prediction in Wireless ATM Networks," *IEEE J. Select. Areas Commun.*, vol. 16, pp. 922–936, Aug. 1998.

[73] Z. R. Zaidi and B. L. Mark, "Real-time mobility tracking algorithms for cellular networks based on Kalman filtering," *IEEE Trans. Mobile Comput.*, vol. 4, pp. 195–208, Mar. 2005.

[74] R. G. Brown and P. Y. Hwang, *Introduction to Random Signals and Applied Kalman Filtering*, 3rd ed. New York: John Wiley & Sons, 1997.

[75] J. Shuhong, S. Xicai, and K. Fanru, "A Time-of Arrival Location Algorithm for Maneuvering Target on Two-dimensional Surface," in *IEEE International Conference on Signal Processing*, Oct. 1998, pp. 1700–1703.

[76] M. Nájar and J. Vidal, "Kalman Tracking Based on TDOA for UMTS Mobile Location," in *IEEE International Symposium on Personal, Indoor and Mobile Radio Communications*, Sep. 2001, pp. 45–49.

[77] ——, "Kalman Tracking for Mobile Location in NLOS Situations," in *IEEE International Symposium on Personal, Indoor and Mobile Radio Communications*, Sep. 2003, pp. 2203–2207.

[78] Y. Qi, T. Asai, H. Yoshino, and N. Nakajima, "On Geolocation in Ill-Conditioned BS-MS Layouts," in *IEEE International Conference on Acoustics, Speech, and Signal Processing Proceedings*, Mar. 2005, pp. 697–700.

[79] P. C. Chen, "A Cellular Based Mobile Location Tracking," in *IEEE Vehicular Technology Conference*, May 1999, pp. 1979–1983.

[80] A. Sayed, A. Tarighat, and N. Khajehnouri, "Network-based Wireless Location: Challenges Faced in Developing Techniques for Accurate Wireless Location Information," *IEEE Signal Processing Mag.*, vol. 22, no. 4, pp. 24–40, Jul. 2005.

[81] Y. Shen, H. Wymeersch, and M. Z. Win, "Fundamental Limits of Wideband Localization - Part II: Cooperative Networks," *IEEE Trans. Inform. Theory*, vol. 56, no. 10, pp. 4981 –5000, Oct. 2010.

[82] H. Wymeersch, J. Lien, and M. Z. Win, "Cooperative Localization in Wireless Networks," *Proc. IEEE*, vol. 97, no. 2, pp. 427–450, Feb. 2009.

[83] A. T. Ihler, J. W. Fisher III, R. L. Moses, and A. S. Willsky, "Nonparametric Belief Propagation for Self-Localization of Sensor Networks," *IEEE J. Select. Areas Commun.*, vol. 23, no. 4, pp. 809–819, Apr. 2005.

[84] M. Heidari and K. Pahlavan, "Markov Model for Dynamic Behavior of Ranging Errors in Indoor Geolocation Systems," *IEEE Commun. Lett.*, vol. 11, no. 12, pp. 934–936, Dec. 2007.

[85] J.-F. Liao and B.-S. Chen, "Robust Mobile Location Estimator with NLOS Mitigation using Interacting Multiple Model Algorithm," *IEEE Trans. Wireless Commun.*, vol. 5, no. 11, pp. 3002–3006, Nov. 2006.

[86] B.-S. Chen, C.-Y. Yang, F.-K. Liao, and J.-F. Liao, "Mobile Location Estimator in a Rough Wireless Environment Using Extended Kalman-Based IMM and Data Fusion," *IEEE Trans. Veh. Technol.*, vol. 58, no. 3, pp. 1157–1169, Mar. 2009.

[87] C. Fritsche, U. Hammes, A. Klein, and A. M. Zoubir, "Robust Mobile Terminal Tracking in NLOS Environments using Interacting Multiple Model Algorithm," in *IEEE International Conference on Acoustics, Speech and Signal Processing (ICASSP)*, Apr. 2009, pp. 3049–3052.

[88] C. Morelli, M. Nicoli, V. Rampa, and U. Spagnolini, "Hidden Markov Models for Radio Localization in Mixed LOS/NLOS Conditions," *IEEE Trans. Signal Processing*, vol. 55, no. 4, pp. 1525–1542, Apr. 2007.

[89] M. Nicoli, C. Morelli, and V. Rampa, "A Jump Markov Particle Filter for Localization of Moving Terminals in Multipath Indoor Scenarios," *IEEE Trans. Signal Processing*, vol. 56, no. 8, pp. 3801–3809, Aug. 2008.

[90] L. Chen, S. Ali-Lytty, R. Pich, and L. Wu, "Mobile Tracking in Mixed Line-of-Sight/Non-Line-of-Sight Conditions: Algorithm and Theoretical Lower Bound," *Wireless Personal Communications*, pp. 1–19, 2011.

[91] S. McGinnity and G. Irwin, "Multiple Model Bootstrap Filter for Maneuvering Target Tracking," *IEEE Trans. Aerosp. Electron. Syst.*, vol. 36, no. 3, pp. 1006–1012, Jul, 2000.

[92] M. S. Arulampalam, S. Maskell, N. Gordon, and T. Clapp, "A Tutorial on Particle Filters for Online Nonlinear/Non-Gaussian Bayesian Tracking," *IEEE Trans. Signal Processing*, vol. 50, no. 2, pp. 174–188, Feb. 2002.

[93] G. Kitagawa, "Monte Carlo Filter and Smoother for Non-Gaussian Nonlinear State Space Models," *Journal of Computational and Graphical Statistics*, vol. 5, no. 1, pp. 1–25, 1996.

[94] *LAN/MAN Standards Committee of the IEEE Computer Society, IEEE Standard for Part 15.4: Wireless Medium Access Control (MAC) and Physical Layer (PHY) Specifications for Low Rate Wireless Personal Area Networks (LR-WPANs)*, IEEE, 2006.

Publication List

Paper in Submission

S-4. Cheng-Tse Chiang, Po-Hsuan Tseng, and Kai-Ten Feng, "Hybrid Unified Kalman Tracking Algorithms for Heterogeneous Wireless Location Systems,"

S-3. Po-Hsuan Tseng and Kai-Ten Feng, "Geometry-Assisted Linearized Localization Algorithms for Wireless Networks,"

S-2. Po-Hsuan Tseng and Kai-Ten Feng, "Geometric Analysis of Linear Least Squares Estimator for Wireless Location Systems,"

S-1. Po-Hsuan Tseng, Zhi Ding, and Kai-Ten Feng, "Cooperative Self-Navigation in a Mixed LOS and NLOS Environment,"

Journal Paper

J-3. Po-Hsuan Tseng, Kai-Ten Feng, Yu-Chiun Lin, and Chao-Lin Chen , "Wireless Location Tracking Algorithms for Environments with Insufficient Signal Sources," in *IEEE Trans. on Mobile Computing*, vol.8, issue 12, pp. 1676 - 1689, Dec. 2009

J-2. Po-Hsuan Tseng and Kai-Ten Feng, "Hybrid Network/Satellite-Based Location Estimation and Tracking Systems for Wireless Network," *IEEE Trans. on Vehicular Technology*, Vol.58, Issue 9, pp. 5174 - 5189, Nov. 2009

J-1. Chien-Hua Chen, Kai-Ten Feng, Chao-Lin Chen, and Po-Hsuan Tseng, "Wireless Location Estimation with the Assistance of Virtual Base Stations," *IEEE Trans. on Vehicular Technology*, Vol. 58, Issue 1, pp. 93 - 106, Jan. 2009

Book Chapter

B-1. Po-Hsuan Tseng, and Kai-Ten Feng, "Chapter 31. Cellular-based Positioning for Next Generation Telecommunication Systems," accept and to appear as a book chapter of *Handbook of Position Location: Theory, Practice and Advances*, Wiley-IEEE Press, ISBN: 978-0-470-94342-7

Conference Paper

C-9. Cheng-Tse Chiang, Po-Hsuan Tseng, and Kai-Ten Feng, "Hybrid TOA/TDOA Based Unified Kalman Tracking Algorithm for Wireless Networks," in Proc. *IEEE International Symposium on Personal, Indoor and Mobile Radio Communications (PIMRC 2010)*, Istanbul, Turkey, 27 Sep 2010

C-8. Po-Hsuan Tseng and Kai-Ten Feng, "An Enhanced Predictive Location Tracking Scheme with Deficient Signal Sources for Wireless Networks," in Proc. *IEEE International Symposium on Personal, Indoor and Mobile Radio Communications (PIMRC 2009)*, Tokyo, Japan, 14 Sep. 2009, pp. 1913 - 1917

C-7. Kai-Ten Feng, Wen-Hsuan Fan, and Po-Hsuan Tseng, "Lifetime-Enhanced Adaptive Routing Protocol for Mobile Ad Hoc Networks, in Proc. *IEEE VTS Asia Pacific Wireless Communications Symposium (APWCS 2009)*, 21 Aug. 2009, Seoul, Korea

C-6. Lin-Chih Chu, Po-Hsuan Tseng, and Kai-Ten Feng, "GDOP-Assisted Location Estimation Algorithms in Wireless Location Systems," in Proc. *IEEE Global Communications Conference (GLOBECOM 2008)*, New Orleans, USA, 3 Dec. 2008, pp. 1 - 5

C-5. Po-Hsuan Tseng and Kai-Ten Feng, "Location Tracking Assisted Handover Algorithms for Broadband Wireless Networks," in Proc. *IEEE International Symposium on Personal, Indoor and Mobile Radio Communications (PIMRC 2008)*, Cannes, France, 18 Sep. 2008, pp. 1 - 5

C-4. Po-Hsuan Tseng and Kai-Ten Feng, "A Predictive Movement Based Handover Algorithm for Broadband Wireless Networks," in Proc. *IEEE Wireless Communication and Networking Conference (WCNC 2008)*, Las Vegas, US, 3 Apr. 2008, pp. 2834 - 2839

C-3. Hsin-Lung Tseng, Yu-Pin Hsu, Chung-Hsien Hsu, Po-Hsuan Tseng, and Kai-Ten Feng, "A Maximal Power-Conserving Scheduling Algorithm for Broadband Wireless Networks," in Proc. *IEEE Wireless Communication and Networking Conference (WCNC 2008)*, Las Vegas, US, 3 Apr. 2008, pp. 1877 - 1882

C-2. Yu-Chiun Lin, Po-Hsuan Tseng, and Kai-Ten Feng, "A Predictive Location Tracking Algorithm for Mobile Devices with Deficient Signal Sources," in Proc. *IEEE Vehicular Technology Conference Spring (VTC2007-Spring)*, Dublin, Ireland, 25 Apr. 2007, pp. 859 - 863

C-1. Po-Hsuan Tseng, Chao-Lin Chen, and Kai-Ten Feng, "An Unified Kalman Tracking Technique for Wireless Location Systems," in Proc. *IEEE 2nd International Symposium on Wireless Pervasive Computing (ISWPC 2007)*, San Juan, Puerto Rico, 8 Feb. 2007

Technical Contribution

T-3. 3GPP RAN WG1#59 R1-100447, "Performance of UTDOA Using LMUs," 2010/01/18 - 01/22

T-2. IEEE C802.16m-09/1901, "Hybrid Measurement-Based Methods for LBS (LBS)," (Po-Hsuan Tseng, Kai-Ten Feng, Yih-Shen Chen, Paul Cheng; 2009-08-29)

T-1. IEEE C802.16m-08/1034r1, "Location Update Mechanism for IEEE 802.16m Location Based Service," (Mei-Dai Chen, Po-Hsuan Tseng, Stanley Hsu, Kai-Ten Feng and Paul Cheng; 2008-09-12)

Submitted Patent

P-2. Hsin-Lung Tseng, Yu-Pin Hsu, Chung-Hsien Hsu, Po-Hsuan Tseng, and Kai-Ten Feng, "Power-Saving Scheduling Method of Mobile Subscriber Station of Broadband Wireless Network," submitted to *U.S. Patent* in Apr. 2008

P-1. Po-Hsuan Tseng and Kai-Ten Feng, "Predictive Movement-Based Handover Method and System for Cellular Networks," submitted to *U.S. Patent* in Mar. 2008

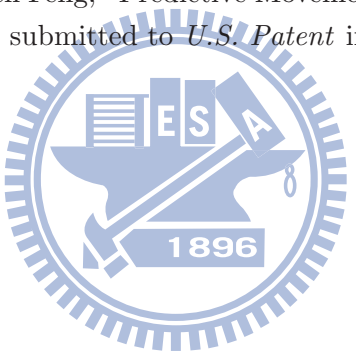

Vita

Po-Hsuan Tseng received the Ph.D. degree in the Institute of Communications Engineering in 2011 from the National Chiao Tung University, Hsinchu, Taiwan, where he recieved the B.S. degree with the Department of Communication Engineering in 2005. From January 2010 to October 2010, he was also a visiting researcher in University of California, Davis. His current research interests include statistical signal processing, wireless location estimation and tracking technologies, and MAC protocol design for mobile broadband wireless network system.

- Citizenship: Taiwan, R.O.C.
- Education: **National Chiao Tung University**, Taiwan
  - . **Ph.D.**, Institute of Communications Engineering **Sep. 2006 to May 2011**
    - ∗ Advisor: Prof. Kai-Ten Feng
  - . **M.S. program**, Institute of Communications Engineering **Sep. 2005 to June 2006**
    - ∗ Area of Study: Network Communications
  - . **B.S.**, Department of Communication Engineering **Sep. 2001 to June 2005**
- Awards
  - – Graduate Students Study Abroad Program Scholarship by NSC *2010*
  - – CTCI Foundation Scholarship *2009*
  - – NCTU Award for Outstanding Teaching Assistant *Sep. 2008*
  - – Pre-Ph.D Teacher Assistance Scholarship *Fall 2007, Spring 2008, Fall 2008*
  - – NCTU-MediaTek Research Center Outstanding Student Research Award *July 2007*
  - – Ph.D Student Scholarship by NCTU/CM *Fall 2006, Spring 2007, Spring 2008*
  - – 3rd Educational Scholarship from OKWAP Inc. *July 2006*
  - – Garmin Ltd. Graduate Student Scholarship *May 2006*
  - – Presidential Award NCTU/CM *Fall 2005*
  - – Graduate Entrance Scholarship NCTU/CM *2005*